UNIVERSITY OF CALIFORNIA
RIVERSIDE

Development of New Portable Flow Tubes to Study Secondary Aerosol: Designs, Characterizations and Applications

A Dissertation submitted in partial satisfaction
of the requirements for the degree of

Doctor of Philosophy

in

Chemical and Environmental Engineering

by

Ningjin Xu

March 2023

Dissertation Committee:
Dr. Don R. Collins, Chairperson
Dr. David R. Cocker III
Dr. Haofei Zhang

The Dissertation of Ningjin Xu is approved:

Chairperson

Committee

Committee

University of California, Riverside

Acknowledgements

I would like to thank many individuals for making my success at UCR.

First, I would like to thank my advisor, Dr. Don R. Collins, for his unlimited support on my projects and the topics he gave me to work on that interest me. I am extremely fortunate to meet him during new student symposium and join his group in 2018. He is humble and responsive to his students. He is always there whenever I am struggling with my projects. I like to stop by his office, chat with him about my problems, and listen to his suggestions, which always helps me solve the issues. I appreciate his patience on editing my writing. Thanks again for his support throughout my Ph.D. program.

I would like to thank Dr. David R. Cocker III for his continued help with my VOC project and his kind instruction on AMS operation. I also want to thank him for introducing the fundamental knowledge of aerosol and techniques in ENVE 133 class when I just transfer my research area from green energy devices to aerosol and oxidation flow reactor design.

I would like to thank Dr. Haofei Zhang for serving as my committee chair. I still remember the time I went to ask him if he can serve as my committee member during my qualifying exam and he replied “Yes, I am glad to be your committee member” immediately. I appreciate his suggestions on my qualifying exam and generously insights on my future work.

I would like to thank Dr. Roya Bahraini for her continued help and support with my CARB and DMS projects and her kind instruction on AMS operation. And thanks for organizing

the biweekly meeting for DMS project and I appreciate your suggestions and comments on the DMS manuscript. I would like to thank Dr. Ying-Hsuan Lin for her generous support on the CIMS measurements for VOC and DMS projects. I appreciate your suggestions on the DMS meeting and I always benefit from some random chats with her about the project I am working on.

I would like to thank Dr. Alex B. MacDonald and Yumeng Cui for their supports on AMS operation for the CARB and DMS projects. I would like to thank the former and current Collins group members Candice Sirmollo, Zihan Zhu, Xuanlin Du, Ying Zhou, and all the undergraduate students, from whom I got a lot of assistance, support, such as research ideas, background knowledge, instrumentation, scientific writing, and plotting etc.

I would like to recognize the funding sources including California Air Resources Board (CARB), National Science Foundation (NSF) for the projects that made this dissertation possible.

The text of Chapter 2 of this dissertation, in part or in full, is reprinted from Atmos. Meas. Tech paper, No. 14-2891-2021; Xu and Don R. Collins. Design and characterization of a new oxidation flow reactor for laboratory and long-term ambient studies, Copyright (2021), with permission from AMT. The text of Chapter 3 of this dissertation, in part or in full, is reprinted from Atmos. Meas. Tech preprint amt-2022-285; Ningjin Xu, Chen Le, David R. Cocker, and Don R. Collins. An oxidation flow reactor for simulating and accelerating secondary aerosol formation in aerosol liquid water and cloud droplets, Copyright (2022), with permission from AMT.

Dedication

I dedicate this work to my father Changchun Xu, mother Hui Xu for their love, understanding of and support throughout my whole life.

ABSTRACT OF THE DISSERTATION

Development of New Portable Flow Tubes to Study Secondary Aerosol: Designs, Characterizations and Applications

by

Ningjin Xu

Doctor of Philosophy, Graduate Program in Chemical and Environmental Engineering
University of California, Riverside, March 2023
Dr. Don R. Collins, Chairperson

Atmospheric secondary aerosol (SA) is comprised of an array of low volatility organic and inorganic compounds that are produced from atmospheric chemical reactions. It contributes significantly to overall aerosol burden and, consequently, plays an important role in air quality and regional and global climate change. Secondary organic aerosol (SOA), which makes up a substantial fraction of SA, forms when reaction of volatile organic compounds (VOCs) with gas-phase oxidants (e.g., O_3, OH radical, and NO_3 radical) produces less-volatile functionalized compounds followed by nucleation and/or gas-particle partitioning (gasSOA). An alternative pathway is when water-soluble organics dissolve in the aqueous phase (aerosol water or cloud droplets) and are subsequently oxidized (aqSOA). Most traditional investigations of SA formation in the laboratory have been carried out in environmental smog chambers. For the past decade or so, oxidation flow reactors (OFRs) have been increasingly used to study the formation and evolution of secondary aerosol in the atmosphere and have become valuable tools for improving the accuracy of model simulations and for depicting and accelerating realistic atmospheric

chemistry. However, the pathways and mechanisms of SOA formation via aqueous-phase chemistry in aqueous aerosols and clouds have received comparatively little attention compared with that involving only gas-phase chemistry.

In this dissertation, driven by rapid development of OFR techniques and the increasing appreciation of their wide application, a number of studies were carried out to understand the formation and evolution of SA formation under both gas- and aqueous-phase oxidation. This includes the designs of two newly-built all-Teflon reactors – the Particle Formation Accelerator (PFA) and the Accelerated Production and Processing of Aerosols (APPA) reactor, intended for the study of gas-phase atmospheric chemistry and aqueous secondary aerosol (aqSA) formation.

Characterization tests of the two reactors have been performed. Computational fluid dynamics (CFD) simulations were combined with experimental determination of the residence time distribution (RTD) to optimize the flow tube design and the atmospheric relevance of the measurements. Studies of SA produced via gas-phase oxidation and subsequent partitioning (gasSA) were carried out in the PFA and APPA reactors operating in low RH mode, for which no liquid water was initially present. These studies include gasSA yields from various precursors in a laboratory environment and ambient observation in Riverside. The potential applications of measurement of SA formation though aqueous phase oxidation in the APPA reactor will be presented in the second part. Several studies of aqSA formation using the APPA reactor are presented, including developing a description of the relative gas phase and aqueous phase yields from different precursors,

quantifying the sensitivity of the aqSA to several parameters (droplet surface area concentration, droplet pH, temperature, and particle composition) and exploring brown carbon formation from aqueous SA and droplet evaporation during one or more field studies.

Table of Contents

List of Figures

List of Tables

Acronyms and Abbreviations

ALW	Aerosol liquid water
aqSOA	SOA formation through aqueous-phase oxidation
aqSA	Aqueous-phase secondary aerosol
APPA	Accelerated Production and Processing of Aerosols reactor
AS	Ammonium sulfate
APS	Aerodynamic particle sizer
CARB	California Air Resources Board
CE-CERT	College of Engineering-Center for Environmental Research and Technology (University of California, Riverside)
CPOT	Caltech Photooxidation Flow Tube
CFD	Computational fluid dynamics
CPC	Condensation particle counter
CESM2	Community Earth System Model Version 2
DMA	Differential mobility analyzer
D_p	Particle diameter
DMS	Dimethyl sulfide
ECCC-OFR	Environment and Climate Change Canada OFR
ER	Relative enhancement
EPA	Environmental Protection Agency
ePTFE	Expanded PTFE

FIGAERO-ToF-CIMS .....Time-of-flight chemical ion mass spectrometry implemented with the Filter Inlet for Gases and AEROsols system

gasSA .....Gas-phase secondary aerosol

GAMMA.....Gas-Aerosol Model for Mechanism Analysis

GC-FID .....Gas chromatograph with flame ionization detector

HR-ToF-AMS .....Aerodyne high-resolution time-of-flight aerosol mass spectrometer

H_2SO_4.....Sulfuric acid

H_2O_2 .....Hydrogen peroxide

IEPOX.....Isoprene epoxydiols

K_2SO_4.....Potassium sulfate

LWC.....Liquid water content

MFC .....Mass flow controller

mAMS.....Mini time-of-flight aerosol mass spectrometer

MSA.....Methanesulfonic acid

O_3 .....Ozone

OFR.....Oxidation flow reactor

OH_{exp}.....OH exposure

OA.....Organic aerosol

PAM.....Potential Aerosol Mass reactor

PFA OFR .....Particle Formation Accelerator

POA.....Primary OA

PFA .....PerfluoroAlkoxy

PTFE .....Polytetrafluoroethylene

PDF .....Probability distribution function

PM.....Particulate matter

RH .....Relative humidity

RTD.....Residence time distribution

SA .....Secondary aerosol

SOA.....Secondary organic aerosol

SMPS .....Scanning mobility particle sizer

TPOT.....Toronto Photo-Oxidation Tube

TSAR .....TUT Secondary Aerosol Reactor

VOC .....Volatile organic compound

VCP.....Volatile chemical product

1. Introduction

1.1. Background and Motivation

Air pollution continues to present one of the biggest health hazards in the world. Air pollution contributes to about 7 million early deaths annually, while burdening the global economy upwards of $2.9 trillion per year (IQAir, 2021). Particulate matter (PM), one of the six criteria air pollutants defined by the U.S. Environmental Protection Agency (EPA), is defined as solid/liquid droplets suspended in the atmosphere, with size spanning the range from nanometers to micrometers. PM has significant impact on human mortality and the environment, with important impacts on regional and global climate change and atmospheric visibility (Seinfeld and Pandis, 2016; Shrivastava et al., 2017). Aerosol particles are both emitted directly to the atmosphere (primary aerosols) or produced in the atmosphere from reactions involving precursor gases (secondary aerosols) (Myhre et al., 2013; Boucher, 2015). Secondary aerosols (SA) consist of inorganic species including inorganic nitrate (NO_3^-), sulfate (SO_4^{2-}), and ammonium (NH_4^+) components (Kang et al., 2004), as well as organic components (secondary organic aerosol or SOA) (Hallquist et al., 2009).

SOA is a substantial fraction of SA that forms through condensation of low-volatility or semi-volatile functionalized compounds produced via gas-phase reactions of volatile organic compounds (VOCs) with atmospheric oxidants or by multiphase and

heterogeneous processes (Pankow, 1994; Jimenez et al., 2009). Several studies have evaluated the mechanisms and significance of multiphase reactions in SOA formation (Gelencser and Varga, 2005; Pun et al., 2006; Pun and Seigneur, 2007; Ziemann and Atkinson, 2012). However, the formation is a complex process that involves a large number of VOCs in the atmosphere with numerous oxidation reactions (Aljawhary et al., 2016). Also, the formed SOA can continuously evolve through multi-generational processes either in the gas or particulate phase, resulting in a range of multi-functional products evolved from the complex gaseous and particulate phase oxidation pathways (Shrivastava et al., 2017; Chen et al., 2019; Shao et al., 2022). Thus, the atmospheric mechanisms and kinetics of SOA formation are currently poorly understood and are continuously extended and refined.

There is a growing appreciation of the importance of SOA formation through chemical processes in the aqueous phase of aerosol liquid water (ALW) or cloud droplets (Blando and Turpin, 2000). In clouds and aqueous aerosols, water-soluble organics generated through gas-phase photochemistry can dissolve in the aqueous phase and subsequently be oxidized, resulting in lower-volatility products that are retained in the particle phase (aqSOA) (Lim et al., 2010; Ervens et al., 2011; Ervens et al., 2014). Liquid water in aqueous aerosols and clouds plays an important role in aerosol formation and such aqueous formation pathways remain a major obstacle in estimating secondary aerosol production and properties. Current SOA models that only include gas-phase chemistry often fail to reproduce the properties of SOA, and often underestimate the SOA mass burden (Volkamer et al., 2006; Hodzic et al., 2010). Additional evidence for the role of

aqSOA production comes from several laboratory and field studies that have observed substantial organic aerosol formed in cloud and aerosol water (Bateman et al., 2011; Ervens et al., 2014; Yli-Juuti et al., 2021; Wang et al., 2021). Those and other studies suggest the formation of aqSOA might contribute substantially to the total SOA mass and might help explain discrepancies between observed and predicted SOA properties. However, the current understanding of SOA formation via aqueous-phase reactions in aqueous aerosols and clouds is insufficient, not only because of limited knowledge of the precursors and formation mechanisms of aqSOA, but also because of experimental limitations for simulating the aqueous chemistry at diluted conditions (Odum et al., 1996; Claeys et al., 2004; Carter et al., 2005; Kroll and Seinfeld, 2008; Donahue et al., 2012; Aljawhary et al., 2016; Lamkaddam et al., 2021). Fundamental questions remain about the contribution of aerosol formation through aqueous-phase oxidation to total aerosol burden. Among the challenges is the difficulty of quantifying aqSOA formation from products of gas-phase oxidation of VOCs.

For decades, most laboratory studies on the precursors, formation processes, aging, and health impacts of SOA have been conducted in environmental chambers, also known as smog chambers (Pandis et al., 1995; Cocker et al., 2001; Carter et al., 2005; Nakao et al., 2012; Jahn et al., 2021). Although smog chambers have been critical for developing and evaluating chemical mechanisms for secondary aerosol formation, results from their use are affected by the loss of semi-volatile compounds and particles to the walls (Zhang et al., 2014; Boyd et al., 2017; Nah et al., 2017), limitations on size and experiment duration

(Wang et al., 2011; Tkacik et al., 2017), and by potential leakage of room or outside air into the Teflon bags (Pierce et al., 2008; Matsunaga and Ziemann, 2010).

Oxidation flow reactors (OFRs) have been developed as a complement to traditional smog chambers (Lambe et al., 2011; Chen and Jang, 2012; Li et al., 2015b; Simonen et al., 2017). Inside an OFR, extremely high concentrations of hydroxyl radical and/or other oxidants are maintained (up to 10^{10} molec. cm^{-3} for OH), such that sampled air experiences the equivalent of several hours to days or even weeks of oxidative chemistry over the residence time of just a few minutes (Kang et al., 2007; Li et al., 2015b; Peng et al., 2015). They offer advantages such as minimizing interaction of the gases and particles with walls (Keller and Burtscher, 2012), providing oxidant exposure that can greatly exceed that possible in smog chambers and is variable over a wide range (Kroll and Seinfeld, 2008), portability for use in the field (Ortega et al., 2013; Palm et al., 2016; Palm et al., 2017), and the ability to investigate time-varying sources of SA (Simonen et al., 2017).

Reactor design is a vital step in the development of an OFR system and determines overall applicability and performance. The reactor design mainly includes the geometry and dimensions, the inlet configuration, the selection of materials, the strategies for mixing the reactants, relative humidity/temperature control and the mode(s) of generating the hydroxyl radical or other oxidant(s). The geometry and dimensions of the reactor have substantial impacts on velocity profiles, residence time distributions, wall effects, and extent of reaction. Recent studies have addressed the importance of inlet configuration on

SOA-forming systems (Mitroo et al., 2018). Selection of wall materials and any surface treatments is guided by an application-dependent balance of the importance of loss of gas-phase compounds or delays in their transfer, loss of charged particles to non-conductive materials, and UV transmittance for designs for which the lamps are outside of the reactor. Common materials used in OFRs include chromated aluminum (e.g., PAM; Kang et al., 2007), silicon-coated stainless steel (e.g., TPOT; George et al., 2007; Lambe et al., 2011), and quartz (e.g., CPOT; Huang et al., 2017). In addition, the position and power output of the UV lamp(s) are determined by the reactor materials, the transparency of the materials, and the temperature control requirements during operation (Kang et al., 2007; Ezell et al., 2010). The UV intensity, emitted wavelengths, and intensity uniformity are also important considerations in reactor design that directly impact performance and range of application (Li et al., 2015a; Peng et al., 2017).

This dissertation describes steps taken to obtain a better understanding of both gas- and aqueous-phase SA (aqSA) formation using two new OFR reactors. The first two chapters are driven by rapid development of OFR techniques and the increasing appreciation of their wide application. Two reactors - the Particle Formation Accelerator (PFA) and the Accelerated Production and Processing of Aerosols (APPA) reactor were developed and are described. Prior to using these two reactors for research, computational fluid dynamics (CFD) simulations were combined with experimental determination of the residence time distribution (RTD) to optimize the flow tube design and the atmospheric relevance of the measurements. The remaining three chapters seek to expand the understanding of secondary aerosol formation through gas- and aqueous-phase oxidation

by using the newly-built reactors in both laboratory and field measurements. The application of those two oxidation flow reactors includes characterization of secondary aerosol formation through both gas-and aqueous-phase oxidation of 17 water-insoluble VOCs and, through a separate study, dimethyl sulfide (DMS). In addition to those laboratory studies, results of continuous long-term ambient measurements in Riverside are presented. We quantified the gasSA and aqSA formation from various precursors in a laboratory environment and develop mathematical descriptions of the measured aqueous phase yields, as a function of parameters such photochemical age, relative humidity, and seed aerosol types. Data collected during the field campaign can help bridge the gap between laboratory experimental results and ambient observations of SA formation, and can be integrated in models and/or model parameterizations.

1.2. **Outline of Dissertation**

Chapter 2 is a reprint of the published work Xu and Collins (2021). We designed a new all-Teflon reactor, the PFA OFR, and characterized it in the laboratory and with ambient air. We characterized the flow profiles in the reactor using CFD simulations, the UV intensity distribution in the reactor and the influence of it and varying O_3 concentration and relative humidity (RH) on the resulting equivalent OH exposure (OH_{exp}), transmission efficiencies for gases and particles, residence time distributions for gases and particles, the production yield of SOA from oxidation of α-pinene and *m*-xylene, the effect of seed particles on resulting SA concentration, and SA production from ambient air in Riverside, CA. The reactor response and characteristics are compared with those of a smog chamber

(Caltech) and of other oxidation flow reactors: the Toronto Photo-Oxidation Tube (TPOT), the Caltech Photooxidation Flow Tube (CPOT), the TUT Secondary Aerosol Reactor (TSAR), quartz and aluminum versions of Potential Aerosol Mass reactors (PAMs), and the Environment and Climate Change Canada OFR (ECCC-OFR). Our studies show that (1) OH_{exp} can be varied over a range comparable to that of other OFRs; particle transmission efficiency is over 75 % in the size range from 50 to 200 nm, after minimizing static charge on the Teflon surfaces; the penetration efficiencies of CO_2 and SO_2 are 0.90 ± 0.02 and 0.76 ± 0.04, respectively, the latter of which is comparable to estimates for LVOCs; a near-laminar flow profile is expected based on CFD simulations and suggested by the RTD experiment results; *m*-xylene SOA and α-pinene SOA yields were 0.22 and 0.37, respectively, at about 3×10^{11} molec. cm^{-3} s OH exposure; the mass ratio of seed particles to precursor gas has a significant effect on the amount of SOA formed; and during measurements of SA production when sampling ambient air in Riverside, the mass concentration of SA formed in the reactor was an average of 1.8 times that of the ambient aerosol at the same time.

Chapter 3 is a reprint of a manuscript that is currently in review Xu et al. (2022). a new oxidation flow reactor, the APPA reactor was developed, to measure secondary aerosol formed through gas- and aqueous-phase reactions, both for laboratory gas mixtures containing one or more precursors and for ambient air. For simulating in-cloud processes, droplets formed on monodisperse seed particles are introduced into the top of the reactor and the RH inside it is controlled to 100 %. Similar measurements made with the RH in the reactor <100 % provide contrasts for aerosol formation with no liquid water and with

varying amounts of aerosol liquid water. The reactor was characterized through a series of experiments and used to form secondary aerosol from known concentrations of an organic precursor and from ambient air. The transmission efficiency of O_3 and CO_2 for all RH and of SO_2 for low RH exceeds 90 %, while it falls to about 70 % for SO_2 at 100 % RH. Particle transmission efficiency increases with increasing particle diameter from 0.67 for 0.050 μm particles to 0.98 at 0.20 μm, while that of the ~3.3 μm droplets formed on seed particles is greater than 80 %. The residence time distributions of both gases and particles are narrow relative to other OFRs and lack the tails at long residence time expected with laminar flow. Initial cloud processing experiments focused on the well-studied oxidation of dissolved SO_2 by O_3, with observed growth of seed particles resulting from the added sulfuric acid agreeing well with estimates based on the relevant set of aqueous phase reactions. The OH_{exp} for low RH, high RH, and in-cloud conditions was determined experimentally from the loss of SO_2 and benzene and simulated from the KinSim chemical kinetics solver with inputs of measured 254 nm UV intensity profile through the reactor and loss of O_3 due to photolysis. The aerosol yield for benzene at high OH_{exp} ranged from 18 % at low RH with dry seed particles present in the reactor to 59 % with cloud droplets present. Measurement of the composition of the secondary aerosol formed from ambient air using an aerosol mass spectrometer showed that the oxygen to carbon ratio (O : C) of the organic component increased with increasing RH (and liquid water content).

Chapter 4 focuses on secondary organic aerosol formed via aqueous-phase reactions of water-insoluble VOCs. Laboratory measurements of aerosol formation are made using the APPA flow reactor. Water insoluble VOCs from source categories of

vehicle exhaust, biogenic, biomass burning, and volatile chemical products (VCPs) and investigate their secondary aerosol formation through gas- and aqueous-phase oxidation under equivalent photochemical age of approximately one day to two weeks. Highly oxidized secondary products with higher molecular weight are generated from aqueous-phase oxidation of VOCs relative to that from gas-phase only oxidation. Compared with the secondary products formed through gas-phase oxidation, we show that aerosol liquid water and clouds effectively boost the amount of secondary aerosol. Especially for those generated from the oxidation reactions of VOCs from vehicle exhaust with an average factor of 3 and 5 increase with the presence of aerosol water and cloud droplet, respectively. On a global scale, the SOA production from biogenic and anthropogenic precursor sources is considerable but the importance aerosol through aqueous-phase remains uncertain, so that we conclude that secondary aerosol formation from the total biogenic and anthropogenic sources is probably underestimated in most areas.

Chapter 5 presents secondary aerosol formed in the APPA flow reactor from gas- and aqueous-phase processing of ambient air in Riverside, CA. the APPA flow reactor was operated continuously for one month to measure the amount and properties of secondary aerosol formed in the presence of dry seed, aqueous seed particles or cloud droplets, for simulating the gasSA formation through gas-phase oxidation and in-cloud aqSA formation from oxidation of soluble gases produced from gas-phase photochemistry. A mini time-of-flight aerosol mass spectrometer (mAMS) and a scanning mobility particle sizer (SMPS) alternated sampling ambient aerosol and the aerosol formed from oxidation of the gases in ambient air. The reactor repeatedly stepped through a measurement matrix that included

two levels of OH exposure (corresponding to 5.9 -9.1 hours and 1.3-2.3 days atmospheric equivalent) and three levels of liquid water content (none, aerosol liquid water, and cloud). More enhancement and variation of SOA mass formation was observed at the higher OH exposure level, with an average factor of 1.1 increase for gas-phase oxidation and a factor of 1.8 increase for aqueous-phase oxidation compared with ambient organic aerosol (OA). Compare with reactor SOA formed at low OH_{exp} level in the presence of dry seed particles, more secondary aerosols were formed under aqueous-phase oxidation with increasing liquid water content, with an average factor of 1.7 and 3.5 increase in the presence of aerosol liquid water and cloud droplets, respectively. Reactor SOA mass formed in the reactor was highest in the morning and night. The contribution of highly oxidized compounds to the organic mass was higher when aerosol liquid water and cloud droplets were present in the reactor than when only dry seed particles were. These results demonstrate the importance of aqSOA in urban environments and can help constrain SOA models.

Chapter 6 describes work aimed at understanding the formation pathways and physicochemical properties of secondary aerosol from gas- and aqueous-phase oxidation of DMS. Secondary marine aerosol influences clouds and climate. DMS, a dominant natural volatile organic compound released from the ocean, can form new particles or add to existing ones after being oxidized to sulfuric acid (H_2SO_4) and SA. Although the detailed processes of DMS leading to SA formation have been reported in model studies, more information is needed for predicting and quantifying the distribution of oxidation products under varying atmospheric conditions. Systematic studies of gas- and aqueous-phase

oxidation of DMS were carried out in the APPA flow reactor. Experiments were performed in the presence of dry, aqueous, or activated seed particles inside the APPA, where the RH was maintained between 40 and 100%. We characterized the chemical composition and mass yields of SOA produced from the oxidation of DMS with OH and O_3 under variable precursor concentration, aerosol seed type, and oxidation time scale. Further, we characterized secondary aerosol formation yield as a function of the OH/O_3 oxidant ratio for simulating in-cloud aqSA formation from oxidation of soluble gases produced from gas-phase photochemistry. Significant secondary aerosol mass formed under both gas- and aqueous-phase oxidation. Our analysis revealed that the DMS-derived secondary aerosol formation through gas- and aqueous-phase oxidation is strongly affected by the photochemical age and the amount of liquid water present. The influence of aerosol liquid water/cloud droplets and OH exposure levels on the chemical composition of the secondary aerosol was also investigated. The formation and contribution of H_2SO_4 in resulting aerosols showed strong dependence on OH_{exp} under all studied conditions, while methanesulfonic acid (MSA; CH3S(O)(O)OH) formation was more complicated, and its formation depended both on OH_{exp} and RH. The results are used to develop an improved understanding of the atmospheric fate of DMS and the potential impact of its oxidation products on global marine aerosol burden.

1.3. **References**

IQAir, 2021. World air quality report region and city PM2.5 ranking. https://www.iqair.com/world-most-polluted-cities/world-air-quality-report-2021-en.pdf. https://www.iqair.com/world-air-quality-report

Aljawhary, D., Zhao, R., Lee, A. K., Wang, C., and Abbatt, J. P.: Kinetics, mechanism, and secondary organic aerosol yield of aqueous phase photo-oxidation of α-pinene oxidation products, The Journal of Physical Chemistry A, 120, 1395-1407, 2016.

Bateman, A. P., Nizkorodov, S. A., Laskin, J., and Laskin, A.: Photolytic processing of secondary organic aerosols dissolved in cloud droplets, Physical Chemistry Chemical Physics, 13, 12199-12212, 2011.

Blando, J. D. and Turpin, B. J.: Secondary organic aerosol formation in cloud and fog droplets: a literature evaluation of plausibility, Atmospheric Environment, 34, 1623-1632, 2000.

Boucher, O.: Atmospheric aerosols, in: Atmospheric Aerosols, Springer, 9-24, 2015.

Boyd, C. M., Nah, T., Xu, L., Berkemeier, T., and Ng, N. L.: Secondary organic aerosol (SOA) from nitrate radical oxidation of monoterpenes: effects of temperature, dilution, and humidity on aerosol formation, mixing, and evaporation, Environmental science & technology, 51, 7831-7841, 2017.

Carter, W. P., Cocker III, D. R., Fitz, D. R., Malkina, I. L., Bumiller, K., Sauer, C. G., Pisano, J. T., Bufalino, C., and Song, C.: A new environmental chamber for evaluation of gas-phase chemical mechanisms and secondary aerosol formation, Atmospheric Environment, 39, 7768-7788, 2005.

Chen, T. and Jang, M.: Secondary organic aerosol formation from photooxidation of a mixture of dimethyl sulfide and isoprene, Atmospheric environment, 46, 271-278, 2012.

Chen, T., Liu, Y., Ma, Q., Chu, B., Zhang, P., Liu, C., Liu, J., and He, H.: Significant source of secondary aerosol: formation from gasoline evaporative emissions in the presence of SO 2 and NH 3, Atmospheric Chemistry and Physics, 19, 8063-8081, 2019.

Claeys, M., Graham, B., Vas, G., Wang, W., Vermeylen, R., Pashynska, V., Cafmeyer, J., Guyon, P., Andreae, M. O., and Artaxo, P.: Formation of secondary organic aerosols through photooxidation of isoprene, Science, 303, 1173-1176, 2004.

Cocker, D. R., Flagan, R. C., and Seinfeld, J. H.: State-of-the-art chamber facility for studying atmospheric aerosol chemistry, Environmental science & technology, 35, 2594-2601, 2001.

Donahue, N. M., Henry, K. M., Mentel, T. F., Kiendler-Scharr, A., Spindler, C., Bohn, B., Brauers, T., Dorn, H. P., Fuchs, H., and Tillmann, R.: Aging of biogenic secondary organic aerosol via gas-phase OH radical reactions, Proceedings of the National Academy of Sciences, 109, 13503-13508, 2012.

Ervens, B., Turpin, B., and Weber, R.: Secondary organic aerosol formation in cloud droplets and aqueous particles (aqSOA): a review of laboratory, field and model studies, Atmospheric Chemistry and Physics, 11, 11069-11102, 2011.

Ervens, B., Sorooshian, A., Lim, Y. B., and Turpin, B. J.: Key parameters controlling OH-initiated formation of secondary organic aerosol in the aqueous phase (aqSOA), Journal of Geophysical Research: Atmospheres, 119, 3997-4016, 2014.

Ezell, M. J., Johnson, S. N., Yu, Y., Perraud, V., Bruns, E. A., Alexander, M. L., Zelenyuk, A., Dabdub, D., and Finlayson-Pitts, B. J.: A new aerosol flow system for photochemical and thermal studies of tropospheric aerosols, Aerosol Science and Technology, 44, 329-338, 2010.

Gelencser, A. and Varga, Z.: Evaluation of the atmospheric significance of multiphase reactions in atmospheric secondary organic aerosol formation, Atmospheric Chemistry and Physics, 5, 2823-2831, 2005.

George, I., Vlasenko, A., Slowik, J., Broekhuizen, K., and Abbatt, J.: Heterogeneous oxidation of saturated organic aerosols by hydroxyl radicals: uptake kinetics, condensed-phase products, and particle size change, Atmospheric Chemistry and Physics, 7, 4187-4201, 2007.

Hallquist, M., Wenger, J. C., Baltensperger, U., Rudich, Y., Simpson, D., Claeys, M., Dommen, J., Donahue, N., George, C., and Goldstein, A.: The formation, properties and impact of secondary organic aerosol: current and emerging issues, Atmospheric chemistry and physics, 9, 5155-5236, 2009.

Hodzic, A., Jimenez, J. L., Madronich, S., Canagaratna, M., DeCarlo, P. F., Kleinman, L., and Fast, J.: Modeling organic aerosols in a megacity: potential contribution of semi-volatile and intermediate volatility primary organic compounds to secondary organic aerosol formation, Atmospheric Chemistry and Physics, 10, 5491-5514, 2010.

Huang, Y., Coggon, M. M., Zhao, R., Lignell, H., Bauer, M. U., Flagan, R. C., and Seinfeld, J. H.: The Caltech Photooxidation Flow Tube reactor: design, fluid dynamics and characterization, Atmospheric Measurement Techniques, 10, 839-867, 2017.

Jahn, L. G., Wang, D. S., Dhulipala, S. V., and Ruiz, L. H.: Gas-Phase Chlorine Radical Oxidation of Alkanes: Effects of Structural Branching, NO x, and Relative Humidity Observed during Environmental Chamber Experiments, The Journal of Physical Chemistry A, 125, 7303-7317, 2021.

Jimenez, J. L., Canagaratna, M., Donahue, N., Prevot, A., Zhang, Q., Kroll, J. H., DeCarlo, P. F., Allan, J. D., Coe, H., and Ng, N.: Evolution of organic aerosols in the atmosphere, Science, 326, 1525-1529, 2009.

Kang, E., Root, M., Toohey, D., and Brune, W.: Introducing the concept of potential aerosol mass (PAM), Atmospheric Chemistry and Physics, 7, 5727-5744, 2007.

Keller, A. and Burtscher, H.: A continuous photo-oxidation flow reactor for a defined measurement of the SOA formation potential of wood burning emissions, Journal of aerosol science, 49, 9-20, 2012.

Kroll, J. H. and Seinfeld, J. H.: Chemistry of secondary organic aerosol: Formation and evolution of low-volatility organics in the atmosphere, Atmospheric Environment, 42, 3593-3624, 2008.

Lambe, A., Ahern, A., Williams, L., Slowik, J., Wong, J., Abbatt, J., Brune, W., Ng, N., Wright, J., and Croasdale, D.: Characterization of aerosol photooxidation flow reactors: heterogeneous oxidation, secondary organic aerosol formation and cloud condensation nuclei activity measurements, Atmospheric Measurement Techniques, 4, 445-461, 2011.

Lamkaddam, H., Dommen, J., Ranjithkumar, A., Gordon, H., Wehrle, G., Krechmer, J., Majluf, F., Salionov, D., Schmale, J., and Bjelić, S.: Large contribution to secondary organic aerosol from isoprene cloud chemistry, Science Advances, 7, eabe2952, 2021.

Li, M., Cao, H., Han, D., Li, X., and He, M.: Kinetics and Mechanism of the reactions of OH radicals with p-nitroaniline in Gas-phase and Aqueous Solution, Computational and Theoretical Chemistry, 1055, 10.1016/j.comptc.2014.12.028, 2015a.

Li, R., Palm, B. B., Ortega, A. M., Hlywiak, J., Hu, W., Peng, Z., Day, D. A., Knote, C., Brune, W. H., and De Gouw, J. A.: Modeling the radical chemistry in an oxidation flow reactor: Radical formation and recycling, sensitivities, and the OH exposure estimation equation, The Journal of Physical Chemistry A, 119, 4418-4432, 2015b.

Lim, Y., Tan, Y., Perri, M., Seitzinger, S., and Turpin, B.: Aqueous chemistry and its role in secondary organic aerosol (SOA) formation, Atmospheric Chemistry and Physics, 10, 10521-10539, 2010.

Matsunaga, A. and Ziemann, P. J.: Gas-wall partitioning of organic compounds in a Teflon film chamber and potential effects on reaction product and aerosol yield measurements, Aerosol Science and Technology, 44, 881-892, 2010.

Mitroo, D., Sun, Y., Combest, D. P., Kumar, P., and Williams, B. J.: Assessing the degree of plug flow in oxidation flow reactors (OFRs): a study on a potential aerosol mass (PAM) reactor, Atmospheric Measurement Techniques, 11, 1741-1756, 2018.

Myhre, G., Myhre, C., Samset, B., and Storelvmo, T.: Aerosols and their relation to global climate and climate sensitivity, Nature Education Knowledge, 4, 7, 2013.

Nah, T., McVay, R. C., Pierce, J. R., Seinfeld, J. H., and Ng, N. L.: Constraining uncertainties in particle-wall deposition correction during SOA formation in chamber experiments, Atmospheric Chemistry and Physics, 17, 2297-2310, 2017.

Nakao, S., Liu, Y., Tang, P., Chen, C.-L., Zhang, J., and Cocker Iii, D.: Chamber studies of SOA formation from aromatic hydrocarbons: observation of limited glyoxal uptake, Atmospheric Chemistry and Physics, 12, 3927-3937, 2012.

Odum, J. R., Hoffmann, T., Bowman, F., Collins, D., Flagan, R. C., and Seinfeld, J. H.: Gas/particle partitioning and secondary organic aerosol yields, Environmental science & technology, 30, 2580-2585, 1996.

Ortega, A., Day, D., Cubison, M., Brune, W. H., Bon, D., De Gouw, J., and Jimenez, J.: Secondary organic aerosol formation and primary organic aerosol oxidation from biomass-burning smoke in a flow reactor during FLAME-3, Atmospheric Chemistry and Physics, 13, 11551-11571, 2013.

Palm, B. B., Campuzano-Jost, P., Day, D. A., Ortega, A. M., Fry, J. L., Brown, S. S., Zarzana, K. J., Dube, W., Wagner, N. L., and Draper, D. C.: Secondary organic aerosol formation from in situ OH, O 3, and NO 3 oxidation of ambient forest air in an oxidation flow reactor, Atmospheric Chemistry and Physics, 17, 5331-5354, 2017.

Palm, B. B., Campuzano-Jost, P., Ortega, A. M., Day, D. A., Kaser, L., Jud, W., Karl, T., Hansel, A., Hunter, J. F., and Cross, E. S.: In situ secondary organic aerosol formation from ambient pine forest air using an oxidation flow reactor, Atmospheric Chemistry and Physics, 16, 2943-2970, 2016.

Pandis, S. N., Wexler, A. S., and Seinfeld, J. H.: Dynamics of tropospheric aerosols, The Journal of Physical Chemistry, 99, 9646-9659, 1995.

Pankow, J. F.: An absorption model of the gas/aerosol partitioning involved in the formation of secondary organic aerosol, Atmospheric Environment, 28, 189-193, 1994.

Peng, J., Hu, M., Guo, S., Du, Z., Shang, D., Zheng, J., Zheng, J., Zeng, L., Shao, M., and Wu, Y.: Ageing and hygroscopicity variation of black carbon particles in Beijing measured by a quasi-atmospheric aerosol evolution study (QUALITY) chamber, Atmospheric Chemistry and Physics, 17, 10333-10348, 2017.

Peng, Z., Day, D., Stark, H., Li, R., Lee-Taylor, J., Palm, B., Brune, W., and Jimenez, J.: HO x radical chemistry in oxidation flow reactors with low-pressure mercury lamps systematically examined by modeling, Atmospheric Measurement Techniques, 8, 4863-4890, 2015.

Pierce, J., Engelhart, G., Hildebrandt, L., Weitkamp, E., Pathak, R., Donahue, N., Robinson, A., Adams, P., and Pandis, S.: Constraining particle evolution from wall losses, coagulation, and condensation-evaporation in smog-chamber experiments: optimal estimation based on size distribution measurements, Aerosol Science and Technology, 42, 1001-1015, 2008.

Pun, B. and Seigneur, C.: Investigative modeling of new pathways for secondary organic aerosol formation, Atmospheric Chemistry and Physics, 7, 2199-2216, 2007.

Pun, B. K., Seigneur, C., and Lohman, K.: Modeling secondary organic aerosol formation via multiphase partitioning with molecular data, Environmental science & technology, 40, 4722-4731, 2006.

Seinfeld, J. H. and Pandis, S. N.: Atmospheric chemistry and physics: from air pollution to climate change, John Wiley & Sons2016.

Shao, Y., Voliotis, A., Du, M., Wang, Y., Pereira, K., Hamilton, J., Alfarra, M. R., and McFiggans, G.: Chemical composition of secondary organic aerosol particles formed from mixtures of anthropogenic and biogenic precursors, Atmospheric Chemistry and Physics Discussions, 1-41, 2022.

Shrivastava, M., Cappa, C. D., Fan, J., Goldstein, A. H., Guenther, A. B., Jimenez, J. L., Kuang, C., Laskin, A., Martin, S. T., and Ng, N. L.: Recent advances in understanding secondary organic aerosol: Implications for global climate forcing, Reviews of Geophysics, 55, 509-559, 2017.

Simonen, P., Saukko, E., Karjalainen, P., Timonen, H., Bloss, M., Aakko-Saksa, P., Rönkkö, T., Keskinen, J., and Maso, M. D.: A new oxidation flow reactor for measuring secondary aerosol formation of rapidly changing emission sources, Atmospheric Measurement Techniques, 10, 1519-1537, 2017.

Tkacik, D. S., Robinson, E. S., Ahern, A., Saleh, R., Stockwell, C., Veres, P., Simpson, I. J., Meinardi, S., Blake, D. R., and Yokelson, R. J.: A dual-chamber method for quantifying the effects of atmospheric perturbations on secondary organic aerosol formation from biomass burning emissions, Journal of Geophysical Research: Atmospheres, 122, 6043-6058, 2017.

Volkamer, R., Jimenez, J. L., San Martini, F., Dzepina, K., Zhang, Q., Salcedo, D., Molina, L. T., Worsnop, D. R., and Molina, M. J.: Secondary organic aerosol formation from anthropogenic air pollution: Rapid and higher than expected, Geophysical Research Letters, 33, 2006.

Wang, J., Doussin, J.-F., Perrier, S., Perraudin, E., Katrib, Y., Pangui, E., and Picquet-Varrault, B.: Design of a new multi-phase experimental simulation chamber for

atmospheric photosmog, aerosol and cloud chemistry research, Atmospheric Measurement Techniques, 4, 2465-2494, 2011.

Wang, J., Ye, J., Zhang, Q., Zhao, J., Wu, Y., Li, J., Liu, D., Li, W., Zhang, Y., and Wu, C.: Aqueous production of secondary organic aerosol from fossil-fuel emissions in winter Beijing haze, Proceedings of the National Academy of Sciences, 118, 2021.

Xu, N. and Collins, D. R.: Design and characterization of a new oxidation flow reactor for laboratory and long-term ambient studies, Atmospheric Measurement Techniques, 14, 2891-2906, 2021.

Xu, N., Le, C., Cocker, D. R., and Collins, D. R.: An oxidation flow reactor for simulating and accelerating secondary aerosol formation in aerosol liquid water and cloud droplets, Atmospheric Measurement Techniques Discussions, 1-41, 2022.

Yli-Juuti, T., Mielonen, T., Heikkinen, L., Arola, A., Ehn, M., Isokääntä, S., Keskinen, H.-M., Kulmala, M., Laakso, A., and Lipponen, A.: Significance of the organic aerosol driven climate feedback in the boreal area, Nature communications, 12, 1-9, 2021.

Zhang, X., Cappa, C. D., Jathar, S. H., McVay, R. C., Ensberg, J. J., Kleeman, M. J., and Seinfeld, J. H.: Influence of vapor wall loss in laboratory chambers on yields of secondary organic aerosol, Proceedings of the National Academy of Sciences, 111, 5802-5807, 2014.

Ziemann, P. J. and Atkinson, R.: Kinetics, products, and mechanisms of secondary organic aerosol formation, Chemical Society Reviews, 41, 6582-6605, 2012.

2. Design and Characterization of a New OFR for Laboratory and Long-Term Ambient Studies

2.1. Abstract

Oxidation flow reactors (OFRs) are frequently used to study the formation and evolution of secondary aerosol (SA) in the atmosphere and have become valuable tools for improving the accuracy of model simulations and for depicting and accelerating realistic atmospheric chemistry. Driven by rapid development of OFR techniques and the increasing appreciation of their wide application, we designed a new all-Teflon reactor, the Particle Formation Accelerator (PFA) OFR, and characterized it in the laboratory and with ambient air. A series of simulations and experiments were performed to characterize: (1) flow profiles in the reactor using computational fluid dynamics (CFD) simulations, (2) the UV intensity distribution in the reactor and the influence of it and varying O_3 concentration and relative humidity (RH) on the resulting equivalent OH exposure (OH_{exp}), (3) transmission efficiencies for gases and particles, (4) residence time distributions (RTD) for gases and particles using both computational simulations and experimental verification, (5) the production yield of secondary organic aerosol (SOA) from oxidation of α-pinene and *m*-xylene, (6) the effect of seed particles on resulting SA concentration, and (7) SA production from ambient air in Riverside, CA, U.S. The reactor response and characteristics are compared with those of a smog chamber (Caltech) and of other oxidation flow reactors (the Toronto Photo-Oxidation Tube (TPOT), the Caltech Photooxidation Flow Tube (CPOT),

the TUT Secondary Aerosol Reactor (TSAR), quartz and aluminum versions of Potential Aerosol Mass reactors (PAMs), and the Environment and Climate Change Canada OFR (ECCC-OFR)).

Our studies show that: (1) OH_{exp} can be varied over a range comparable to that of other OFRs, (2) particle transmission efficiency is over 75 % in the size range from 50 to 200 nm, after minimizing static charge on the Teflon surfaces, (3) the penetration efficiencies of CO_2 and SO_2 are 0.90 ± 0.02 and 0.76 ± 0.04, respectively, the latter of which is comparable to estimates for LVOCs, (4) a near laminar flow profile is expected based on CFD simulations and suggested by the RTD experiment results, (5) *m*-xylene SOA and α-pinene SOA yields were 0.22 and 0.37, respectively, at about 3×10^{11} molec. cm^{-3} s OH exposure, (6) the mass ratio of seed particles to precursor gas has a significant effect on the amount of SOA formed, and (7) during measurements of SA production when sampling ambient air in Riverside, the mass concentration of SA formed in the reactor was an average of 1.8 times that of the ambient aerosol at the same time.

2.2. **Introduction**

Atmospheric aerosols play major roles in air pollution, global climate change, and visibility reduction (Seinfeld and Pandis, 2006). The complex mixtures of inorganic and organic species present in atmospheric aerosols originate from both direct, or primary, emissions and production of secondary aerosol (SA) from atmospheric reactions. Organic aerosol (OA) makes up a substantial fraction of atmospheric aerosols, and is comprised of primary OA (POA) that is directly emitted in the particle phase and secondary OA (SOA) that is formed in the atmosphere through reactions of gas phase precursors. SOA forms when reaction of volatile organic compounds (VOCs) with gas phase oxidants produces less-volatile functionalized compounds (Pankow, 1994; Jimenez et al., 2009; George and Abbatt, 2010) and when water-soluble organics dissolve in the aqueous phase (aerosol water or cloud droplets) and are subsequently oxidized (Lim et al., 2010; Ervens et al., 2011). However, the mechanisms of SOA formation are still poorly understood and are continuously extended and refined. Part of the complexity of SOA formation arises from the numerous oxidation reactions involving the large number of VOCs in the atmosphere (Aljawhary et al., 2016). Additionally, after formation from precursor gases the SOA can evolve through multiphase and multi-generational processes, forming more complex distributions of compounds comprised of thousands of molecules (Xu et al., 2015; Chen et al., 2018; Shrivastava et al., 2019).

For decades, comprehensive laboratory studies on the sources, formation, and aging of SOA have been conducted in batch-mode atmospheric reactors, which are also known

as environmental chambers or smog chambers (Pandis et al., 1991; Carter et al., 2005; Song et al., 2005; Weitkamp et al., 2007). Though such chambers can create environments that closely simulate the complexity of the atmosphere, results from their use are affected by the loss of particles and semi-volatile compounds to the walls (Zhang et al., 2014; Nah et al., 2016, 2017), by limitations on experiment duration and extent of reaction, and by potential leakage of room or outside air into the Teflon bags (Pierce et al., 2008; Matsunaga and Ziemann, 2010; Krechmer et al., 2015). Moreover, the size of common smog chambers, which typically range from about 5 to 250 m^3 (Lonneman et al., 1981; Mentel et al., 1996; Wang et al., 2014; Tkacik et al., 2017), imposes a substantial restriction on their use for studying aerosol formation in ambient air (Bruns et al., 2015). Oxidation flow reactors (OFRs) have been developed as a complement to traditional smog chambers and offer advantages such as providing oxidant exposure that can greatly exceed that possible in smog chambers and is variable over a wide range (Kroll et al., 2009), portability for use in the field (Wong et al., 2011), and the ability to investigate time-varying sources of SA (Kang et al., 2007). Inside an OFR, extremely high concentrations of hydroxyl radical and/or other oxidants are maintained (up to 10^{10} molec. cm^{-3} for OH), such that sampled air experiences the equivalent of several hours to days or even weeks of oxidative chemistry over the residence time of just a few minutes. Shorter residence times minimize interaction of the gases and particles with walls (Keller and Burtscher, 2012) and permit measurements of dynamic environments and sources. The portability and flexibility of OFRs also make them versatile, with the same experimental system applicable for a variety of laboratory and field measurements. Their fast response also makes them better suited

than smog chambers for experiments probing the influence of a matrix of parameters on SOA formation (Slowik et al., 2012; Palm et al., 2018).

Previous investigations of potential SA formation using different types of OFRs have resulted in optimized designs and strategies for studying specific sources or processes, such as measuring time-resolved SOA formation from gasoline vehicles during a transient driving cycle (Karjalainen et al., 2016) and from rapidly changing vehicular emission sources (Simonen et al., 2017). Several groups have employed OFRs to study SA formation from ambient air, with examples including investigation of the variability of precursor gases and the resulting SOA in a ponderosa pine forest (Palm et al., 2016), high time resolution quantification of SOA formation from ambient air in central Amazonia (Palm et al., 2018), and observation of SOA formation and aging from urban air (Ortega et al., 2016). For laboratory-based studies, the concentrations and SOA yield (Y) for certain precursors can serve as a reference to estimate total SOA potential (Iinuma et al., 2004; Loza et al., 2014). Yields determined for common precursors can also provide a quantitative measure of performance of a reactor relative to others of varying design and purpose (Kang et al., 2011; Lambe et al., 2015). Numerous studies have been conducted investigating differences in the SOA yield between OFRs and large environmental smog chambers (Matsunaga and Ziemann, 2010; Bruns et al., 2015; Lambe et al., 2011, 2015). For example, Lambe et al. (2011) showed that the SOA yield they observed in a PAM reactor is similar to that reported for the Caltech smog chamber. Other studies focused on SOA produced from different precursor gas sources. For example, Li et al. (2019) used a new OFR (the Environment and Climate Change Canada OFR; ECCC- OFR) to evaluate

the SOA yields of single compounds (alkanes and α-pinene) and of complex precursor mixtures, such as emissions from oil sands. Ahlberg et al. (2017) found that using single precursor experiment yields could lead to underestimated SOA mass loadings if aerosol dynamics is not properly accounted for. Cubison et al. (2011) characterized the evolution of laboratory biomass burning emissions using a PAM reactor and Kang et al. (2011) estimated the SOA-forming potential of model organic compounds.

Reactor design is a critical step in the development of an OFR system and determines overall applicability and performance. The geometry and dimensions of the reactor have substantial impacts on velocity profiles, residence time distributions, wall effects, and extent of reaction. The reactor design mainly includes the selection of materials, the inlet configuration, the diameter-to-length ratio, the body length, the strategies for mixing the reactants, and the mode(s) of generating the hydroxyl radical or other oxidant(s). For example, some inlet designs can lead to dead zones near the reactor walls, increasing the difficulty of achieving laminar flow in the entrance of the reactor and broadening the RTD (Mitroo et al., 2018). The position and power output of the UV lamp(s) are determined by the reactor materials and their transparency and by temperature control requirements during operation (Kang et al., 2007; Ezell et al., 2010). With most OFRs, the lamps are either mounted on the inner surface for metal-wall reactors or outside for quartz-based reactors. The emitted wavelengths and intensity uniformity of the UV lamp(s) are also important considerations in reactor design (Li et al., 2015). Selection of wall materials and any surface treatments is guided by an application-dependent balance of the importance of loss of gas-phase compounds or delays in their transfer, loss of charged

particles to non-conductive materials, and UV transmittance for designs for which the lamps are outside of the reactor. Common materials used in OFRs include chromated aluminum (e.g., PAM), silicon-coated stainless steel (e.g., TPOT), and quartz (e.g., CPOT, TSAR and ECCC-OFR). Recent studies of organic gas transmission through common tubing types described by Deming et al. (2019) suggest PerfluoroAlkoxy (PFA) and Fluorinated ethylene propylene (FEP) Teflon may be alternative choices for applications for which minimizing wall losses of gases is a priority. Kang et al. (2007) described the prototype PAM chamber, a 19 L cylinder made of Teflon FEP film. To the best of our knowledge, there are no previous studies describing that all-Teflon OFR and no data are available that show the advantages and disadvantages of the all-Teflon reactor compared with those constructed from other materials such as quartz and metal.

Here we present the design of a new all-Teflon OFR called the Particle Formation Accelerator or PFA OFR. The reactor consists of a vertically oriented tube, with the inlet at the bottom and outlet at the top. One notable design difference between the PFA OFR and other OFRs is its use of a relatively small and low power lamp at the top of the reactor, which promotes thermal stratification and minimizes convective mixing. We report the results of computational, laboratory, and field studies through which it was characterized. UV intensity and total OH exposure (OH_{exp}) were quantified inside the flow tube. The flow profile in the OFR was modeled and the resulting residence time distributions of gases and particles were both modeled and experimentally verified. Two precursor species were used to investigate SOA yield and the dependence of that yield on variations in parameters such as precursor concentrations, OH exposure, and the presence and concentration of seed

particles. SOA mass yields are compared with those reported in the literature for the same VOCs. Field testing was conducted by measuring SA formation in ambient air sampled in Riverside, CA, U.S. Collectively, these tests confirm the utility of the PFA OFR for both laboratory and field studies.

2.3. Design and Experimental Setup

2.3.1. Reactor Design

2.3.1.1. PFA OFR and Flow Dynamic Characterization

A cutaway view of the Particle Formation Accelerator (PFA) OFR is shown in Figure 2.1. It consists of a PFA-Teflon tube sealed between inlet and outlet end caps that were machined from blocks of polytetrafluoroethylene (PTFE). The reactor is oriented vertically, with the inlet at the bottom and outlet at the top. The PFA tube has a volume of 7.5 L and dimensions of 151 cm L × 7.8 cm ID. Both end caps have an OD of 10.2 cm and are sealed with the reactor tube by FEP-encapsulated O-rings. The small diameter-to-length ratio of the reactor section of 0.052 was selected to result in a narrow residence time distribution in the flow tube and a more uniform OH exposure (Lambe et al., 2011). However, the small diameter also results in a reactor surface area to volume ratio of 0.53 cm^{-1} that is higher than that of the TPOT (0.33 cm^{-1}) and PAM (0.23 cm^{-1}).

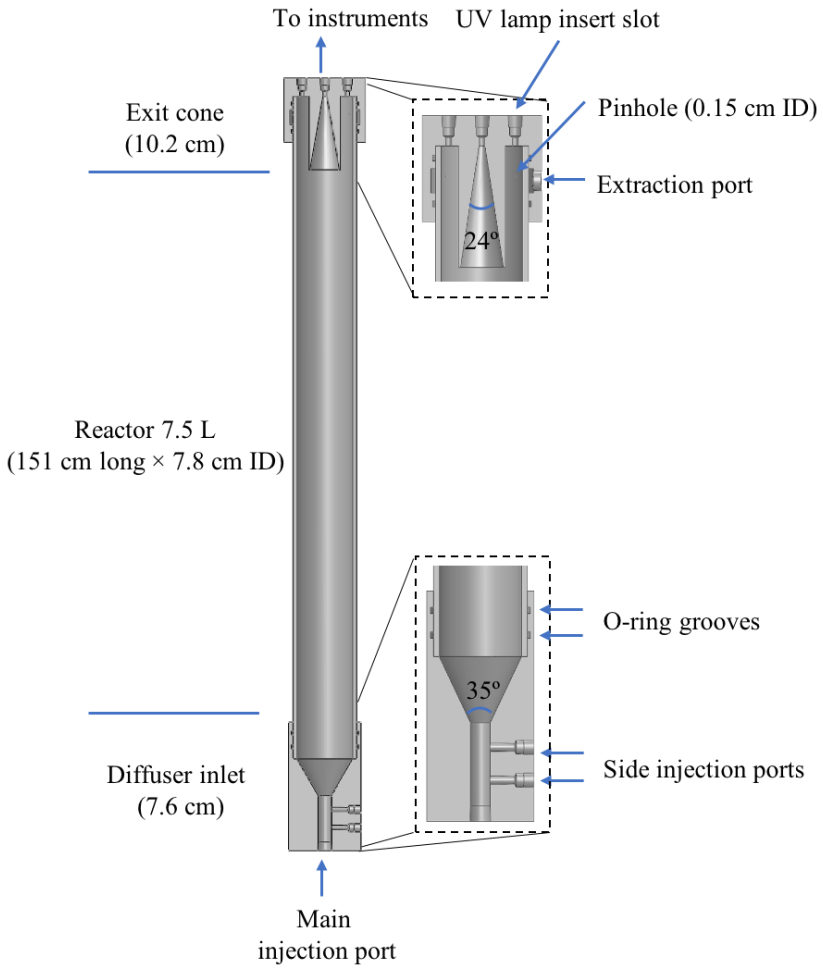

Figure 2.1: Cutaway view of the PFA OFR.

Some design elements of the PFA OFR are similar to those of other recently developed OFRs (Kang et al., 2007; Karjalainen et al., 2016; Huang et al., 2017), though there are some important differences as well. The inlet end cap has a 5.1 cm L × 1.3 cm ID bore used as the main sample air injection port, two side injection ports for introducing seed particles and O_3, and a cone-shape diffuser. That cone, which serves as the transition between the inlet injection port and the reactor tube, has an angle of 35 degrees, which is

close to that suggested by Huang et al. (2017) for minimizing recirculation. The sample flow gradually expands and is expected to be fully developed shortly after entering the reactor tube. A single length of PFA tube (Ametek FPP P/N 33HPSC40x3.00) is used as the main body in order to simplify construction. Only the central ~50 % of the flow through the reactor is extracted and analyzed. That sample flow converges through an exit cone in the outlet end cap that tapers at an angle of 24 degrees from an ID of 4 cm to the 0.33 cm ID of the outlet bore through the top of the end cap. The outer ~50 % of the flow that is most influenced by interactions with the reactor walls flows into an annulus surrounding it. From there, it is pulled through 12 uniformly spaced ~0.15 cm ID pinholes drilled through the PFA pipe about 3 cm from the top. The flow extracted through those pinholes travels into a channel between the flow tube and the end cap and then through a port on the top cap where it is purged by a vacuum pump. The diameter of the opening into the sample exit cone was selected such that, for the expected parabolic velocity profile, the nominal 1:1 sample:side flow ratio does not perturb gas streamlines.

To characterize the flow field and velocity distribution profile inside the PFA OFR, computational fluid dynamics (CFD) simulations were performed using a 3D geometry model in COMSOL Multiphysics 5.4 software, which has been used by several research groups to optimize and evaluate their reactor designs and to explore suitability for applications in atmospheric and aerosol chemistry studies (Renbaum-Wolff et al., 2013; Zhang et al., 2015; Huang et al., 2017). The 2-D geometry velocity profile simulation result is shown in Figure 2.2. The simulation used the actual design and dimensions of the PFA OFR. The flow at the entrance to the sample outlet tube of the main body is assumed to be

fully developed and laminar, while an atmospheric pressure boundary condition at the annular outflow boundary and the no-slip condition at all the other boundaries were applied. Though high velocity extends into the central tube flow region above the inlet, within 15 cm from the entrance of the diffuser cone the velocity profile is nearly parabolic, with a decrease in the maximum velocity over the entrance length from 12 cm s^{-1} to 3 cm s^{-1}. The simulation suggests that jetting is minimal and that the area influenced by recirculation is negligible.

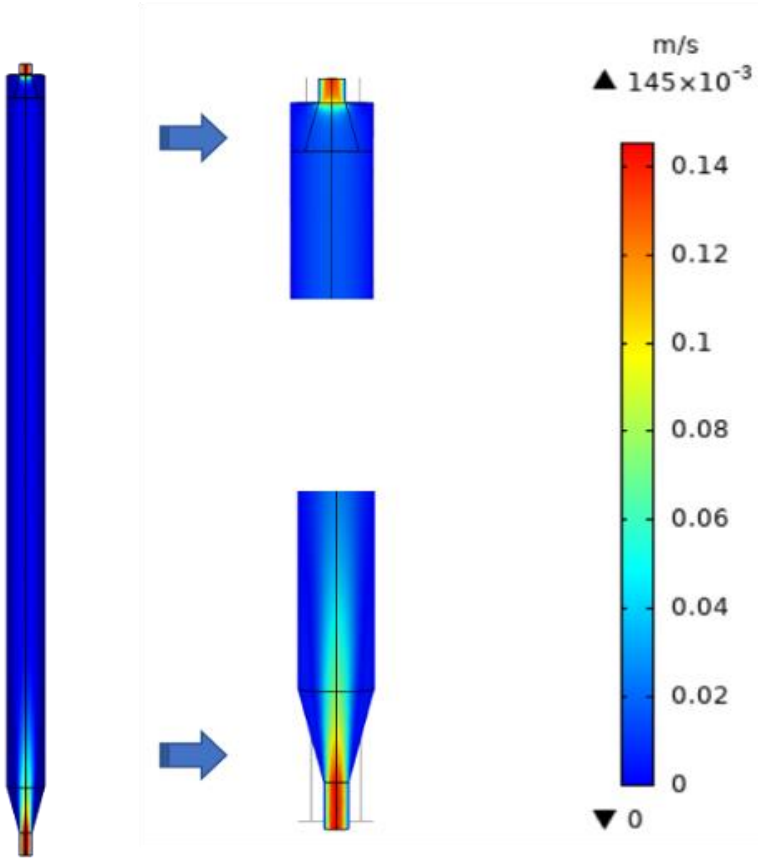

Figure 2.2: CFD simulation results of the velocity distribution in the PFA OFR.

2.3.1.2. **UV Source and Intensity Profile**

The outlet end cap has NPT thread ports to accommodate one or two 0.5 cm OD lamps. For the results discussed here, one 5.1 cm L × 0.5 cm OD ozone-free (254 nm only) low-pressure mercury lamp (BHK. Inc; PN 80-1057-01) was inserted into the cap. Though the lamp is not isolated from the flow, its position in the side purge flow annulus prevents any contact between it and the sampled flow. The handle of the UV lamp is secured and sealed with a Swagelok male connector fitting. Use of a relatively small and low power lamp at one end of the reactor is perhaps the most significant design difference between the PFA OFR and others. One objective of the approach was to promote thermal stratification caused by the hot lamp at the top of the reactor in order to minimize convective mixing. An obvious complication is that UV intensity, and therefore OH production, is expected to decay with distance through the long reactor tube. To mitigate that decay, materials were selected that are highly UV reflective, such that emitted photons penetrate far down the reactor tube as they are repeatedly reflected by the walls. The PFA tube is non-absorbing at 254 nm but is not opaque and would allow UV to leak out. Thus, the tube is wrapped with an inner layer of highly reflective 0.32 cm thick expanded PTFE gasket (ePTFE; Inertech) and an outer layer of aluminized Mylar (Vivosun). Though the combination of materials results in sufficiently high reflectance for the 254 nm emission peak of a mercury lamp. Silva et al. (2010) showed that the reflectance of ePTFE at 175 nm is significantly lower, with the difference thought to be due to absorption by O_2 trapped in pores. Reflectance at the 185 nm emission peak of a mercury lamp is expected to be slightly higher than that at 175 nm, but it is likely that a significant intensity gradient would

still exist and so a 254 nm-only lamp is used and ozone generated externally and introduced with the sample flow. The high reflectance of the ePTFE at 254 nm directs UV back into the reactor tube and results in increased intensity and uniformity. This illumination approach reduces power consumption and heat generation, thereby simplifying temperature control and long-term deployment for use in the field.

2.3.1.3. **Temperature Control**

Temperature uniformity within an OFR and temperature stability over time impact overall performance. Incomplete removal of the lamp heat can cause convective mixing through the reactor, resulting in increased loss of particles and gases and broadening of the RTD (Lambe et al., 2011; Mitroo et al., 2018). Techniques used to minimize heating by the lamps include enclosing them in sleeves that are continuously flushed with N_2, but continuously controlling temperature during long-term field studies can still be challenging (Li et al., 2019). The PFA OFR assembly is protected by a shell made from 13 × 13 cm square aluminum tube. Two U-bolts mounted through the surface of the aluminum shell hold the reactor securely, preventing accumulation of static charge that could otherwise result from shifting between the reactor body and the ePTFE and Mylar layers. The shell also provides a barrier to reduce the accumulation of static charge from inadvertent touching or other contact. A total of four fans are mounted on opposite faces near the top and bottom of the shell. The fans near the bottom bring air into the space between the reactor and the shell and those near the top exhaust it, which removes heat generated by the low-power UV lamp and weakens the temperature gradient through the whole system.

The average working temperature for the tests reported below was approximately 23.6 ˚C, which is close to the average room temperature of 22.7 ˚C. A temperature rise of less than 2 C was observed during continuous operation over several days.

2.3.2. **Experimental Setup**

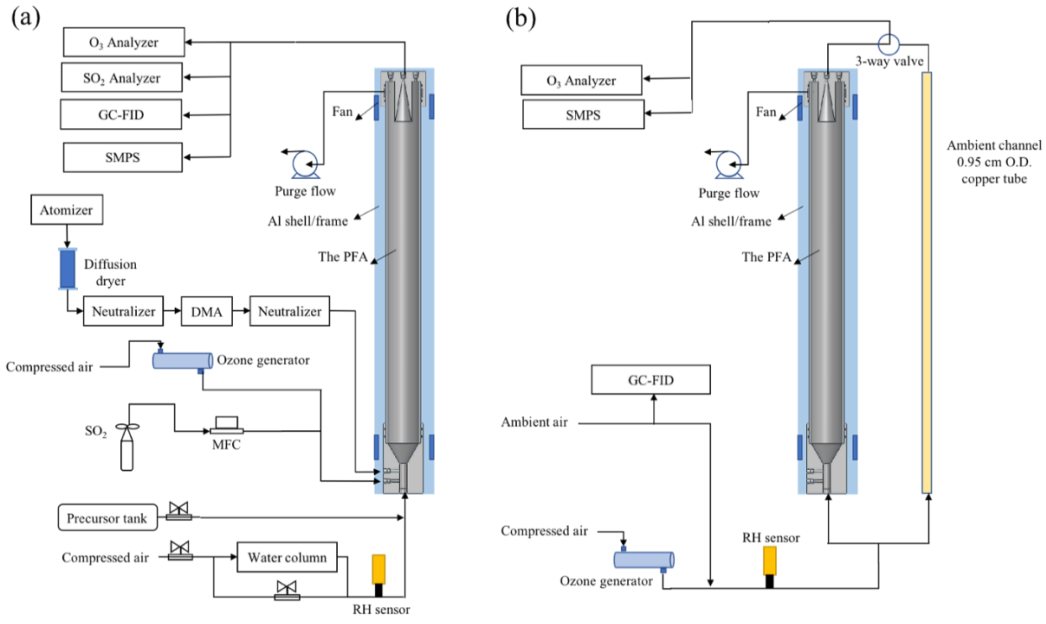

Figure 2.3: Schematic diagram of the PFA OFR and associated experimental setup for (a) the laboratory and (b) field experiments.

The PFA OFR is an OFR254-type oxidation flow reactor, in which O_3 must be generated externally and introduced with the sample flow (Li et al., 2015). Among the advantages of OFR185-type oxidation flow reactors is their ability to be operated without an inlet, which is often desirable for field investigations. As noted above, reflectance of 185 nm UV by the ePTFE is insufficient to produce the intensity and spatial uniformity required to rely on photolysis of O_2 and H_2O for generation of O_3 and OH. Instead, the OH

radicals are produced as the 254 nm UV radiation photolyzes O_3 introduced with the sample to generate excited oxygen atoms, $O(^1D)$, which then react with H_2O in ambient air or humidified laboratory air. For the laboratory experiments described here, O_3 and humidified zero air were mixed with the tracer or precursor gas(es) prior to being introduced into the reactor inlet. The schematic of the PFA OFR and associated experimental equipment for laboratory and field experiments are shown in Figure 2.3, respectively. Ozone was produced by flowing zero air through an O_3 generator (Jelight Company Inc. Model 610). The flow rate was controlled to 0.4 L min^{-1} and the O_3 mixing ratio was monitored by an O_3 analyzer (Teledyne Model T400U). The resulting O_3 concentration can be easily and precisely adjusted by changing the position of a sleeve that covers a portion of the UV lamp or by adjusting the flow rate of air through the generator. When used, seed particles were generated using an atomizer and differential mobility analyzer, DMA, as is described in the RTD experiment section. The flow at the outlet of the reactor was split using a Swagelok tee. From one leg of the tee a 150 cm L × 0.635 cm OD PFA tube was connected to gas measurement instruments including the O_3 analyzer, an SO_2 analyzer (Teledyne Model T100UP), and a gas chromatograph with flame ionization detector (GC-FID, SRI Inc. Model 8610C). A 0.95 cm OD stainless tube was connected to the other leg of the tee and carried the aerosol exiting the reactor to a fabricated scanning mobility particle sizer (SMPS), which measured the particle size distribution roughly once every 4 min. For the ambient air experiments, outdoor air was brought inside the lab and to the PFA OFR with a 200 cm L × 0.95 cm OD anti-static PFA tube (Fluorotherm H2 PFA). A 150 cm × 0.95 cm OD length of copper tube was used as

a bypass in parallel with the OFR, with sampling alternated between the two through the use of an automated 3-way valve. The residence time of the bypass line was approximately 2 s. Instrument operation and experimental sequencing were controlled using National Instruments LabVIEW software.

The total flow rate for the laboratory tests was 3.5 L min^{-1}, corresponding to an average residence time of 130 s, while those of the PAM, TPOT, and CPOT are about 100, 110, and 1500 s, respectively. A purge flow rate of 1 L min^{-1} was extracted from the annulus outside of the sample exit cone as described above. The ambient experiments were conducted using a slightly lower flow rate of 3 L min^{-1}, resulting in a residence time of 150 s, with a 1.5 L min^{-1} purge flow.

2.3.3. **RTD Experiments**

The residence time distributions of particles and gases were experimentally characterized and compared with results obtained from an ideal laminar flow model simulation. The experimental configuration is illustrated in Figure 2.3. Monodisperse ammonium sulfate (AS) particles were generated by atomizing a 0.04 M aqueous AS solution with an atomizer (TSI Inc. Model 3076). The atomized particles were dried by directing them through a silica gel/ molecular sieve diffusion column. The size of the particles was selected using a differential mobility analyzer (DMA). The aerosol was brought to a steady state charge distribution before and after size classification by the DMA using soft x-ray neutralizers. The residence time distributions (RTDs) for particles were characterized by introducing 30 s pulses of 200 nm AS particles into the PFA OFR while

measuring the particle counts in the outlet flow with a condensation particle counter (CPC, TSI Inc. Model 3762).

RTDs for gases were characterized by injecting 10 s pulses of SO_2 and CO_2. Pulses of a compressed gas mixture containing 27.5 ppm SO_2 in nitrogen (Airgas) were injected into a continuous zero air flow, with the pulse width controlled by opening and closing a mass-flow controller (Alicat Scientific, PN MC-100SCCM-D/5M). The SO_2 concentration was monitored from the sampling outlet of the PFA OFR with an SO_2 analyzer. Prior to the measurements, the reactor was purged with zero air for as long as required to reach a measured SO_2 mixing ratio that was stable at less than 0.5 ppb. To test the response function of a gas that would not react on or be taken up by the walls, 10 s pulses of CO_2 were injected from a custom-made CO_2 tank, with the pulses controlled by manually opening and closing a valve. The CO_2 concentration was measured at the outlet of the PFA OFR by a CO_2/H_2O gas analyzer (Li-COR Biosciences, Model Li-840A). A CO_2 background of 400 ppm was subtracted from the results because it was not removed by the zero air generator. The residence time distributions of both gases and particles were determined with the UV lamp turned on and turned off. The whole process described above was repeated three times.

2.3.4. **Gas and Particle Loss Quantification**

Particle losses in the reactor were characterized using AS particles within the diameter range from 50 to 200 nm. The monodisperse AS particles were size-selected by a differential mobility analyzer (DMA) and then passed through a soft x-ray neutralizer after size classification. Upon exiting the neutralizer, the size-dependent fraction of particles

that possess at least one positive or negative charge varies from about 41 % for 50 nm particles to 71 % for 200 nm particles (Wiedensohler, 1988). The flow rate through the reactor was kept at 3.5 L min^{-1}.

Particles were directed through the reactor or through a 150 cm L × 0.95 cm OD copper tube bypass, with sampling alternated between the two through the use of an automated 3-way valve. The particle transmission efficiency was calculated from the ratio of the particle concentrations measured at the outlets of the reactor and bypass using a CPC (TSI Inc. Model 3760A). After a set of initial tests, the static charge on the PFA, PTFE, and ePTFE surfaces was minimized by pushing concentrated bipolar ions generated with an electronic ionizer (Simco-Ion Inc., Fusion) through and around the flow tube for more than 12 hours. Additional measurements of 50 and 100 nm particles were made after minimizing the static charge. The measurements were repeated two or three times for each particle size, with agreement between measurements found to be to within ± 5 % when sampling the same diameter.

Gas losses were determined by continuously injecting CO_2 and SO_2 gases and measuring the ratio of the concentrations downstream and upstream of the reactor with the CO_2 and SO_2 analyzers identified above. For the SO_2 transmission efficiency tests, the PFA OFR walls were first passivated by flowing SO_2 gas through the OFR for at least 15 min and until stable concentration was measured by the SO_2 analyzer connected to the outlet.

2.3.5. **UV Intensity Profile and OH Exposure Level**

The 254 nm intensity at multiple positions inside the reactor was examined using a spectroradiometer (OceanView, Model USB4000 UV-FL) via a fiber optic cable. The influence of the reflective material(s) wrapped around the flow tube was assessed by measuring when it was wrapped only with aluminum-coated Mylar and when it was wrapped with a combination of ePTFE gasket (inner layer) and Mylar (outer layer). The OH production rate and corresponding equivalent exposure was varied by changing the UV intensity, RH, and injected O_3 concentration. Here, OH_{exp} is defined as the OH concentration (molec. cm^{-3}) multiplied by the mean residence time of the sample in the reactor. The UV intensity from the lamp was controlled over a range of 50 to 100 % using a lamp manager (BHK. Inc, PN IM10003) by stepping the control voltage from 0 to 5 V. The O_3 concentration in the reactor was varied by adjusting the position of a sleeve over the lamp in the ozone generator. To quantify OH_{exp}, SO_2 was injected with initial mixing ratios ranging from 150 to 250 ppb. For each test, the UV lamp was initially off, and was turned on only after the SO_2 concentration measured at the outlet was stable. After the lamp was turned on, the concentration of SO_2 was monitored at the reactor outlet. The distribution of the O_3 and OH within the PFA OFR was not measured in the current study. Future studies will be designed to investigate their profiles that result from that of UV. The typical concentration pattern observed is shown in Figure 2.13. OH exposure was quantified for each UV lamp intensity and O_3 concentration combination using Eqs. (1) and (2) (Davis et al., 1979; Atkinson et al., 2004). The procedure was repeated two or three times at each UV intensity.

$$d\,[SO_2]/dt = -k_{OH\text{-}SO2}[OH][SO_2] \quad (1)$$

$$OH_{exp} = k_{OH\text{-}SO2}^{-1} \times \ln [SO_2]_0 / [SO_2]_f \quad (2)$$

Where:

$k_{OH\text{-}SO2}$ — 9×10^{-13} cm^3 $molec.^{-1}$ s^{-1}

$[SO_2]_0$ *and* $[SO_2]_f$ — SO_2 concentrations measured at the reactor outlet without and with the UV lamp turned on

2.4. **Results and Discussions**

2.4.1. **UV Intensity Distribution and OH_{exp} Level**

The normalized UV intensity as a function of distance from the lamp located at the top of the reactor is shown in **Error! Reference source not found.**(a). The n ormalized UV intensity is calculated as the intensity at a specified position divided by the maximum measured inside the PFA OFR. As expected, an intensity gradient exists, with decreasing intensity with distance from the lamp. The gradient is much steeper when the flow tube is not wrapped with the ePTFE gasket. Without the ePTFE gasket, the intensity near the bottom of the tube is only 15 % of that at the top. Adding the ePTFE resulted in an intensity 30 cm from the bottom that was approximately five times higher than that with only the Mylar. The relative UV intensity enhancement (ERIntensity) is shown as a function of position in **Error! Reference source not found.**(b). The UV intensity is enhanced by a factor of between about 2 and 6 with the addition of the ePTFE layer. In addition to increasing the average UV intensity, the use of the reflective gasket reduced the gradient in intensity, resulting in more uniform OH generation throughout the reactor.

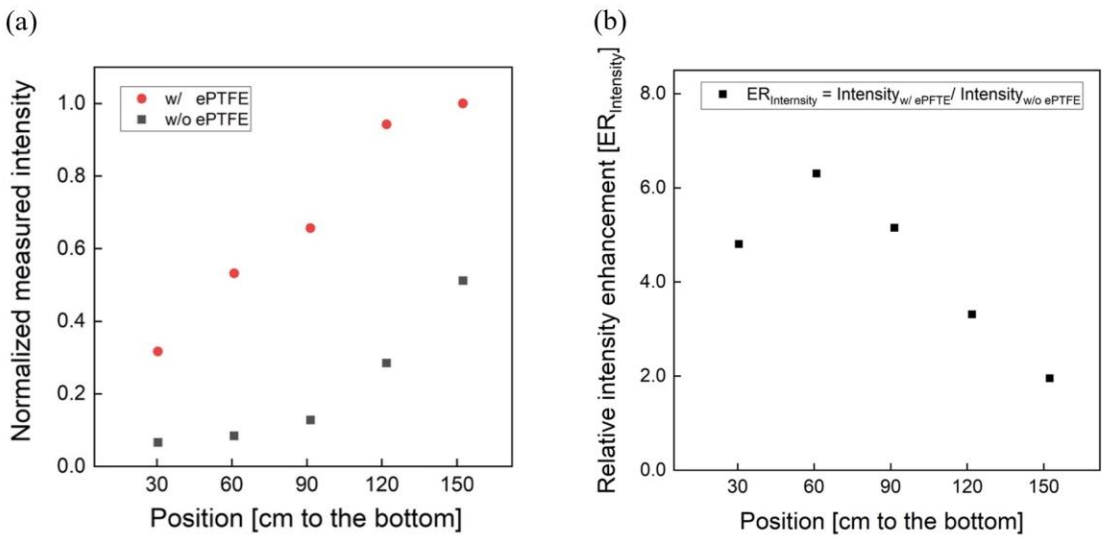

Figure 2.4 : Relative UV intensity profile (a) and intensity enhancement (b) achieved when the flow tube was wrapped with reflective ePTFE gasket.

The maximum photon flux (with the maximum lamp power) was estimated for ozone concentration measured at the exit of the OFR and known RH using a photochemical model used in previous studies (Li et al., 2015; Peng et al., 2015, 2019). The input photon flux of the model was adjusted to match the measured ozone concentration and OH exposure, which resulted in a maximum photon flux estimate of $\sim 2.4 \times 10^{14}$ photons cm^{-2} s^{-1} and 1.1×10^{15} without and with the ePTFE layer, resulting in about 1.5 and 7 times, respectively, that calculated from the lamp output power when neglecting any reflection. The OH concentration and resulting OH_{exp} were varied by varying the UV intensity, the added O_3 concentration, and the RH. Figure 2.5 shows the sensitivity of OH exposure as a function of photon flux at 254 nm with and without ePTFE wrapped around the flow tube. Without the ePTFE wrap around the reactor (black solid symbols), the OH concentration ranged from approximately 1.3×10^8 to 2.2×10^9 molec. cm^{-3}. The corresponding OH_{exp}

ranges from 2×10^{10} to 3.3×10^{11} molec. cm^{-3} s, which is approximately equivalent to 0.15 to 2.5 days of atmospheric exposure based on the reference average OH concentration of 1.5×10^{6} molec. cm^{-3}. The increased reflectance and UV intensity with the ePTFE wrap (red solid symbols), resulted in a maximum OH_{exp} of approximately 1.1×10^{12} molec. cm^{-3} s, equivalent to 8.5 days of atmospheric OH exposure, for the same RH (40 %) and O_3 mixing ratio (3.3 ppm). Overall, the highly reflective (and non-absorbing) materials used result in OH exposure comparable to that in other OFRs despite the use of a relatively low power output lamp.

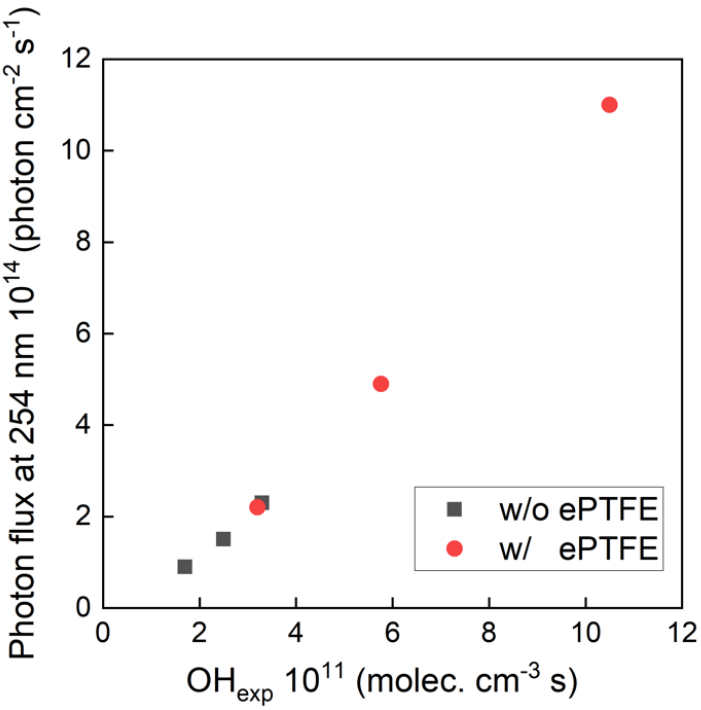

Figure 2.5: Variations in the concentration of OH as a function of photon flux at 254 nm with (red solid points) and without ePTFE (black solid points) wrapped around the flow tube.

2.4.2. **Gas and Particle Transmission Efficiency**

Figure 2.6 shows the transmission efficiency of AS particles with mobility diameter ranging from 50 to 200 nm. As stated above, particle transmission efficiency is calculated as the ratio of the concentration exiting the reactor to that exiting a copper tube bypass. Concentrations measured upstream and downstream of the copper tube agreed within ±1 %, confirming minimal loss in the bypass line. We performed two sets of tests: first, following the removal of static charge on the inner surface of the reactor tube (preliminary removal process), and second, following the additional removal of static charge between the ePTFE/Mylar wrap and the outer surface of the reactor tube (secondary removal process). The particle transmission efficiency after removal of only the charge on the inner surface of the tube was 0.39, 0.75 and 0.93 for 50 nm, 80 nm, and 100 nm diameter particles, respectively. With the removal of the static charge on the outer surface of the tube, the transmission efficiency of 50 nm and 80 nm particles increased from 0.39 to 0.75 and from 0.75 to 0.84, respectively. Each experiment was repeated twice, with agreement within ±10 % when sampling the same particle size and with the same flow rate. These results indicate that loss of small particles in the reactor can be significantly reduced by minimizing the static charge on both the inner and outer surfaces of the reactor tube. The similarity in the resulting 36 % of the 50 nm particles that are no longer lost and the 41 % of those 50 nm particles that are expected to be charged (Wiedensohler, 1988), suggests electrostatic loss was minimal after the static charge was minimized. Comparison with the particle transmission efficiency of other types of flow tube reactors with non-conductive wall materials is included in Figure 2.6. The PAM reactor referenced is the horizontal 46

cm L × 22 cm ID glass cylindrical chamber with a volume of 15 L that was described by Lambe et al. (2011), hereafter referred to as the quartz-PAM. The results show that the particle transmission efficiencies through the PFA OFR, TSAR, and ECCC-OFR are higher than those for the quartz-PAM, TPOT, and CPOT reactors, which may in part be due to their use of similar cone-shaped inlets and of centerline sampling. The particle transmission efficiencies of the quartz-PAM, CPOT, and TPOT for 50-100 nm particles are 30-50 %, 15-25 %, and 35-65 % lower than that of the PFA-OFR, respectively. On the other hand, the transmission efficiency through the TSAR and the ECCC-OFR is 5-25 % higher than for the PFA-OFR, though at least some of this difference is caused by the longer residence time of the PFA OFR than that of the other two reactors.

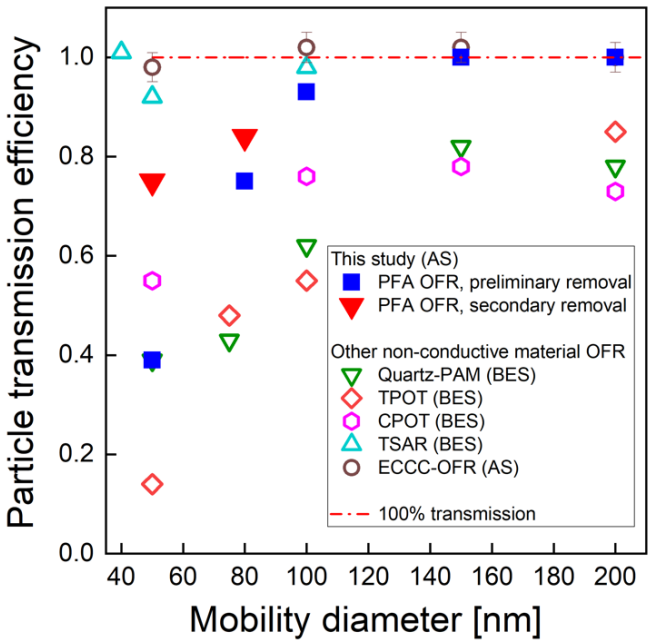

Figure 2.6: Measured particle transmission efficiency of the PFA OFR, quartz-PAM, TPOT, and ECCC-OFR flow reactors as a function of mobility diameter for bis(2-ethylhexyl) sebacate (BES) and ammonium sulfate (AS). Our results are shown as blue squares and red triangles.

The experimental configuration used to measure the loss of SO_2 and CO_2 is similar to that used to characterize the gas RTD. The penetration efficiencies of CO_2 and SO_2 were 0.90 ± 0.02 and 0.76 ± 0.04, respectively. The wall loss for most precursor species is expected to be equal to or less than the 24 % found for SO_2 because it is a good surrogate for wall-adhering species (Lambe et al., 2011; Ahlberg et al., 2017; Huang et al., 2017). For comparison, Lambe et al. (2011) reported that the measured CO_2 and SO_2 transmission efficiencies for the TPOT were 0.97 ± 0.10 and 0.45 ± 0.13, respectively, and for the quartz-PAM were 0.91 ± 0.09 and 1.2 ± 0.4, respectively.

The fate of low-volatility organic compounds (LVOC) that can condense onto particles, stick to the reactor walls, react with OH, or exit the reactor before condensing can be evaluated using the approach described by Palm et al. (2016). Based on the simple model they present, LVOC wall losses for the PFA OFR have an upper limit of approximately 30 % for a residence time of 130 s, which is comparable to that observed for SO_2 (24 %). Although the LVOC fate method is strongly dependent on the design and the geometry of the reactor, the consistency between the estimated loss and that measured for SO_2 suggests the value is a reasonable estimate of the vapor loss for our design. Losses of some gases are expected to be greater in this OFR than in most others because of its larger surface area to volume (A/V) ratio of 0.53 cm^{-1}, which is greater than that of the PAM reactor, while the mean residence times of the two are similar. However, losses of some gases may be lower as well because only the central core flow is subsampled, all Teflon materials are used, and, as is described in the next section, the RTD is comparatively narrow, which suggests less mixing than in other OFRs.

2.4.3. **Gas and Particle Residence Time Distributions**

The residence time probability distribution functions for particles and gases are shown in Figure 2.7 (a) and (b). Reporting the results as normalized distribution functions facilitates comparison of the flow characteristics of reactors of different shapes and sizes. RTDs of idealized devices and those reported for CPOT and quartz-PAM are also shown in Figure 2.7(a) and (b) for comparison (PAMWiki, 2019). The residence time probability distribution function is defined as the normalized measured concentration ($C_{out}(t)$)

divided by the total area of the normalized pulse (Fogler, 2006; Simonen et al., 2017), as described in Eq. (3) below. The average residence time was calculated as the summation of the product of the measured concentration and the corresponding residence time, all divided by the total area of the pulse.

$$PDF(t) = \frac{C_{out}\,(t)}{\int_0^\infty C_{out}\,(t)dt} \qquad (3)$$

The residence time distributions of particles and gases in the PFA OFR shown in Figure 2.7 (a) and (b) approach those expected for laminar developed flow. Measured RTDs for both particles and gases have relatively short tails at longer times compared with the ideal laminar flow pulse, as is expected because only the center ~50 % of the sample flow is subsampled and directed to the analyzers. Relative to the total flow through the reactor, the subsampled core has a narrower velocity range and less interaction with the walls. Extraction of the side purge flow also helps by preventing recirculation near the outlet. The RTDs measured with the UV lamp turned on are only slightly broader than those with it turned off. Previous studies report that UV lamps broaden the RTD because they heat the reactor walls and enhance convection inside the reactor (Simonen et al., 2017). Significant degradation is not observed in the PFA OFR, presumably because of the use of a comparatively low-power light source, circulation of air through the reactor housing, and the reactor being oriented vertically with the lamp at the top to promote stratification and to minimize convective mixing. Reversible uptake by the walls is responsible for the broader RTD for SO_2 relative to that for CO_2.

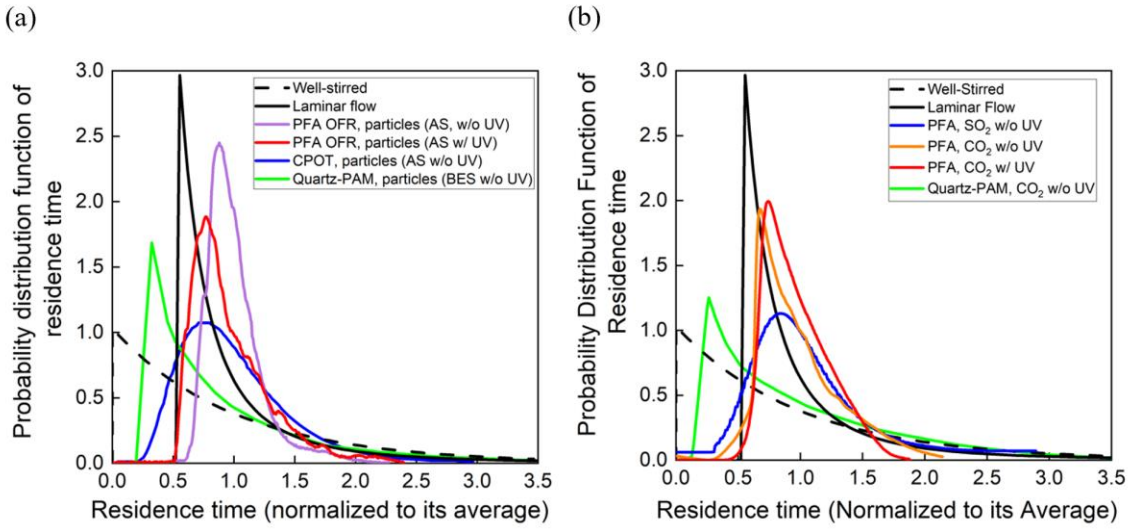

Figure 2.7: Residence time probability distribution functions of the PFA OFR, CPOT (Huang et al.,2017), and quartz-PAM flow tubes (Lambe et al., 2011) as a function of residence time for (a) particles and (b) gases.

We also investigated the effect of the ratio of the sample to side flow on the RTD for AS particles. The condition without the side purge flow was numerically simulated in COMSOL 5.4 by coupling the Laminar Flow and the Transport in Dilute Species packages. This result is compared with the RTD of that obtained experimentally with different sample:side flow ratios in Figure 2.14. The experimental results show the improved RTD response measured with the main:side ratio as close to 1. We expect future efforts to add some simulation studies, such as the model-derived relationship between the ratio of sample: side flow and the losses of particles and gases.

2.4.4. **SOA Yield Measurements**

Secondary organic aerosol yields (Y) are defined as the mass of OA formed (ΔC_{OA}) per reacted precursor mass (ΔHC) (Odum et al., 1996). The measured yields of *m*-xylene and α-pinene SOA as a function of OH exposure and organic aerosol concentration (C_{OA}) are shown in Figure 2.8(a) and (b). Here, the SOA yields are corrected for size-dependent gas and particle losses, with an average magnitude of the combined correction of 25 %. For comparison, the magnitude of the particle wall loss correction of the PAM reactor was 32 % ± 15 % (Lambe et al., 2015). The C_{OA} was calculated by multiplying the volume concentration measured with an SMPS by an assumed density of 1.2 g cm^{-3}. The mixing ratios of *m*-xylene and α-pinene introduced into the PFA OFR were in the ranges of 20-118 ppb and 13-145 ppb, respectively. The OH_{exp} was not measured simultaneously during the yield experiments, but applying the OFR254 OH exposure estimation equation as a function of O_3, RH, and UV lamp power (Peng et al., 2015) and the assumption that the OH reactivity was the same for both sets of measurements resulted in estimated values that are consistent with the measured OHexp described in Sect. 3.1. As expected, the SOA yield was observed to be dependent on OH exposure and aerosol mass concentration. The *m*-xylene SOA yield was 0.22 at 3×10^{11} molec. cm^{-3} s OH exposure and an OA mass concentration of 46 µg m^{-3} and the α-pinene SOA yield was 0.37 at 3×10^{11} molec. cm^{-3} s OH exposure and a mass concentration of 178 µg m^{-3}.

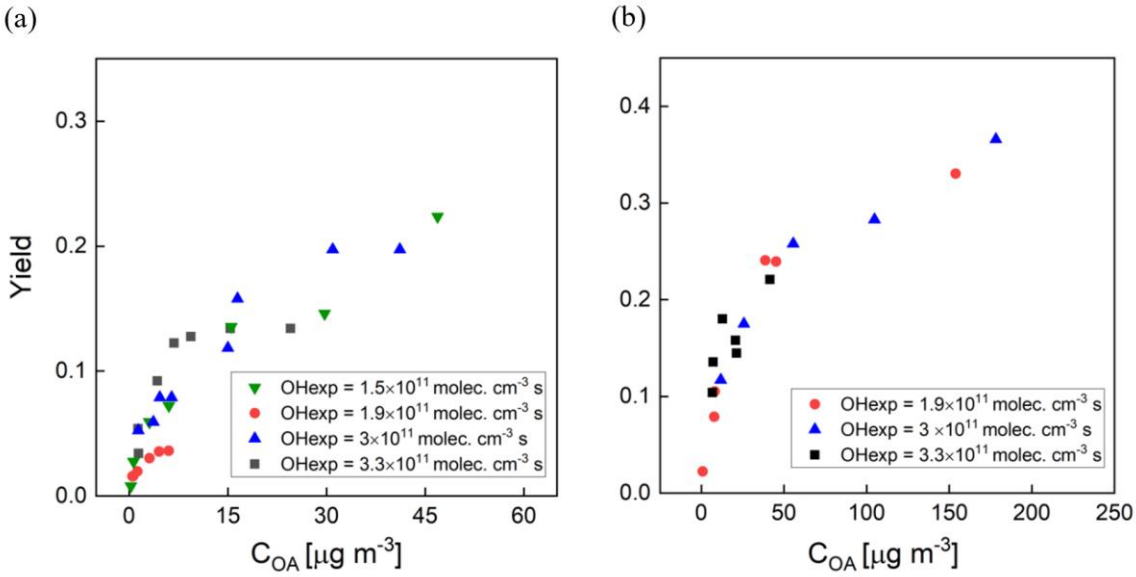

Figure 2.8: SOA yield as a function of organic aerosol concentration (C_{OA}) for (a) *m*-xylene SOA and (b) α-pinene SOA generated in the PFA OFR. Marker color reflects experimental combinations of UV intensity, O_3 mixing ratio, and RH. Each marker represents one VOC concentration.

The measured yields are compared with those reported by Lambe et al. (2011) for the TPOT (for 262–263 ppb precursor mixing ratio), the quartz-PAM (78–88 ppb), and the Caltech environmental chamber (14–48 ppb), and by Ahlberg et al. (2017) for the aluminum PAM (14-179 ppb of α-pinene and 43-395 ppb of *m*-xylene). The comparisons as a function of C_{OA} are shown in Figure 2.9(a) and (b). The SOA yields are higher in the PFA OFR than those in the quartz-PAM and TPOT but lower than in the aluminum PAM. The α-pinene SOA yields in the PFA OFR (0.37 ± 0.02) and Caltech chamber (0.42 ± 0.06) agreed within 12 % for comparable OH exposures (~10^{11} molec. cm^{-3} s). A contributor to differences in yield among the OFRs is variation in OH_{exp}, which, as noted above, was not measured during the yield experiments. Our estimates of OH_{exp} neglect the impact of varying OH reactivity (OHR), which is defined as the summation of the product of the

concentrations of species that react with OH and their reaction rate constants (Li et al., 2015; Peng et al., 2015). During our experiments, the maximum OH reactivities for the *m*-xylene and α-pinene experiments were 34 s^{-1} and 103 s^{-1}, respectively, which is higher than the 5.5 s^{-1} estimated for the SO_2 experiments that were used to determine the dependence of OH_{exp} on RH, O_3 concentration, and lamp power. This is also a source of uncertainty in PAM yields that were reported in Lambe et al. (2011) and is estimated by Li et al. (2015) to result in a factor of 2 uncertainty in OH_{exp} obtained from their model-derived equation. Differences in O_3 concentrations and resulting partitioning between reaction with O_3 and OH are expected to be more important for α-pinene than for *m*-xylene. The formed SOA is dependent on the reactivity of one or more of the SOA-forming compounds and the oxidant concentrations (McFiggans et al., 2019). For the same O_3 mixing ratio (3.3 ppm) and OH exposure (3×10^{11} molec. cm^{-3} s) described above, the reactivities of α-pinene towards O_3 and OH are estimated to be 6.8×10^{-3} s^{-1} and 111×10^{-3} s^{-1}, while that of *m*-xylene towards OH is estimated to be 50×10^{-3} s^{-1}.

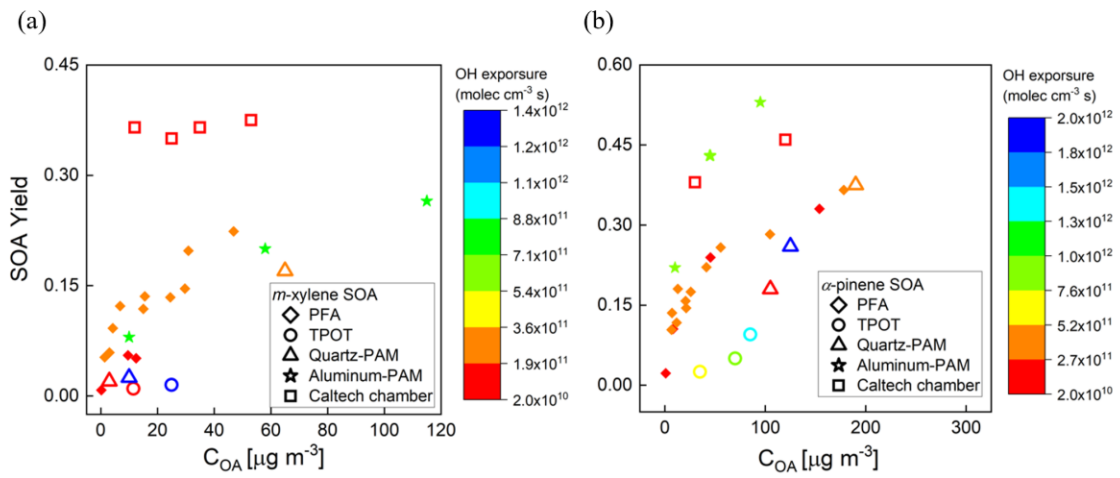

Figure 2.9 : Comparison of SOA yields as a function of organic aerosol concentration (C_{OA}) with those reported for other OFRs and one large Teflon chamber. (a) *m*-xylene SOA and (b) α-pinene SOA. Marker color reflects the OH_{exp}.

2.4.5. Seed Particle SOA Enhancement

The influence of seed particle concentration was investigated by measuring SOA yield for varying ratios of the mass concentrations of α-pinene and AS seed. For all experiments a constant flow rate (0.7 L min^{-1}) containing the AS seed particles was introduced together with a varying mixing ratio of α-pinene (8-30 ppb). Using the same method that was presented in Sect. 2.4, a DMA generated a narrow mode of AS seed particles centered at a diameter of 200 nm. The average mass concentration of the AS aerosol throughout the experiments was 40 μg m^{-3}. The O_3 concentration, RH, and UV lamp power were the same for all measurements, with a resulting OH_{exp} of about 2×10^{11} molec. cm^{-3} s, which is consistent with the OH_{exp} estimated from the model-derived equation (Peng et al., 2015). Measurements for each precursor concentration were repeated two or three times, with agreement between measurements to within ± 10 %. Figure 2.10(a)

and (b) show the volume size distributions for one set of experiments with and without added AS particles. The results show that the addition of seed particles suppresses the nucleation mode as condensation on the larger particles is favored. The concentration of α-pinene SOA increased with the addition of high concentrations of seed particles, as is expected because the increased surface area promotes condensation on the aerosol and decreases the fraction of low volatility oxidation products that reach and are lost to the walls or are further oxidized in the gas phase. In these experiments, the yield increased by as much as a factor of 3 at the minimum precursor:seed mass ratio of about 2. The magnitude of the enhancement decreased with increasing precursor:seed ratio and was within the run-to-run variability for ratios exceeding about 5, which is shown in Figure 2.15.

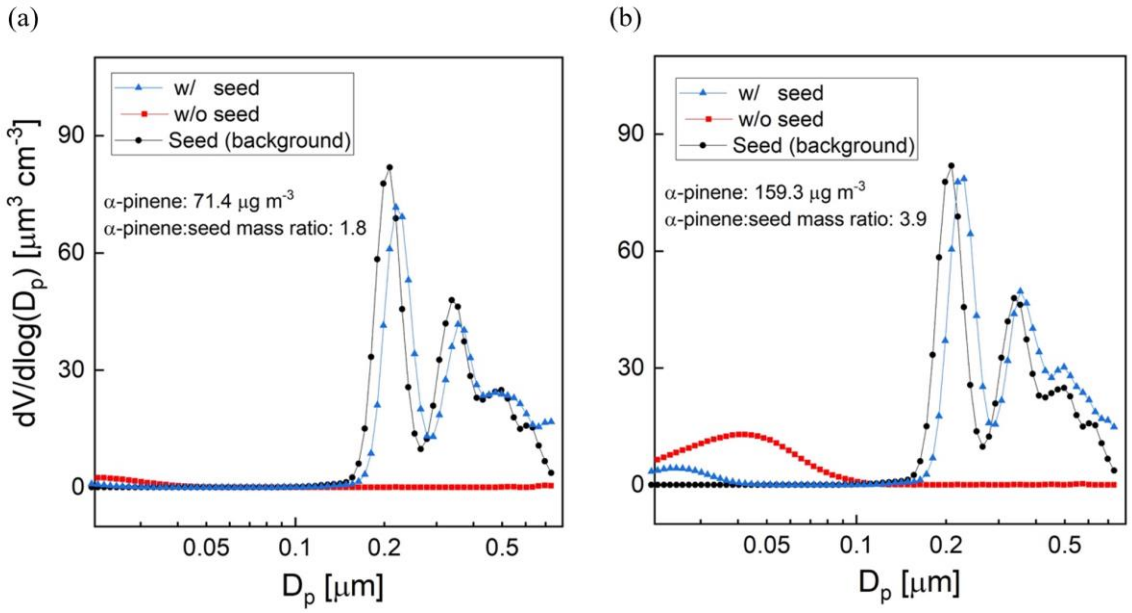

Figure 2.10: Example sets of volume size distributions from experiments evaluating the impact of adding AS seed particles on SOA yield. The precursor:seed mass ratio is (a) 1.8 (b) 3.9.

2.4.6. **Aerosol Formed From Oxidation of Ambient Air**

Ambient air from outside our lab at the UCR College of Engineering - Center for Environmental Research and Technology (CE-CERT) in Riverside, CA was processed by the PFA OFR for several days in January, 2020. Figure 2.11(a) and (b) show results for a 30-hour period (Jan. 7-8, 2020) and a 6-hour period on Jan. 8, 2020. Throughout the sampling period, the SMPS alternated through sets of three measurements of the processed aerosol at the exit of the reactor and sets of two measurements of unprocessed aerosol that bypassed the reactor through a copper tube. Each cycle of 5 measurements lasted 21 min. The OHexp during the sampling period estimated from the model-derived equation

introduced in Section 3.4 was in the range of 1-4 × 10^{11} molec. cm^{-3} s for the maximum lamp power and measured ozone concentration and RH.

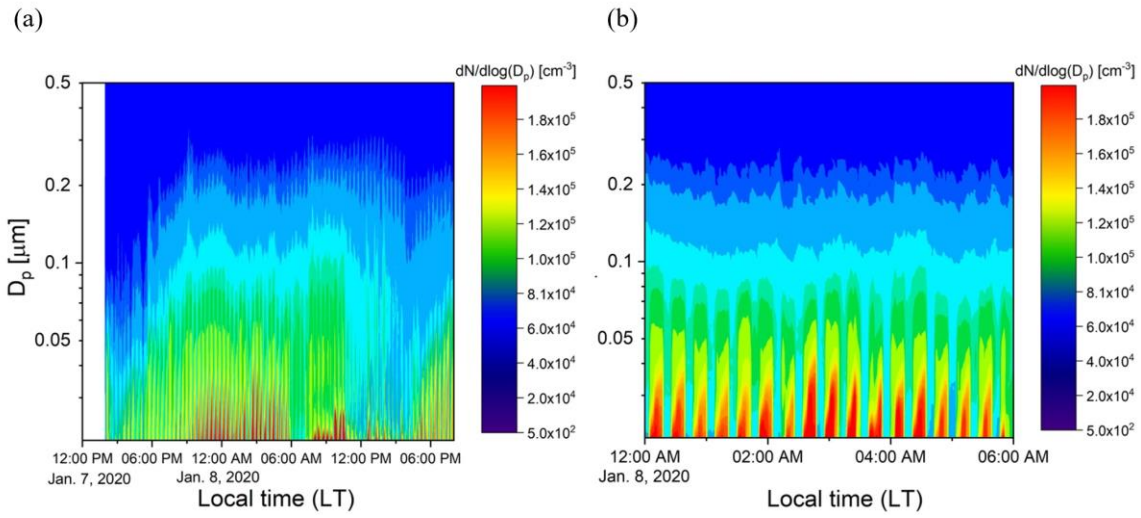

Figure 2.11: Example time series of size distributions of the aerosol processed by the PFA OFR and that which bypassed it over (a) 30 hours on Jan. 7-8, 2020 and (b) 6 hours on Jan. 8, 2020. The bands of high concentration were measured when the aerosol and ambient air were processed through the reactor.

Time series of aerosol mass concentrations calculated from integration of the SMPS size distributions are shown in Figure 2.12(a). The mass concentration of the aerosol exiting the reactor was corrected for the fractional dilution by the injected O_3 flow and for size-dependent gas and particle transmission efficiencies. The aerosol mass concentration increased significantly in the reactor during the oxidation process. A relative SA enhancement (ER_{SA}) is defined here as the ratio of the mass concentration of SA divided by that of the ambient (unprocessed) aerosol, with the SA simply defined as the difference between the processed and unprocessed aerosols. The ER_{SA} for the same sampling period is shown in Figure 2.12(b). A consistent diurnal pattern was not observed throughout the

sampling period. The SA mass concentration was an average of 1.8 times that of the ambient aerosol during the selected period. More SA formation was observed during nighttime on Jan 8, while decreasing amounts formed until around noon. The maximum enhancement due to SA formation was observed in the late afternoon on Jan. 7, when the SA mass concentration was approximately 7 times that of the ambient aerosol. A small SA enhancement was also observed during the late afternoon on Jan. 8. The overall temporal pattern likely reflects the impact of traffic related emissions from nearby roads, including a major highway that is about 1.5 km away. In the future there is a need to add more comprehensive measurements of the chemical composition of the particulate and gaseous species.

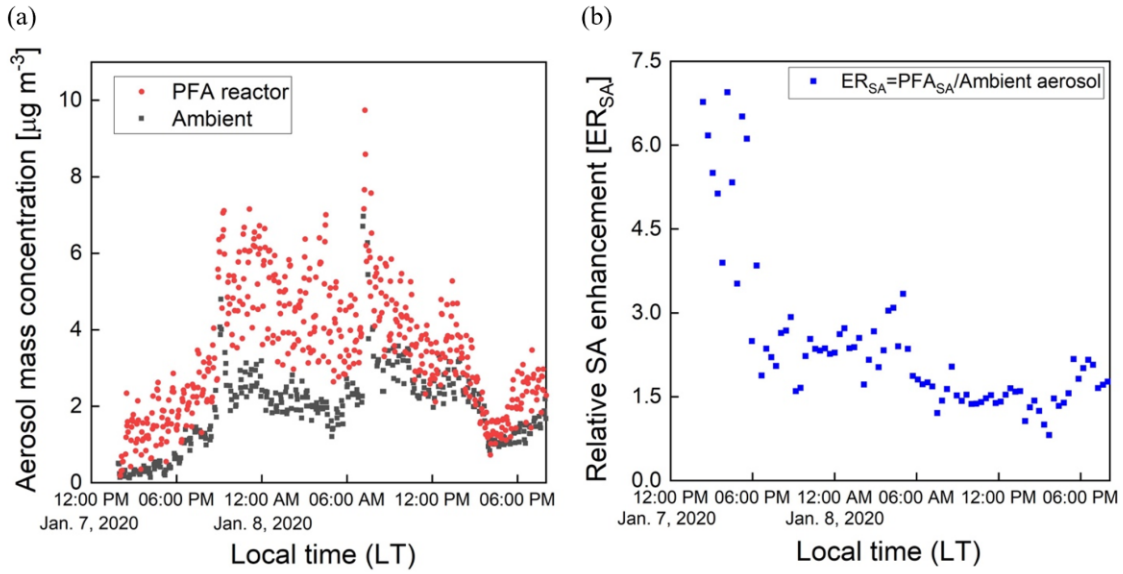

Figure 2.12: Time series of mass concentrations of the aerosol exiting the PFA OFR and that bypassing it (a), and (b) the relative enhancement of the mass concentration due to SA formation.

2.5. **Summary**

A new all-Teflon reactor, the Particle Formation Accelerator (PFA) OFR, was designed, constructed, and characterized using both experimental measurements and CFD modeling. Its performance was examined and evaluated through laboratory measurements and with ambient air. The reactor response and characteristics were compared with those from a smog chamber (Caltech) and other oxidation flow reactors (the Toronto Photo-Oxidation Tube (TPOT), Caltech Photooxidation Flow Tube (CPOT), the TUT Secondary Aerosol Reactor (TSAR), quartz and aluminum versions of Potential Aerosol Mass reactors (PAMs), and the Environment and Climate Change Canada OFR (ECCC-OFR)).

Our results show that OH_{exp} can be varied over a range comparable to that of other OFRs, with the dependence on UV lamp power, RH, and O_3 concentration characterized and reported. The particle transmission efficiency is over 75 % in the size range from 50 to 200 nm after minimizing static charge on the PFA, PTFE, and ePTFE surfaces. The gas transmission efficiencies of CO_2 and SO_2 are 0.90 ± 0.02 and 0.76 ± 0.04, respectively, with the latter comparable to estimated transmission of LVOCs through the PAM reactor. Computational simulation and experimental verification of particle and gas residence time distributions (RTDs) show that the flow through the reactor is nearly laminar, with narrower RTDs than reported for OFRs with greater diameter-to-length ratios.

The mass yields of SOA from the oxidation of α-pinene and *m*-xylene, and the effect of seed particles on those yields, were investigated. At comparable OH exposure, the *m*-xylene and α-pinene SOA yields are slightly higher than those in the quartz-PAM and

TPOT, but lower than in the aluminum-PAM. A likely contributor to differences in yields between the PFA OFR and other OFRs is the uncertainty in OH_{exp}, which was not measured simultaneously during the yield measurements and was determined from separate experiments for which the OH reactivity differed. The α-pinene SOA yields in the PFA OFR (0.37 ± 0.02) and Caltech chamber (0.42 ± 0.06) agree within 12 % for comparable OH exposures ($\sim 10^{11}$ molec. cm^{-3} s). The presence and concentration of seed particles was shown to have a significant effect on SOA yield. At a nominally fixed OH exposure of 2×10^{11} molec. cm^{-3} s, the α-pinene SOA yield for the minimum precursor:seed mass ratio of about 2 was about 3 times that when no seed particles were added. The magnitude of the enhancement decreased with increasing precursor:seed ratio and was within the run-to-run variability for ratios exceeding about 5. The SA production from ambient air was studied in Riverside, CA. The mass concentration of SA formed in the reactor was about twice the mass concentration of the ambient aerosol at the same time.

Overall, the computational and experimental results indicate that the PFA OFR is suitable for laboratory studies and for field use that includes measurement of rapidly changing ambient concentrations. Future efforts will include adding direct measurement of OHexp during measurements, development of an OHexp estimation description for the PFA OFR comparable to that reported for other OFRs, and further exploring the influence of OH reactivity on OHexp and of seed particles on SOA yield. We will also expand upon measurements of the composition of the particulate products and gaseous precursors during one or more field studies to evaluate how well the PFA OFR simulates atmospheric chemistry that typically requires hours or days.

2.6. **References**

Ahlberg, E., Falk, J., Eriksson, A., Holst, T., Brune, W. H., Kristensson, A., Roldin, P., and Svenningsson, B.: Secondary organic aerosol from VOC mixtures in an oxidation flow reactor, Atmospheric Environment, 161, 210-220, 2017.

Aljawhary, D., Zhao, R., Lee, A. K., Wang, C., and Abbatt, J. P.: Kinetics, mechanism, and secondary organic aerosol yield of aqueous phase photo-oxidation of α-pinene oxidation products, The Journal of Physical Chemistry A, 120, 1395-1407, 2016.

Atkinson, R., Baulch, D., Cox, R., Crowley, J., Hampson, R., Hynes, R., Jenkin, M., Rossi, M., and Troe, J.: Evaluated kinetic and photochemical data for atmospheric chemistry: Volume I-gas phase reactions of O x, HO x, NO x and SO x species, Atmospheric chemistry and physics, 4, 1461-1738, 2004.

Bruns, E., El Haddad, I., Keller, A., Klein, F., Kumar, N., Pieber, S., Corbin, J., Slowik, J., Brune, W., and Baltensperger, U.: Inter-comparison of laboratory smog chamber and flow reactor systems on organic aerosol yield and composition, Atmospheric Measurement Techniques, 8, 2315-2332, 2015.

Carter, W. P., Cocker III, D. R., Fitz, D. R., Malkina, I. L., Bumiller, K., Sauer, C. G., Pisano, J. T., Bufalino, C., and Song, C.: A new environmental chamber for evaluation of gas-phase chemical mechanisms and secondary aerosol formation, Atmospheric Environment, 39, 7768-7788, 2005.

Chen, L., Huang, Y., Xue, Y., Cao, J., and Wang, W.: Effect of oligomerization reactions of Criegee intermediate with organic acid/peroxy radical on secondary organic aerosol formation from isoprene ozonolysis, Atmospheric Environment, 187, 218-229, 2018.

Cubison, M., Ortega, A., Hayes, P., Farmer, D., Day, D., Lechner, M., Brune, W., Apel, E., Diskin, G., and Fisher, J.: Effects of aging on organic aerosol from open biomass burning smoke in aircraft and laboratory studies, Atmospheric Chemistry and Physics, 11, 12049-12064, 2011.

Davis, D., Heaps, W., Philen, D., and McGee, T.: Boundary layer measurements of the OH radical in the vicinity of an isolated power plant plume: SO2 and NO2 chemical conversion times, Atmospheric Environment (1967), 13, 1197-1203, 1979.

Deming, B. L., Pagonis, D., Liu, X., Day, D. A., Talukdar, R., Krechmer, J. E., de Gouw, J. A., Jimenez, J. L., and Ziemann, P. J.: Measurements of delays of gas-phase compounds in a wide variety of tubing materials due to gas–wall interactions, Atmospheric Measurement Techniques, 12, 3453-3461, 2019.

Ervens, B., Turpin, B., and Weber, R.: Secondary organic aerosol formation in cloud droplets and aqueous particles (aqSOA): a review of laboratory, field and model studies, Atmospheric Chemistry and Physics, 11, 11069-11102, 2011.

Ezell, M. J., Johnson, S. N., Yu, Y., Perraud, V., Bruns, E. A., Alexander, M. L., Zelenyuk, A., Dabdub, D., and Finlayson-Pitts, B. J.: A new aerosol flow system for photochemical and thermal studies of tropospheric aerosols, Aerosol Science and Technology, 44, 329-338, 2010.

George, I., Vlasenko, A., Slowik, J., Broekhuizen, K., and Abbatt, J.: Heterogeneous oxidation of saturated organic aerosols by hydroxyl radicals: uptake kinetics, condensed-phase products, and particle size change, Atmospheric Chemistry and Physics, 7, 4187-4201, 2007.

Huang, Y., Coggon, M. M., Zhao, R., Lignell, H., Bauer, M. U., Flagan, R. C., and Seinfeld, J. H.: The Caltech Photooxidation Flow Tube reactor: design, fluid dynamics and characterization, Atmospheric Measurement Techniques, 10, 839-867, 2017.

Iinuma, Y., Böge, O., Gnauk, T., and Herrmann, H.: Aerosol-chamber study of the α-pinene/O3 reaction: influence of particle acidity on aerosol yields and products, Atmospheric Environment, 38, 761-773, 2004.

Jimenez, J. L., Canagaratna, M., Donahue, N., Prevot, A., Zhang, Q., Kroll, J. H., DeCarlo, P. F., Allan, J. D., Coe, H., and Ng, N.: Evolution of organic aerosols in the atmosphere, science, 326, 1525-1529, 2009.

Kang, E., Toohey, D., and Brune, W.: Dependence of SOA oxidation on organic aerosol mass concentration and OH exposure: experimental PAM chamber studies, Atmospheric Chemistry and Physics, 11, 1837-1852, 2011.

Kang, E., Root, M., Toohey, D., and Brune, W.: Introducing the concept of potential aerosol mass (PAM), Atmospheric Chemistry and Physics, 7, 5727-5744, 2007.

Karjalainen, P., Timonen, H., Saukko, E., Kuuluvainen, H., Saarikoski, S., Aakko-Saksa, P., Murtonen, T., Bloss, M., Dal Maso, M., and Simonen, P.: Time-resolved characterization of primary particle emissions and secondary particle formation from a modern gasoline passenger car, Atmospheric Chemistry and Physics, 16, 8559-8570, 2016.

Keller, A. and Burtscher, H.: A continuous photo-oxidation flow reactor for a defined measurement of the SOA formation potential of wood burning emissions, Journal of aerosol science, 49, 9-20, 2012.

Krechmer, J. E., Day, D. A., and Jimenez, J. L.: Always lost but never forgotten: Gas-phase wall losses are important in all teflon environmental chambers, Environmental Science & Technology, 54, 12890-12897, 2020.

Kroll, J. H. and Seinfeld, J. H.: Chemistry of secondary organic aerosol: Formation and evolution of low-volatility organics in the atmosphere, Atmospheric Environment, 42, 3593-3624, 2008.

Lambe, A., Ahern, A., Williams, L., Slowik, J., Wong, J., Abbatt, J., Brune, W., Ng, N., Wright, J., and Croasdale, D.: Characterization of aerosol photooxidation flow reactors: heterogeneous oxidation, secondary organic aerosol formation and cloud condensation nuclei activity measurements, Atmospheric Measurement Techniques, 4, 445-461, 2011.

Lambe, A., Chhabra, P., Onasch, T., Brune, W., Hunter, J., Kroll, J., Cummings, M., Brogan, J., Parmar, Y., and Worsnop, D.: Effect of oxidant concentration, exposure time, and seed particles on secondary organic aerosol chemical composition and yield, Atmospheric Chemistry and Physics, 15, 3063-3075, 2015.

Li, K., Liggio, J., Lee, P., Han, C., Liu, Q., and Li, S.-M.: Secondary organic aerosol formation from α-pinene, alkanes, and oil-sands-related precursors in a new oxidation flow reactor, Atmospheric Chemistry and Physics, 19, 9715-9731, 2019.

Li, R., Palm, B. B., Ortega, A. M., Hlywiak, J., Hu, W., Peng, Z., Day, D. A., Knote, C., Brune, W. H., and De Gouw, J. A.: Modeling the radical chemistry in an oxidation flow reactor: Radical formation and recycling, sensitivities, and the OH exposure estimation equation, The Journal of Physical Chemistry A, 119, 4418-4432, 2015.

Lim, Y., Tan, Y., Perri, M., Seitzinger, S., and Turpin, B.: Aqueous chemistry and its role in secondary organic aerosol (SOA) formation, Atmospheric Chemistry and Physics, 10, 10521-10539, 2010.

Lonneman, W. A., Bufalini, J. J., Kuntz, R. L., and Meeks, S. A.: Contamination from fluorocarbon films, Environmental Science & Technology, 15, 99-103, 1981.

Loza, C., Craven, J., Yee, L., Coggon, M., Schwantes, R., Shiraiwa, M., Zhang, X., Schilling, K., Ng, N., and Canagaratna, M.: Secondary organic aerosol yields of 12-carbon alkanes, Atmospheric Chemistry and Physics, 14, 1423-1439, 2014.

Mao, J., Ren, X., Brune, W., Olson, J., Crawford, J., Fried, A., Huey, L., Cohen, R., Heikes, B., and Singh, H.: Airborne measurement of OH reactivity during INTEX-B, Atmospheric Chemistry and Physics, 9, 163-173, 2009.

Matsunaga, A. and Ziemann, P. J.: Gas-wall partitioning of organic compounds in a Teflon film chamber and potential effects on reaction product and aerosol yield measurements, Aerosol Science and Technology, 44, 881-892, 2010.

McFiggans, G., Mentel, T. F., Wildt, J., Pullinen, I., Kang, S., Kleist, E., Schmitt, S., Springer, M., Tillmann, R., and Wu, C.: Secondary organic aerosol reduced by mixture of atmospheric vapours, Nature, 565, 587-593, 2019.

Mentel, T. F., Bleilebens, D., and Wahner, A.: A study of nighttime nitrogen oxide oxidation in a large reaction chamber—The fate of NO2, N2O5, HNO3, and O3 at different humidities, Atmospheric Environment, 30, 4007-4020, 1996.

Mitroo, D., Sun, Y., Combest, D. P., Kumar, P., and Williams, B. J.: Assessing the degree of plug flow in oxidation flow reactors (OFRs): a study on a potential aerosol mass (PAM) reactor, Atmospheric Measurement Techniques, 11, 1741-1756, 2018.

Nah, T., Sanchez, J., Boyd, C. M., and Ng, N. L.: Photochemical Aging of α-pinene and β-pinene Secondary Organic Aerosol formed from Nitrate Radical Oxidation, Environmental science & technology, 50, 222-231, 2016.

Nah, T., McVay, R. C., Pierce, J. R., Seinfeld, J. H., and Ng, N. L.: Constraining uncertainties in particle-wall deposition correction during SOA formation in chamber experiments, Atmospheric Chemistry and Physics, 17, 2297-2310, 2017.

Odum, J. R., Hoffmann, T., Bowman, F., Collins, D., Flagan, R. C., and Seinfeld, J. H.: Gas/particle partitioning and secondary organic aerosol yields, Environmental science & technology, 30, 2580-2585, 1996.

Ortega, A., Day, D., Cubison, M., Brune, W. H., Bon, D., De Gouw, J., and Jimenez, J.: Secondary organic aerosol formation and primary organic aerosol oxidation from biomass-burning smoke in a flow reactor during FLAME-3, Atmospheric Chemistry and Physics, 13, 11551-11571, 2013.

Palm, B. B., Campuzano-Jost, P., Day, D. A., Ortega, A. M., Fry, J. L., Brown, S. S., Zarzana, K. J., Dube, W., Wagner, N. L., and Draper, D. C.: Secondary organic aerosol formation from in situ OH, O 3, and NO 3 oxidation of ambient forest air in an oxidation flow reactor, Atmospheric Chemistry and Physics, 17, 5331-5354, 2017.

Palm, B. B., Campuzano-Jost, P., Ortega, A. M., Day, D. A., Kaser, L., Jud, W., Karl, T., Hansel, A., Hunter, J. F., and Cross, E. S.: In situ secondary organic aerosol formation from ambient pine forest air using an oxidation flow reactor, Atmospheric Chemistry and Physics, 16, 2943-2970, 2016.

Pandis, S. N., Paulson, S. E., Seinfeld, J. H., and Flagan, R. C.: Aerosol formation in the photooxidation of isoprene and β-pinene, Atmospheric Environment. Part A. General Topics, 25, 997-1008, 1991.

Pankow, J. F.: An absorption model of the gas/aerosol partitioning involved in the formation of secondary organic aerosol, Atmospheric Environment, 28, 189-193, 1994.

Peng, Z., Day, D., Stark, H., Li, R., Lee-Taylor, J., Palm, B., Brune, W., and Jimenez, J.: HO x radical chemistry in oxidation flow reactors with low-pressure mercury lamps

systematically examined by modeling, Atmospheric Measurement Techniques, 8, 4863-4890, 2015.

Peng, Z., Day, D. A., Ortega, A. M., Palm, B. B., Hu, W., Stark, H., Li, R., Tsigaridis, K., Brune, W. H., and Jimenez, J. L.: Non-OH chemistry in oxidation flow reactors for the study of atmospheric chemistry systematically examined by modeling, Atmospheric Chemistry and Physics, 16, 4283-4305, 2016.

Pierce, J., Engelhart, G., Hildebrandt, L., Weitkamp, E., Pathak, R., Donahue, N., Robinson, A., Adams, P., and Pandis, S.: Constraining particle evolution from wall losses, coagulation, and condensation-evaporation in smog-chamber experiments: optimal estimation based on size distribution measurements, Aerosol Science and Technology, 42, 1001-1015, 2008.

Renbaum-Wolff, L., Grayson, J. W., Bateman, A. P., Kuwata, M., Sellier, M., Murray, B. J., Shilling, J. E., Martin, S. T., and Bertram, A. K.: Viscosity of α-pinene secondary organic material and implications for particle growth and reactivity, Proceedings of the National Academy of Sciences, 110, 8014-8019, 2013.

Seinfeld, J. H. and Pandis, S. N.: Atmospheric chemistry and physics: from air pollution to climate change, John Wiley & Sons2016.

Shrivastava, M., Andreae, M. O., Artaxo, P., Barbosa, H. M., Berg, L. K., Brito, J., Ching, J., Easter, R. C., Fan, J., and Fast, J. D.: Urban pollution greatly enhances formation of natural aerosols over the Amazon rainforest, Nature communications, 10, 1-12, 2019.

Silva, C., Pinto da Cunha, J., Pereira, A., Chepel, V., Lopes, M., Solovov, V., and Neves, F.: Reflectance of polytetrafluoroethylene for xenon scintillation light, Journal of Applied Physics, 107, 064902, 2010.

Simonen, P., Saukko, E., Karjalainen, P., Timonen, H., Bloss, M., Aakko-Saksa, P., Rönkkö, T., Keskinen, J., and Maso, M. D.: A new oxidation flow reactor for measuring secondary aerosol formation of rapidly changing emission sources, Atmospheric Measurement Techniques, 10, 1519-1537, 2017.

Slowik, J., Wong, J., and Abbatt, J.: Real-time, controlled OH-initiated oxidation of biogenic secondary organic aerosol, Atmospheric Chemistry and Physics, 12, 9775-9790, 2012.

Song, C., Zaveri, R. A., Alexander, M. L., Thornton, J. A., Madronich, S., Ortega, J. V., Zelenyuk, A., Yu, X. Y., Laskin, A., and Maughan, D. A.: Effect of hydrophobic primary organic aerosols on secondary organic aerosol formation from ozonolysis of α-pinene, Geophysical Research Letters, 34, 2007.

Steiner, A., Cohen, R., Harley, R., Tonse, S., Goldstein, A., Millet, D., and Schade, G.: VOC reactivity in central California: comparing an air quality model to ground-based measurements, Atmospheric Chemistry and Physics Discussions, 7, 13077-13119, 2007.

Tkacik, D. S., Robinson, E. S., Ahern, A., Saleh, R., Stockwell, C., Veres, P., Simpson, I. J., Meinardi, S., Blake, D. R., and Yokelson, R. J.: A dual-chamber method for quantifying the effects of atmospheric perturbations on secondary organic aerosol formation from biomass burning emissions, Journal of Geophysical Research: Atmospheres, 122, 6043-6058, 2017.

Wang, X., Liu, T., Bernard, F., Ding, X., Wen, S., Zhang, Y., Zhang, Z., He, Q., Lü, S., and Chen, J.: Design and characterization of a smog chamber for studying gas-phase chemical mechanisms and aerosol formation, Atmospheric Measurement Techniques, 7, 301-313, 2014.

Weitkamp, E. A., Sage, A. M., Pierce, J. R., Donahue, N. M., and Robinson, A. L.: Organic aerosol formation from photochemical oxidation of diesel exhaust in a smog chamber, Environmental science & technology, 41, 6969-6975, 2007.

Wiedensohler, A.: An approximation of the bipolar charge distribution for particles in the submicron size range, Journal of aerosol science, 19, 387-389, 1988.

Wong, J. P., Lee, A. K., and Abbatt, J. P.: Impacts of sulfate seed acidity and water content on isoprene secondary organic aerosol formation, Environmental science & technology, 49, 13215-13221, 2015.

Xu, L., Guo, H., Boyd, C. M., Klein, M., Bougiatioti, A., Cerully, K. M., Hite, J. R., Isaacman-VanWertz, G., Kreisberg, N. M., and Knote, C.: Effects of anthropogenic emissions on aerosol formation from isoprene and monoterpenes in the southeastern United States, Proceedings of the National Academy of Sciences, 112, 37-42, 2015.

Zhang, X., Cappa, C. D., Jathar, S. H., McVay, R. C., Ensberg, J. J., Kleeman, M. J., and Seinfeld, J. H.: Influence of vapor wall loss in laboratory chambers on yields of secondary organic aerosol, Proceedings of the National Academy of Sciences, 111, 5802-5807, 2014.

Zhang, Y., Sanchez, M., Douet, C., Wang, Y., Bateman, A., Gong, Z., Kuwata, M., Renbaum-Wolff, L., Sato, B., and Liu, P.: Changing shapes and implied viscosities of suspended<? xmltex\newline?> submicron particles, Atmospheric Chemistry and Physics, 15, 7819-7829, 2015.

2.7. **Supplementary Materials**

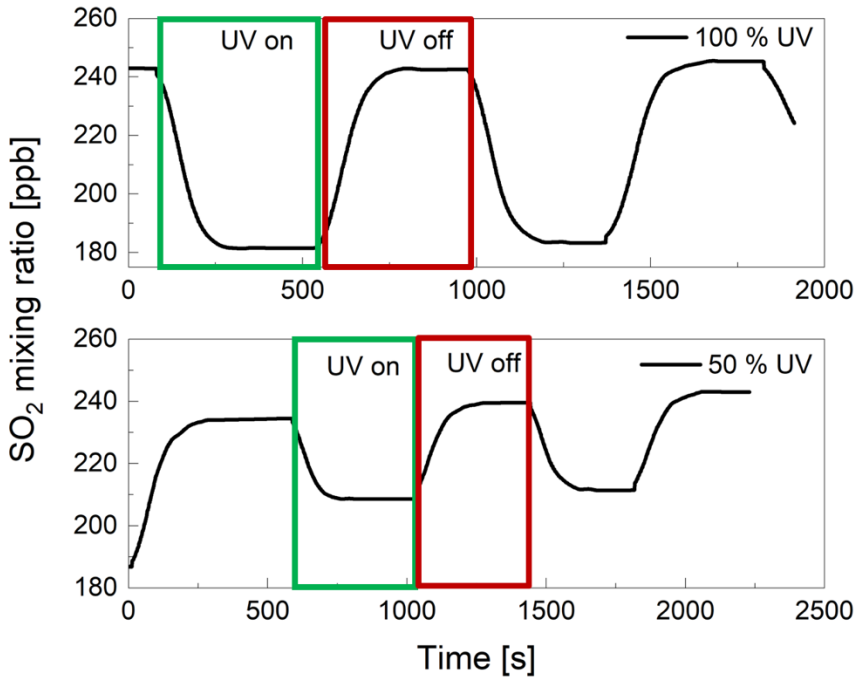

Figure 2.13: Example results from experiments to characterize OH exposure using injected SO_2.

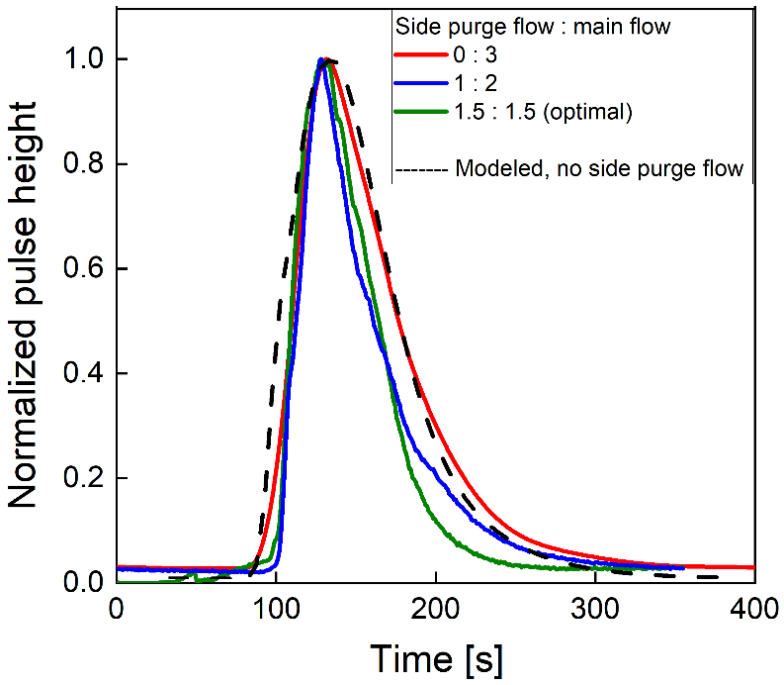

Figure 2.14: Measured response of pulse injection of AS particles with the side purge flow on (blue solid line) and off (red solid line), and the COMSOL simulation of the configuration with it turned off (black dashed line).

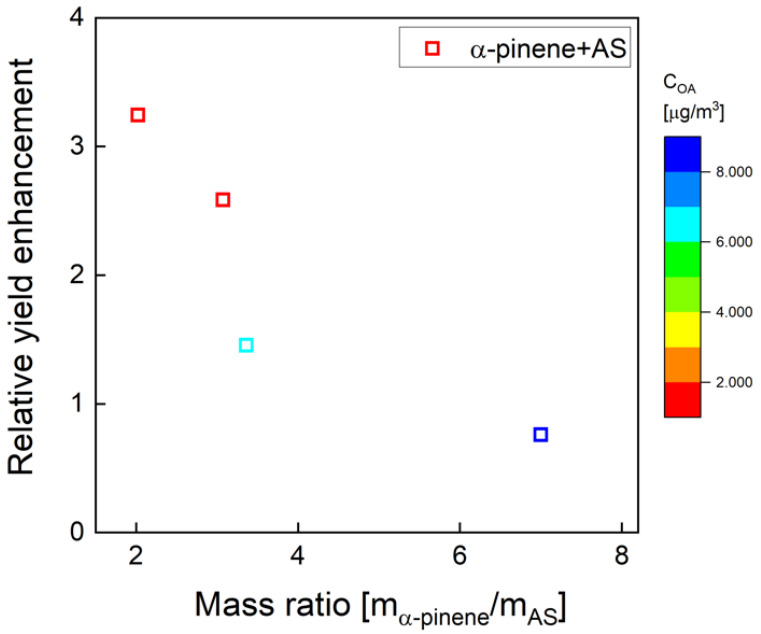

Figure 2.15: Relative α-pinene SOA yield enhancement as a function of mass ratio of α-pinene and AS seed particles. Marker color reflects aerosol mass concentration.

3. An Oxidation Flow Reactor for Simulating and Accelerating Secondary Aerosol Formation in Aerosol Liquid Water and Cloud Droplets

3.1. Abstract

Liquid water in cloud droplets and aqueous aerosols serves as an important reaction medium for the formation of secondary aerosol through aqueous-phase reactions (aqSA). Large uncertainties remain in estimates of the production and chemical evolution of aqSA in the dilute solutions found in cloud droplets and the concentrated solutions found in aerosol liquid water, which is partly due to the lack of available measurement tools and techniques. A new oxidation flow reactor (OFR), the Accelerated Production and Processing of Aerosols (APPA) reactor, was developed to measure secondary aerosol formed through gas- and aqueous-phase reactions, both for laboratory gas mixtures containing one or more precursors and for ambient air. For simulating in-cloud processes, droplets formed on monodisperse seed particles are introduced into the top of the reactor and the relative humidity (RH) inside it is controlled to 100 %. Similar measurements made with the RH in the reactor <100 % provide contrasts for aerosol formation with no liquid water and with varying amounts of aerosol liquid water.

The reactor was characterized through a series of experiments and used to form secondary aerosol from known concentrations of an organic precursor and from ambient air. The transmission efficiency of O_3 and CO_2 for all RH and of SO_2 for low RH exceeds

90 %, while it falls to about 70 % for SO_2 at 100 % RH. Particle transmission efficiency increases with increasing particle diameter from 0.67 for 0.050 mm particles to 0.98 at 0.20 mm, while that of the ~3.3 mm droplets formed on seed particles is greater than 80 %. The residence time distributions of both gases and particles are narrow relative to other OFRs and lack the tails at long residence time expected with laminar flow. Initial cloud processing experiments focused on the well-studied oxidation of dissolved SO_2 by O_3, with observed growth of seed particles resulting from the added sulfuric acid agreeing well with estimates based on the relevant set of aqueous phase reactions. The OH exposure (OH_{exp}) for low RH, high RH, and in-cloud conditions was determined experimentally from the loss of SO_2 and benzene, and simulated from the KinSim chemical kinetics solver with inputs of measured 254 nm UV intensity profile through the reactor and loss of O_3 due to photolysis. The aerosol yield for benzene at high OH_{exp} ranged from 18 % at low RH with dry seed particles present in the reactor to 59 % with cloud droplets present. Measurement of the composition of the secondary aerosol formed from ambient air using an aerosol mass spectrometer showed that the oxygen to carbon ratio (O:C) of the organic component increased with increasing RH (and liquid water content).

3.2. **Introduction**

Atmospheric aerosols have significant roles in air quality and climate (Akimoto, 2003; Seinfeld and Pandis, 2016; Shiraiwa et al., 2017). They consist of organic and inorganic compounds, with the organic component (organic aerosol; OA) being a substantial contributor to submicron aerosols, accounting for 20 ~ 90 % of aerosol mass loadings worldwide (Kanakidou et al., 2005; Jimenez et al., 2009; Knopf et al., 2018). Aerosol particles are both emitted directly into the atmosphere (primary aerosol) and produced in the atmosphere from reactions involving precursor gases (secondary aerosol) (Canagaratna et al., 2007; Andreae and Rosenfeld, 2008; Myhre et al., 2013). Secondary aerosol species include inorganic nitrate (NO_3^-), sulfate (SO_4^{2-}), and ammonium (NH_4^+), as well as thousands of organic compounds (secondary organic aerosol; SOA) that, collectively, account for a significant fraction of OA mass (Salcedo et al., 2006; Docherty et al., 2008; Froyd et al., 2009; Hallquist et al., 2009; Ehn et al., 2014). Considerable progress has been made towards understanding the efficiency with which secondary aerosol forms from gas-phase oxidation of important anthropogenic and biogenic precursors (Shrivastava et al., 2017; Schroder et al., 2018; Bianchi et al., 2019). Much less is known about the production rate and properties of secondary aerosol formed through aqueous-phase reactions in atmospheric liquid water (aqSA). Despite differences of orders of magnitude in liquid water content (LWC), both cloud droplets and aqueous aerosol particles serve as important reaction mediums for the formation and evolution of aqSA. Experimental and modeling efforts to determine the contribution of aqSA to the total secondary aerosol burden are complicated by the diversity of organic and inorganic

precursor gases, the complexity of the chemical pathways and products formed in liquid water, and uncertainties in quantities such as the concentration, composition, and size distribution of droplets. Nevertheless, laboratory and modeling studies have revealed that the contribution of aqueous reactions of dissolved inorganics and organics to secondary aerosol formation is significant (Lim et al., 2005; Carlton et al., 2006; Carlton et al., 2007; Volkamer et al., 2009; McNeill et al., 2012; Budisulistiorini et al., 2017; Ma et al., 2021; Wang et al., 2021).

Though sulfate formation from aqueous-phase oxidation of sulfur dioxide (SO_2) has been recognized and studied for decades, recent efforts have explored new pathways as part of an effort to explain rapid formation during severe haze events such as those observed in Beijing. Liu et al. (2020) measured sulfate formation in hygroscopic, pH-buffered aerosol particles and demonstrated that the oxidation of SO_2 by hydrogen peroxide (H_2O_2) in aqueous aerosol particles can explain the missing sulfate source during severe haze pollution events. Ge et al. (2021) used the Community Earth System Model Version 2 (CESM2) to evaluate the effects of in-cloud aqueous-phase reaction mechanisms on SO_2 oxidation and the importance for sulfate formation on hazy days.

Formation of SOA through aqueous-phase chemistry (aqSOA) was argued to potentially be significant by Blando and Turpin (2000) and has since been the subject of numerous laboratory, field, and modeling studies. Interest in aqSOA is partly due to its potential to help explain discrepancies between observed mass loadings and model estimates that include only gas-phase chemistry (Carlton et al., 2008; Ervens and

Volkamer, 2010; Ervens et al., 2011; Guo et al., 2012; McNeill, 2015; Gilardoni et al., 2016). A large fraction of aqSOA is believed to form through photochemistry as water-soluble products of gas-phase chemistry enter cloud droplets or aerosol liquid water (ALW) and react in the aqueous phase with hydroxyl radical (OH) or other oxidants, with some of the reaction products then remaining in the particle phase after evaporation of the water (Perri et al., 2009; Lim et al., 2010; Liu et al., 2012a; McNeill et al., 2012; Lin et al., 2014). Lamkaddam et al. (2021) found that 50-70 % of the products of gas-phase OH-oxidation of isoprene partitioned into a liquid water film and subsequently reacted with dissolved OH, resulting in the production of more oxygenated and less volatile products that would remain in the aerosol phase. Aqueous SOA is also produced as aldehydes such as glyoxal and methylglyoxal partition into water droplets and undergo nonoxidative reactions that are not dependent on UV or visible light (De Haan et al., 2009; Galloway et al., 2014), and by the aqueous oxidation of organic compounds by singlet molecular oxygen ($^1O_2$*), triplet excited states of organic compounds (^{3}C*), and hydroperoxyl radicals (HO_2) (Smith et al., 2014; Smith et al., 2015; Kaur and Anastasio, 2018). Ye et al. (2020) used results from experiments focused on the aqueous-phase photochemistry of three phenolic compounds to demonstrate the importance of aqueous-phase oxidation of moderately-soluble compounds to SOA formation. Tsui et al. (2017) used an updated version of the Gas-Aerosol Model for Mechanism Analysis (GAMMA) that includes uptake of isoprene epoxydiols (IEPOX) and subsequent formation of SOA to compare formation of IEPOX SOA in cloud water and aqueous aerosol for simulated laboratory and atmospheric conditions.

Unlike experimental studies of secondary aerosol formation through gas-phase reactions (gasSA), for which realistic atmospheric conditions can more easily be simulated, laboratory investigation of aqSA mechanisms, products, and yields is usually performed in bulk aqueous solutions with high oxidant and precursor concentrations (Liu et al., 2012b; Lim et al., 2013). The experimental concentrations and conditions often differ from those in the atmosphere, which can introduce uncertainty when results are implemented into multiphase models. Among the sources of constraints on experimental conditions is the lack of suitable and sensitive measurement and detection technology (Ervens et al., 2011; Spracklen et al., 2011). Some laboratory-based studies of aqueous-phase oxidation have been conducted using cloud chambers, which can offer measurement over a range in temperature and pressure and with artificial solar illumination. Such chambers have been used to study multiphase atmospheric photochemistry with one or more cloud formation and evaporation cycles (Berndt et al., 2007; Wang et al., 2011; Hoyle et al., 2016). However, challenges of creating an environment in which there is both active photochemistry and a controlled population of cloud droplets has limited the number of such facilities.

Oxidation flow reactors (OFRs) are commonly used to study secondary aerosol formation and evolution, both in the laboratory and in the field (Kang et al., 2007; Lambe et al., 2011; Keller and Burtscher, 2012; Ortega et al., 2013; Simonen et al., 2017). Photolysis of injected or in situ-formed ozone (O_3) inside a typical OFR results in OH concentrations that are orders of magnitude higher than found in the atmosphere. However, almost all OFRs are designed for studying gas-phase chemistry and are not generally

suitable for studying aqSA formation because of issues such as temperature gradients caused by the UV lights, wall losses of gases at high relative humidity (RH), and settling losses of droplets (Li et al., 2015; Huang et al., 2017; Mitroo et al., 2018; Cao et al., 2020). To our knowledge, only one study has been conducted in which a flow-through reactor was used to simulate in-cloud aqSA formation from oxidation of soluble gases produced from gas-phase photochemistry (Lamkaddam et al., 2021). Inside the wet-walled flow reactor used in that study, precursor gases react with OH over a timescale of minutes as with a standard OFR, whereas the subsequent aqueous-phase oxidation occurs in a thin layer of water surrounding the flow cell over a timescale of several hours for each experiment.

In this work, we describe the Accelerated Production and Processing of Aerosols (APPA) reactor, which is an OFR that can be used to study gas- and aqueous-phase secondary aerosol formation from prescribed concentrations of precursors in the lab and from the complex mixture of gases present in ambient air. Reported here is the design and laboratory characterization of the reactor, including examination of transmission efficiencies and residence time distributions for both particles and gases, size distributions of the droplets used in experiments simulating in-cloud chemistry, UV intensity and spatial variability, and OH exposure (OH_{exp}) estimation from measurement of the consumption of SO_2 and benzene. The observed growth of seed particles on which droplets formed as sulfate was produced from the S(IV)-O_3 reaction is compared with a prediction derived from the cloud model kinetic expression presented in Caffrey et al. (2001). We report the production of SOA from OH-oxidation of benzene with minimal liquid water present (RH = 40 %), with ALW (RH = 85 %), and for simulated in-cloud conditions (RH = 100 %).

Example results are also provided from measurements of the composition of secondary aerosol formed from ambient air processed under that same set of humidity and liquid water content conditions. Though not described here, the reactor can also be used to study the impact of cloud cycling on the composition and properties of ambient or generated particles.

3.3. **Design and Experimental Setup**

3.3.1. **Reactor Design and Operation Overview**

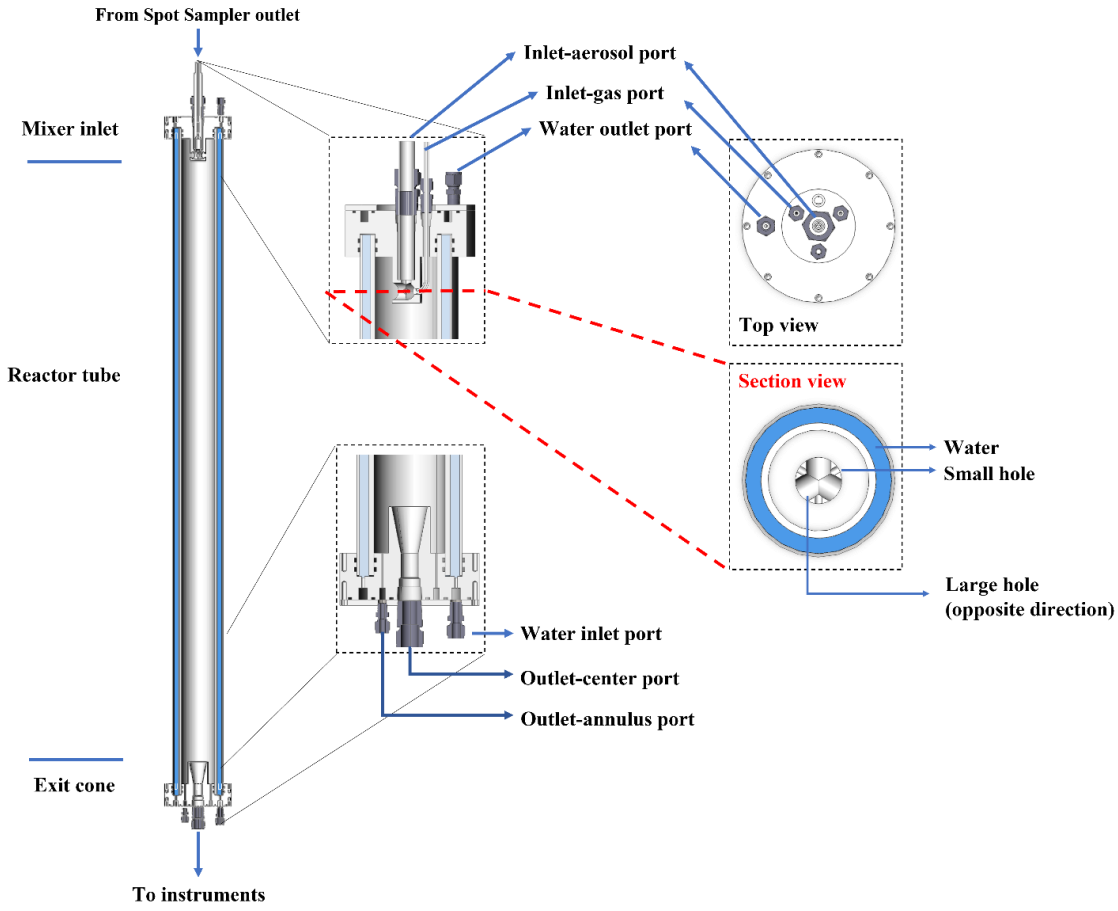

Figure 3.1: Vertical cross-section views of the APPA reactor (left) and horizontal cross-section views of the top cap (right).

A cross-sectional view of the APPA reactor is shown in Figure 3.1. The core of the reactor is a 148 cm L × 8.9 cm OD × 7.8 cm ID PFA Teflon tube (Ametek FPP) with a total internal volume of 7.5 L, which is identical to that used in the Particle Formation Accelerator OFR described by Xu and Collins (2021). The PFA tube is surrounded by a

148 cm L × 11.5 cm OD × 11.0 cm ID cylindrical quartz tube (Technical Glass Products, Inc.), which is used to create a water jacket as described below. Machined PTFE end caps seal the PFA and quartz tubes at the top and bottom. The APPA reactor is typically operated as a 254 nm-type OFR, with OH produced from photolysis of O_3 that is produced externally by an O_3 generator (Jelight Co., Inc., Model 610) and introduced into the reactor. The reactor is oriented vertically, with inlet flows introduced at the top and outlet flows extracted at the bottom. The nominal total flow rate of 3.0 L min^{-1} results in a mean gas residence time of 150 s. The bottom cap was adapted from the design used in the reactor described by Xu and Collins (2021). To minimize the influence of the reactor walls and to narrow the particle residence time distribution (RTD), the central 50 % (1.5 L min^{-1}) of the total flow is subsampled through the conical sample extraction port and directed to the aerosol and/or droplet analyzers. The outer 50 % (also 1.5 L min^{-1}) of the total flow is extracted through eight 0.15 cm holes at the base of the annulus between the reactor ID and the extraction port in the center of the tube, and is directed to one or more gas analyzers. Those two outlet flows and their corresponding ports in the bottom PTFE cap are hereafter referred to as *outlet-center* and *outlet-annulus*. The flow rates are actively controlled, with dilution or make-up flow used as needed such that they are always 1.5/1.5 L min^{-1} and are unaffected by the flow rates of the sets of analyzers used for different experiments. The reactor system is fully controlled using National Instruments Labview software and is capable of unattended operation for multiple days.

To precisely control the reactor cell temperature and to minimize any radial or axial temperature gradients that would promote convective mixing and cause droplet growth or

evaporation, temperature-controlled ultrapure water from a chiller (Cole Parmer, Model 10124) is pumped upward through the 1.0 cm annulus between the outside of the PFA tube and the inside of the quartz tube. To achieve uniform upward velocity around the annulus, the water flows through eight equally-spaced 0.32 cm holes as it enters through the bottom PTFE cap and as it exits through the top PTFE cap. Thermistors measure the temperature of the water entering and exiting the water jacket, with an average difference between the two of only about 0.2 ^{o}C with the solar simulating or UV lamps described below turned on.

The most novel aspect of the APPA reactor is its use for studying aqueous phase secondary aerosol formation in ALW and in cloud droplets. This is achieved by introducing cloud droplets formed on hygroscopic seed particles at the top and controlling the dew point and temperature in the reactor to produce either a prescribed RH or saturated conditions. To minimize losses of soluble and reactive gases to liquid water on the walls of the tubing and droplet generator upstream of the reactor, separate flows containing the gas mixture and the seed aerosol/droplets are used and are rapidly mixed inside the reactor. Those two inlet flows and their corresponding ports in the top PTFE cap are hereafter referred to as *inlet-gas* and *inlet-aerosol*. For the experiments reported here, the inlet-gas flow was controlled to 1.64 L min^{-1} and the inlet-aerosol flow was 1.36 L min^{-1}. The stability of two flows over time is evident in the time series shown in Figure 3.18(a). The inlet-gas flow is subsaturated and particle-free and contains the precursor gas(es) and O_3, while the inlet-aerosol flow is typically saturated zero air and, for most experiments, contains droplets formed on monodisperse seed particles. The

inlet-aerosol flow is injected through the center injection port shown in the horizontal cross-sectional view of the top cap in Figure 3.1 and the inlet-gas flow is introduced through three equally spaced ports that surround it.

3.3.2. **Inlet-Aerosol Flow and Droplet Generation**

Typical operation of the APPA involves injection of droplets formed on monodisperse seed particles into the top of the reactor and then measurement of the amount, properties, and/or composition of secondary aerosol that was added to them after they exit from the bottom and are dried. Because an objective of many of the experiments is to contrast aerosol formation in cloud droplets with that when dry or aqueous seed particles are present, droplets are typically injected even when the RH in the reactor is controlled to less than 100 % in order to minimize bias between the different reactor conditions. The flow path and components of the aerosol and droplet generation system are shown in Figure 3.2. To date, most experiments have used potassium sulfate (K_2SO_4) seed particles because they are non-acidic, have a dynamic shape factor close to 1, and effloresce at an RH of about 60 % (Freney et al., 2009), which permits measurements without ALW at higher RH than would be possible with common aerosol types such as ammonium sulfate and sodium chloride. The aerosol is generated by atomizing a 0.1 M aqueous K_2SO_4 solution with an atomizer (TSI Inc., Model 3076), drying with a diffusion dryer consisting of a perforated tube surrounded by molecular sieve pellets, and size classifying with a high flow differential mobility analyzer (DMA) (Stolzenburg et al., 1998). The aerosol is charge-neutralized in one soft x-ray neutralizer upstream of the DMA and then again in

another downstream of the DMA in order to reduce the charged fraction and resulting electrostatic losses of the particles. Additionally, static charge on the inside of the reactor is minimized prior to the start of a series of experiments by pushing compressed zero air through a bipolar ionizer (SIMCO Inc., Model 4012229) and through the reactor. The particle diameter used for most experiments to date is 0.1 mm, which was selected to balance the desire to use smaller particles to maximize the relative change in size accompanying growth from addition of secondary aerosol and the desire to use larger particles to provide sufficiently high surface area concentration for non-cloud experiments to maximize the fraction of oxidation products that condense on them. For that diameter, the seed particle concentration inside the reactor can be varied between about 3,000 and 30,000 cm^{-3} using an actively controlled dilution flow. For the seed particle concentration of approximately 20,000 cm^{-3} that was used for most experiments reported here, the resulting surface area concentration was between 1,200 and 1,400 μm^2 cm^{-3} for low RH operation with no ALW or cloud droplets.

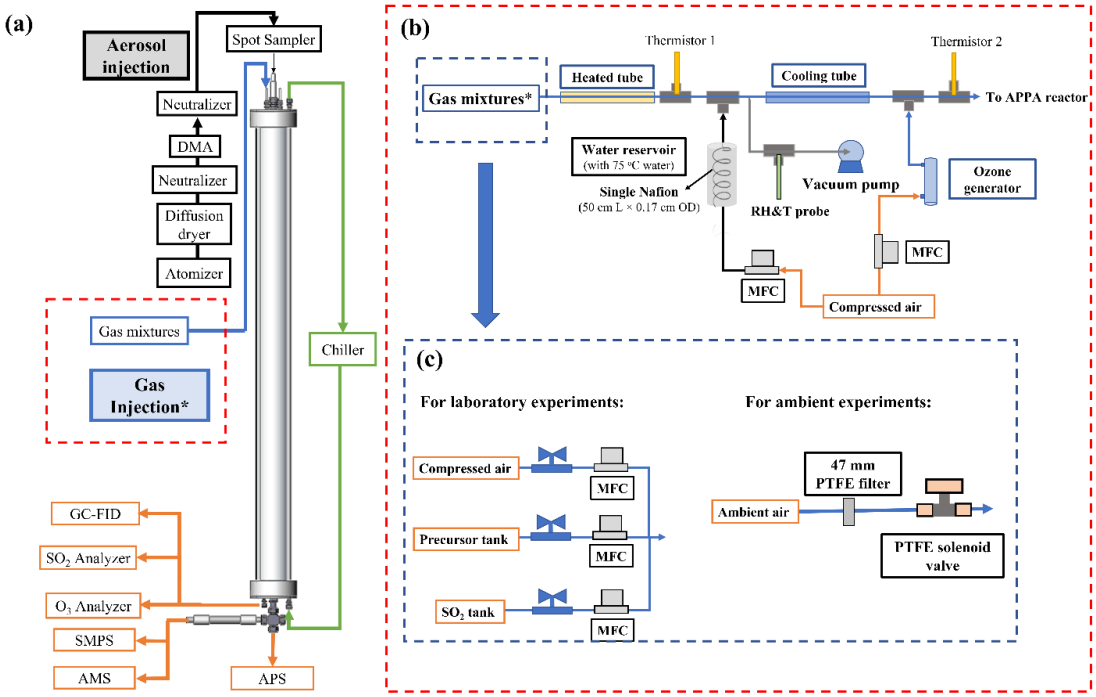

Figure 3.2 (a) Schematic diagram of the APPA reactor and (b) associated experimental setup of the gas mixture injection with (c) configurations shown for laboratory and ambient measurements.

Droplets are formed on the monodisperse particles as they pass through a modified Spot Sampler (Aerosol Devices, Inc., Model 110A) that is positioned on top of the reactor assembly and connected to the top cap through a short interface tube as depicted in Figure 3.3. The Spot Sampler uses a three-stage, moderated, laminar flow water condensation growth tube similar to that described by Hering et al. (2014). Particles activate as they are exposed to a supersaturated environment and grow into droplets with diameters between about 3 and 4 mm, effectively forming a fog (Hering and Stolzenburg, 2005; Eiguren Fernandez et al., 2014). The resulting LWC inside the reactor is between approximately 0.1 and 1.0 g m^{-3} for the range in seed particle concentration described above. The Spot Sampler used for this application was modified by increasing the bore diameter of the

condensation growth tube to about 6 mm and using more powerful fans for the heat sinks on the thermoelectric coolers in the moderator section. The focusing nozzle at the outlet of the standard Spot Sampler was replaced with a machined interface tube that carries the droplets to the inlet-aerosol port. Cooling water is pumped through coiled tubing wrapped around that interface to prevent warming of the flow that would result in evaporation of the droplets.

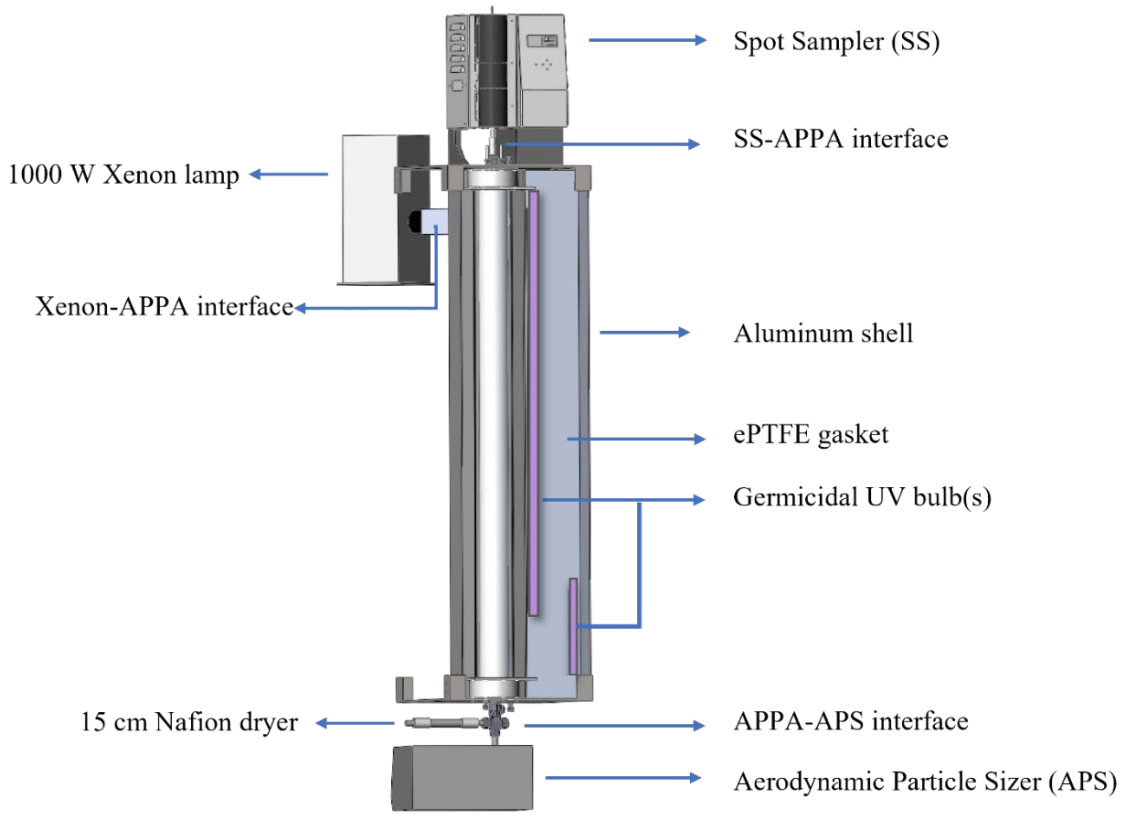

Figure 3.3: Assembly view of APPA reactor.

3.3.3. **Inlet-Gas Flow and RH Control**

The gas mixture introduced into the reactor contains O_3, water vapor, and either prescribed concentrations of aerosol precursors or particle-filtered ambient air. Almost all tubing and fittings in the flow path are made of PFA Teflon, with the exceptions being the solenoid valve, for which all wetted parts are PTFE, two thermistors that are covered in PTFE thread tape, and, for measurements of ambient air, the 47 mm PTFE membrane filter (Sartorius Stedim Biotech., Product 36229-44) used to remove ambient particles (the filter housing is PFA). The O_3 concentration is controlled using a mass flow controller (MFC; AALBORG Inc., GFC17-500SCCM) that varies the flow of zero air that is pushed through a generator in which O_2 is photolyzed (Jelight, Inc., Model 610). Because O_3 production in the generator is relatively insensitive to the air flow rate through it, a small purge flow is extracted through a critical flow orifice immediately downstream of the generator such that the amount of O_3 added to the gas mixture varies with the difference between the total flow through the generator and that purged through the orifice. Using that approach, the O_3 mixing ratio in the reactor can be controlled from 0.1 to 5.0 ppm. For laboratory experiments for which a precursor gas is injected, its concentration is controlled by an MFC (Alicat Scientific, Inc., Model MC-100SCCM) downstream of a pressurized cylinder or tank containing the precursor in a balance of zero air. The gas mixture is heated (typically to 55 ^{o}C) just upstream of the point at which water vapor is added in order to prevent localized saturation and condensation, which could otherwise cause losses of soluble gases. The water vapor concentration is controlled to create saturated conditions or to produce the desired RH in the reactor after mixing with the cool and saturated droplet flow and brought

to the controlled reactor temperature. To minimize dilution of the gas mixture flow for measurements with ambient air, concentrated water vapor is added from a hot, nearly saturated flow that is generated by pushing zero air controlled by an MFC (Alicat Scientific, Inc., Model MC-500SCCM) through a 50 cm L × 0.17 cm OD Nafion tube that is submerged in water inside a stainless tank that is maintained at a fixed temperature (typically 75 ^{o}C). Immediately downstream of the tee where the water vapor is added, the mixed flow is forced through a small orifice to promote efficient mixing. To prevent contact of the gas mixture flow with the RH/T sensor (Vaisala, Model HMP110) that is used to determine the water vapor pressure, a 0.8 L min^{-1} flow is split off and pulled past the sensor and then purged. Just upstream of the reactor, the humid gas mixture is cooled in a segment of the PFA tube that is submerged in a temperature-controlled water bath and is then split between three PFA tubes that extend through the three inlet-gas injection ports shown in Fig. 1. The three tubes extend into the interior of the reactor where they are press-fit into the outer curved surface of the hollow mixer also shown in that figure. Each of the three parts of the inlet-gas flow is introduced inward and perpendicular to the inlet-aerosol flow entering from above. The three gas mixture flows mix with the droplets and are pushed through holes on the opposite side of the hollow mixer to promote rapid and efficient mixing, while also minimizing impaction losses and any evaporation/growth of the droplets.

The RH in the reactor cell is calculated from the cell temperature and the water content in the two inlet flows and, independently, from the cell temperature and the water content in the outlet-annulus flow. The calculation based on the inlet flows is used for the

RH control, while that based on the outlet flow is used as a check. To date, the cell temperature has typically been maintained at 20 ^{o}C. The flow exiting the Spot Sampler is saturated, with a dew point of approximately the minimum temperature reached by the flow as it exits the base of the cold moderator section. Though the moderator temperature has typically been maintained at the 3 ^{o}C lower limit possible, that is the temperature of the growth tube wall, and the air temperature is significantly higher. By mixing the flow from the Spot Sampler with zero air and measuring the resulting RH in the temperature-controlled reactor cell, it was determined that the flow exiting the Spot Sampler has a dew point of about 14.5 ^{o}C. The temperature to which the inlet-gas flow is controlled is optimized for each experiment, but is fixed throughout an experiment to minimize the time needed to switch between measurements at different RH. During a multi-hour to multi-day experiment, the water content in the inlet-aerosol flow and the temperatures of the inlet-gas and inlet-aerosol flows and of the reactor are all fixed and the cell RH varies only with the water vapor concentration in the inlet-gas flow, which is actively controlled by adjusting the flow rate of zero air pushed through the submerged Nafion tube.

Figure 3.4 provides a graphical depiction of the inlet-gas flow RH needed to result in the commonly used set of 40 % RH (dry seed), 85 % RH (ALW), and saturated (cloud) conditions for the typical inlet-aerosol, reactor, and inlet-gas temperatures of 14.5 ^{o}C, 20.0 ^{o}C, and 31.0 ^{o}C, respectively. As shown in the figure, the RH in the inlet-gas flow is controlled to be higher than that needed to result in 100 % RH in the reactor for cloud conditions, which was experimentally found to be necessary to prevent droplet evaporation.

Figure 3.18(b) shows an example time series of the dew points of the two inlet flows and the temperature of the reactor for the same set of conditions depicted in Figure 3.4.

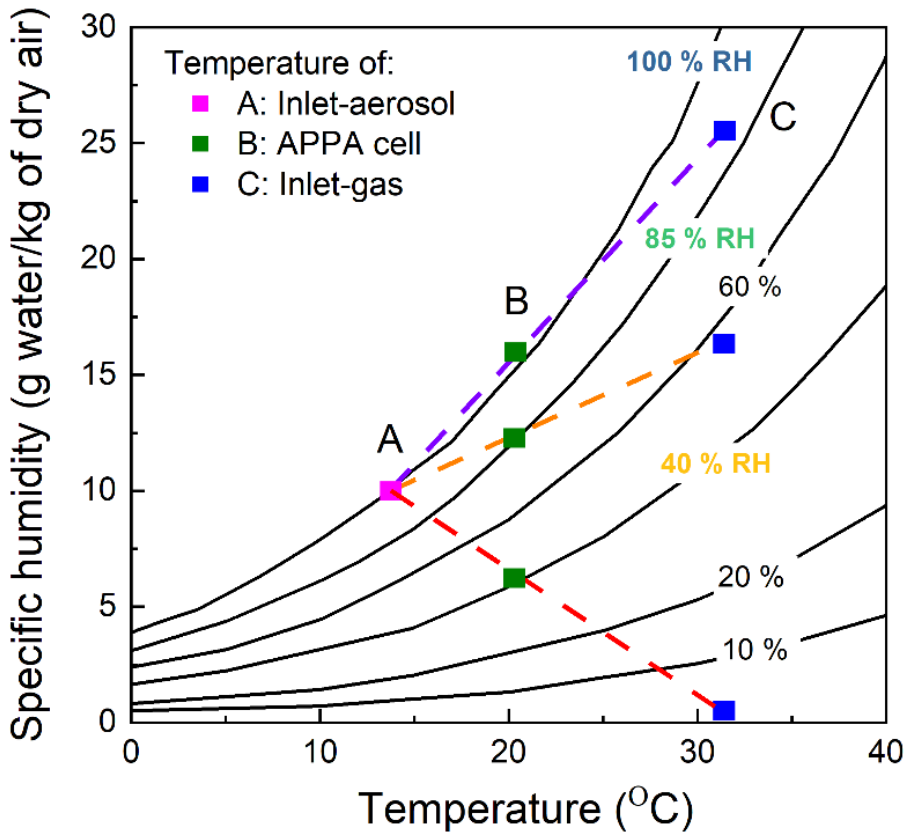

Figure 3.4: Relationship between the temperature and water vapor content of the two inlet flows and the resulting RH in the reactor.

3.3.4. **Outlet Flows and Gas and Aerosol Measurements**

As shown in Figure 3.2 and Figure 3.3, a ¾" (1.9 cm) Swagelok cross is mounted directly to the outlet-center port at the base of the reactor. For the orientation shown in the figures, the bottom and right legs of the cross are used only for measuring the size distribution of the droplets with an aerodynamic particle sizer (APS; TSI, Inc., Model 3321) that is permanently positioned below the reactor. For normal operation, the outlet-center flow containing the processed seed particles or droplets turns 90^{o} in that cross and then immediately enters a 15.2 cm L x 1.7 cm OD Nafion tube (Perma Pure, Model MD 700), where it is dried sufficiently to evaporate the large droplets that would otherwise have high loss rates due to settling and impaction. The flow is then further dried in a 61 cm L bundle of eighteen 0.17 cm OD Nafion tubes (Perma Pure, Model PD-070-18T) to reduce the RH to below 20 %. The size distribution and non-refractory composition of the initially single-component and monodisperse particles are then measured with a scanning mobility particle sizer (SMPS; fabricated in-house) and an Aerodyne high-resolution time-of-flight aerosol mass spectrometer (HR-ToF-AMS; DeCarlo et al., 2006). When measuring the droplet size distribution, the 1 L min^{-1} sample flow of the APS is pulled through a thin-walled stainless steel tube that is press fit on the sample flow inlet of the APS and extends up through the cross and to a point just below the conical extraction section in the reactor cap. For the orientation shown in Figures 2 and 3, 3.5 of the 4 L min^{-1} humidified sheath flow of the APS is introduced through the right leg of the cross, with the remaining 0.5 L min^{-1} pulled from the outlet-center flow around the thin-walled tube carrying the APS sample flow. As with the interface between the Spot Sampler and reactor, that between the

reactor and APS is cooled to the temperature of the reactor to prevent droplet evaporation. The outlet-annulus flow is always connected to an O_3 analyzer (Teledyne, Model T400U) and always flows past an RH/T sensor (Vaisala, Model HMP110). For some experiments, the flow is also sampled with an SO_2 analyzer (Teledyne, Model T100UP) and/or a gas chromatograph with flame ionization detector (GC-FID; SRI Inc., Model 8610C).

3.3.5. **Light Source and Intensity Profile**

As depicted in the assembly view in Figure 3.3, the reactor is housed in a 158 cm H × 20 cm L × 20 cm W aluminum shell that is in two halves that swing open and shut with hinges. The light sources are located outside of the quartz tube (which is outside of the PFA reactor). This configuration is similar to that in OFRs with UV lights surrounding a quartz tube reactor such as the Caltech photooxidation flow tube (CPOT; Huang et al., 2017) and Toronto photooxidation tube (TPOT; George et al., 2007; Lambe et al., 2011), with the important difference here that the UV must also be transmitted through the water layer and PFA tube. The quartz tube, ultrapure water, and PFA tube all absorb little visible or UV radiation (Beder et al., 1971; Litjens et al., 1999; Peng et al., 2017). However, the thick-walled PFA tube is translucent but dull white in appearance and much of the light incident upon it is reflected and not transmitted to reach the interior of the reactor. To maximize the UV intensity and uniformity inside the reactor, all interior surfaces of the aluminum shell are covered by 6 mm thick, highly UV-reflective expanded PTFE (ePTFE) gasket (Intertech, Inc., Product SQ-S). The intent is to mimic an integrating sphere, with photons repeatedly reflected by the gasket and onto the outer surface of the PFA tube to

maximize the fraction that reach the interior of the reactor and to make the UV uniform and nearly isotropic. The spectral intensity inside the reactor is measured using a UV-Vis spectrometer (StellarNet, Model BLK-CXR-SR) through a fiber optic cable that is terminated with a cosine receptor and permanently secured in a threaded port in the top cap.

For standard operation as an OFR, a pair of 254 nm-emitting germicidal UV bulbs that collectively span the length of the reactor (OSRAM, Model G36T8; 122 cm and USHIO, Model G10T8; 46 cm) are mounted on the inside of the ePTFE gasket as shown in Figure 3.3. The output of the UV lamps is computer controlled using a dimmable lamp ballast and is typically maintained at a level for each RH that results in loss of 15±2 % of the added O_3 between the top and bottom of the reactor, which represents a balance between maximizing the OH:O_3 concentration ratio and minimizing the O_3 (and consequently OH) gradient over the length of the reactor.

An alternate use of the APPA reactor is for studying the impact of solar radiation on biological particles or other particle types. To achieve this, a 1000 W xenon lamp (Newport Inc., Model 66924-1000XF-RI) is mounted externally, with its focusing lens housing inserted into one end of a 7.6 cm × 7.6 cm square tube interface that leads to a to a hole through the aluminum shell and ePTFE gasket surrounding the reactor. That interface is attached to the aluminum shell at a 45 degree angle so that the focused beam is incident upon the inner surface of the ePTFE gasket and not the quartz tube in order to minimize local heating and to maximize light intensity uniformity. A 7.6 cm × 7.6 cm B270

or borosilicate glass window is secured in the interface to produce a spectrum that most closely matches the solar spectrum, especially in the short UV wavelength range close to 300 nm. The light intensity inside the reactor can be adjusted over a wide range through a combination of adjustment of the voltage output of the xenon lamp controller, partial blocking of the beam using a sliding baffle in the interface tube, and swapping the standard 1000 W bulb with an interchangeable 450 W bulb.

3.4. Result and Discussion

3.4.1. Reactor Characterization

3.4.1.1. Gas and Particle Transmission Efficiencies

The particle transmission efficiency through the reactor was evaluated with continuous injections of size-classified ammonium sulfate (AS) particles with mobility diameters ranging from 0.050 to 0.20 mm. The transmission efficiency was calculated as the ratio of particle concentrations downstream of the reactor and downstream of a 150 cm L × 0.95 cm OD copper tube bypass measured with a condensation particle counter (CPC; TSI Inc., Model 3760A). As with the gas transmission efficiency tests described below, the flow rate through the reactor was the same 3.0 L min^{-1} used during normal operation. The measurements were repeated 2 or 3 times for each particle size, with agreement between measurements found to be to within ±5 % for each diameter. The particle transmission efficiency increases with increasing particle size, from 0.67 for 0.050 mm particles, to 0.94 at 0.080 mm, and 0.98 at 0.20 mm. As shown in Figure 3.5(a), the size-dependent particle transmission efficiency through the APPA reactor is similar to that for the OFR described by Xu and Collins (2021), which is not surprising given the similarity in the materials and designs of the reactor tubes and end caps of the two. Figure 3.5(b) compares the particle transmission efficiencies of the APPA OFR and several flow tube reactors with non-metal wall materials. The potential aerosol mass (PAM) reactor for which data are provided is the 15 L glass cylindrical chamber described in Lambe et al. (2011). The particle transmission efficiency of the APPA reactor is significantly higher

than those of the quartz PAM, TPOT, and CPOT, though somewhat lower than those of the Environment and Climate Change Canada OFR (ECCC-OFR; Li et al., 2019) and the TUT Secondary Aerosol Reactor (TSAR; Simonen et al. (2017) at the smallest particle sizes evaluated. The exact causes of the differences in transmission efficiencies among the reactors are unknown, though subsampling of the center flow at the outlet of the APPA likely contributes to its higher efficiency relative to the quartz PAM, TPOT, and CPOT, while its lower efficiency relative to the ECCC-OFR and TSAR may in part be due to differing residence times (150, 120, and 40 s for the APPA, ECCC-OFR, and TSAR, respectively).

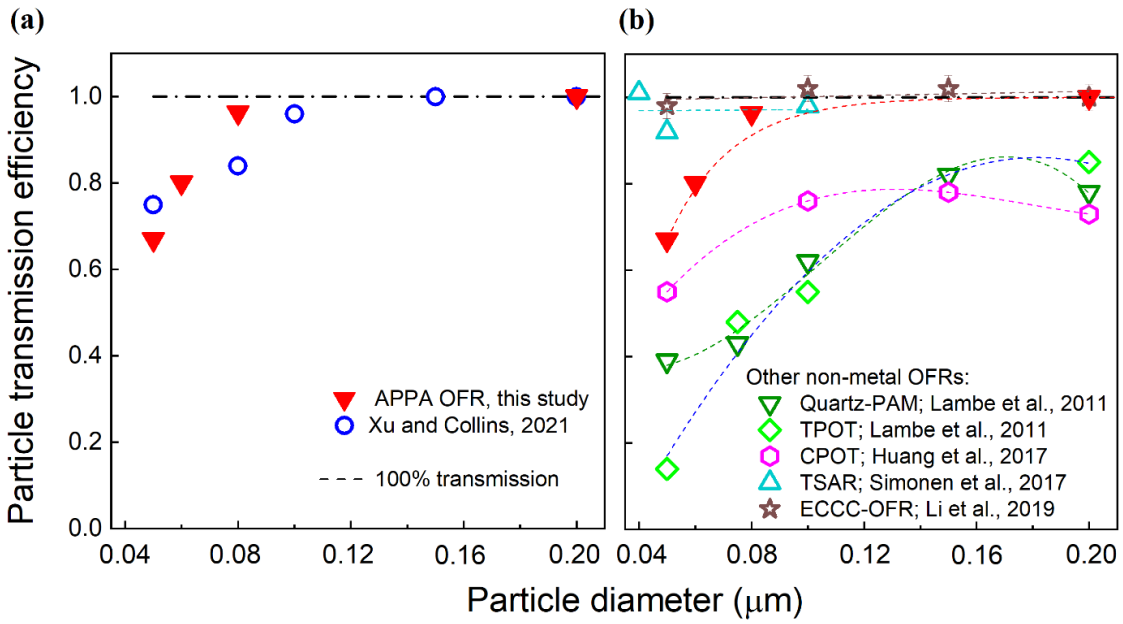

Figure 3.5: Particle transmission efficiency of the APPA reactor compared with those reported (a) for the OFR described by Xu and Collins (2021) and (b) for several non-metal OFRs reported in the literature, as described in the text.

Gas transmission efficiency was evaluated for SO_2, O_3, and CO_2, which were selected as representative of gases that adhere to, react on, and are unaffected by reactor walls, respectively (Lambe et al., 2011; Ahlberg et al., 2017; Huang et al., 2017). Transmission efficiencies were calculated as the ratios of the SO_2, O_3, and CO_2 concentrations measured downstream and upstream of the reactor using the SO_2 and O_3 analyzers described in Section 2.4 and an NDIR analyzer (Li-COR Biosciences, Model Li-840A) for CO_2. Prior to measurement of the SO_2 transmission efficiency, the SO_2 gas mixture was pushed through the reactor for about 20 min to passivate the tubing and reactor surfaces, following the approach described by Lambe et al. (2011). Figure 3.6 shows the gas transmission efficiencies for 0 % < RH ≤ 100 %. The transmission efficiencies of CO_2 and O_3 were over 90 % over the RH range tested for each. For SO_2, transmission decreases

from over 90 % at an RH of 40 % to 0.8 and 0.73 at RH of 85 % and 100 %, respectively. For comparison, Lambe et al. (2011) reported that the measured CO_2 and SO_2 transmission efficiencies for the TPOT were 0.97 ± 0.10 and 0.45 ± 0.13, respectively, and for the quartz PAM were 0.91 ± 0.09 and 1.20 ± 0.40, respectively.

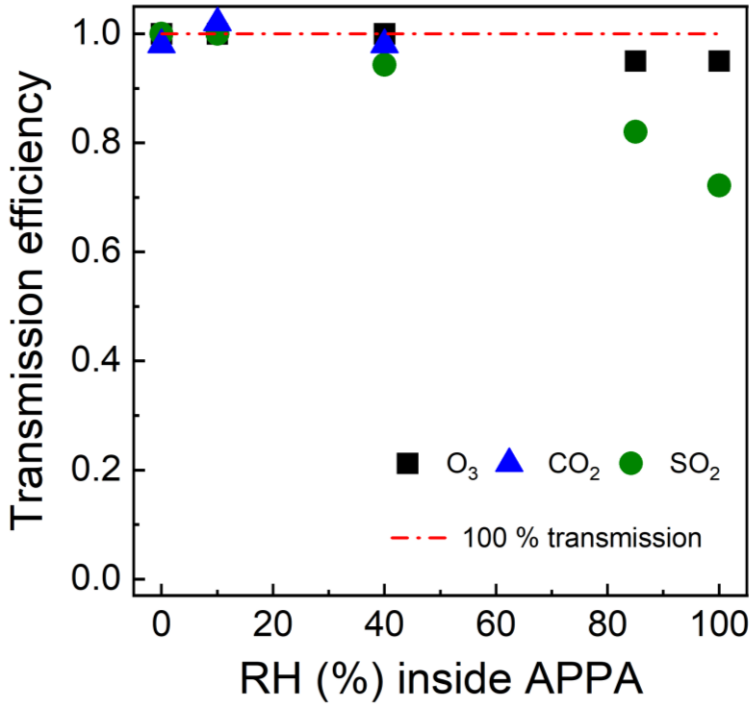

Figure 3.6: Gas transmission efficiencies of the APPA reactor as a function of relative humidity.

3.4.1.2. Gas and Particle Residence Time Distributions

Though the extent of processing of gases and particles inside an OFR is typically reported as a single value such as OH exposure or equivalent photochemical age, developed flow velocity profiles and mixing due to convection and/or flow cell geometry lead to a continuum of residence times and corresponding extent of processing. The spread in

exposure is typically reported as a residence time probability distribution function, as described in by (Mitroo et al., 2018). Such functions are often referred to simply as residence time distributions or RTDs.

The approach used to characterize the RTDs of particles and gases is the same as that described in Xu and Collins (2021). Briefly, an MFC was used to introduce 10 s pulses of either 0.20 mm AS particles or pure CO_2. The particle and CO_2 concentrations in the outlet-center flow were measured with the CPC and CO_2 analyzers identified in the previous section. Both the particle and gas RTD measurements were repeated three times. The resulting distribution functions for particles and gas are shown for the APPA and other reactors in Figure 3.7(a) and (b), respectively. The combination of a relatively small inner diameter, a uniform and constant reactor temperature maintained by the water jacket, and the subsampling of the center flow at the outlet results in gas and, especially, particle RTDs of the APPA that are narrow relative to the other reactors included in the figures and that lack the long tail expected even for ideal laminar flow.

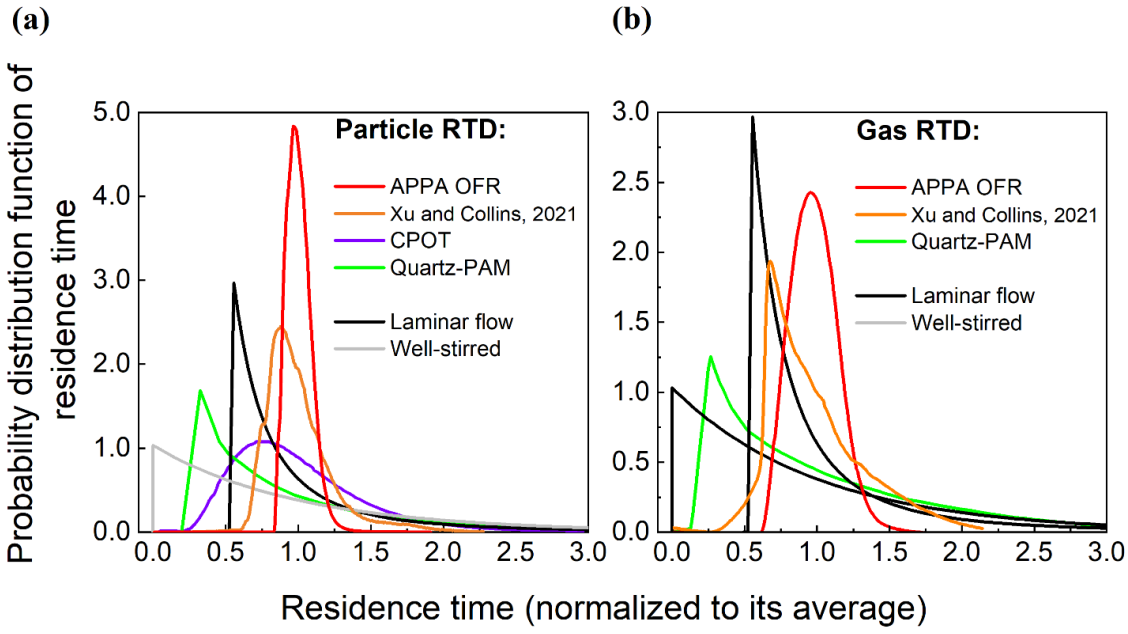

Figure 3.7: Residence time probability distribution function of (a) particles and (b) gases in the APPA and in other reactors as reported for the PAM by Lambe et al. (2011), CPOT by Huang et al. (2017), and PFA by Xu and Collins (2021) and downloaded from PAMWiki (2022).

3.4.1.3. Droplet Size Distribution and Temperature Control

Droplet size distributions measured at the outlet of the APPA by the APS are shown in Figure 3.8. As is true for most of the experiments reported here, the droplets formed inside the Spot Sampler on 0.1 µm diameter K_2SO_4 particles and were introduced into the top of the reactor in the 1.36 L min^{-1} inlet-aerosol flow. For these characterization experiments, the seed particle, and consequently droplet, concentration was varied from 20,000 to 70,000 cm^{-3}. The measured droplet size distributions shown in Fig. 8 are normalized by the integrated concentrations to emphasize changes, or lack thereof, in shape and peak location with varying concentration. The mean diameter of the droplets is stable at approximately 3.3 µm for the range in concentration examined here. As shown in Figure

3.19, the shape of the droplet size distribution was also stable over a period of several months, with the mean diameter varying by only ± 5 %. For the 20,000 cm^{-3} concentration used for most experiments, the resulting LWC is approximately 0.3 g m^{-3}. Compared with the droplet size distribution measured directly from the Spot Sampler, which is similar to that reported by (Lewis and Hering, 2013), the distribution measured at the outlet of the APPA has a tail at the left side, which is thought to be caused by partial evaporation of droplets near the walls in the interface between the Spot Sampler and inlet-aerosol port. The efficiency with which the droplets were transmitted through the reactor and the Nafion tube and bundle was found to be over 80 % from experiments in which the seed particle concentration upstream of the Spot Sampler was measured with a CPC (Aerosol Device Inc., Model MAGIC 210) and compared with that calculated from the size distribution measured by the SMPS located downstream of the APPA and Nafion dryers.

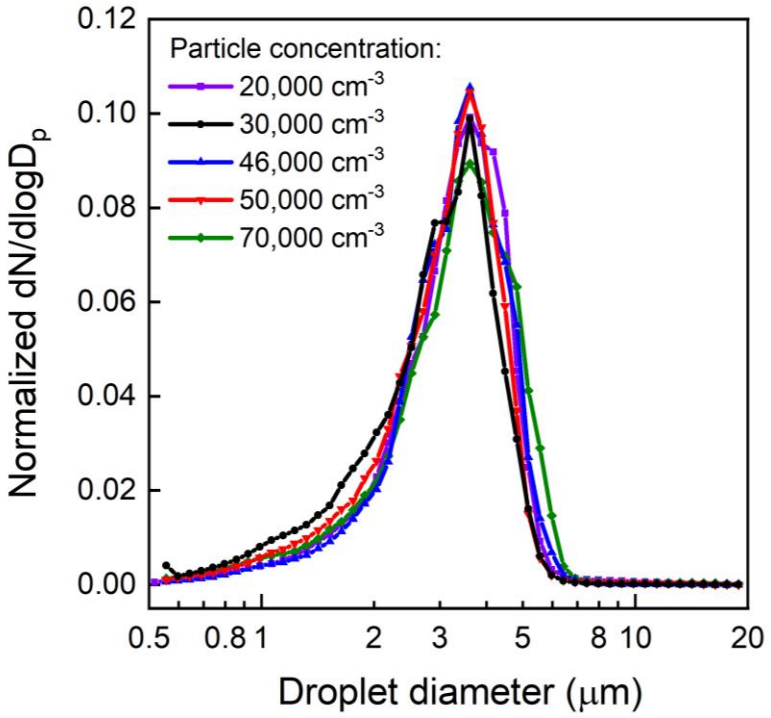

Figure 3.8: Droplet size distributions measured at the outlet of the APPA reactor for a range in concentration.

3.4.1.4. **Sulfate Formation in Cloud Droplets**

Though, like most OFRs, the APPA reactor is most often used to measure aerosol formation resulting from OH chemistry, conditions inside the reactor during cloud chemistry experiments were first evaluated through the well-studied oxidation of dissolved SO_2 by O_3, leading to formation of sulfuric acid and growth of the particles on which the droplets formed. The experimental conditions for these tests differed from those for standard operation only in that the UV lights were not turned on and the diameter of the K_2SO_4 seed particles was varied. The use of ~pH-neutral K_2SO_4 for these experiments

minimized the influence of the seed particles for the highly pH-dependent reaction. The SO_2 and O_3 mixing ratios at the top (inlet) of the reactor were fixed at 50 ppb and 1.5 ppm, respectively.

Figure 3.20 shows the initial and cloud-processed dry particle size distributions measured with the SMPS when 0.040 mm diameter seed particles were injected. Figure 3.9 summarizes the relationship between the mode diameters of the initial and cloud-processed particles for that experiment and for others that differed only in the size of the injected K_2SO_4 seed particles, with 0.030, 0.050, and 0.10 mm particles observed to grow to 0.0418, 0.0569, and 0.102 mm, respectively. Also shown in that figure are estimates of the particle growth from a 0-D model that includes reactions for this system as described by Caffrey et al. (2001) and that assumes a cloud droplet diameter of 3.3 mm. The measured and modeled dry diameters of the cloud-processed particles agree within 5 %.

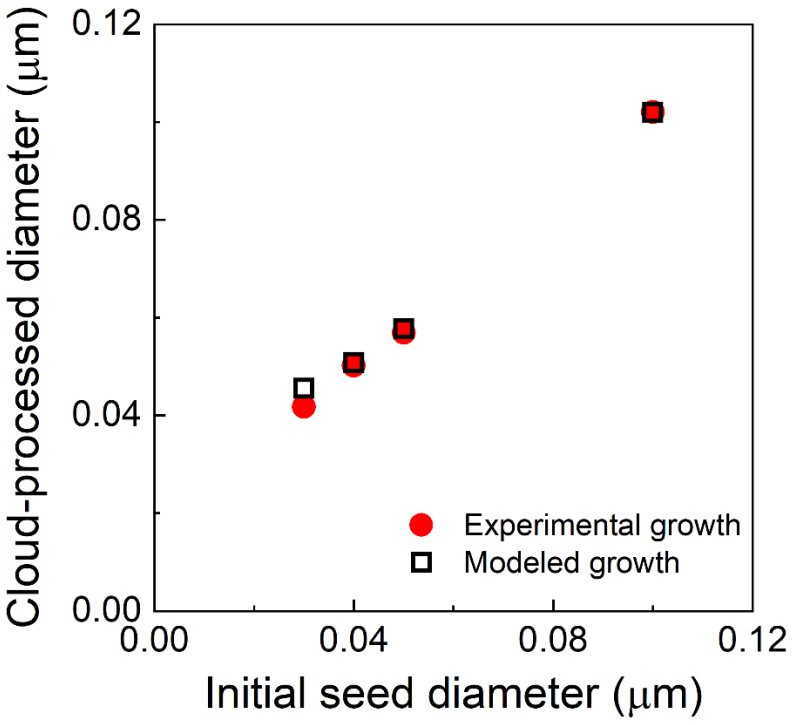

Figure 3.9: Measured diameters of cloud-processed and evaporated particles as a function of the diameter of the injected K_2SO_4 seed particles (red solid points), and the expected diameters calculated for the reactor conditions (3.3 mm droplet diameter, 50 ppb SO_2, and 1.5 ppm O_3) and the set of relevant aqueous-phase reactions (black hollow squares).

3.4.1.5. Light Intensity Spectrum and Profile

As described in Section 2.5, a 1000 W xenon lamp is used instead of the 254-nm mercury lamps for experiments such as those designed to assess the germicidal efficacy of solar radiation. Spectral irradiances shown in Figure 3.10 were measured i) inside the reactor and ii) outdoors with the fiber optic cosine receptor pointed at the sun around noon on a sunny day in April. The data are normalized to more clearly show the similarity in spectral shapes. Actinic fluxes were calculated from the measured irradiance spectra and

approximate actinic flux to irradiance ratios for nearly isotropic (reactor) and mostly direct (solar) radiation taken from Hofzumahaus et al. (1999). Actinic flux is the radiant quantity used to calculate photodissociation rates that are used to describe the photochemistry of the atmosphere and is also the most relevant quantity for many biological systems (Kylling et al., 2003). The ratio of the reactor and outdoor actinic fluxes is also included in Figure 10, with an average inside the reactor of 1.9 times that in direct sun for 300 nm ≤ l ≤ 400 nm.

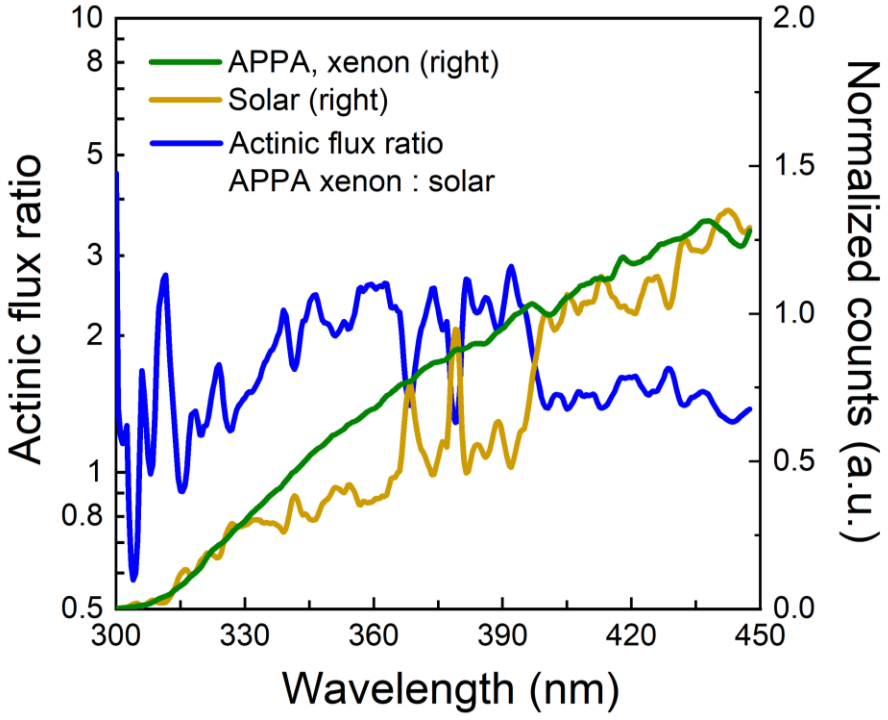

Figure 3.10: Spectral actinic fluxes inside the reactor when illuminated by the xenon lamp (green curve) and outdoors around noon on a sunny day in April (yellow curve), and the wavelength-dependent ratio of the two (blue curve). The approach used to calculate actinic flux from spectral irradiance measured with a spectrometer is described in the text.

The uniformity of the 254 nm UV from the germicidal mercury lamps was evaluated by attaching the receptor of the fiber optic-coupled spectrometer to a metal rod that was inserted through the outlet-center port and moved to five approximately evenly spaced positions between the top and bottom of the reactor. The UV photon counts and normalized intensity at 254 nm as a function of position are shown in Figure 3.11(a). The 254 nm intensity varies by approximately ± 10 % throughout the reactor.

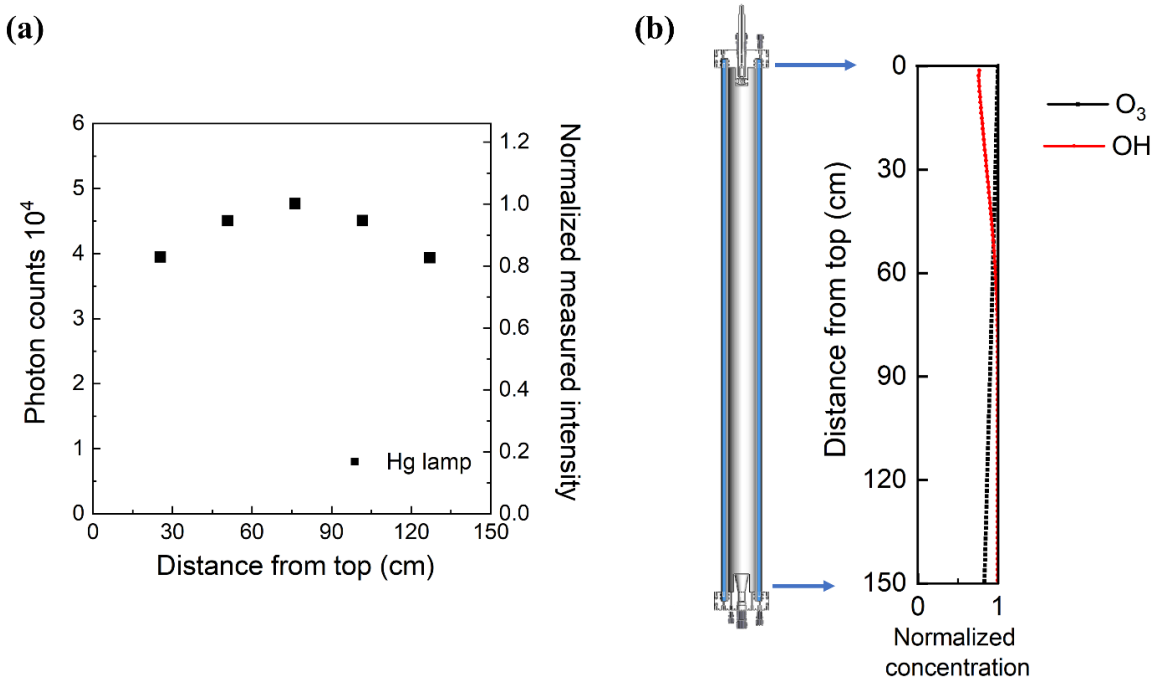

Figure 3.11: (a) Relative UV intensity profile and (b) normalized ratio of O_3 and OH concentration as a function of position in the reactor cell.

The rate of OH formation from O_3 photolysis at any position in the reactor is dependent upon the local 254 nm UV intensity and the local water vapor and O_3 concentrations. The water vapor concentration varies minimally inside the reactor while, as noted above, the UV lamp output is generally set at a level that results in loss of ~15 %

of the added O_3 between the inlet and outlet. Though the OH formation rate can be estimated from the UV and O_3 profiles, estimating the more relevant OH concentration profile requires consideration of reactions involving an array of radicals and other species. Here, the position-dependent concentrations of OH and other important species were simulated using the KinSim chemical-kinetics solver (Peng et al., 2016; Peng and Jimenez, 2019). Environmental parameters such as temperature and RH and a scaling array for the 254 nm UV intensity based on the data shown in Figure 3.11(a) were provided as inputs. The reactions used in the simulator included the default set of gas-phase reactions in the KinSim "OFR radical chemistry" module, relevant photolysis rate constants for 254 nm UV, and the aqueous-phase reactions listed in Table 3.1 for which effective reaction rate constants were calculated for an LWC of 0.3 g m^{-3} and assuming aqueous phase concentrations are described by Henry's Law. The peak 254 nm photon flux specified in the model for each RH was then iteratively determined such that the simulated loss of O_3 matched that measured. The photon fluxes determined in that way ranged from $\sim 4.6 \times 10^{14}$ photons cm^{-2} s^{-1} for 100 % RH measurements (2.3 V sent to the adjustable lamp ballast) to 1.1×10^{15} photons cm^{-2} s^{-1} for 40 % RH measurements (3.0 V sent to ballast). The UV intensity required to result in the same fractional loss of O_3 is higher at low RH because a larger percentage of the $O(^1D)$ produced from O_3 photolysis undergoes collisional deactivation to form $O(^3P)$, which subsequently reacts with O_2 to reform O_3. Figure 3.11(b) shows an example of the profiles of simulated concentrations of O_3 and OH through the length of the reactor, each normalized by its maximum concentration. The OH

concentration increases with time (and distance from the inlet) over roughly the top 1/3rd of the reactor and is nearly constant through the lower 2/3rd.

The oxidizing environment inside OFRs is often expressed as the OH exposure (OH_{exp}), which is normally defined as the product of the average OH concentration in cm^{-3} and the mean residence time of the sample flow in seconds. Here, OH_{exp} was calculated from the reactive loss of SO_2 and benzene gas as a function of UV intensity, RH, and added O_3 concentration. Those experimentally determined values were compared with estimates from the KinSim model with the photon fluxes specified above. Reactive loss of SO_2 was used to determine OH_{exp} at 40 % RH and that of benzene to determine OH_{exp} at 40 %, 85 %, and 100 % RH. Sulfur dioxide was not used for the high RH measurements because oxidation by O_3 and OH in the ALW or cloud droplets would cause a high OH_{exp} bias. Sulfur dioxide and benzene were used because their OH reaction rate constants of 1.3×10^{-12} and 1.23×10^{-12} cm^3 $molec^{-1}$ s^{-1}, result in significant, but not complete, reactive loss over the OH_{exp} range of interest. For both SO_2 and benzene, mixing ratios of between 150 ppb and 250 ppb were injected and the those of the air exiting the chamber were measured by the SO_2 analyzer and GC-FID, respectively. The reactive loss was determined from the ratio of the concentration measured with the UV lights on to that with them off. As with normal operation of the reactor, OH_{exp} was varied by changing the added O_3 concentration, with the UV lamp intensity at each RH fixed (and, again, selected to result in the loss of approximately 15 % of the O_3).

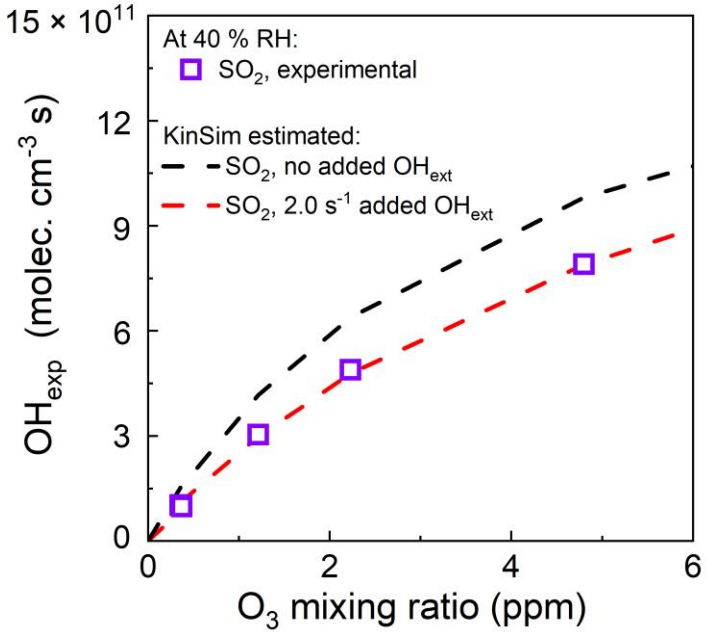

Figure 3.12: Variation of OH_{exp} estimated from SO_2 decay as a function of initial O_3 mixing ratio for 40 % RH.

The points in Figure 3.12 represent OH_{exp} calculated from measured SO_2 loss as a function of initial O_3 concentration for a series of experiments at 40 % RH. The two dashed curves in that figure are OH_{exp} estimated from KinSim for the experimental conditions. For the simulations resulting in the values along the upper (black) curve, the only source of "external" OH reactivity (OH_{ext}) (Peng et al., 2015) was the added SO_2. For the values shown with the lower (red) dashed curve, an additional reactant and reaction were included in KinSim that added 2.0 s^{-1} external OH reactivity without directly affecting any other species. Though it is unknown whether that change improves agreement because of the presence of one or more species that react with OH, because of loss of OH to the walls, and/or because of sources of error in the experiments and simulations, it is assumed to

improve simulation for all conditions and is included in KinSim for all other experiments reported here as well.

The OH_{exp} values calculated from measurement of the reactive loss of benzene for RH = 40 % RH (dry seed particles), 85 % RH (aqueous seed particles), and 100 % RH (cloud droplets) are presented as the markers in Figure 3.13(a), (b), and (c), respectively. Whereas the sulfuric acid resulting from the oxidation of SO_2 by one OH radical does not undergo any subsequent reaction with OH, oxidation of most organics results in a multi-generation cascade of products that are also reactive with OH. The distribution of products and their OH reaction rate constants are generally unknown. The upper curves in Figure 13 represent OH_{exp} from KinSim simulations in which OH reacts only with the added benzene, while the lower curves are from simulations in which OH also reacts with the first-generation oxidation products with a reaction rate constant of 10x that of OH reaction with benzene. Reaction of 1st and higher generation oxidation products is expected to increase with increasing OH concentration, resulting in the sort of downward shift in experimentally determined OH_{exp} towards and beyond the lower curve with increasing O_3 concentration (and OH production). Additional reaction of oxidation products in the aqueous phase may explain the slightly greater downward shift in data in Figure 3.13(c) for the 100 % RH experiments. Based on the comparisons of the experimental and simulation OH_{exp} for all of the SO_2 and benzene experiments, a reasonable estimate of uncertainty in the OH_{exp} estimated from KinSim is approximately ±20 %.

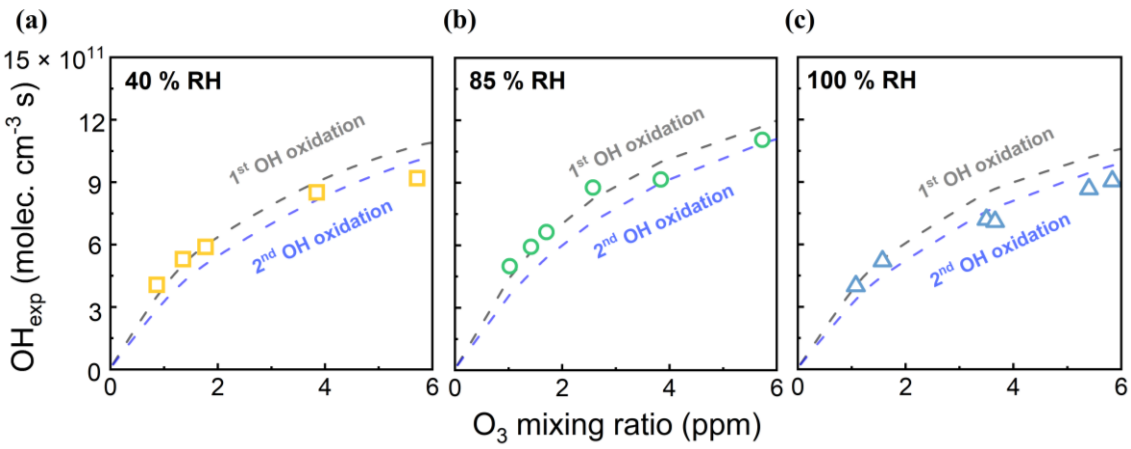

Figure 3.13: Variation of OH_{exp} as a function of initial O_3 mixing ratio for (a) low RH mode (40 %) (b) high RH mode (85 %) and (c) cloud mode (100 %).

3.4.2. Measurement of Secondary Aerosol Formation

3.4.2.1. Gas- and Aqueous-Phase SOA Formation From Oxidation of Benzene

Secondary organic aerosol formation from a single precursor was studied by injecting between 94 and 101 ppb of benzene and then measuring the growth of the added K_2SO_4 seed particles over a range in both OH_{exp} and RH. An example of a set of number size distributions of seed particles without and with added SOA are shown in Figure 3.14. The nucleation mode evident in the distributions measured when dry seed particles were present in the reactor (40 % RH) and when ALW was present (85 % RH) were often observed, but typically contributed negligibly to the total mass concentration. The SOA mass concentration was calculated from distributions such as those from the increase in aerosol volume concentration above that of the seed particles and an assumed SOA density of 1.3 g cm^{-3} (Schnitzler et al., 2014). SOA yields were then calculated as the ratio of the mass concentration of SOA to the mass concentration of reacted benzene, which was

measured with the GC-FID. Figure 3.15 summarizes the SOA yields as a function of RH and OH_{exp}. As shown in that figure, the SOA yield for each RH increased with OH_{exp} up to the maximum of 1.04 – 1.20 × 10^{12} molec. cm^{-3} s, which corresponds to a photochemical age of 8 – 9 days for an assumed average atmospheric [OH] of 1.5 × 10^{6} cm^{-3}. Also evident in the figure is the significant dependence of the yield on the presence and amount of liquid water. Maximum yields of 0.18, 0.43, and 0.59 were measured when dry seed particles, aqueous seed particles, and cloud droplets were present in the reactor, respectively. Future studies will evaluate SOA formation from other precursors and will add more comprehensive measurements of the chemical composition of the aerosol- and gas-phase species formed in the presence of varying amounts of liquid water.

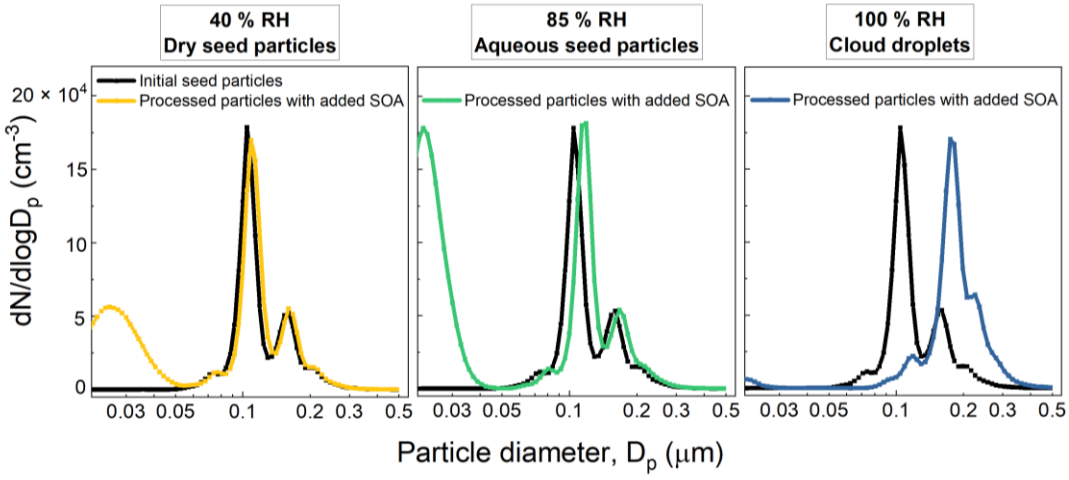

Figure 3.14: Example of a set of number size distributions of seed particles without and with added SOA formed from OH-oxidation of benzene for 40 % RH (left), 85 % RH (middle), and 100 % RH (right). The initial benzene mixing ratio was 90 ppb and the OH_{exp} estimated from KinSim is 3 × 10^{11} molec. cm^{-3} s.

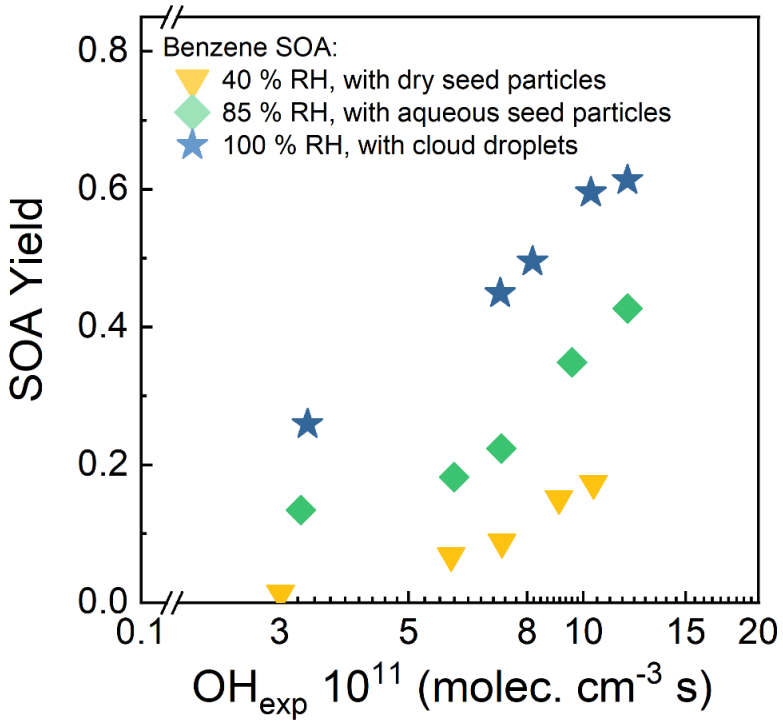

Figure 3.15: Benzene SOA yields as a function of OH_{exp} in low RH (40 %), high RH (85 %), and cloud (100 %) modes.

3.4.2.2. Aerosol Formed From Oxidation of Ambient Air

The potential contribution of aqueous-phase chemistry to secondary aerosol formation potential of ambient air is assessed by cycling through RH (and liquid water content) as quickly as possible to minimize the influence of changing ambient concentrations between measurements. Approximately 15 min is required for measurement at each RH/OH_{exp}, which includes time to reach steady-state and then time to measure two size distributions with the SMPS, with aerosol composition often simultaneously measured with the AMS. Measurement at several OH_{exp} as with the benzene experiments summarized in Figure 3.15 would take too long for most study locations. The example RH time series

shown in Figure 3.16 is a segment of a period of several weeks during which ambient air was processed through the APPA at the standard RH steps of 40 %, 85 %, and 100 % and with OH_{exp} steps corresponding to approximately 8 hours and 4 days photochemical age. That repeated matrix of 6 RH/OH_{exp} pairs required approximately 1.75 h, which includes a few minutes of flushing with dry air after the 100 % RH measurements to ensure no liquid water remains on the reactor walls.

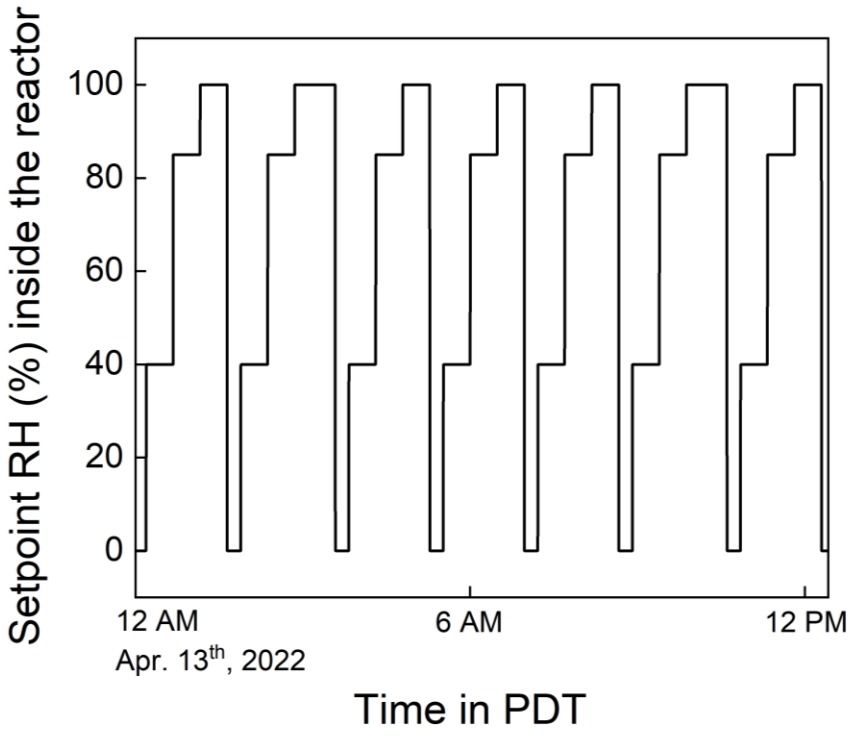

Figure 3.16: A typical RH cycle showing steps in the sequence of 40 %, 85 %, and 100 % RH. The short periods with very low RH follow the 100 % RH measurements and are designed to evaporate any residual liquid water from the walls before the start of the next 40 % RH measurement.

Figure 3.17 provides an example of the influence of aerosol liquid water and cloud water on the composition of the organic fraction of secondary aerosol that formed as

ambient air in Riverside, CA was exposed to a fixed OH_{exp} of approximately 5×10^{11} molec. cm^{-3} s (~3.8 days photochemical age). As shown in the figure, the O:C ratio calculated from the high resolution AMS data increased significantly with increased liquid water content, from an average of 0.34 when only dry seed particles were present, to an average of 0.64 with aqueous seed particles, and an average of 0.89 with cloud droplets. This sort of enhancement in O:C in aqSOA is among the possible explanations for the frequent observation that ambient aerosol has a higher O:C than that formed in environmental chambers (Reinhardt et al., 2007; Chhabra et al., 2011). Results from continuous processing of ambient air over periods of weeks will be presented in future publications.

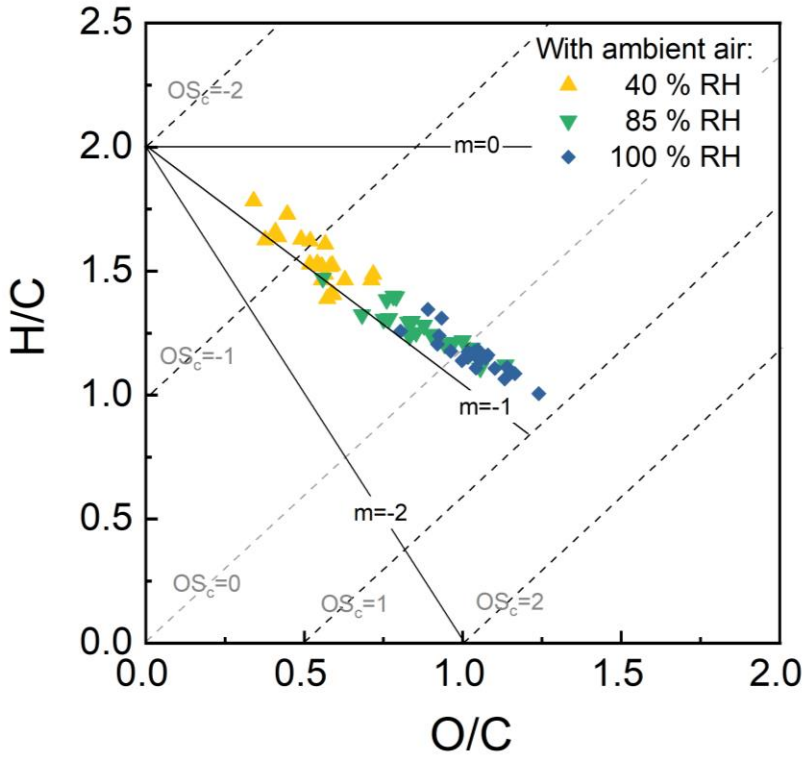

Figure 3.17: O/C and H/C ratios determined from AMS measurements of SOA formed as ambient air was processed in the reactor. The significant decrease in H/C ratio and increase in O/C ratio with the progression from no liquid water in the reactor (40 %) to ALW (85 %) to cloud droplets (100 %) suggests oxidation in the aqueous phase was important.

3.5. **Summary**

A new all-Teflon flow cell reactor was developed to study i) secondary aerosol formation from gas- and aqueous-phase chemistry and ii) changes in aerosols resulting from cloud processing or exposure to simulated solar or other light sources. To date, the Accelerated Production and Processing of Aerosols (APPA) reactor has primarily been used as an oxidation flow reactor, with photolysis of externally generated O_3 providing an OH exposure of between 8×10^{10} molec. cm^{-3} s and 1.2×10^{12} molec. cm^{-3} s over the ~150 s mean gas residence time. The geometry, inlet and outlet designs, and tight temperature control result in minimal mixing and a narrow residence time distribution. The most unique aspect of the reactor is the ability to vary the liquid water content present in aqueous aerosol or ~3.3 mm diameter cloud droplets that are formed on monodisperse seed particles and flow through the reactor together with the O_3, OH, and reactive precursor gases. A set of measurements for a prescribed gas mixture or ambient air can thus investigate the amount, properties, and composition of secondary aerosol formed across a matrix of conditions spanning both OH_{exp} and RH/LWC. The experimental system is fully automated and designed for continuous operation over extended periods of time. A series of experiments and numerical simulations summarized here explored the characteristics and capabilities of the reactor system. Example results reported here provide a preview into ongoing work investigating the roles of aerosol liquid water and cloud water in aerosol formation for i) a range of organic precursor gases and ii) ambient air over multi-week sampling periods.

3.6. **References**

Ahlberg, E., Falk, J., Eriksson, A., Holst, T., Brune, W. H., Kristensson, A., Roldin, P., and Svenningsson, B.: Secondary organic aerosol from VOC mixtures in an oxidation flow reactor, Atmospheric Environment, 161, 210-220, 2017.

Akimoto, H.: Global air quality and pollution, Science, 302, 1716-1719, 2003.

Andreae, M. and Rosenfeld, D.: Aerosol–cloud–precipitation interactions. Part 1. The nature and sources of cloud-active aerosols, Earth-Science Reviews, 89, 13-41, 2008.

Beder, E., Bass, C., and Shackleford, W.: Transmissivity and absorption of fused quartz between 0.22 μ and 3.5 μ from room temperature to 1500° C, Applied Optics, 10, 2263-2268, 1971.

Berndt, T., Böge, O., and Stratmann, F.: Atmospheric H 2 SO 4/H 2 O Particle Formation: Mechanistic Investigations, in: Nucleation and Atmospheric Aerosols, Springer, 69-72, 2007.

Bianchi, F., Kurtén, T., Riva, M., Mohr, C., Rissanen, M. P., Roldin, P., Berndt, T., Crounse, J. D., Wennberg, P. O., and Mentel, T. F.: Highly oxygenated organic molecules (HOM) from gas-phase autoxidation involving peroxy radicals: A key contributor to atmospheric aerosol, Chemical reviews, 119, 3472-3509, 2019.

Blando, J. D. and Turpin, B. J.: Secondary organic aerosol formation in cloud and fog droplets: a literature evaluation of plausibility, Atmospheric Environment, 34, 1623-1632, 2000.

Budisulistiorini, S. H., Nenes, A., Carlton, A. G., Surratt, J. D., McNeill, V. F., and Pye, H. O.: Simulating aqueous-phase isoprene-epoxydiol (IEPOX) secondary organic aerosol production during the 2013 Southern Oxidant and Aerosol Study (SOAS), Environmental science & technology, 51, 5026-5034, 2017.

Caffrey, P., Hoppel, W., Frick, G., Pasternack, L., Fitzgerald, J., Hegg, D., Gao, S., Leaitch, R., Shantz, N., and Albrechcinski, T.: In-cloud oxidation of SO2 by O3 and H2O2: Cloud chamber measurements and modeling of particle growth, Journal of Geophysical Research: Atmospheres, 106, 27587-27601, 2001.

Canagaratna, M., Jayne, J., Jimenez, J., Allan, J., Alfarra, M., Zhang, Q., Onasch, T., Drewnick, F., Coe, H., and Middlebrook, A.: Chemical and microphysical characterization of ambient aerosols with the aerodyne aerosol mass spectrometer, Mass spectrometry reviews, 26, 185-222, 2007.

Cao, J., Wang, Q., Li, L., Zhang, Y., Tian, J., Chen, L. A., Ho, S. S. H., Wang, X., Chow, J. C., and Watson, J. G.: Evaluation of the oxidation flow reactor for particulate matter emission limit certification, Atmospheric Environment, 224, 117086, 2020.

Carlton, A. G., Turpin, B. J., Lim, H. J., Altieri, K. E., and Seitzinger, S.: Link between isoprene and secondary organic aerosol (SOA): Pyruvic acid oxidation yields low volatility organic acids in clouds, Geophysical Research Letters, 33, 2006.

Carlton, A. G., Turpin, B. J., Altieri, K. E., Seitzinger, S., Reff, A., Lim, H.-J., and Ervens, B.: Atmospheric oxalic acid and SOA production from glyoxal: Results of aqueous photooxidation experiments, Atmospheric Environment, 41, 7588-7602, 2007.

Carlton, A. G., Turpin, B. J., Altieri, K. E., Seitzinger, S. P., Mathur, R., Roselle, S. J., and Weber, R. J.: CMAQ model performance enhanced when in-cloud secondary organic aerosol is included: comparisons of organic carbon predictions with measurements, Environmental science & technology, 42, 8798-8802, 2008.

Chhabra, P., Ng, N., Canagaratna, M., Corrigan, A., Russell, L., Worsnop, D., Flagan, R., and Seinfeld, J.: Elemental composition and oxidation of chamber organic aerosol, Atmospheric Chemistry and Physics, 11, 8827-8845, 2011.

De Haan, D. O., Corrigan, A. L., Tolbert, M. A., Jimenez, J. L., Wood, S. E., and Turley, J. J.: Secondary organic aerosol formation by self-reactions of methylglyoxal and glyoxal in evaporating droplets, Environmental science & technology, 43, 8184-8190, 2009.

DeCarlo, P. F., Kimmel, J. R., Trimborn, A., Northway, M. J., Jayne, J. T., Aiken, A. C., Gonin, M., Fuhrer, K., Horvath, T., and Docherty, K. S.: Field-deployable, high-resolution, time-of-flight aerosol mass spectrometer, Analytical chemistry, 78, 8281-8289, 2006.

Docherty, K. S., Stone, E. A., Ulbrich, I. M., DeCarlo, P. F., Snyder, D. C., Schauer, J. J., Peltier, R. E., Weber, R. J., Murphy, S. M., and Seinfeld, J. H.: Apportionment of primary and secondary organic aerosols in Southern California during the 2005 Study of Organic Aerosols in Riverside (SOAR-1), Environmental science & technology, 42, 7655-7662, 2008.

Ehn, M., Thornton, J. A., Kleist, E., Sipilä, M., Junninen, H., Pullinen, I., Springer, M., Rubach, F., Tillmann, R., and Lee, B.: A large source of low-volatility secondary organic aerosol, Nature, 506, 476-479, 2014.

Eiguren Fernandez, A., Lewis, G. S., and Hering, S. V.: Design and laboratory evaluation of a sequential spot sampler for time-resolved measurement of airborne particle composition, Aerosol Science and Technology, 48, 655-663, 2014.

Ervens, B. and Volkamer, R.: Glyoxal processing by aerosol multiphase chemistry: towards a kinetic modeling framework of secondary organic aerosol formation in aqueous particles, Atmospheric Chemistry and Physics, 10, 8219-8244, 2010.

Ervens, B., Turpin, B., and Weber, R.: Secondary organic aerosol formation in cloud droplets and aqueous particles (aqSOA): a review of laboratory, field and model studies, Atmospheric Chemistry and Physics, 11, 11069-11102, 2011.

Freney, E. J., Martin, S. T., and Buseck, P. R.: Deliquescence and efflorescence of potassium salts relevant to biomass-burning aerosol particles, Aerosol Science and Technology, 43, 799-807, 2009.

Froyd, K., Murphy, D., Sanford, T., Thomson, D., Wilson, J., Pfister, L., and Lait, L.: Aerosol composition of the tropical upper troposphere, Atmospheric Chemistry and Physics, 9, 4363-4385, 2009.

Galloway, M. M., Powelson, M. H., Sedehi, N., Wood, S. E., Millage, K. D., Kononenko, J. A., Rynaski, A. D., and De Haan, D. O.: Secondary organic aerosol formation during evaporation of droplets containing atmospheric aldehydes, amines, and ammonium sulfate, Environmental science & technology, 48, 14417-14425, 2014.

Ge, W., Liu, J., Yi, K., Xu, J., Zhang, Y., Hu, X., Ma, J., Wang, X., Wan, Y., and Hu, J.: Influence of atmospheric in-cloud aqueous-phase chemistry on global simulation of SO 2 in CESM2, Atmospheric Chemistry and Physics Discussions, 1-35, 2021.

George, I., Vlasenko, A., Slowik, J., Broekhuizen, K., and Abbatt, J.: Heterogeneous oxidation of saturated organic aerosols by hydroxyl radicals: uptake kinetics, condensed-phase products, and particle size change, Atmospheric Chemistry and Physics, 7, 4187-4201, 2007.

Gilardoni, S., Massoli, P., Paglione, M., Giulianelli, L., Carbone, C., Rinaldi, M., Decesari, S., Sandrini, S., Costabile, F., Gobbi, G. P., Pietrogrande, M. C., Visentin, M., Scotto, F., Fuzzi, S., and Facchini, M. C.: Direct observation of aqueous secondary organic aerosol from biomass-burning emissions, Proceedings of the National Academy of Sciences of the United States of America, 113, 10013-10018, 10.1073/pnas.1602212113, 2016.

Guo, J., Wang, Y., Shen, X., Wang, Z., Lee, T., Wang, X., Li, P., Sun, M., Collett Jr, J. L., and Wang, W.: Characterization of cloud water chemistry at Mount Tai, China: Seasonal variation, anthropogenic impact, and cloud processing, Atmospheric Environment, 60, 467-476, 2012.

Hallquist, M., Wenger, J. C., Baltensperger, U., Rudich, Y., Simpson, D., Claeys, M., Dommen, J., Donahue, N., George, C., and Goldstein, A.: The formation, properties and impact of secondary organic aerosol: current and emerging issues, Atmospheric chemistry and physics, 9, 5155-5236, 2009.

Hering, S. V. and Stolzenburg, M. R.: A method for particle size amplification by water condensation in a laminar, thermally diffusive flow, Aerosol Science and Technology, 39, 428-436, 2005.

Hering, S. V., Spielman, S. R., and Lewis, G. S.: Moderated, water-based, condensational particle growth in a laminar flow, Aerosol Science and Technology, 48, 401-408, 2014.

Hofzumahaus, A., Kraus, A., and Müller, M.: Solar actinic flux spectroradiometry: A technique for measuring photolysis frequencies in the atmosphere, Applied Optics, 38, 4443-4460, 1999.

Hoyle, C., Fuchs, C., Järvinen, E., Saathoff, H., Dias, A., Haddad, I. E., Gysel, M., Coburn, S., Tröstl, J., and Bernhammer, A.-K.: Aqueous phase oxidation of sulphur dioxide by ozone in cloud droplets, Atmospheric Chemistry and Physics, 16, 1693-1712, 2016.

Huang, Y., Coggon, M. M., Zhao, R., Lignell, H., Bauer, M. U., Flagan, R. C., and Seinfeld, J. H.: The Caltech Photooxidation Flow Tube reactor: design, fluid dynamics and characterization, Atmospheric Measurement Techniques, 10, 839-867, 2017.

Jimenez, J. L., Canagaratna, M., Donahue, N., Prevot, A., Zhang, Q., Kroll, J. H., DeCarlo, P. F., Allan, J. D., Coe, H., and Ng, N.: Evolution of organic aerosols in the atmosphere, Science, 326, 1525-1529, 2009.

Kanakidou, M., Seinfeld, J., Pandis, S., Barnes, I., Dentener, F. J., Facchini, M. C., Dingenen, R. V., Ervens, B., Nenes, A., and Nielsen, C.: Organic aerosol and global climate modelling: a review, Atmospheric Chemistry and Physics, 5, 1053-1123, 2005.

Kang, E., Root, M., Toohey, D., and Brune, W.: Introducing the concept of potential aerosol mass (PAM), Atmospheric Chemistry and Physics, 7, 5727-5744, 2007.

Kaur, R. and Anastasio, C.: First measurements of organic triplet excited states in atmospheric waters, Environmental science & technology, 52, 5218-5226, 2018.

Keller, A. and Burtscher, H.: A continuous photo-oxidation flow reactor for a defined measurement of the SOA formation potential of wood burning emissions, Journal of aerosol science, 49, 9-20, 2012.

Knopf, D. A., Alpert, P. A., and Wang, B.: The role of organic aerosol in atmospheric ice nucleation: a review, ACS Earth and Space Chemistry, 2, 168-202, 2018.

Kylling, A., Webb, A., Bais, A., Blumthaler, M., Schmitt, R., Thiel, S., Kazantzidis, A., Kift, R., Misslbeck, M., and Schallhart, B.: Actinic flux determination from measurements of irradiance, Journal of Geophysical Research: Atmospheres, 108, 2003.

Lambe, A., Ahern, A., Williams, L., Slowik, J., Wong, J., Abbatt, J., Brune, W., Ng, N., Wright, J., and Croasdale, D.: Characterization of aerosol photooxidation flow reactors: heterogeneous oxidation, secondary organic aerosol formation and cloud condensation nuclei activity measurements, Atmospheric Measurement Techniques, 4, 445-461, 2011.

Lamkaddam, H., Dommen, J., Ranjithkumar, A., Gordon, H., Wehrle, G., Krechmer, J., Majluf, F., Salionov, D., Schmale, J., and Bjelić, S.: Large contribution to secondary organic aerosol from isoprene cloud chemistry, Science Advances, 7, eabe2952, 2021.

Lewis, G. S. and Hering, S. V.: Minimizing concentration effects in water-based, laminar-flow condensation particle counters, Aerosol Science and Technology, 47, 645-654, 2013.

Li, K., Liggio, J., Lee, P., Han, C., Liu, Q., and Li, S.-M.: Secondary organic aerosol formation from α-pinene, alkanes, and oil-sands-related precursors in a new oxidation flow reactor, Atmospheric Chemistry and Physics, 19, 9715-9731, 2019.

Li, R., Palm, B. B., Ortega, A. M., Hlywiak, J., Hu, W., Peng, Z., Day, D. A., Knote, C., Brune, W. H., and De Gouw, J. A.: Modeling the radical chemistry in an oxidation flow reactor: Radical formation and recycling, sensitivities, and the OH exposure estimation equation, The Journal of Physical Chemistry A, 119, 4418-4432, 2015.

Lim, H.-J., Carlton, A. G., and Turpin, B. J.: Isoprene forms secondary organic aerosol through cloud processing: Model simulations, Environmental science & technology, 39, 4441-4446, 2005.

Lim, Y., Tan, Y., and Turpin, B.: Chemical insights, explicit chemistry, and yields of secondary organic aerosol from OH radical oxidation of methylglyoxal and glyoxal in the aqueous phase, Atmospheric Chemistry and Physics, 13, 8651-8667, 2013.

Lim, Y., Tan, Y., Perri, M., Seitzinger, S., and Turpin, B.: Aqueous chemistry and its role in secondary organic aerosol (SOA) formation, Atmospheric Chemistry and Physics, 10, 10521-10539, 2010.

Lin, G., Sillman, S., Penner, J., and Ito, A.: Global modeling of SOA: the use of different mechanisms for aqueous-phase formation, Atmospheric Chemistry and Physics, 14, 5451-5475, 2014.

Litjens, R. A., Quickenden, T. I., and Freeman, C. G.: Visible and near-ultraviolet absorption spectrum of liquid water, Applied optics, 38, 1216-1223, 1999.

Liu, T., Clegg, S. L., and Abbatt, J. P.: Fast oxidation of sulfur dioxide by hydrogen peroxide in deliquesced aerosol particles, Proceedings of the National Academy of Sciences, 117, 1354-1359, 2020.

Liu, Y., Monod, A., Tritscher, T., Praplan, A., DeCarlo, P., Temime-Roussel, B., Quivet, E., Marchand, N., Dommen, J., and Baltensperger, U.: Aqueous phase processing of secondary organic aerosol from isoprene photooxidation, Atmospheric Chemistry and Physics, 12, 5879-5895, 2012a.

Liu, Y., Siekmann, F., Renard, P., El Zein, A., Salque, G., El Haddad, I., Temime-Roussel, B., Voisin, D., Thissen, R., and Monod, A.: Oligomer and SOA formation through aqueous phase photooxidation of methacrolein and methyl vinyl ketone, Atmospheric Environment, 49, 123-129, 2012b.

Ma, P., Quan, J., Jia, X., Liao, Z., Wang, Q., Cheng, Z., Dou, Y., Su, J., and Pan, Y.: Effects of ozone and relative humidity in secondary inorganic aerosol formation during haze events in Beijing, China, Atmospheric Research, 264, 105855, 2021.

McNeill, V. F.: Aqueous organic chemistry in the atmosphere: Sources and chemical processing of organic aerosols, 2015.

McNeill, V. F., Woo, J. L., Kim, D. D., Schwier, A. N., Wannell, N. J., Sumner, A. J., and Barakat, J. M.: Aqueous-phase secondary organic aerosol and organosulfate formation in atmospheric aerosols: a modeling study, Environmental science & technology, 46, 8075-8081, 2012.

Mitroo, D., Sun, Y., Combest, D. P., Kumar, P., and Williams, B. J.: Assessing the degree of plug flow in oxidation flow reactors (OFRs): a study on a potential aerosol mass (PAM) reactor, Atmospheric Measurement Techniques, 11, 1741-1756, 2018.

Myhre, G., Myhre, C., Samset, B., and Storelvmo, T.: Aerosols and their relation to global climate and climate sensitivity, Nature Education Knowledge, 4, 7, 2013.

Ortega, A., Day, D., Cubison, M., Brune, W. H., Bon, D., De Gouw, J., and Jimenez, J.: Secondary organic aerosol formation and primary organic aerosol oxidation from biomass-burning smoke in a flow reactor during FLAME-3, Atmospheric Chemistry and Physics, 13, 11551-11571, 2013.

Peng, J., Hu, M., Guo, S., Du, Z., Shang, D., Zheng, J., Zheng, J., Zeng, L., Shao, M., and Wu, Y.: Ageing and hygroscopicity variation of black carbon particles in Beijing measured by a quasi-atmospheric aerosol evolution study (QUALITY) chamber, Atmospheric Chemistry and Physics, 17, 10333-10348, 2017.

Peng, Z. and Jimenez, J. L.: KinSim: A Research-Grade, User-Friendly, Visual Kinetics Simulator for Chemical-Kinetics and Environmental-Chemistry Teaching, 2019.

Peng, Z., Day, D., Stark, H., Li, R., Lee-Taylor, J., Palm, B., Brune, W., and Jimenez, J.: HO x radical chemistry in oxidation flow reactors with low-pressure mercury lamps

systematically examined by modeling, Atmospheric Measurement Techniques, 8, 4863-4890, 2015.

Peng, Z., Day, D. A., Ortega, A. M., Palm, B. B., Hu, W., Stark, H., Li, R., Tsigaridis, K., Brune, W. H., and Jimenez, J. L.: Non-OH chemistry in oxidation flow reactors for the study of atmospheric chemistry systematically examined by modeling, Atmospheric Chemistry and Physics, 16, 4283-4305, 2016.

Perri, M. J., Seitzinger, S., and Turpin, B. J.: Secondary organic aerosol production from aqueous photooxidation of glycolaldehyde: Laboratory experiments, Atmospheric Environment, 43, 1487-1497, 2009.

Reinhardt, A., Emmenegger, C., Gerrits, B., Panse, C., Dommen, J., Baltensperger, U., Zenobi, R., and Kalberer, M.: Ultrahigh mass resolution and accurate mass measurements as a tool to characterize oligomers in secondary organic aerosols, Analytical Chemistry, 79, 4074-4082, 2007.

Salcedo, D., Onasch, T. B., Dzepina, K., Canagaratna, M., Zhang, Q., Huffman, J., DeCarlo, P., Jayne, J., Mortimer, P., and Worsnop, D. R.: Characterization of ambient aerosols in Mexico City during the MCMA-2003 campaign with Aerosol Mass Spectrometry: results from the CENICA Supersite, Atmospheric Chemistry and Physics, 6, 925-946, 2006.

Schnitzler, E. G., Dutt, A., Charbonneau, A. M., Olfert, J. S., and Jäger, W.: Soot aggregate restructuring due to coatings of secondary organic aerosol derived from aromatic precursors, Environmental science & technology, 48, 14309-14316, 2014.

Schroder, J., Campuzano-Jost, P., Day, D., Shah, V., Larson, K., Sommers, J., Sullivan, A., Campos, T., Reeves, J., and Hills, A.: Sources and secondary production of organic aerosols in the northeastern United States during WINTER, Journal of Geophysical Research: Atmospheres, 123, 7771-7796, 2018.

Seinfeld, J. H. and Pandis, S. N.: Atmospheric chemistry and physics: from air pollution to climate change, John Wiley & Sons2016.

Shiraiwa, M., Li, Y., Tsimpidi, A. P., Karydis, V. A., Berkemeier, T., Pandis, S. N., Lelieveld, J., Koop, T., and Pöschl, U.: Global distribution of particle phase state in atmospheric secondary organic aerosols, Nature communications, 8, 1-7, 2017.

Shrivastava, M., Cappa, C. D., Fan, J., Goldstein, A. H., Guenther, A. B., Jimenez, J. L., Kuang, C., Laskin, A., Martin, S. T., and Ng, N. L.: Recent advances in understanding secondary organic aerosol: Implications for global climate forcing, Reviews of Geophysics, 55, 509-559, 2017.

Simonen, P., Saukko, E., Karjalainen, P., Timonen, H., Bloss, M., Aakko-Saksa, P., Rönkkö, T., Keskinen, J., and Maso, M. D.: A new oxidation flow reactor for measuring secondary aerosol formation of rapidly changing emission sources, Atmospheric Measurement Techniques, 10, 1519-1537, 2017.

Smith, J. D., Kinney, H., and Anastasio, C.: Aqueous benzene-diols react with an organic triplet excited state and hydroxyl radical to form secondary organic aerosol, Physical Chemistry Chemical Physics, 17, 10227-10237, 2015.

Smith, J. D., Sio, V., Yu, L., Zhang, Q., and Anastasio, C.: Secondary organic aerosol production from aqueous reactions of atmospheric phenols with an organic triplet excited state, Environmental science & technology, 48, 1049-1057, 2014.

Spracklen, D., Jimenez, J., Carslaw, K., Worsnop, D., Evans, M., Mann, G., Zhang, Q., Canagaratna, M., Allan, J., and Coe, H.: Aerosol mass spectrometer constraint on the global secondary organic aerosol budget, Atmospheric Chemistry and Physics, 11, 12109-12136, 2011.

Stolzenburg, M., Kreisberg, N., and Hering, S.: Atmospheric size distributions measured by differential mobility optical particle size spectrometry, Aerosol Science and Technology, 29, 402-418, 1998.

Tsui, W. G., Rao, Y., Dai, H.-L., and McNeill, V. F.: Modeling photosensitized secondary organic aerosol formation in laboratory and ambient aerosols, Environmental science & technology, 51, 7496-7501, 2017.

Volkamer, R., Ziemann, P., and Molina, M.: Secondary Organic Aerosol Formation from Acetylene (C 2 H 2): seed effect on SOA yields due to organic photochemistry in the aerosol aqueous phase, Atmospheric Chemistry and Physics, 9, 1907-1928, 2009.

Wang, J., Doussin, J.-F., Perrier, S., Perraudin, E., Katrib, Y., Pangui, E., and Picquet-Varrault, B.: Design of a new multi-phase experimental simulation chamber for atmospheric photosmog, aerosol and cloud chemistry research, Atmospheric Measurement Techniques, 4, 2465-2494, 2011.

Wang, S., Wang, L., Wang, N., Ma, S., Su, F., and Zhang, R.: Formation of droplet-mode secondary inorganic aerosol dominated the increased PM2. 5 during both local and transport haze episodes in Zhengzhou, China, Chemosphere, 269, 128744, 2021.

Xu, N. and Collins, D. R.: Design and characterization of a new oxidation flow reactor for laboratory and long-term ambient studies, Atmospheric Measurement Techniques, 14, 2891-2906, 2021.

Ye, Z., Zhuang, Y., Chen, Y., Zhao, Z., Ma, S., Huang, H., Chen, Y., and Ge, X.: Aqueous-phase oxidation of three phenolic compounds by hydroxyl radical: Insight into secondary

organic aerosol formation yields, mechanisms, products and optical properties, Atmospheric Environment, 223, 117240, 2020.

3.7. **Supplementary Materials**

Supplement S1- Control and stability of flows, RH, temperature, and droplet size distributions

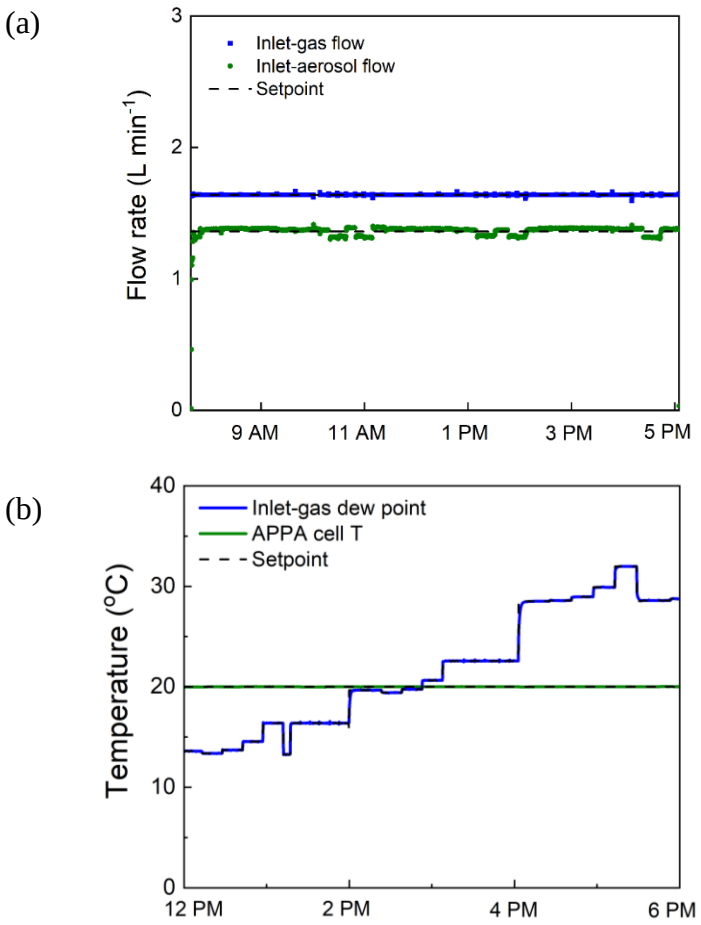

Figure 3.18: Example of control over several hours of (a) the inlet-gas and inlet-aerosol flow rates and (b) the temperature of the reactor and dew point of the inlet-gas flow. The steps in the inlet gas dew point reflect changes in the humidified air flow rate, which themselves result from changes in the flow rate from the O_3 generator. The inlet-aerosol flow dew point is assumed to always be 14.5 °C, which was determined experimentally using the approach described in the text.

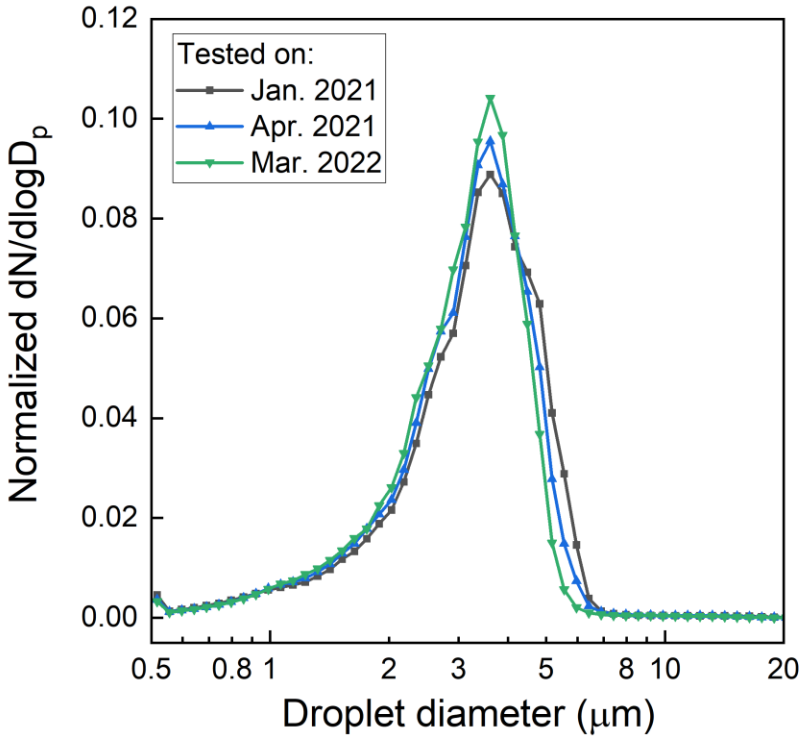

Figure 3.19: Consistency of the droplet size distribution measured at the outlet of the APPA over more than one year.

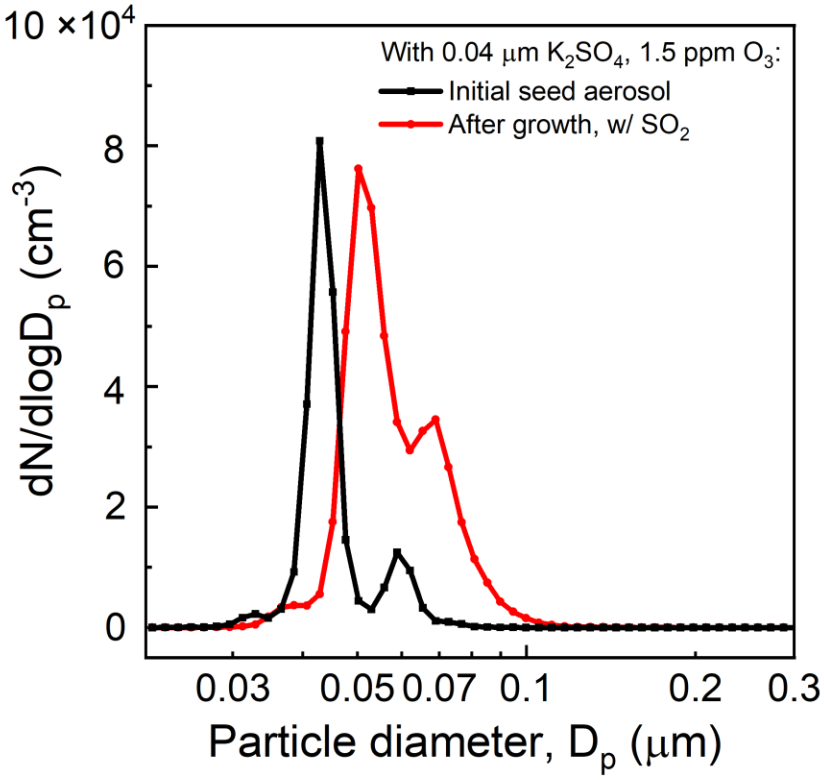

Figure 3.20: Dry particle number size distributions of the initial K_2SO_4 seed particles (black) and of the cloud-processed particles exiting the reactor (red) that had grown as dissolved SO_2 was oxidized by O_3 to form aerosol-phase sulfuric acid.

Figure 3.20 shows an example of the dry size distributions measured at the outlet of the APPA by the SMPS for an experiment in which the cloud droplets formed on injected 0.04 mm seed particles. Ozone was injected during both measurements, while SO_2 was for only the experiment resulting in the red distribution in the figure. The small mode to the right of the main peak corresponds to particles having two elementary charges when separated by the DMA shown in Figure 3.2 in the main text, and that subsequently lost one of those charges in the neutralizer downstream of it. The separation between the singly-

charged and doubly-charged particle modes decreases accompanying the formation of sulfuric acid in part because the mass added to both modes is the same, which causes a greater relative change in size for the smaller singly-charged particles than the larger doubly-charged ones. The dry particle mode diameter increased from 0.040 mm to 0.051 mm.

Table 3.1: Aqueous-phase reactions added to the KinSim "OFR radical chemistry" module. The rate constants are effective values used to express the rates as if the reactions occur in the gas-phase per cm^3 of air in the reactor. They were calculated for an LWC of 0.3 g m^{-3} and with the assumption that aqueous phase concentrations are described by Henry's Law.

No.	Reaction	Effective rate constant (cm^3 $molec^{-1}$ s^{-1})
R1	$OH + HO_2 \rightarrow H_2O + O_2$	8.37×10^{-11}
R2	$OH + O_3 \rightarrow HO_2 + O_2$	5.29×10^{-17}
R3	$HO_2 + HO_2 \rightarrow H_2O_2 + O_2$	5.22×10^{-11}
R4	$OH + H_2O_2 \rightarrow HO_2 + H_2O$	7.87×10^{-12}
R5	$HO_2 + O_3 \rightarrow 2O_2 + OH$	7.65×10^{-15}
R6	$OH + CO_2 \rightarrow HCO_3$	1.3×10^{-18}

4. Insights Into Secondary Organic Aerosol Formed via Aqueous-Phase Reactions of Water Insoluble VOCs

4.1. Abstract

Aerosol liquid water and cloud droplets play essential roles in aerosol formation and remain a major obstacle in estimating the aerosol production through aqueous-phase reactions. Fundamental questions remain about the contribution of aerosols that formed through aqueous-phase oxidation to total aerosol burden because laboratory studies fail to quantify aerosols formed from the water insoluble precursors through aqueous-phase oxidation. Laboratory measurements of aerosol formation are made using the APPA flow reactor. Water insoluble VOCs from source categories of vehicle exhaust, biogenic, biomass burning, and volatile chemical products (VCPs) and investigate their secondary aerosol formation through gas- and aqueous-phase oxidation under equivalent photochemical age of approximately one day to two weeks. Highly oxidized secondary products with higher molecular weight are generated from aqueous-phase oxidation of VOCs relative to that from gas-phase only oxidation. Compared with the secondary products formed through gas-phase oxidation, we show that aerosol liquid water and clouds effectively boost the amount of secondary aerosol. Especially for those generated from the oxidation reactions of VOCs from vehicle exhaust with an average factor of 3 and 5 increase with the presence of aerosol water and cloud droplet, respectively. On a global scale, the SOA production from biogenic and anthropogenic precursor sources is

considerable but the importance aerosol through aqueous-phase remains uncertain, so that we conclude that secondary aerosol formation from the total biogenic and anthropogenic sources is probably underestimated in most areas.

4.2. **Introduction**

Atmospheric aerosol particles are linked to the cloud formation and direct radiative forcing and have adverse impacts on human health (Jimenez et al., 2009; Zhang et al., 2011; Shiraiwa et al., 2013). Organic aerosol (OA) is a dominant contributor to the fine particulate matter, especially in polluted areas (Volkamer et al., 2006; Ortega et al., 2016). Secondary organic aerosol (SOA), which consists of a prominent fraction of OA in the atmosphere, produced through the atmospheric gas-phase oxidation reactions of volatile organic compounds (VOCs) that mainly originate from anthropogenic and biogenic sources (gasSOA) (Mølhave, 1991; Mohamed et al., 2002; Chen et al., 2021). For decades, the formation of SOA in cloud and aerosol water (aqSOA) in the atmosphere has received increased attention. Substantial mass of organic aerosol formed in cloud and aerosol water has been observed from field observations and laboratory studies (Bateman et al., 2011; Ervens et al., 2014; Wang et al., 2021a; Yli-Juuti et al., 2021). Most of studies have investigated that the SOA formation from bulk photochemical aqueous-phase experiments by dissolving the VOCs in dilute aqueous solutions. Aqueous phase photooxidation experiments of carbonyl products (glyoxal, methylglyoxal) (Carlton et al., 2007; Lim et al., 2010; Tan et al., 2010; Kua et al., 2011), biogenic compounds (α-pinene, isoprene) (Nozière et al., 2010; Huang et al., 2011; Liu et al., 2012) and aromatic compounds (phenol and its methoxylated derivates guaiacol) (Sun et al., 2010; Yu et al., 2016; Ye et al., 2020) has been discussed in recent detailed studies and used to develop reaction mechanisms for the possible formation. However, the pathways and mechanisms of SOA formation via aqueous-phase processing by aqueous aerosols and clouds have been inappreciably

investigated compared with that under gas-phase chemistry (Odum et al., 1996; Claeys et al., 2004; Carter et al., 2005; Kroll and Seinfeld, 2008; Donahue et al., 2012; Aljawhary et al., 2016).

The production and properties of aqSOA that implemented into the theoretical model are made based on the current set of data from bulk aqueous phase experiments (Ervens, 2015). While the observed bulk processes have a major restriction due to the selection of VOCs or oxidized intermediates need to be mainly water-soluble. However, almost half of the biogenic volatile organic compounds and most of the aromatic compounds are water insoluble (Heglund and Tilotta, 1996; Song et al., 2007; Favez et al., 2008). Hence, understanding and quantifying the aqSOA formation by aqueous processes in cloud and aerosol water from those water insoluble VOCs and the complex mixture of its oxidation products from the gas-phase chemistry are necessary for assessing the impact of photochemical oxidation of those gas-phase precursors in cloud water on the global SOA burden. Few studies related to in-cloud aqSOA formation from precursor compounds and their soluble oxidation products from gas-phase photochemistry are performed in laboratory experiments (Lamkaddam et al., 2021) and partly caused by the major experimental limitations that can simulate aqueous chemistry at diluted conditions characteristic of atmospheric clouds (Carlton et al., 2009; Ervens et al., 2015; Herrmann et al., 2015; Shrivastava et al., 2017; Ervens et al., 2018; Tomaz et al., 2018).

The simulated model bias exists when the global SOA budget was dominated by certain types of precursors (McNeill et al., 2012; Wang et al., 2021b; Xu et al., 2022a).

Quantifying the secondary aerosols produced through aqueous-phase oxidation reactions derived from a wide type of VOCs is critical to intensively understand global SOA budget. To date, global models consider a number of different precursor types in estimating the formation of SOA and suggest that biogenic sources contribute 74 % to 95 % to the annual global total SOA production rate (Farina et al., 2010; Tsigaridis et al., 2014). However, simulated model bias was minimized when the global SOA budget was dominated by anthropogenic precursors, with an anthropogenic SOA production rate of $\sim$ 100 Tg (SOA) a^{-1} and a biogenic SOA production rate of 13 Tg (SOA) a^{-1} (Spracklen et al., 2011b; Rap et al., 2018). Hence, whether the biogenic dominance of global SOA production remain highly uncertain, partially because of the anthropogenic precursor magnitude and distributions (Myriokefalitakis et al., 2008; Stavrakou et al., 2009). The discrepancies may also indicate that the reaction yield derived from laboratory studies underestimated the contribution of aerosol formed through aqueous-phase oxidation (Murphy and Pandis, 2010; Gentner et al., 2017; Shrivastava et al., 2017). Biomass burning VOCs can contribute to SOA formation (Cubison et al., 2011). The global SOA production rate from biomass burning was estimated approximately 1-26 Tg(SOA)a^{-1} from and field observations (Hodzic et al., 2016; Spracklen et al., 2011a) which is significantly lower than that predicted from global models 44–95 Tg(SOA)a^{-1} (Shrivastava et al., 2015). Hence, implementing biomass burning S/IVOCs into global models remains highly uncertain caused by the limited knowledge of biomass burning carbonaceous emissions chemistry. Also, emissions of volatile chemical products (VCPs) that mostly generated from consumer and industrial products, now contribute as much as 50 % to total petrochemical VOCs in

major urban areas (Coggon et al., 2021). Recent studies have shown that VCPs are as important to ozone and fine particulate matter production as fossil fuel VOCs and the emissions and atmospheric chemistry to VCPs can have significant impacts on air quality and near field modeling model simulations of key atmospheric processes (Fantke et al., 2016; Mcdonald et al., 2018; Gkatzelis et al., 2021; Qin et al., 2021). However, the VCP SOA formation through aqueous-phase photooxidation and its contribution on total SOA mass remain uncertain.

To simulate the secondary aerosol formation with the presence of aerosol liquid water and cloud droplets, we selected water insoluble volatile organic compounds (VOC) from source categories of vehicle exhaust, biogenic, biomass burning and VCPs and show experimental results of SOA formation through gas- and aqueous-phase oxidation using a newly developed multiphase oxidation flow reactor (OFR). Experiments were performed by oxidizing these VOCs along with ozone, OH radicals, and water vapor. The temperature and RH of the gas mixture flow and the temperatures of the droplet-containing flow and the reactor are controlled inside the reactor, in which experiments were performed at 40-100 % relative humidity (RH). We simulate ta wide range of atmospheric conditions in which aerosol liquid water or clouds are present, for assessing the secondary aerosol yields and chemical properties of the formed particles from each precursor and its oxidized products through the aqueous oxidation.

4.3. **Experimental Methods**

4.3.1. **Chemical and Reagents**

The chemical and reagents used in this study and their purities and suppliers are listed below: 1,8-cineole (≥98.0% (GC), Sigma Aldrich), 3-carene (≥90.0%, Sigma Aldrich), *α*-pinene (98 %, Sigma Aldrich), *β*-pinene (≥98.0% (GC), Sigma Aldrich), camphene (analytical standard, Sigma Aldrich), isoprene (analytical standard, Sigma Aldrich), *m*-xylene (analytical standard, Sigma Aldrich), *p*-xylene (analytical standard, Sigma Aldrich), benzene (analytical standard, Sigma Aldrich), cyclohexane (ACS reagent, ≥99%, Sigma Aldrich), ethylbenzene (analytical standard, Sigma Aldrich), octane (analytical standard, Sigma Aldrich), toluene (HPLC-Grade Sigma Aldrich), d_5-siloxane(certified reference material, Sigma Aldrich), tetrahydrofuran(analytical standard, Sigma Aldrich), 2-methylfuran(analytical standard, Sigma Aldrich), furan(analytical standard, Sigma Aldrich) , potassium sulfate (≥ 99.0 %, Sigma Aldrich), ammonium sulfate (≥ 99.0 %, Sigma Aldrich). All chemicals were used without further purification.

4.3.2. **APPA Operation**

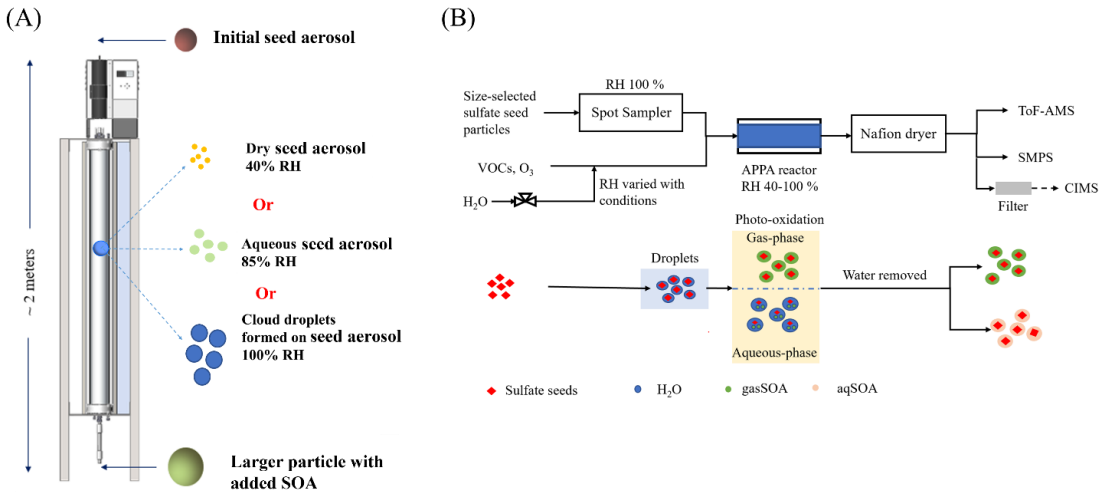

Figure 4.1: (A) Schematic of APPA reactor. (B) Experimental setup. Seed particles were maintained in a liquid droplet through the Spot Sampler. The VOC, ozone and water vapor was mixed prior to the reactor. Total flow through the reactor was 3 L min^{-1} and only the center flow (50 % of the total flow) was extracted to analysis instruments. RH inside the reactor was kept at 40 -100 % by varying the RH of the humid flow.

All the experiments were performed in the APPA reactor, which is shown in Figure 4.1(A). Details of the APPA reactor and its operation are described in the Xu et al., (2022). Unlike the other OFRs reported in the literatures for only simulating the gas-phase aerosol formation, it is a multiphase system that also used to simulate aqueous-phase chemistry in ALW and in cloud droplets. The experimental setup is shown in Figure 4.1(B). For both gas and aqueous-phase oxidation experiments, ozone is generated externally and introduced into the reactor where it is photolyzed by 254-nm emitting germicidal UV lamps, resulting $O(^1D)$ reacts with water vapor to create OH concentrations ranging from ~10^8 to ~10^{10} molec. cm^{-3}, which for the average reactor residence time of 140 s, results in

equivalent exposure, or photochemical age, of between about 6 hours and 2 weeks for an assumed average atmospheric OH concentration of 1.5×10^6 molec. cm^{-3}. OH exposure were simulated using the KinSim chemical-kinetics solver (Peng et al., 2016; Peng and Jimenez, 2019) and detail mechanisms were described in previous study (Xu et al., 2022b). Gas-phase mixing ratio of O_3 were monitored by a UV photometric ozone analyzer (T400, Teledyne). The mixing ratio of ozone inside the reactor is varying from ~90 to 5000 parts per billion by volume (ppb_v) by adjusting the flow rate of zero air. The VOCs was injected into the reactor by flowing 10 cm^3 min^{-1} of each compound in a custom-made tank, to achieve a mixing ratio of ~60-80 ppb_v in the reactor. After allowing the parameters of reactor to stable for at least 10 min, UV lights (peak radiation intensity at ~254 nm) surrounding the reactor were turned on to initiate photooxidation. During all the oxidation experiments listed in this study, background contamination in the reactor before the reaction was less than 0.1 μg.

The monodisperse seed particles pass through a modified Spot Sampler (Aerosol Devices, Inc., Model 110A) to grow into droplets with the mean diameter around 3.3 μm. The generated droplets are rapidly mixed with a gas mixture containing O_3, the VOCs, and humidified zero air. Dew point and temperature in the reactor are precisely controlled by circulating water from a chiller outside of the reactor tube, resulting in the RH inside the reactor varied from 40 % to 100 %. Hereafter the 40 %, 85 % and 100 % RH maintained inside the reactor referred to as the dry seed, ALW, cloud mode, respectively. The aerosol formed inside the reactor pass through a 15 cm long Nafion bundles, to reduce the RH to below 20 %. A fabricated scanning mobility particle sizer (SMPS) and a condensation

particle counter (CPC, TSI Inc. Model 3762) were used to measure the size distribution and number concentrations of the SOA from 0.02 to 0.5 μm with 90 size bins.

4.3.3. **SOA Chemical Characterization**

During each experiments, chemical composition of SOA was measured using an Aerodyne high-resolution time-of-flight aerosol mass spectrometer (HR-ToF-AMS) (DeCarlo et al., 2006) and analyzed to obtain O : C and H : C ratios by applying the method reported in the previous studies (Canagaratna et al., 2015). Data processing was performed using the ToF-AMS Analysis Toolkit 1.57 and PIKA 1.16 on Igor Pro 6.36. After the formed SOA mass concentration was stable at highest OH_{exp} (equivalent photochemical age ~ 2 weeks), SOA samples were collected on 25 mm polytetrafluoroethylene (PTFE) membrane filters (Tisch Scientific) at 1.5 L min^{-1} for 20 min, allowing for a total collected SOA mass of 5-8 μg, estimated based on the measured aerosol effective densities of 1.4 μg cm^{-3}. The collected SOA samples were stored at -20 C until further offline analysis, with time-of-flight chemical ion mass spectrometry implemented with the Filter Inlet for Gases and AEROsols system (FIGAERO-ToF-CIMS, Aerodyne Research Inc.) was employed to characterize the molecular compositions of SOA constituents. Iodide ion (I-) was used as the adduct ion for soft ionization of the oxidized products. Detailed instrumental setup of ToF-CIMS and temperature profiles of FIGAERO is introduced in our previous studies (Jiang et al., 2019).

4.4. **Results and Discussions**

4.4.1. **Secondary Organic Aerosol Formation Through Gas- and Aqueous-Phase Oxidation**

The effects of OH exposure (OH_{exp}) on the SOA formation through gas- and aqueous-phase oxidation were first investigated (Figure 4.2), to gain a better understanding of the secondary aerosol production derived from water insoluble VOCs and the effect of aerosol water and cloud on aerosol formation. Upon the rapid consumption of 60-80 ppb_v of these VOCs by OH radicals, multigeneration oxidized products are formed and further oxidized through aqueous-phase reactions with the presence of aerosol water and cloud droplets. The details of SOA yield as a function of OH_{exp} are shown in Figure 4.6. Details of VOCs, experiments conditions and maximum yield are summarized in Table 4.1.

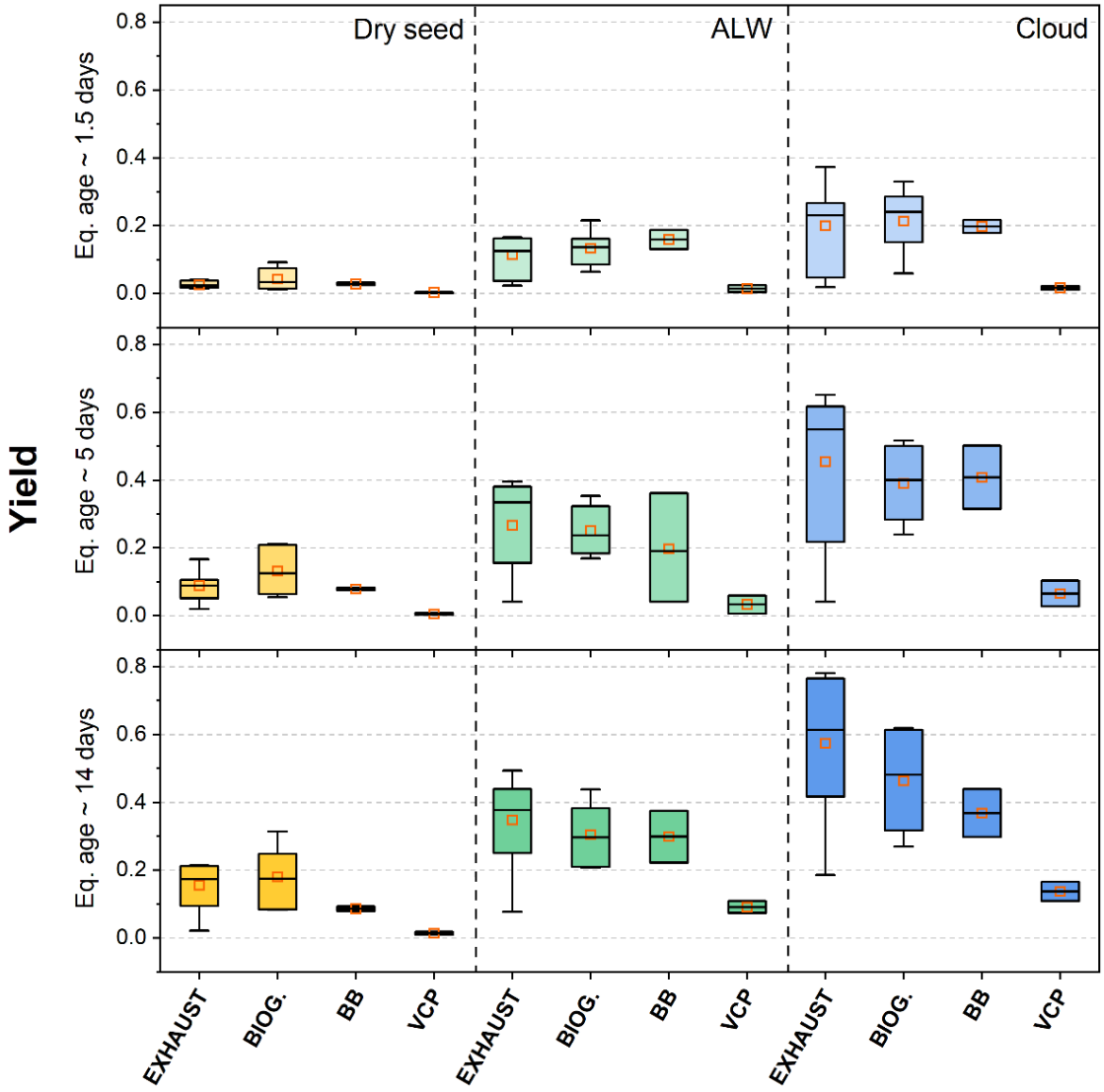

Figure 4.2: SOA yield under eq. photochemical age of 1.5 days (top), 5 days (middle) and 14 days (bottom) for selected volatile organic compounds from four categories under the relative humidity (RH) of 40 % RH (dry seed mode; yellow), 85% RH (ALW; green) and 100% RH (cloud, blue).

SOA formation from vehicle exhaust, biogenic increased with the equivalent photochemical age under all three modes. Under dry seed mode, the mean SOA yields derived from vehicle exhaust and biogenic are 0.04, 0.05 at the equivalent photochemical age of 1.5 days, while increase to 0.16, 0.19 at the equivalent photochemical age of 2 weeks. Also, the results show that most of the biogenic VOCs formed more SOA under same OH_{exp} compared to other three source categories at dry seed mode, which is consistent with the laboratory and model studies demonstrated that biogenic VOCs are main contributor for gas-phase SOA formation (Alfarra et al., 2013; Xavier et al., 2019). Relatively low SOA mass yield through the oxidation of biomass burning VOCs and VCP (yields ≤ 0.03) has been observed with increasing photochemical age under dry seed mode. In later context in this section, three compounds (α-pinene, isoprene and toluene) were selected to be discussed, as the representatives from biogenic and anthropogenic sources. Note that α-pinene and toluene formed significant amount of SOA even at dry seed mode, with yields of 0.32 and 0.22, respectively, assuming a density of 1.4 g cm^{-3} (Kostenidou et al., 2007; Nakao et al., 2011). The larger SOA mass formed from toluene and α-pinene indicated that OH chemistry with these compounds may be an important SOA source, particularly in anthropogenic and biogenic sources where these compounds are readily found (Lim et al., 2005; Kleindienst et al., 2007; Lamkaddam et al., 2021). Isoprene has a relatively low mass yield (0.08) compared with the other two compounds, but its SOA formation at the global scale is still significant because of its high emission rate (Guenther et al., 1993). Our SOA mass yields are relatively consistent with the literature. By comparison, the SOA mass yields reported in other studies are 0.38 for α-pinene, 0.30 for

toluene and 0.06 ± 0.02 for isoprene (Ng et al., 2007; Lambe et al., 2011; Ahlberg et al., 2017) under comparable OH exposures (~10^{11} molec. cm^{-3} s), which agree within ±10 % with our measurements.

Note that the SOA formed from anthropogenic and biomass burning VOCs increased dramatically with the presence of aerosol liquid water or cloud droplets. Slight increase of SOA production from vehicle exhaust and biogenic VOCs at the equivalent photochemical age of 1.5 days. The mean deviation of vehicle exhaust and biomass burning SOA yield is 0.11 and 0.17, respectively, which is a factor of 3.5 increase compared with that under same conditions. Significant SOA relative enhancement from biomass burning VOCs oxidation has been observed at the equivalent photochemical age of 1.5 days, with a factor of 8 increase compared with that under same conditions. More VCP-forming SOA have been observed at the equivalent photochemical age of two weeks when the aerosol liquid water exists. As shown in **Figure 4.6**B, the SOA maximum yield of α-pinene and toluene were 0.42 and 0.44 at OH_{exp} roughly 1.2×10^{12} molec. cm^{-3} s, which were enhanced by a factor of 1.3 and 2 compared with that under dry seed mode. The yield isoprene-forming SOA is approximately 0.21 under ALW mode at OH_{exp} roughly 1.2×10^{12} molec. cm^{-3} s, which is increased by a factor of 2.6 compared with that under dry seed mode. The results are consistent with the previous studies that reported larger yield under high RH conditions (Zhou et al., 2011; Liu et al., 2018) and can explained by small highly soluble compounds (eg., glyoxal) or advanced oxidation products with lower volatility produced by aqueous photochemistry, partitioned in aerosol liquid water and consequently promoting SOA formation.

For all of the VOCs listed in this study, substantial relative enhancement of SOA mass yield has been observed with the presence of cloud droplets. Vehicle-exhaust-derived SOA has much higher yield than that formed from biogenic VOCs, with a relative mass yield enhancement of 1.4 times at the equivalent photochemical age of 14 days, which indicate that the contribution of vehicle exhaust to aqSOA formation may be underestimated by current model. The SOA yields of experiments exhibited approximately linear increase with the increasing of OH_{exp}, and showed no evidence of plateau at high aerosol mass (**Figure 4.6**C). This may indicate that the first-generation and later generation products formed through gas-phase oxidation were largely water-soluble and they could be dissolved into cloud droplets and then further oxidized by increasing the OH concentration under aqueous phase. VCP and biomass burning VOCs may be important contributors to the aqSOA formation, though their SOA mass yield through gas-phase photooxidation is small. Note that the formation of toluene derived SOA is strongly affected by amount of liquid water added in. For the toluene SOA yield was 0.78 under cloud condition, which were about 3.5 times higher than that at dry seed mode. While α-pinene derived SOA yield slightly increased by a factor of 1.9, which is from 0.32 at dry seed mode to 0.61 at cloud mode. It may cause by a branch ratio that could determine the fraction of soluble components in the gas phase might be oxidized by the OH radical or very little gas phase components could be condensed on the surface of wet particles. Isoprene has a low yield (<8 %) under dry mode, yet obtained a higher yield of 30 % with the presence of cloud droplets, which is consistent with the what reported in previous study (Lamkaddam et al., 2021). This may be due to OH uptake can reach higher values under high humidity

conditions (Park et al., 2008; Slade and Knopf, 2014), facilitating the continued photochemistry through a combination of gas-phase processes in addition to aqueous-phase chemistry.

4.4.2. **Effect of Liquid Water on Secondary Aerosol Formation**

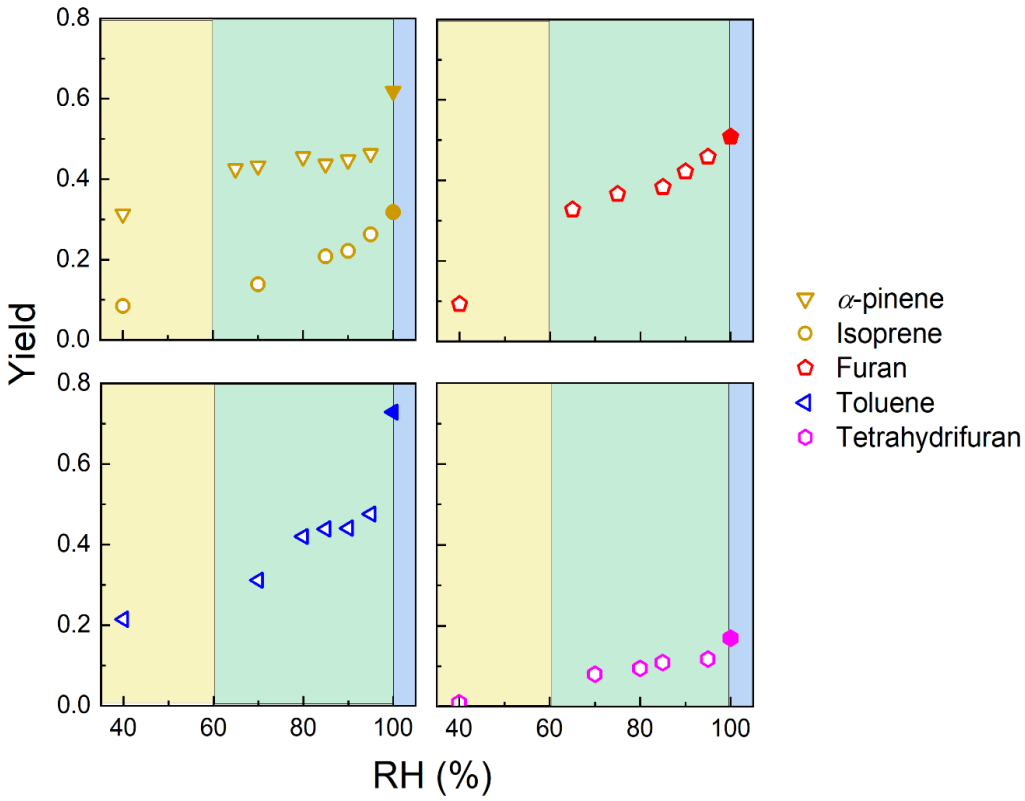

Figure 4.3: SOA mass yield as a function of relative humidity ranging from 40 ± 0.5 to 100.0 ± 0.5% under eq. photochemical age of 5 days. The stepping RH here is directly linked to an increase in water content. The yellow, green, blue background indicates dry seed, aqueous seed and cloud droplets presented in the system.

Figure 4.3 shows how increasing aerosol liquid water concentration (here referring to relative humidity controlled inside ethe reactor) on the secondary aerosol formed from those VOCs. Shown in the green background (60-95 % RH), the increasing aerosol liquid water content has limit effect on the α-pinene-derived SOA. But for other four VOCs (furan, tetrahydrofuran, isoprene and toluene), the SOA formed from the photo-oxidation is gradually increase with the increasing aerosol liquid water concentration. This enhanced SOA formation with increasing aerosol liquid water might be due to the fact the increasing aerosol liquid water facilitated the partitioning of gas-phase hydrophilic solutes into the particle phase. On the other hand, increasing aerosol liquid water provided a medium for aqueous reactions that could irreversibly drive gas uptake, forming high-molecular-weight products of low volatility with dissolved OH and other oxidants that significantly promoted aqSOA formation.

4.4.3. **SOA Chemical Compositions Though Gas- and Aqueous-Phase Oxidation**

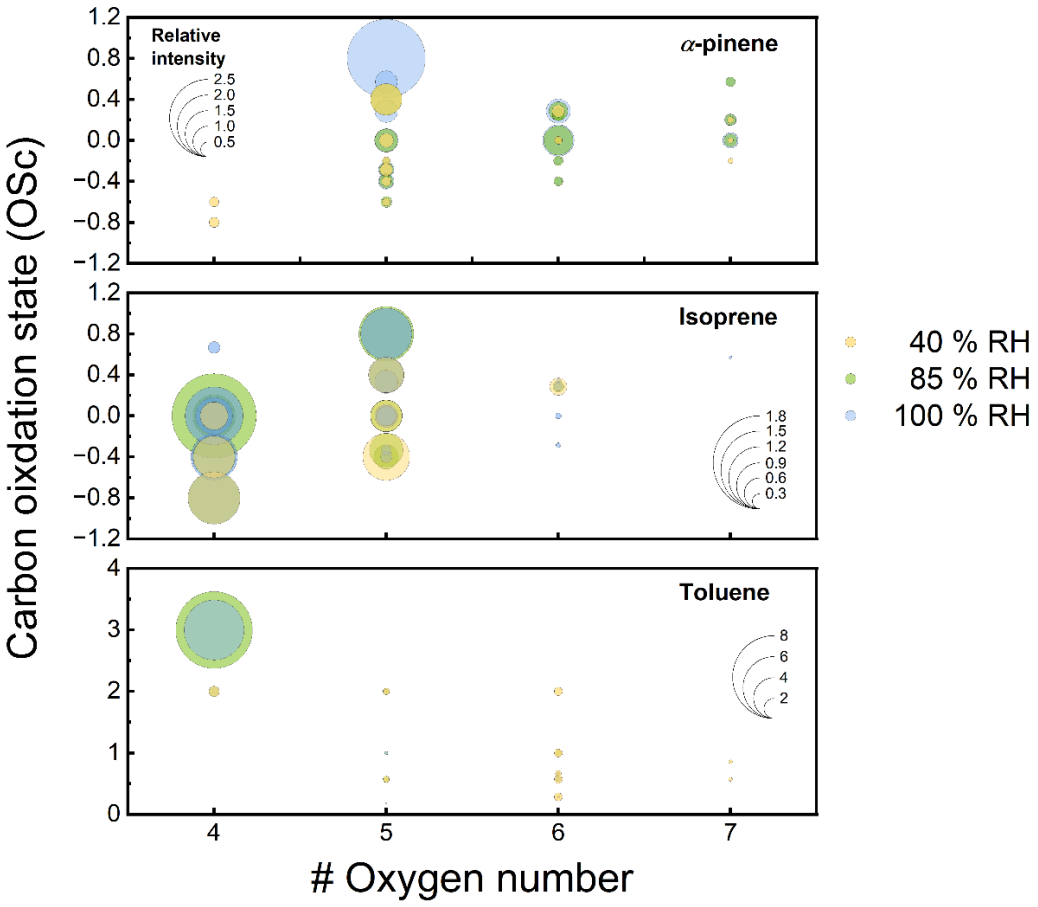

Figure 4.4: Carbon oxidation state of oxidation products derived from isoprene, *α*-pinene and toluene in the particle phase that generated inside the APPA reactor, as a function of their oxygen number. The color indicates the relative contributions of the oxidation products.

The mass spectra/relative contributions of particle-phase species of isoprene (Figure 4.7), toluene and *α*-pinene (Figure 4.8) oxidation obtained from FIGAERO-HR-ToF-CIMS. A more distinct difference is observed between different modes with the presence of different amount of liquid water. More products with higher molecular weight were detected as increasing aerosol liquid water concentration Figure 4.4: Carbon

oxidation state of oxidation products derived from isoprene, α-pinene and toluene in the particle phase that generated inside the APPA reactor, as a function of their oxygen number. The color indicates the relative contributions of the oxidation products.(Figure 4.4). The major compounds from low RH oxidation reported in isoprene + OH system include $C_5H_{10\text{-}12}O_4$ and $C_5H_{8\text{-}12}O_5$. $C_5H_8O_4$ was not detected under dry mode (40 %) but became the highest peak under ALW and cloud modes (85 % and 100 %). $C_5H_6O_5$ was not detected under dry mode (40 %) but emerged under ALW and cloud modes (85 % and 100 %). This significant contribution from species containing C_5 indicated the minor contribution of fragmentation process that probably is not a preferred pathway in low NO_x conditions. With the presence of cloud droplets, highly oxidized molecules are formed. Under cloud condition, the contribution from species containing C>5 is minimal in the OH aqueous oxidation condition. In α-pinene + OH system, $C_5H_6O_5$ is the dominant peak under cloud mode (100 %), which is likely that $C_5H_6O_5$ could be a promising tracer to study the evolution of α-pinene -derived secondary aerosol under cloud processes. In toluene + OH system, $C_4H_4O_6$ and $C_{11}H_8O_5$ were only detected under dry mode (40 %). $C_2H_2O_4$ was not detected under dry mode (40 %) but became the highest peak under ALW and cloud modes (85 % and 100 %).

The evolution of the aerosol oxygen-to-carbon (O/C) and hydrogen-to-carbon (H/C) ratios for isoprene, toluene and α-pinene SOA is shown in Figure 4.9. The OH exposure for all RH conditions is approximately 4×10^{11} molec. cm^{-3} s, which is equivalent to 3 days of the atmospheric exposure at [OH] = 1.5×10^6 molec. cm^{-3}. A significant difference of O/C and H/C ratios was observed in isoprene derived SOA. The measured

O/C and H/C ratios of isoprene under dry mode is 1.4 and 0.60, respectively. As the amount of liquid water increased, the measured O/C ratio increased to 0.82 and 1.15, under ALW and cloud conditions, respectively. The corresponding H/C ratios decreased to 1.79 under cloud condition. This result is consistent with the O/C ratio of 0.64 - 1.1 reported in previous chamber studies (Song et al., 2015; Galeazzo et al., 2021), indicating that the isoprene generated SOA was more oxidized with the increasing of liquid water. Slight increase of O/C ratios were observed from the gas- to aqueous-phase oxidation of toluene and α-pinene. At the same OH exposures, the O/C ratio of α-pinene SOA fell from 0.69 of gas-phase to 0.53 of aqueous-phase, with corresponding H/C ratios from 1.51 of gas-phase to 1.43 of aqueous-phase. This may be caused by the design of the APPA reactor, since the O_3 and α-pinene were injected and react prior to OH exposure, leading to approximately 10% of injected α-pinene reacted with ozone to form ozonolysis products. The O/C ratio of toluene SOA increased from 0.84 of dry mode to 0.85 of ALW mode, with corresponding H/C ratios decreased from 1.20 to 1.19. Under cloud condition, the O/C was decreased to 0.80, which may cause by the SOA fragmentation to smaller, more volatile oxidation products and rapid gas-phase oxidation happened.

It is necessary to investigate the secondary aerosols due to the large amount of inorganic species present in the atmosphere. Hence, effects of seed on the SOA formation through aqueous-phase oxidation were also investigated. The inorganic salt aerosols are categorized into two types; the introduced $(NH_4)_2SO_4$ seed particles are considered as aqueous acidic seeds with pH is approximate 5.8 calculated with the Aerosol Inorganic model (AIM) and K_2SO_4 seed particles are considered as aqueous neutral seeds. The

increase in SOA yield from isoprene, toluene and α-pinene with different types of seed at dry seed, ALW and cloud modes is shown in Figure 4.5. The dry seed surface area concentrations were around 1200 cm^2/cm^3, to eliminate the effect of dry seed surface area on the result Figure 4.10. Here, we detected a significantly seed effect on the formation of isoprene derived SOA, which consistent with what reported in previous study (Ahlberg et al., 2019). Under ALW and cloud conditions, the SOA yield was increased by a factor of 1.5 with the presence of ammonium sulfate seed compared with that with potassium sulfate seeds. In addition, the ammonium sulfate seed helps the SOA formation reach plateau. We think this is because of the acidity effect the pathway of the isoprene compositions, which lead to form rapidly than the neutral environments (Surratt et al., 2010; Riva et al., 2016). For comparison, the toluene and a-pinene SOA wasn't observed the seed effect. The observed enhancement of the SOA mass concentration with increasing acidity of the inorganic seed aerosol is consistent with acid-catalyzed particle-phase reactions occurring.

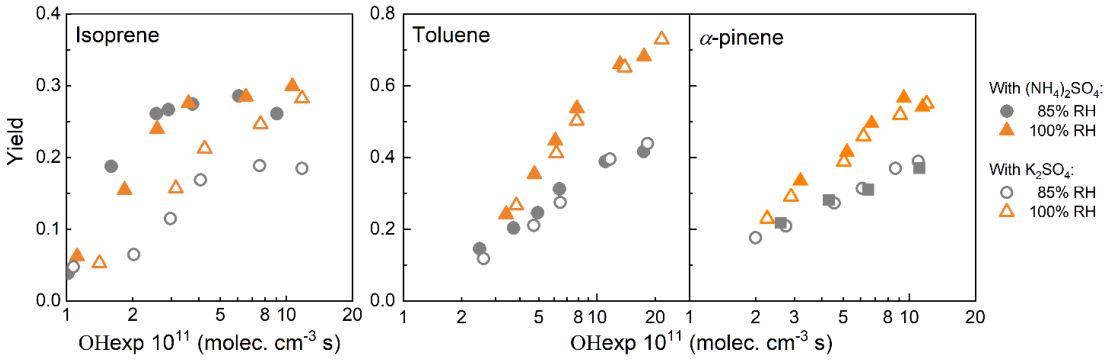

Figure 4.5: Calculated SOA mass yields from (left) isoprene (middle) toluene and (right) α-pinene as a function of OH exposure, with different seed particles.

4.5. **Conclusion and Future Work**

In this study, we have demonstrated that SOA formation from aqueous phase oxidation have significant implications happened in the atmosphere. Considering the relatively high annual global emissions of toluene (up to 4 Tg yr^{-1}), α -pinene (up to 60 Tg yr^{-1}), and isoprene (up to 717 Tg yr^{-1}) (Guenther et al., 1993; Guenther et al., 2006; Wiedinmyer et al., 2006; Misztal et al., 2015), the secondary products from the oxidation of these precursors may be ubiquitous. The aqueous phase oxidation of volatile organic compounds can be significantly contributed to the SOA mass. Overall, our results represent the first step toward a better representation of in-aqueous aerosol and in-cloud aqSOA formation under relevant conditions to be integrated in models, to estimate the relative importance of each precursor to the ambient SOA. Future research is warranted to quantify secondary products from precursors that can react with ozone, study their fates and reactivities, and model their formation processes. And noted that the present data carried out in this study over a range of RH values (referring to the increasing amount of aerosol liquid water or cloud droplets) to evaluate both gas – and aqueous chemistry. Obviously, further studies beyond the limited range of conditions presented here (e.g., moderate room temperature and low NOx regime, smaller droplets) are needed. Hence, our novel results open new possibility of combining the aqueous photooxidation chemistry with the current far- and near-field models, and also the investigation of how the aerosol liquid water influence the secondary aerosol formation under various environmental conditions for other volatile organic compound precursors.

4.6. **References**

Ahlberg, E., Eriksson, A., Brune, W. H., Roldin, P., and Svenningsson, B.: Effect of salt seed particle surface area, composition and phase on secondary organic aerosol mass yields in oxidation flow reactors, Atmospheric Chemistry and Physics, 19, 2701-2712, 10.5194/acp-19-2701-2019, 2019.

Ahlberg, E., Falk, J., Eriksson, A., Holst, T., Brune, W. H., Kristensson, A., Roldin, P., and Svenningsson, B.: Secondary organic aerosol from VOC mixtures in an oxidation flow reactor, Atmospheric Environment, 161, 210-220, 2017.

Alfarra, M., Good, N., Wyche, K. P., Hamilton, J., Monks, P., Lewis, A., and Mcfiggans, G.: Water uptake is independent of the inferred composition of secondary aerosols derived from multiple biogenic VOCs, Atmospheric Chemistry and Physics, 13, 11769-11789, 2013.

Aljawhary, D., Zhao, R., Lee, A. K., Wang, C., and Abbatt, J. P.: Kinetics, mechanism, and secondary organic aerosol yield of aqueous phase photo-oxidation of α-pinene oxidation products, The Journal of Physical Chemistry A, 120, 1395-1407, 2016.

Bateman, A. P., Nizkorodov, S. A., Laskin, J., and Laskin, A.: Photolytic processing of secondary organic aerosols dissolved in cloud droplets, Physical Chemistry Chemical Physics, 13, 12199-12212, 2011.

Canagaratna, M., Jimenez, J., Kroll, J., Chen, Q., Kessler, S., Massoli, P., Hildebrandt Ruiz, L., Fortner, E., Williams, L., and Wilson, K.: Elemental ratio measurements of organic compounds using aerosol mass spectrometry: characterization, improved calibration, and implications, Atmospheric Chemistry and Physics, 15, 253-272, 2015.

Carlton, A., Wiedinmyer, C., and Kroll, J.: A review of Secondary Organic Aerosol (SOA) formation from isoprene, Atmospheric Chemistry and Physics, 9, 4987-5005, 2009.

Carlton, A. G., Turpin, B. J., Altieri, K. E., Seitzinger, S., Reff, A., Lim, H.-J., and Ervens, B.: Atmospheric oxalic acid and SOA production from glyoxal: Results of aqueous photooxidation experiments, Atmospheric Environment, 41, 7588-7602, 2007.

Carter, W. P., Cocker III, D. R., Fitz, D. R., Malkina, I. L., Bumiller, K., Sauer, C. G., Pisano, J. T., Bufalino, C., and Song, C.: A new environmental chamber for evaluation of gas-phase chemical mechanisms and secondary aerosol formation, Atmospheric Environment, 39, 7768-7788, 2005.

Chen, J., Dahlin, M. J., Luuppala, L., Bickford, D., Boljka, L., Burns, V., and Johnson, M. S.: Air pollution and climate change: sustainability, restoration, and ethical implications, Air pollution sources, statistics and health effects, 279-325, 2021.

Claeys, M., Graham, B., Vas, G., Wang, W., Vermeylen, R., Pashynska, V., Cafmeyer, J., Guyon, P., Andreae, M. O., and Artaxo, P.: Formation of secondary organic aerosols through photooxidation of isoprene, Science, 303, 1173-1176, 2004.

Coggon, M. M., Gkatzelis, G. I., McDonald, B. C., Gilman, J. B., Schwantes, R. H., Abuhassan, N., Aikin, K. C., Arend, M. F., Berkoff, T. A., and Brown, S. S.: Volatile chemical product emissions enhance ozone and modulate urban chemistry, Proceedings of the National Academy of Sciences, 118, e2026653118, 2021.

Cubison, M., Ortega, A., Hayes, P., Farmer, D., Day, D., Lechner, M., Brune, W., Apel, E., Diskin, G., and Fisher, J.: Effects of aging on organic aerosol from open biomass burning smoke in aircraft and laboratory studies, Atmospheric Chemistry and Physics, 11, 12049-12064, 2011.

DeCarlo, P. F., Kimmel, J. R., Trimborn, A., Northway, M. J., Jayne, J. T., Aiken, A. C., Gonin, M., Fuhrer, K., Horvath, T., and Docherty, K. S.: Field-deployable, high-resolution, time-of-flight aerosol mass spectrometer, Analytical chemistry, 78, 8281-8289, 2006.

Donahue, N. M., Henry, K. M., Mentel, T. F., Kiendler-Scharr, A., Spindler, C., Bohn, B., Brauers, T., Dorn, H. P., Fuchs, H., and Tillmann, R.: Aging of biogenic secondary organic aerosol via gas-phase OH radical reactions, Proceedings of the National Academy of Sciences, 109, 13503-13508, 2012.

Ervens, B.: Modeling the processing of aerosol and trace gases in clouds and fogs, Chemical reviews, 115, 4157-4198, 2015.

Ervens, B., Sorooshian, A., Lim, Y. B., and Turpin, B. J.: Key parameters controlling OH-initiated formation of secondary organic aerosol in the aqueous phase (aqSOA), Journal of Geophysical Research-Atmospheres, 119, 3997-4016, 10.1002/2013jd021021, 2014.

Ervens, B., Renard, P., Tlili, S., Ravier, S., Clément, J.-L., and Monod, A.: Aqueous-phase oligomerization of methyl vinyl ketone through photooxidation–Part 2: Development of the chemical mechanism and atmospheric implications, Atmospheric Chemistry and Physics, 15, 9109-9127, 2015.

Ervens, B., Sorooshian, A., Aldhaif, A. M., Shingler, T., Crosbie, E., Ziemba, L., Campuzano-Jost, P., Jimenez, J. L., and Wisthaler, A.: Is there an aerosol signature of chemical cloud processing?, Atmospheric Chemistry and Physics, 18, 16099-16119, 10.5194/acp-18-16099-2018, 2018.

Fantke, P., Ernstoff, A. S., Huang, L., Csiszar, S. A., and Jolliet, O.: Coupled near-field and far-field exposure assessment framework for chemicals in consumer products, Environment international, 94, 508-518, 2016.

Farina, S. C., Adams, P. J., and Pandis, S. N.: Modeling global secondary organic aerosol formation and processing with the volatility basis set: Implications for anthropogenic secondary organic aerosol, Journal of Geophysical Research: Atmospheres, 115, 2010.

Favez, O., Sciare, J., Cachier, H., Alfaro, S. C., and Abdelwahab, M. M.: Significant formation of water-insoluble secondary organic aerosols in semi-arid urban environment, Geophysical Research Letters, 35, 2008.

Galeazzo, T., Valorso, R., Li, Y., Camredon, M., Aumont, B., and Shiraiwa, M.: Estimation of secondary organic aerosol viscosity from explicit modeling of gas-phase oxidation of isoprene and α-pinene, Atmospheric Chemistry and Physics, 21, 10199-10213, 2021.

Gentner, D. R., Jathar, S. H., Gordon, T. D., Bahreini, R., Day, D. A., El Haddad, I., Hayes, P. L., Pieber, S. M., Platt, S. M., and de Gouw, J.: Review of urban secondary organic aerosol formation from gasoline and diesel motor vehicle emissions, Environmental science & technology, 51, 1074-1093, 2017.

Gkatzelis, G. I., Coggon, M. M., McDonald, B. C., Peischl, J., Gilman, J. B., Aikin, K. C., Robinson, M. A., Canonaco, F., Prevot, A. S., and Trainer, M.: Observations confirm that volatile chemical products are a major source of petrochemical emissions in US cities, Environmental science & technology, 55, 4332-4343, 2021.

Guenther, A., Karl, T., Harley, P., Wiedinmyer, C., Palmer, P. I., and Geron, C.: Estimates of global terrestrial isoprene emissions using MEGAN (Model of Emissions of Gases and Aerosols from Nature), Atmospheric Chemistry and Physics, 6, 3181-3210, 2006.

Guenther, A. B., Zimmerman, P. R., Harley, P. C., Monson, R. K., and Fall, R.: Isoprene and monoterpene emission rate variability: model evaluations and sensitivity analyses, Journal of Geophysical Research: Atmospheres, 98, 12609-12617, 1993.

Heglund, D. L. and Tilotta, D. C.: Determination of volatile organic compounds in water by solid phase microextraction and infrared spectroscopy, Environmental science & technology, 30, 1212-1219, 1996.

Herrmann, H., Schaefer, T., Tilgner, A., Styler, S. A., Weller, C., Teich, M., and Otto, T.: Tropospheric Aqueous-Phase Chemistry: Kinetics, Mechanisms, and Its Coupling to a Changing Gas Phase, Chemical Reviews, 115, 4259-4334, 10.1021/cr500447k, 2015.

Hodzic, A., Kasibhatla, P. S., Jo, D. S., Cappa, C. D., Jimenez, J. L., Madronich, S., and Park, R. J.: Rethinking the global secondary organic aerosol (SOA) budget: stronger production, faster removal, shorter lifetime, Atmospheric Chemistry and Physics, 16, 7917-7941, 2016.

Huang, D., Zhang, X., Chen, Z., Zhao, Y., and Shen, X.: The kinetics and mechanism of an aqueous phase isoprene reaction with hydroxyl radical, Atmospheric Chemistry and Physics, 11, 7399-7415, 2011.

Jiang, H., Frie, A. L., Lavi, A., Chen, J. Y., Zhang, H., Bahreini, R., and Lin, Y.-H.: Brown carbon formation from nighttime chemistry of unsaturated heterocyclic volatile organic compounds, Environmental Science & Technology Letters, 6, 184-190, 2019.

Jimenez, J. L., Canagaratna, M., Donahue, N., Prevot, A., Zhang, Q., Kroll, J. H., DeCarlo, P. F., Allan, J. D., Coe, H., and Ng, N.: Evolution of organic aerosols in the atmosphere, Science, 326, 1525-1529, 2009.

Kleindienst, T. E., Jaoui, M., Lewandowski, M., Offenberg, J. H., Lewis, C. W., Bhave, P. V., and Edney, E. O.: Estimates of the contributions of biogenic and anthropogenic hydrocarbons to secondary organic aerosol at a southeastern US location, Atmospheric Environment, 41, 8288-8300, 2007.

Kostenidou, E., Pathak, R. K., and Pandis, S. N.: An algorithm for the calculation of secondary organic aerosol density combining AMS and SMPS data, Aerosol Science and Technology, 41, 1002-1010, 2007.

Kroll, J. H. and Seinfeld, J. H.: Chemistry of secondary organic aerosol: Formation and evolution of low-volatility organics in the atmosphere, Atmospheric Environment, 42, 3593-3624, 2008.

Kua, J., Krizner, H. E., and De Haan, D. O.: Thermodynamics and kinetics of imidazole formation from glyoxal, methylamine, and formaldehyde: A computational study, The Journal of Physical Chemistry A, 115, 1667-1675, 2011.

Lambe, A., Ahern, A., Williams, L., Slowik, J., Wong, J., Abbatt, J., Brune, W., Ng, N., Wright, J., and Croasdale, D.: Characterization of aerosol photooxidation flow reactors: heterogeneous oxidation, secondary organic aerosol formation and cloud condensation nuclei activity measurements, Atmospheric Measurement Techniques, 4, 445-461, 2011.

Lamkaddam, H., Dommen, J., Ranjithkumar, A., Gordon, H., Wehrle, G., Krechmer, J., Majluf, F., Salionov, D., Schmale, J., and Bjelić, S.: Large contribution to secondary organic aerosol from isoprene cloud chemistry, Science Advances, 7, eabe2952, 2021.

Lim, H.-J., Carlton, A. G., and Turpin, B. J.: Isoprene forms secondary organic aerosol through cloud processing: Model simulations, Environmental science & technology, 39, 4441-4446, 2005.

Lim, Y., Tan, Y., Perri, M., Seitzinger, S., and Turpin, B.: Aqueous chemistry and its role in secondary organic aerosol (SOA) formation, Atmospheric Chemistry and Physics, 10, 10521-10539, 2010.

Liu, T., Huang, D. D., Li, Z., Liu, Q., Chan, M., and Chan, C. K.: Comparison of secondary organic aerosol formation from toluene on initially wet and dry ammonium sulfate particles at moderate relative humidity, Atmospheric Chemistry and Physics, 18, 5677-5689, 2018.

Liu, Y., Monod, A., Tritscher, T., Praplan, A., DeCarlo, P., Temime-Roussel, B., Quivet, E., Marchand, N., Dommen, J., and Baltensperger, U.: Aqueous phase processing of secondary organic aerosol from isoprene photooxidation, Atmospheric Chemistry and Physics, 12, 5879-5895, 2012.

McDonald, B. C., De Gouw, J. A., Gilman, J. B., Jathar, S. H., Akherati, A., Cappa, C. D., Jimenez, J. L., Lee-Taylor, J., Hayes, P. L., and McKeen, S. A.: Volatile chemical products emerging as largest petrochemical source of urban organic emissions, Science, 359, 760-764, 2018.

McNeill, V. F., Woo, J. L., Kim, D. D., Schwier, A. N., Wannell, N. J., Sumner, A. J., and Barakat, J. M.: Aqueous-phase secondary organic aerosol and organosulfate formation in atmospheric aerosols: a modeling study, Environmental science & technology, 46, 8075-8081, 2012.

Misztal, P. K., Hewitt, C. N., Wildt, J., Blande, J. D., Eller, A. S., Fares, S., Gentner, D. R., Gilman, J., Graus, M., and Greenberg, J.: Atmospheric benzenoid emissions from plants rival those from fossil fuels, Scientific reports, 5, 1-10, 2015.

Mohamed, M. F., Kang, D., and Aneja, V. P.: Volatile organic compounds in some urban locations in United States, Chemosphere, 47, 863-882, 2002.

Mølhave, L.: Volatile organic compounds, indoor air quality and health, Indoor Air, 1, 357-376, 1991.

Murphy, B. N. and Pandis, S. N.: Exploring summertime organic aerosol formation in the eastern United States using a regional-scale budget approach and ambient measurements, Journal of Geophysical Research: Atmospheres, 115, 2010.

Myriokefalitakis, S., Vrekoussis, M., Tsigaridis, K., Wittrock, F., Richter, A., Brühl, C., Volkamer, R., Burrows, J., and Kanakidou, M.: The influence of natural and anthropogenic secondary sources on the glyoxal global distribution, Atmospheric Chemistry and Physics, 8, 4965-4981, 2008.

Nakao, S., Clark, C., Tang, P., Sato, K., and Cocker Iii, D.: Secondary organic aerosol formation from phenolic compounds in the absence of NO x, Atmospheric Chemistry and Physics, 11, 10649-10660, 2011.

Ng, N. L., Kroll, J. H., Chan, A. W. H., Chhabra, P. S., Flagan, R. C., and Seinfeld, J. H.: Secondary organic aerosol formation from m-xylene, toluene, and benzene, Atmos. Chem. Phys., 7, 3909-3922, 10.5194/acp-7-3909-2007, 2007.

Nozière, B., Ekström, S., Alsberg, T., and Holmström, S.: Radical-initiated formation of organosulfates and surfactants in atmospheric aerosols, Geophysical Research Letters, 37, 2010.

Odum, J. R., Hoffmann, T., Bowman, F., Collins, D., Flagan, R. C., and Seinfeld, J. H.: Gas/particle partitioning and secondary organic aerosol yields, Environmental science & technology, 30, 2580-2585, 1996.

Ortega, A. M., Hayes, P. L., Peng, Z., Palm, B. B., Hu, W., Day, D. A., Li, R., Cubison, M. J., Brune, W. H., and Graus, M.: Real-time measurements of secondary organic aerosol formation and aging from ambient air in an oxidation flow reactor in the Los Angeles area, Atmospheric Chemistry and Physics, 16, 7411-7433, 2016.

Park, J.-H., Ivanov, A. V., and Molina, M. J.: Effect of relative humidity on OH uptake by surfaces of atmospheric importance, The Journal of Physical Chemistry A, 112, 6968-6977, 2008.

Peng, Z. and Jimenez, J. L.: KinSim: A Research-Grade, User-Friendly, Visual Kinetics Simulator for Chemical-Kinetics and Environmental-Chemistry Teaching, 2019.

Peng, Z., Day, D. A., Ortega, A. M., Palm, B. B., Hu, W., Stark, H., Li, R., Tsigaridis, K., Brune, W. H., and Jimenez, J. L.: Non-OH chemistry in oxidation flow reactors for the study of atmospheric chemistry systematically examined by modeling, Atmospheric Chemistry and Physics, 16, 4283-4305, 2016.

Qin, M., Murphy, B. N., Isaacs, K. K., McDonald, B. C., Lu, Q., McKeen, S. A., Koval, L., Robinson, A. L., Efstathiou, C., and Allen, C.: Criteria pollutant impacts of volatile chemical products informed by near-field modelling, Nature sustainability, 4, 129-137, 2021.

Rap, A., Scott, C., Reddington, C., Mercado, L., Ellis, R., Garraway, S., Evans, M., Beerling, D., MacKenzie, A., and Hewitt, C.: Enhanced global primary production by biogenic aerosol via diffuse radiation fertilization, Nature Geoscience, 11, 640-644, 2018.

Riva, M., Budisulistiorini, S. H., Chen, Y., Zhang, Z., D'Ambro, E. L., Zhang, X., Gold, A., Turpin, B. J., Thornton, J. A., and Canagaratna, M. R.: Chemical characterization of secondary organic aerosol from oxidation of isoprene hydroxyhydroperoxides, Environmental science & technology, 50, 9889-9899, 2016.

Shiraiwa, M., Yee, L. D., Schilling, K. A., Loza, C. L., Craven, J. S., Zuend, A., Ziemann, P. J., and Seinfeld, J. H.: Size distribution dynamics reveal particle-phase chemistry in organic aerosol formation, Proceedings of the National Academy of Sciences, 110, 11746-11750, 2013.

Shrivastava, M., Cappa, C. D., Fan, J., Goldstein, A. H., Guenther, A. B., Jimenez, J. L., Kuang, C., Laskin, A., Martin, S. T., and Ng, N. L.: Recent advances in understanding secondary organic aerosol: Implications for global climate forcing, Reviews of Geophysics, 55, 509-559, 2017.

Shrivastava, M., Easter, R. C., Liu, X., Zelenyuk, A., Singh, B., Zhang, K., Ma, P. L., Chand, D., Ghan, S., and Jimenez, J. L.: Global transformation and fate of SOA: Implications of low-volatility SOA and gas-phase fragmentation reactions, Journal of Geophysical Research: Atmospheres, 120, 4169-4195, 2015.

Slade, J. H. and Knopf, D. A.: Multiphase OH oxidation kinetics of organic aerosol: The role of particle phase state and relative humidity, Geophysical Research Letters, 41, 5297-5306, 2014.

Song, C., Zaveri, R. A., Alexander, M. L., Thornton, J. A., Madronich, S., Ortega, J. V., Zelenyuk, A., Yu, X. Y., Laskin, A., and Maughan, D. A.: Effect of hydrophobic primary organic aerosols on secondary organic aerosol formation from ozonolysis of α-pinene, Geophysical Research Letters, 34, 2007.

Song, M., Liu, P., Hanna, S., Li, Y., Martin, S., and Bertram, A.: Relative humidity-dependent viscosities of isoprene-derived secondary organic material and atmospheric implications for isoprene-dominant forests, Atmospheric Chemistry and Physics, 15, 5145-5159, 2015.

Spracklen, D., Carslaw, K., Pöschl, U., Rap, A., and Forster, P.: Global cloud condensation nuclei influenced by carbonaceous combustion aerosol, Atmospheric Chemistry and Physics, 11, 9067-9087, 2011a.

Spracklen, D., Jimenez, J., Carslaw, K., Worsnop, D., Evans, M., Mann, G., Zhang, Q., Canagaratna, M., Allan, J., and Coe, H.: Aerosol mass spectrometer constraint on the global secondary organic aerosol budget, Atmospheric Chemistry and Physics, 11, 12109-12136, 2011b.

Stavrakou, T., Müller, J.-F., De Smedt, I., Van Roozendael, M., Kanakidou, M., Vrekoussis, M., Wittrock, F., Richter, A., and Burrows, J.: The continental source of glyoxal estimated by the synergistic use of spaceborne measurements and inverse modelling, Atmospheric Chemistry and Physics, 9, 8431-8446, 2009.

Sun, Y., Zhang, Q., Anastasio, C., and Sun, J.: Insights into secondary organic aerosol formed via aqueous-phase reactions of phenolic compounds based on high resolution mass spectrometry, Atmospheric Chemistry and Physics, 10, 4809-4822, 2010.

Surratt, J. D., Chan, A. W., Eddingsaas, N. C., Chan, M., Loza, C. L., Kwan, A. J., Hersey, S. P., Flagan, R. C., Wennberg, P. O., and Seinfeld, J. H.: Reactive intermediates revealed

in secondary organic aerosol formation from isoprene, Proceedings of the National Academy of Sciences, 107, 6640-6645, 2010.

Tan, Y., Carlton, A. G., Seitzinger, S. P., and Turpin, B. J.: SOA from methylglyoxal in clouds and wet aerosols: Measurement and prediction of key products, Atmospheric Environment, 44, 5218-5226, 2010.

Tomaz, S., Cui, T., Chen, Y., Sexton, K. G., Roberts, J. M., Warneke, C., Yokelson, R. J., Surratt, J. D., and Turpin, B. J.: Photochemical Cloud Processing of Primary Wildfire Emissions as a Potential Source of Secondary Organic Aerosol, Environmental Science & Technology, 52, 11027-11037, 10.1021/acs.est.8b03293, 2018.

Tsigaridis, K., Daskalakis, N., Kanakidou, M., Adams, P., Artaxo, P., Bahadur, R., Balkanski, Y., Bauer, S., Bellouin, N., and Benedetti, A.: The AeroCom evaluation and intercomparison of organic aerosol in global models, Atmospheric Chemistry and Physics, 14, 10845-10895, 2014.

Volkamer, R., Jimenez, J. L., San Martini, F., Dzepina, K., Zhang, Q., Salcedo, D., Molina, L. T., Worsnop, D. R., and Molina, M. J.: Secondary organic aerosol formation from anthropogenic air pollution: Rapid and higher than expected, Geophysical Research Letters, 33, 2006.

Wang, J., Ye, J., Zhang, Q., Zhao, J., Wu, Y., Li, J., Liu, D., Li, W., Zhang, Y., and Wu, C.: Aqueous production of secondary organic aerosol from fossil-fuel emissions in winter Beijing haze, Proceedings of the National Academy of Sciences, 118, 2021a.

Wang, S., Wang, L., Wang, N., Ma, S., Su, F., and Zhang, R.: Formation of droplet-mode secondary inorganic aerosol dominated the increased PM2. 5 during both local and transport haze episodes in Zhengzhou, China, Chemosphere, 269, 128744, 2021b.

Wiedinmyer, C., Tie, X., Guenther, A., Neilson, R., and Granier, C.: Future changes in biogenic isoprene emissions: how might they affect regional and global atmospheric chemistry?, Earth Interactions, 10, 1-19, 2006.

Xavier, C., Rusanen, A., Zhou, P., Dean, C., Pichelstorfer, L., Roldin, P., and Boy, M.: Aerosol mass yields of selected biogenic volatile organic compounds–a theoretical study with nearly explicit gas-phase chemistry, Atmospheric Chemistry and Physics, 19, 13741-13758, 2019.

Xu, B., Zhang, G., Gustafsson, Ö., Kawamura, K., Li, J., Andersson, A., Bikkina, S., Kunwar, B., Pokhrel, A., and Zhong, G.: Large contribution of fossil-derived components to aqueous secondary organic aerosols in China, Nature communications, 13, 1-12, 2022a.

Xu, N., Le, C., Cocker, D. R., and Collins, D. R.: An oxidation flow reactor for simulating and accelerating secondary aerosol formation in aerosol liquid water and cloud droplets, Atmospheric Measurement Techniques Discussions, 1-41, 2022b.

Ye, Z., Zhuang, Y., Chen, Y., Zhao, Z., Ma, S., Huang, H., Chen, Y., and Ge, X.: Aqueous-phase oxidation of three phenolic compounds by hydroxyl radical: Insight into secondary organic aerosol formation yields, mechanisms, products and optical properties, Atmospheric Environment, 223, 117240, 2020.

Yli-Juuti, T., Mielonen, T., Heikkinen, L., Arola, A., Ehn, M., Isokääntä, S., Keskinen, H.-M., Kulmala, M., Laakso, A., and Lipponen, A.: Significance of the organic aerosol driven climate feedback in the boreal area, Nature communications, 12, 1-9, 2021.

Yu, L., Smith, J., Laskin, A., George, K. M., Anastasio, C., Laskin, J., Dillner, A. M., and Zhang, Q.: Molecular transformations of phenolic SOA during photochemical aging in the aqueous phase: competition among oligomerization, functionalization, and fragmentation, Atmospheric Chemistry and Physics, 16, 4511-4527, 2016.

Zhang, Q., Jimenez, J. L., Canagaratna, M. R., Ulbrich, I. M., Ng, N. L., Worsnop, D. R., and Sun, Y.: Understanding atmospheric organic aerosols via factor analysis of aerosol mass spectrometry: a review, Analytical and bioanalytical chemistry, 401, 3045-3067, 2011.

Zhou, Y., Zhang, H., Parikh, H. M., Chen, E. H., Rattanavaraha, W., Rosen, E. P., Wang, W., and Kamens, R. M.: Secondary organic aerosol formation from xylenes and mixtures of toluene and xylenes in an atmospheric urban hydrocarbon mixture: Water and particle seed effects (II), Atmospheric Environment, 45, 3882-3890, 2011.

4.7. **Supplementary Materials**

Table 4.1: Summary of VOCs, and experiment conditions and maximum yield.

Category	**CAS No.**	**Compound**	**Formula**	**k_{OH} ($\times 10^{12}$) (cm^3 $molecule^{-1}$ s^{-1})**	**RH (%)**	**Max. Yield (This study)**
Biogenic	470-82-6	1,8-Cineole	$C_{10}H_{18}O$	11.1	40	0.11
					85	0.24
					100	0.36
	13466-78-9	3-Carene	$C_{10}H_{16}$	80.5	40	0.08
					85	0.21
					100	0.27
	80-56-8	α-pinene	$C_{10}H_{16}$	52.8	40	0.31
					85	0.44
					100	0.62
	127-91-3	β-pinene	$C_{10}H_{16}$	78.1	40	0.24
					85	0.36
					100	0.61
	79-92-5	Camphene	$C_{10}H_{16}$	21	40	0.25
					85	0.38
					100	0.60
	78-79-5	Isoprene	C_5H_8	100	40	0.09
					85	0.21
					100	0.32
Vehicle Exhaust	108-38-3	*m*-xylene	C_8H_{10}	24.5	40	0.20
					85	0.38
					100	0.67
	106-42-3	*p*-xylene	C_8H_{10}	15.7	40	0.17
					85	0.49
					100	0.76
	71-43-2	Benzene	C_6H_6	1.22	40	0.17
					85	0.43
					100	0.61
	108-38-3	*m*-xylene	C_8H_{10}	24.5	40	0.20
					85	0.38
					100	0.67

	106-42-3	*p*-xylene	C_8H_{10}	15.7	40	0.17
					85	0.49
					100	0.76
	71-43-2	Benzene	C_6H_6	1.22	40	0.17
					85	0.43
					100	0.61
	110-82-7	Cyclohexane	C_6H_{12}	6.91	40	0.09
					85	0.25
					100	0.42
	100-41-4	Ethylbenzene	C_8H_{10}	6.9	40	0.21
					85	0.37
					100	0.58
	111-65-9	Octane	C_8H_{18}	8.13	40	0.02
					85	0.08
					100	0.19
	108-88-3	Toluene	C_7H_8	6.16	40	0.28
					85	0.42
					100	0.68
Volatile Chemical Products (VCP)	541-02-6	D_5-Siloxane	$C_{10}H_{30}O_5Si_5$	2.1	40	0.02
					85	0.07
					100	0.11
	109-99-9	Tetrahydrofuran	C_4H_8O	17.88	40	0.01
					85	0.11
					100	0.16
Biomass Burning	534-22-5	2-methylfuran	C_5H_6O	61.9	40	0.08
					85	0.22
					100	0.30
	110-00-9	Furan	C_4H_4O	41.9	40	0.09
					85	0.38
					100	0.51

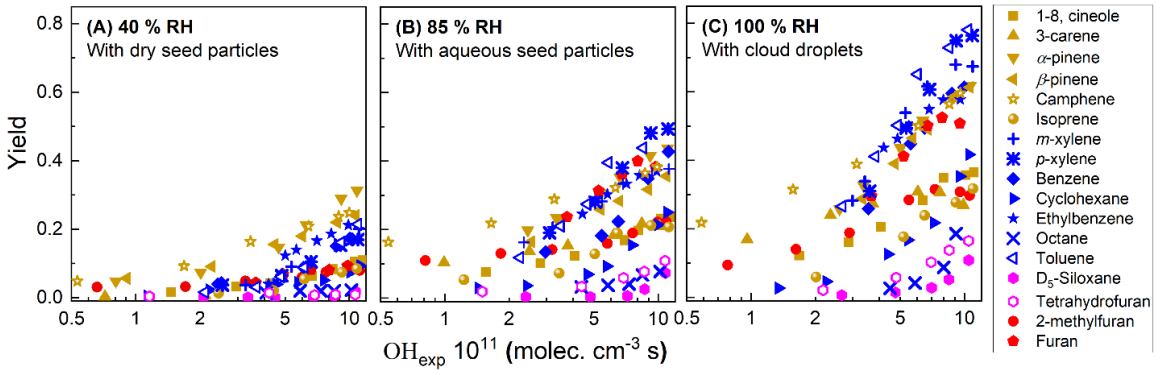

Figure 4.6: SOA yield as a function of OH exposure (OH_{exp}) for VOCs from vehicle exhaust, biogenic, biomass burning and VCP, under the modes of (A) dry seed; 40 % RH (B) ALW; 85 % RH and (C) cloud; 100 % RH.

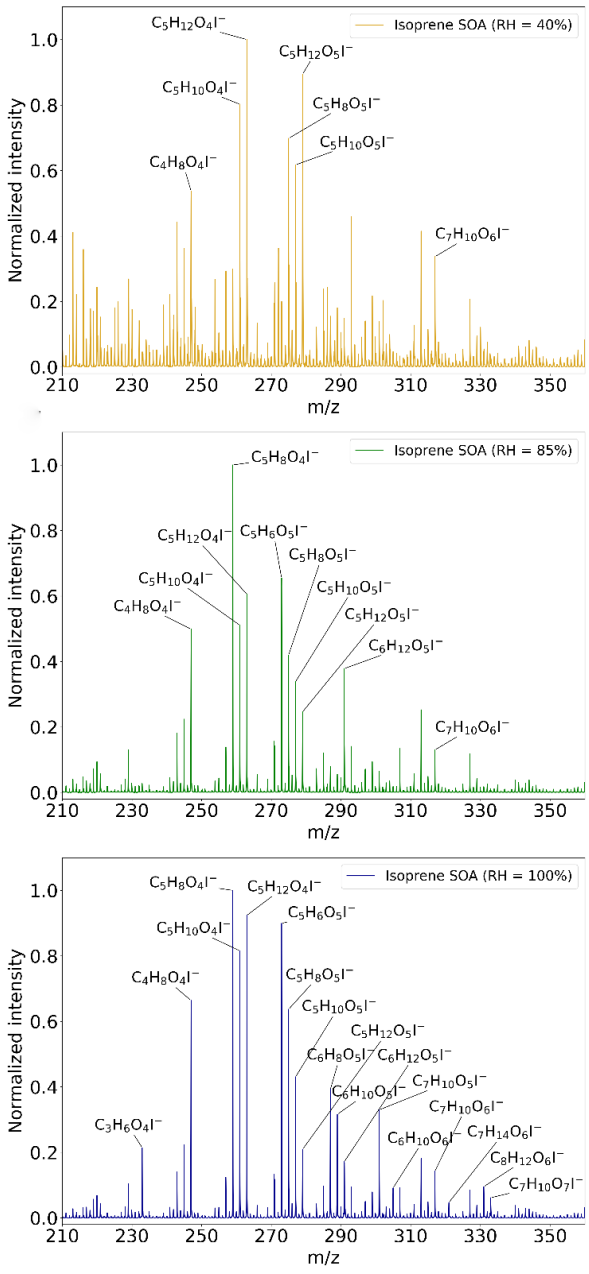

Figure 4.7: Relative contributions of different compounds to the total gas- and aqueous-phase SOA of isoprene.

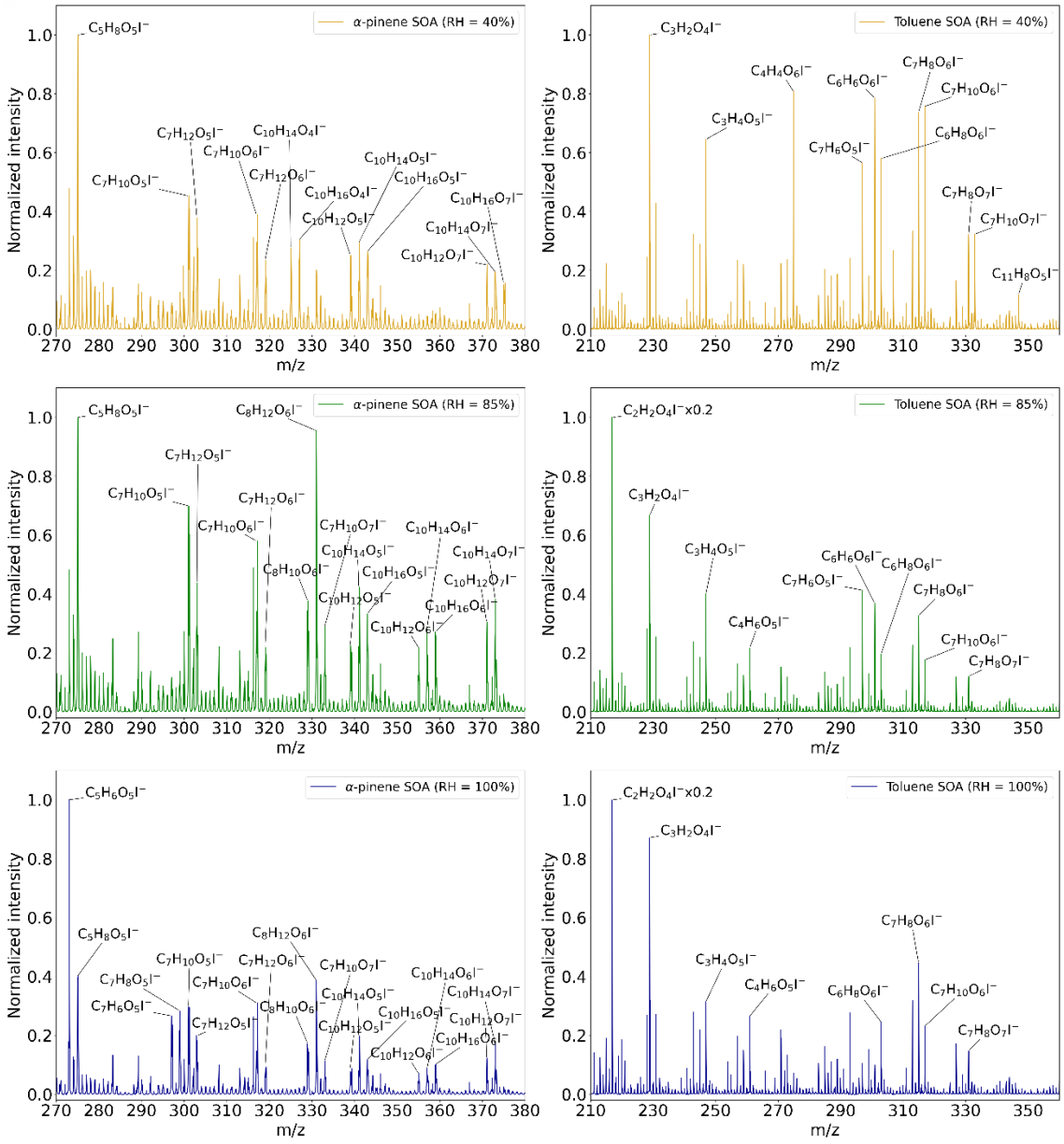

Figure 4.8: Relative contributions of different compounds to the total gas- and aqueous-phase SOA of *α*-pinene (left) and toluene (right).

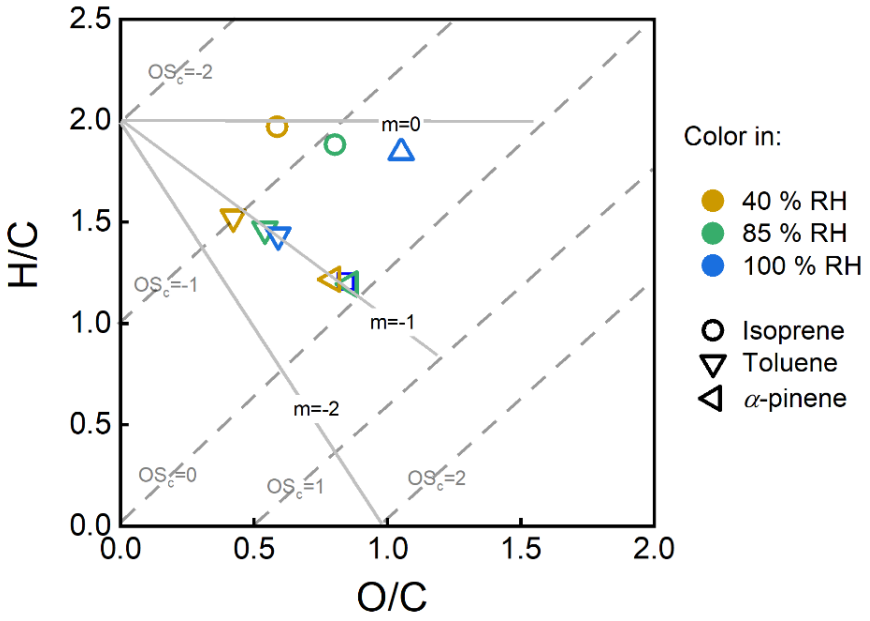

Figure 4.9: Aerosol oxygen-to-carbon (O/C) and hydrogen-to-carbon (H/C) ratios of oxidized product from *α*-pinene, isoprene and toluene.

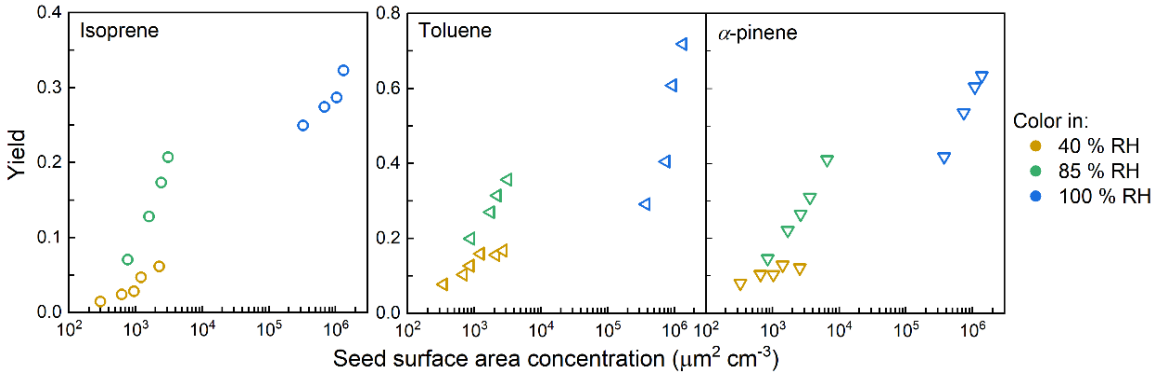

Figure 4.10: Calculated SOA mass yields from (left) isoprene, (middle) toluene and (right) *α*-pinene against the dried seed particle surface area.

5. Secondary Particulate Matter Formed in a Flow Reactor from Gas- and Aqueous-Phase Chemistry of Ambient Air in Riverside, California

5.1. Abstract

Ambient aerosol is a highly complex mixture of different-sized solid and liquid particles originating from both anthropogenic and natural sources. Secondary aerosol contributes a significant fraction of total aerosol in both urban and remote areas. However, identifying and quantifying the importance of specific precursors or precursor categories, such as volatile chemical products (VCP) and biogenic volatile organic compounds (VOCs) on measures of environmental and health-related impacts represent one of the most challenging areas of control of secondary aerosols. In addition, photochemical and aqueous-phase formation of secondary aerosol and its evolution under heavily polluted environments are far from being clearly understood. In this study, the Aerosol Production and Processing of Aerosols (APPA) OFR was operated continuously for one month to measure the amount and properties of secondary aerosol formed through both gas- and gas+aqueous-phase oxidation. A mini time-of-flight aerosol mass spectrometer (mAMS) and a scanning mobility particle sizer (SMPS) alternated sampling ambient and reactor. The reactor repeatedly stepped through a measurement matrix that included two levels of OH exposure (corresponding to 5.9 -9.1 hours and 1.3-2.3 days atmospheric equivalent) and three levels of liquid water content (none, aerosol liquid water, and cloud). More

enhancement and variation of SOA mass formation was observed at the higher OH exposure level, with an average factor of 1.1 increase for gas-phase oxidation and a factor of 1.8 increase for aqueous-phase oxidation compared with ambient organic aerosol (OA). Compare with reactor SOA formed at low OH_{exp} level in the presence of dry seed particles, more secondary aerosols were formed under aqueous-phase oxidation with increasing liquid water content, with an average factor of 1.7 and 3.5 increase in the presence of aerosol liquid water and cloud droplets, respectively. Reactor SOA mass formed in the reactor was highest in the morning and night. The contribution of highly oxidized compounds to the organic mass was higher when aerosol liquid water and cloud droplets were present in the reactor than when only dry seed particles were. These results demonstrate the importance of aqSOA in urban environments and can help constrain SOA models.

5.2. **Introduction**

Atmospheric aerosols induce harmful changes to regional and global climates and have direct negative impacts on human health and visibility (Pandis et al., 1995; Seinfeld and Pandis, 2016). Aerosol could form through atmospheric processing as secondary aerosol (SA), which consists of inorganic species including nitrate (NO_3^-), sulfate (SO_4^{2-}), ammonium (NH_4^+) components, as well as organic components (SOA) (Hallquist et al., 2009; Chen et al., 2019). Secondary organic aerosol is a dominant component of secondary aerosols that is formed by gas-phase photochemistry of volatile organic compounds (VOCs) reacted with atmospheric oxidants (ozone and hydroxyl radicals) to produce less-volatile functionalized compounds followed by partitioning into the aerosol phase (gasSOA) (Pankow, 1994; George et al., 2007; Jimenez et al., 2009). Several field studies in urban regions over the decades have observed large formation of secondary organic aerosol (SOA) that remained poorly captured by models (Volkamer et al., 2006; Dzepina et al., 2009; Hodzic et al., 2010; Hayes et al., 2015). The discrepancies between field observation and model simulation are proposed to explain by missing primary semi-volatile organics and missing processes, such as oligomerization, multigenerational chemistry, and especially aqueous chemistry (Baek et al., 2011; Cappa and Wilson, 2012; Jathar et al., 2015; Li et al., 2021). Among that, aqueous secondary aerosol formed when the semi-volatile compounds further oxidized in the gas phase and partition into the aqueous phase (aerosol water or cloud droplets), react, and form low volatility products that remains in the particle phase after the drop evaporates (Lim et al., 2010; Ervens et al., 2011; Richards-Henderson et al., 2014). An increasing number of experimental and modeling studies point

toward aqueous-phase chemistry as a significant missing pathway for SOA formation (Ervens and Volkamer, 2010; Matsunaga and Ziemann, 2010; Mcneill et al., 2012; El-Sayed et al., 2015; Sareen et al., 2016; Sareen et al., 2017; Peng et al., 2021). However, there is considerable uncertainty over the secondary aerosol formed through aqueous phase when implemented into global model, such as formation mechanisms, yield and its influences on aerosol properties (climate-relevant optical and hygroscopicity) (Pun and Seigneur, 2007; Hallquist et al., 2009; Youn et al., 2013; Ervens et al., 2014). Additionally, evaluating the production of secondary aerosol through aqueous-phase oxidation presents a substantial challenge. Not only because the formation of complex aerosol compounds governed by numerous oxidation reactions of a large number of organic species, but its evolution also vary for different environments with different precursor species, chemical compositions, particle concentrations and emission profiles (Kroll and Seinfeld, 2008; Aljawhary et al., 2016; Faust et al., 2017; Shrivastava et al., 2017; Chen et al., 2019).

Over the last decade or so, the use of oxidation flow reactors (OFRs) to study secondary aerosol formation in ambient air has grown rapidly because of their portability and their ability to provide high-time resolution measurements in dynamic environments than large-scale environmental chambers (George et al., 2007; Kang et al., 2007; Kroll and Seinfeld, 2008). Their fast response also makes them better suited than smog chambers for experiments probing the influence of a matrix of parameters on SOA formation (Lambe et al., 2011; Lambe et al., 2015; Xu and Collins, 2021). Several studies have reported on SOA formation from the OH oxidation of ambient air under field condition by using the oxidation flow reactor (Ortega et al., 2013; Palm et al., 2016; Palm et al., 2017). However,

the use of OFRs has been almost exclusively focused on studying products and yields from gas-phase oxidation of VOCs with little or no liquid water present, to our knowledge. Hence, an improved technique of simulating atmospheric aqueous conditions is necessary, for estimating the atmospheric aqueous-phase oxidation processes and chemical properties of SA.

High pollution levels could be observed frequently in the LA basin, not only due to the meteorological conditions (e.g., the prevailing westerly wind), but also caused by the air ventilation in the surrounding mountain ranges. Several field campaigns have investigated the SOA formation and properties in the LA basin and demonstrated that SOA as a major fraction of total OA in the LA basin and the SOA production was greatly underestimated by the traditional model. (Docherty et al., 2008; Ortega et al., 2013; Docherty et al., 2011; Hersey et al., 2011). However, the production and properties of PM resulting from the presence of aerosol liquid water (ALW) and fogs/boundary layer clouds that are common in many areas of California are still poorly understood. Measurements of secondary aerosol production from oxidation of ambient air through gas-phase and aqueous-phase chemistry are needed, in order to better estimate how the production and properties of particulate matter (PM) varying when the presence of ALW and fog/boundary layer clouds exist in California.

In this study, we oxidized the ambient air with oxidant (O_3 and OH) in a newly developed multiphase oxidation flow reactor, to investigate the amount and properties of secondary aerosol formed through both gas- and aqueous-phase oxidation in Riverside,

CA. The SOA formed from the reactor through both gas- and aqueous-phase oxidation was firstly compared to ambient OA. The enhancement of organic aerosol (OA) with the presence of dry seed, aerosol liquid water and cloud droplets under different the photochemical ages was compared to that through gas-phase oxidation but low OH_{exp} level. The relative aqueous-to-gas enhancement of SOA was compared with that reported in the previous laboratory studies. We investigated the chemical composition of the SOA that was formed as a function of the amount of aerosol liquid water or droplets added in and oxidant exposure in the OFR. The results are used to characterize short-term variability in secondary aerosol precursors and to explore the roles of different formation pathways.

5.3. **Experimental Methods**

5.3.1. **Riverside Field Campaign**

The work in this study focuses on the measurements during the Riverside field spring campaign. The measurement period for the spring campaign is 15 March-7 April 2022, hereafter referred to as the "sampling period". The research site was located at the Center for Environmental Research and Technology (CE-CERT) in Riverside, CA. The Riverside site is a great representative of the inland empire region of southern California, where high concentrations of primary and secondary particular matters blown by the prevailing westerly winds have been observed frequently. Additionally, Riverside is downwind of Los Angeles (satellite image is shown in Figure 5.1) where brings significant influences from emissions associated with the good movement industry. The study site CE-CERT is 2.5 km away from I-215, such that freeway emissions may impact concentrations of particulate matter and pollutant gases. Detailed of meteorological conditions, such as winds speed of the study site, are summarized in Figure 5.10.

Figure 5.1: Location map of Riverside (left) and study area (CE-CERT, right).

5.3.2. **Instrumentation Setup**

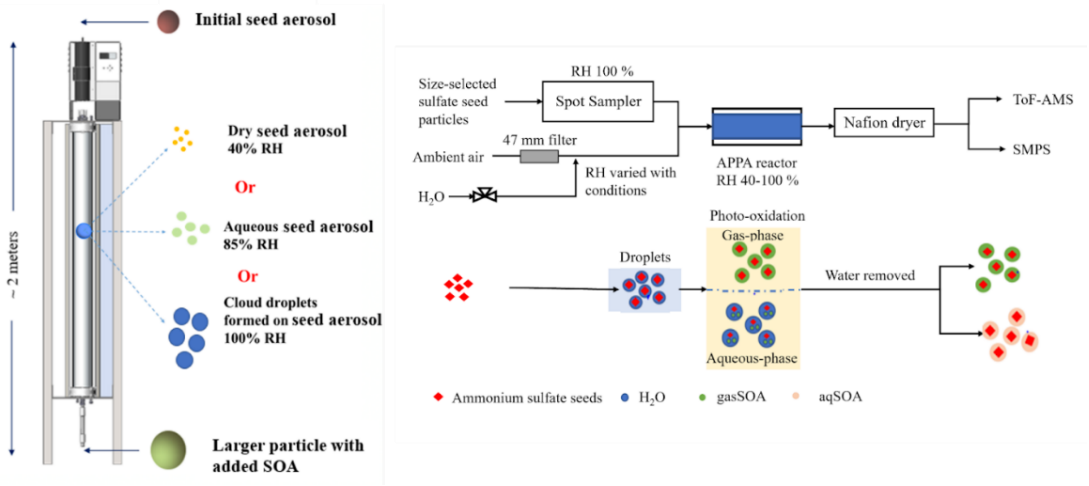

Figure 5.2: Schematic of the Accelerated Production and Processing of Aerosol (APPA) reactor.

The OFR used in this study was the Accelerated Production and Processing of Aerosols (APPA) reactor, which was described in the previous study (Xu et al., 2022). Unlike the previous studies, APPA reactor is a multiphase system that can not only be used

for gas-phase aerosol formation (Kang et al., 2007; Lambe et al., 2015; Peng et al., 2015; Palm et al., 2016; Xu and Collins, 2021) but also simulates secondary products processed through aqueous-phase oxidation with the presence of aerosol liquid water and cloud droplets. Figure 5.2 shows the schematic of the APPA reactor, and the detailed operation was described in Chapter 3 Section 2.1. Basically, the APPA reactor is a cylindrical tube 148 cm L × 8.9 cm OD × 7.8 cm ID PFA Teflon tube with a total internal volume of 7.5 L and was operated with a residence time in 140 s. During the Riverside field campaign, ambient air was sampled through a 0.95 cm OD PFA Teflon tubing and then mixed with a gas mixture passed through the inlet-gas line containing O_3 and humidified zero air. Before the ambient air sampling through the inlet-gas line, ambient particles were removed by the 47 mm PTFE membrane filter. The monodisperse ammonium sulfate seed particles are generated by atomizing a 0.15 M aqueous $(NH_4)_2SO_4$ solution with an atomizer (TSI Inc., Model 3076), drying with a diffusion dryer consisting of a perforated tube surrounded by molecular sieve pellets, and size classifying with a high flow differential mobility analyzer (DMA) (Stolzenburg et al., 1998). The generated monodisperse ammonium sulfate seed particles are injected for all experiments and the particle diameter used for the whole sampling period is 0.1 μm. For the mode with minimal liquid water present (RH = 40 %), the seed particles are directly introduced through the inlet-aerosol line. While for the mode with aerosol liquid water (RH = 85 %), and for simulated in-cloud conditions (RH = 100 %), the seed particles travel through a modified Spot Sampler (Aerosol Devices, Inc., Model 110A) to grow into droplets with a mean diameter of around 3.3 μm. The generated droplets are proposed to mix rapidly efficiently with gas mixture and then entered to the

reactor for further reaction. All temperatures (gas and particle lines, reactor cell) are precisely controlled, such that the resulting relative humidity in the reactor is adjusted between 40 % to 100 % RH. OH radicals were produced in situ inside the OFR by the photolyzed of ozone that externally generated by an ozone generator (Jelight Co., Inc., Model 610). Approximately 15 % of the added ozone was loss between the top and bottom of the reactor by the 254 nm-emitting germicidal UV bulbs to produce OH radicals for all experiments. The OH_{exp} was estimated from the method provided in the previous studies (Peng et al., 2015; Peng and Jimenez, 2019; Xu et al., 2022).

5.3.3. **Sampling Modes**

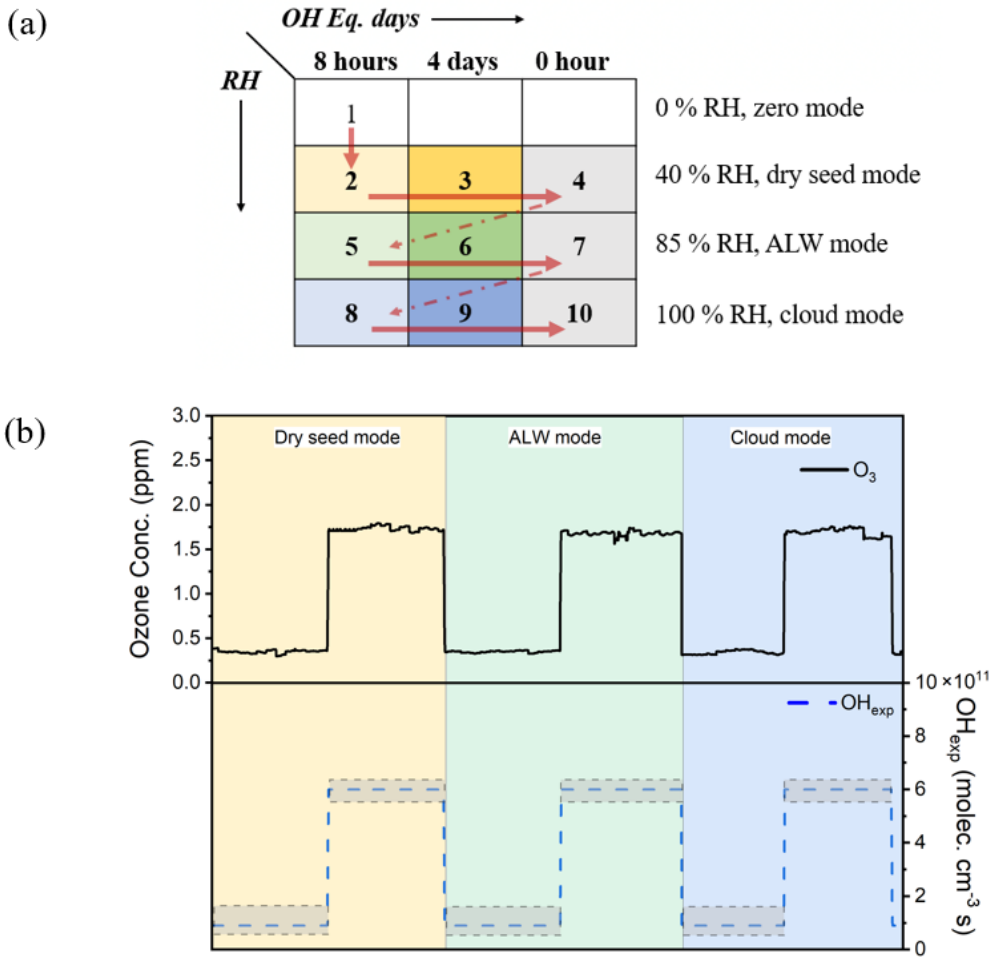

Figure 5.3: (a) Approximate repeating measurement sequences for the sampling periods. (b) A typical OFR sampling cycle, including two steps in ozone concentration and three steps in RH modes in the reactor, grey background indicates the estimated OH_{exp} with external OH reactivity about 6-15 s^{-1}.

To investigate secondary aerosol formation varied with photochemical age and aerosol liquid water or cloud droplets concentration, the OFR was operated with three RH modes. We report the production of SOA from OH-oxidation of ambient air with minimal

liquid water present (dry seed; RH = 40 %), with aerosol liquid water (ALW; RH = 85 %), and for simulated in-cloud conditions (cloud; RH = 100 %), hereafter refer to dry seed, ALW, and cloud mode, respectively. Figure 5.3a shows the repeating measurement sequences during the whole campaign. Zero mode (0 % RH) is specified for switching from cloud mode to dry seed mode, which includes a few minutes of flushing with 10 L min^{-1} dry air after the cloud mode measurements to ensure no liquid water remains on the reactor walls. OH radicals were produced in situ inside the APPA reactor using two different ozone concentration. As shown in Figure 5.3b, the ozone mixing ratio measuring from the outlet of the reactor is 350 ppb and 1.7 ppm, respectively.

The total OH reactivity measured during the CalNex-LA campaign, which ranged from 5 to 70 s^{-1} (Hansen et al., 2021). In our study, we introduced an additional reactant and reaction were included in KinSim chemical kinetics solver, in order to retain external OH reactivity ranged from approximately 6 to 15 s^{-1} that without directly affecting any other species. The two selected OH_{exp} are approximately 0.71 -1.61 × 10^{11} molec. s cm^{-3} and 3.31-6.13 × 10^{11} molec. s cm^{-3}, which is equivalent to 13.1 -31.1 hours and 2.6-4.7 days photochemical age, hereafter refer to low and high OH_{exp} level, respectively. The time needed to complete one cycle was kept as short as possible (∼2h), limited by the number of steps, the residence time of sampling tubing and resolution of SMPS and other instruments. For each five-measurement cycle, dark reactor measurement (only ozone and no UV light) was involved prior to next measurement cycle, to get the background seed concentration without secondary mass produced.

5.3.4. **Particle and Gas Measurements**

Ambient and reactor SOA particle size distribution from 0.02 to 0.5 micrometer (μm) diameter (D_p) was measured by a scanning mobility particle sizer (SMPS, fabricated in-house) with two 4min scan every 8 min. The SMPS consisted of a customized Differential Mobility Analyzer (DMA) column, and a 3762 Condensation Particle Counter (CPC). It was operated with sheath and aerosol flow rates of 20.0 and 1.5 Lmin−1, respectively.

The composition of non-refractory aerosol particles in the submicron range were measured with an Aerodyne compact time-of-flight aerosol mass spectrometer (C-ToF-AMS; (Drewnick et al., 2005). A system of automated valves controlled by a custom automation program written in Labview (National Instruments, Inc.), was used to multiplex the AMS and SMPS to alternate between measuring ambient air and air oxidized in the OFR. Sampled air was dried to <30% RH upstream of the SMPS and AMS, using a Nafion membrane drier ((Perma Pure, Model PD-070- 18T). C-ToF-AMS is equipped with a compact time-of-flight mass spectrometer (C-ToF) and a chopper wheel for obtaining speciated mass distributions (Bahreini et al., 2003; Canagaratna et al., 2007). During sampling period, Mass concentrations and mass distributions of submicron, non-refractory sulfate, nitrate, chloride, ammonium, and organic aerosol (OA) can be obtained every 15 seconds (Allan et al., 2003; Allan et al., 2004). The uncertainty in the measured mass concentrations is estimated to be ~34-38% (Bahreini et al., 2009). Higher-resolution analysis of the OA spectra obtained by C-ToF-AMS is used for providing information on

the oxidation state and the relative contribution of purely hydrocarbon vs. oxygenated hydrocarbon ions to the signal at each fragment (i.e., $C_xH_y^+$ vs. $C_xH_yO_z^+$, where x, y, and z are positive integers).

5.4. **Results and Discussions**

5.4.1. **Ambient vs. Reactor OA Observation**

The time series of the ambient component mass concentration during the sample period is shown in Figure 5.4a. Here, each ambient data point represents three-hour average. Most of the measurement period is characterized by OA dominance, while the last week of the period (April 1st to April 6th) is characterized by high concentrations of OA and nitrate, and ammonium. Considering the site location that affected by the in-basin pollution, we expected the precursors that contributes most to the SOA formation are alkanes, aromatic VOCs and semi-volatile species. A 48-hour snapshot of the ambient data is shown in Figure 5.4b. This period shows the diurnal variation observed from 25 to 27 March 2022. Ambient nitrate concentrations peak in early morning hours before sunrise and later afternoon, while OA peaked prior to the nitrate peak. Compared with Ortega et al. (2016), the nitrate peaked around the same time, while their OA peaks were in the late afternoon. This is probably due to the study site experiences a strong impact from the aged urban emissions from Los Angeles and it took longer for the LA plume transporting to our study site. In addition, ambient species mass concentration may be affected by the meteorology conditions (shown in Figure 5.10). The time series of the reactor organic aerosol and nitrate mass concentrations during the sample period is shown in Figure 5.11-

Figure 5.13. During first one third of the sampling period, inorganic nitrate components were enhanced in the reactor. It may be due to NOx in ambient air (Figure 5.14) is expected to be oxidized to HNO_3 by the OH in the reactor and can then condense onto the aerosols (together with ambient NH_3 for HNO_3).

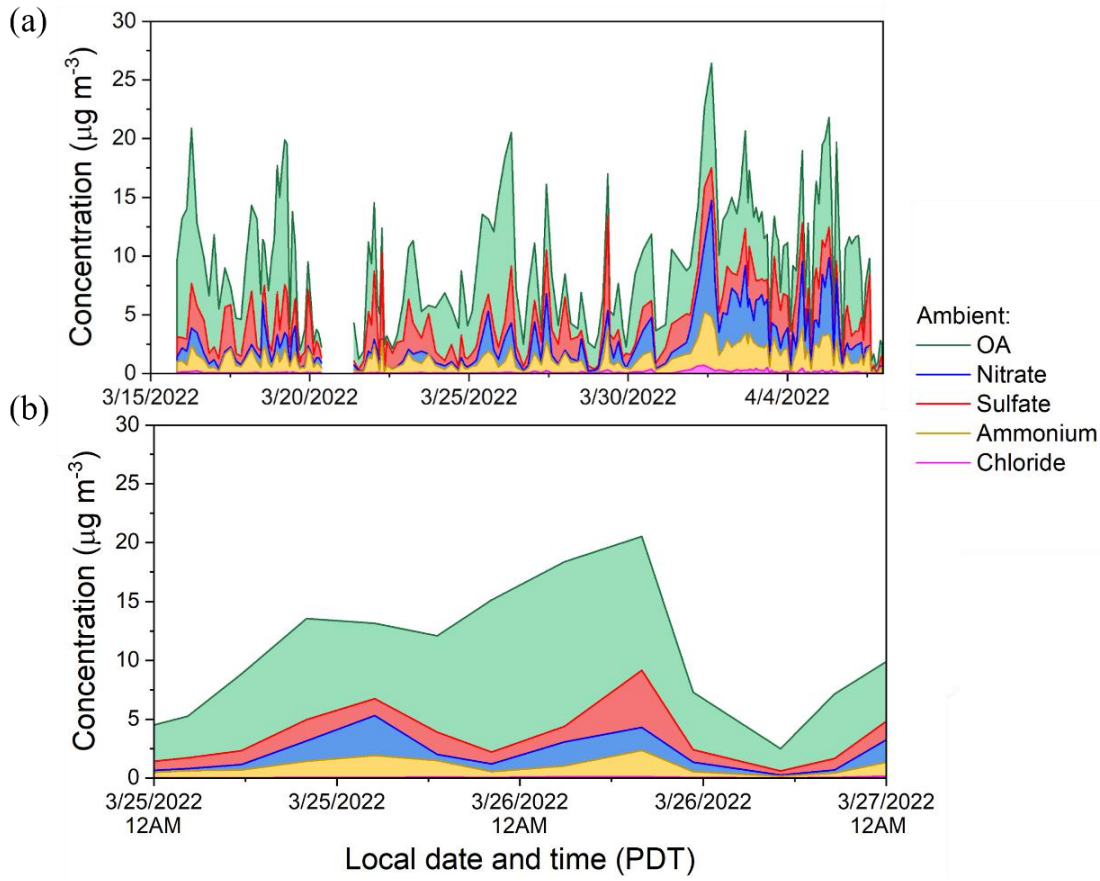

Figure 5.4: (a) Time series of ambient component mass concentrations during the sampling period. (b) Zoom on the time series of the species mass concentrations for 2 representative days.

The relative OA enhancement ratio (ER_{OA} =reactor SOA/ambient OA) for the whole sampling period is plotted vs. OH_{exp} and RH modes in Figure 5.5. Here, we split each day to three 6-hour intervals, and named as morning (4 am-10 am), afternoon (2 pm-

8 pm) and night (10 pm-4 am), respectively. The SOA mass generated inside the reactor didn't follow the trend of the ambient OA. Note that we filtered out all of the ambient particle and only the ambient precursors were sampled through the reactor, so that the trend of OA enhancement compare with the ambient particle may not exist. More variation has been observed under high OH_{exp}. For dry seed mode (40% RH), a smaller enhancement was observed under low OH_{exp} , with an increase up to ~ 5 μg m^{-3}, or a factor of 0.55 × of ambient. Higher OA mass was observed under 4 days of OH aging, which closely overlap with the ambient particle mass. For aerosol liquid water (ALW) mode, the ER_{OA} trends of morning and night are similar compared to that under gas-phase oxidation, but OA was more enhanced from reactor aging in all three cases by an average factor of 2.2 × of ambient and 2.0 × of ambient, for 0.3 and 4 days of OH aging, respectively. Less OA enhancement with the presence of cloud droplets compared to that with the aerosol liquid water, with a factor of 1.8 × of ambient and 1.9 × of ambient, for 0.3 and 4 days of OH aging.

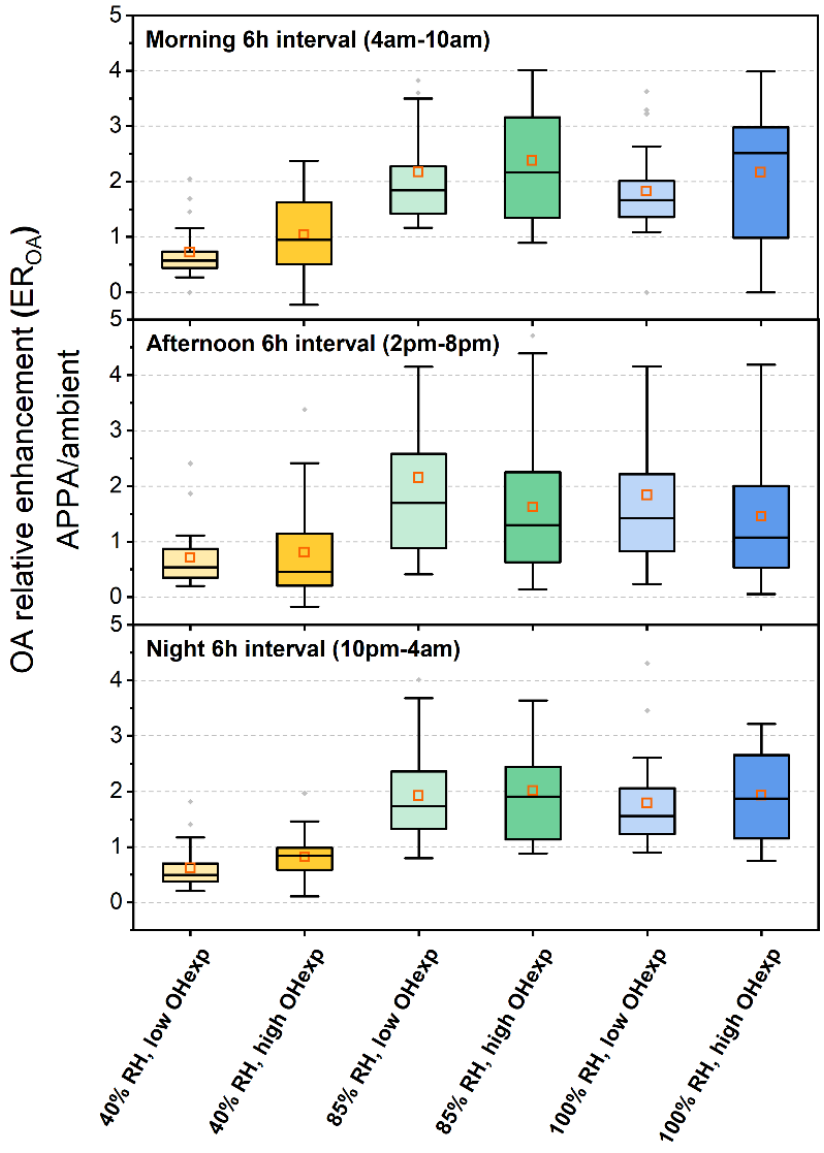

Figure 5.5: Relative OA enhancement (ER_{OA} =reactor OA/ambient OA) vs. estimated reactor photochemical age and sample modes for selected 6-hour interval period of (top) morning (4 am- 10 am), (middle) afternoon (2 pm- 8 am) and (bottom) night (10 pm- 4 am).

5.4.2. **Reactor OA Enhancements Through Gas- and Aqueous-Phase Oxidation**

The relative OA enhancement (ER_{OA}= reactor OA/40% low OH_{exp} OA) compared to gas-phase oxidation (40% low OH_{exp}) for selected 6-hour interval period is shown in Figure 5.6**.** Here, we compared all of the other modes to the 40% low OH_{exp}, to estimate the net OA enhancement factor happened inside the reactor. Under gas-phase oxidation, more OA enhancement has been observed at higher OH_{exp} under morning and night with an average factor of increase of 1.8 × of low OH_{exp}, due to efficient condensation of semi volatile and low-volatility oxidation products generated in the APPA. While smaller enhancement was observed in the afternoon, with an average factor of increase of 1.4× of low OH_{exp}. In previous studies located at Pasadena and Bakersfield (Lindinger et al., 1998; Gentner et al., 2012; Liu et al., 2013; Ortega et al., 2013; Fast et al., 2014), isoprene, terpene, large alkanes, and methyl-vinyl-ketone + methacrolein (MVK+MACR) originate primarily from biogenic emissions, toluene and formaldehyde are associated with anthropogenic emissions were measured. The difference between morning and afternoon enhancements probably because those measured ambient precursor (aromatics, long-chain alkanes and terpenes) accumulated at night due to the absence of photochemistry, while during the afternoon reactive precursors in ambient air are depleted due to reaction with OH. Hayes et al., (2013) suggested that the dominant precursor source takes roughly 0.5 days from downtown LA to Pasadena, with the ambient photochemical age reaching around 0.3 days. SOA production in the reactor becomes more limited, likely due to the depletion of reactive SOA precursors in ambient air. Overall, this enhanced SOA formation in OFR has also been found in the other OFR field studies in both in urban and forest

environments and larger SOA formation potential formed from precursors at night. (Ortega et al., 2013; Palm et al., 2016; Palm et al., 2017; Saha et al., 2018).

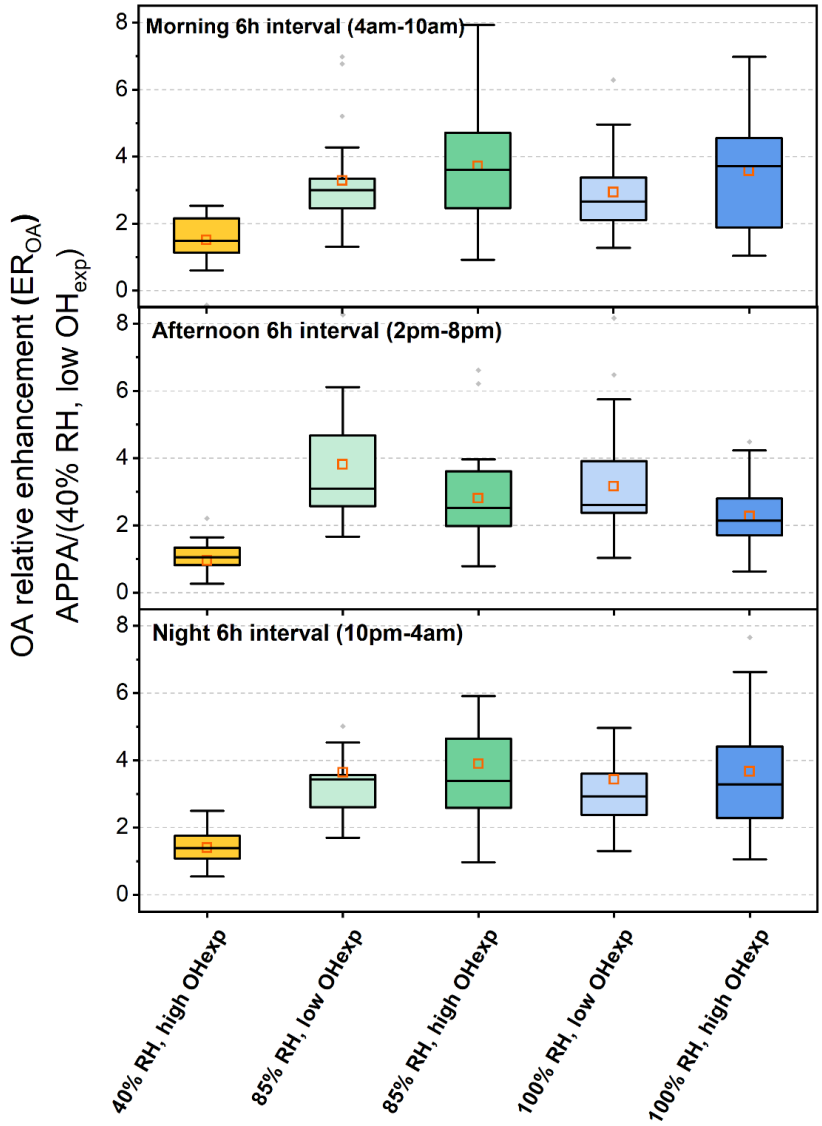

Figure 5.6: Relative OA enhancement (ER_{OA} =reactor SOA/40% low OH_{exp} OA) vs. estimated reactor photochemical age and sample modes for selected 6-hour interval period of (a) morning (4 am- 10 am), (b) afternoon (2 pm- 8 am) and (c) night (10 pm- 4 am).

With the presence of aerosol liquid water, we observed a significant amount of aerosol formed through aqueous phase. For morning and night, the trend is consistent with that under gas-phase oxidation, with an average factor of 3.3× of 40 % low OH_{exp}, 3.9× of 40 % low OH_{exp} under low OH_{exp} and high OH_{exp}, respectively. Additionally, more variations have been observed under higher OH_{exp}, ranging from 1.5 to 8 × of 40 % RH low OH_{exp} in the morning, this is probably related to the composition of the ambient precursor. However, a opposite trend compared to the other two period was observed, which the high OH_{exp} OA enhancement is lower than that at low OH_{exp}, this is probably because the ambient precursors oxidized by the photochemical reaction, so that fragmentation occur in the gas-phase reaction of SVOCs with OH, leading to non-condensable products and decreasing SOA formation. Fragmentation can also be due to heterogeneous oxidation of reactor SOA, producing more volatile species that may evaporate, leading to OA mass loss. Under cloud mode, similar trend has been observed compare with that in the presence of aerosol liquid water, with a smaller enhancement of a factor of 3 and 3.5 × of 40 % low OH_{exp} under low OH_{exp} and high OH_{exp}, respectively. The effects of aerosol liquid water/cloud droplets and aqueous-phase processing on SOA formation and oxidation degrees during the sampling periods are further illustrated in Figure 5.15. Here, we compared all of the other modes to the 85% low OH_{exp}, to estimate the net SOA enhancement factor happened inside the reactor varying with photochemical age and when the cloud droplet exists. Compared with aqueous-phase oxidation in the photochemical age of 5.9-9.1 hours at 85 % RH, higher OA enhancement was observed at morning with the presence of liquid water or cloud droplets, with a smaller enhancement

of a factor of 1.2, 0.95 and 1.3 × of 85 % low OH_{exp} under 85 % high OH_{exp}, 100 % low OH_{exp} and 100 % high OH_{exp}, respectively. In the afternoon compare with 85% low $OH_{exp,}$ the OA mass decreases as the OH_{exp} increase at both with the presence of aerosol liquid water and cloud droplets, which indicates a faster fragmentation that is associated with photochemical processing. Xu et al. (2016) observed a gradual decrease of MO−OOA/LO−OOA and O/CSOA showed as O_x increased at both low and high RH levels caused by the faster formation of LO− OOA than MO−OOA that is associated with photochemical processing. For better link to the laboratory test, here we compared the laboratory test (Chapter 4) with the ambient test, the equal age of 8 hours test was selected to better compare the OH relative enhancement, which is shown in Figure 5.7. Overall, we observed a less OA enhancement during the ambient sampling period than that with selected water insoluble precursors under both 85 % and 100 % RH. With the presence of aerosol liquid water, the ambient OA enhancement decreased by a factor of 0.8 × of laboratory VOCs, while OA decreased by a factor of 0.5 × of laboratory VOCs under cloud conditions.

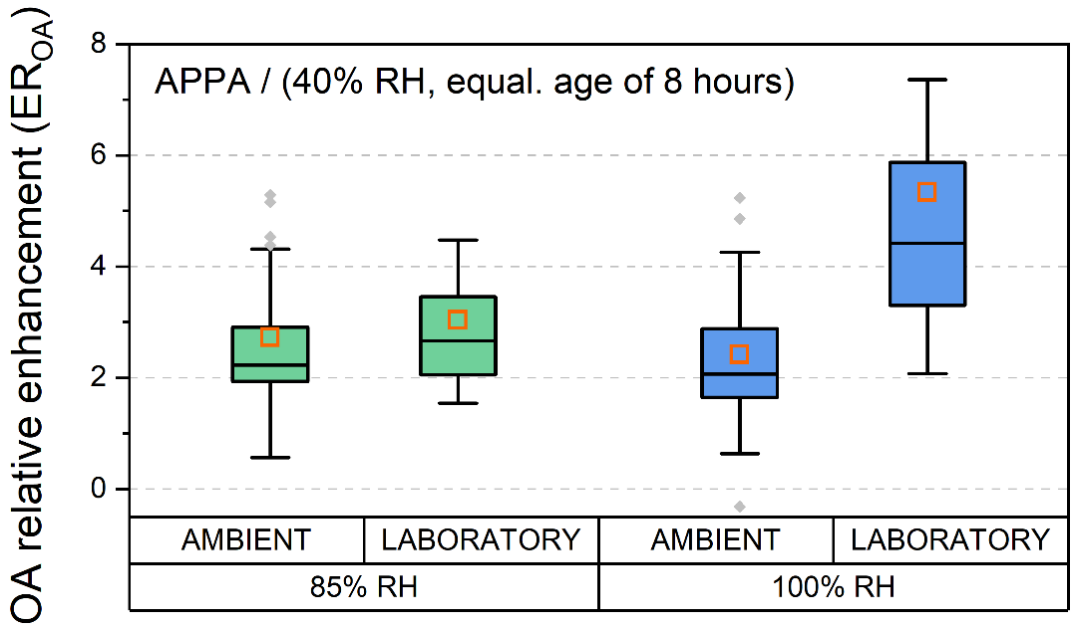

Figure 5.7: Relative OA enhancement (ER_{OA} =reactor SOA/40% low OH_{exp} OA) under aqueous-phase oxidation compare with laboratory measurements.

5.4.3. **OA Chemical Composition and Evolution**

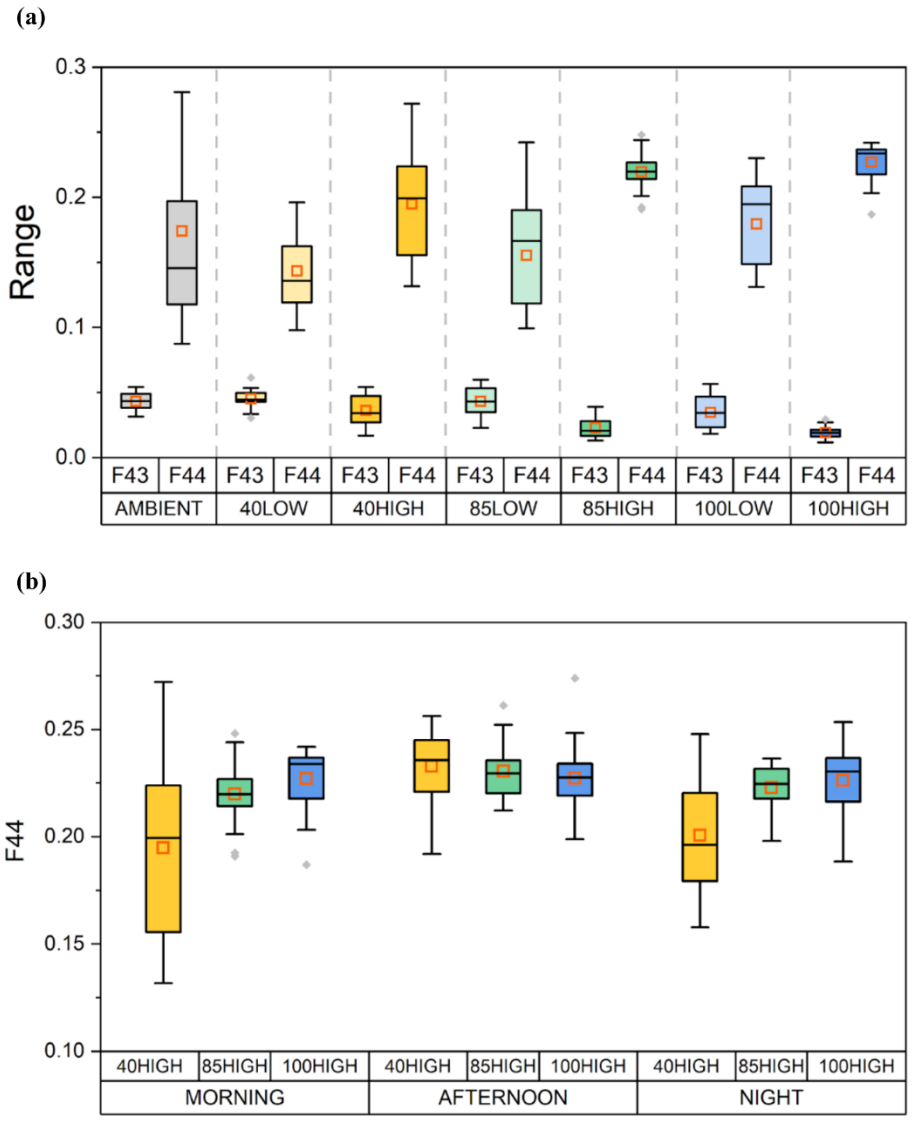

Figure 5.8: (a) Fractional contribution of m/z44 (f_{44}) vs. m/z43 (f_{43}) to OA for the ambient and reactor data in this work. (b) m/z44 (f_{44}) under equivalent photochemical age of 4 days, data separated by the 6-hour interval.

The evolution of OA chemical composition varies with aging and relatively humidity has been reported in several studies under both ambient and reactor conditions (Kroll et al., 2011; Ortega et al., 2013; Tkacik et al., 2014; Lambe et al., 2015). AMS fragments f_{44} (fractional organic contribution at m/z44, mostly CO_2^+) and f_{43} (fractional organic contribution at m/z43, mostly $C_2H_3O^+$) are often used as a tracer for aged OA, and POA or freshly formed SOA, respectively (Ng et al., 2011a). The f_{43} and f_{44} data for all modes are shown in Figure 5.8. In Figure 5.8a, the average f_{44} and f_{43} during the ambient sampling period is 0.17 and 0.05, respectively. Ng et a; (2010) summarized the ambient oxygenated organic aerosols (OOA) from analysis of 43 Northern Hemispheric AMS field datasets. Aiken et al. (2009) identified a single OOA factor having a moderate degree of oxidation (f_{44} = 0.14). For comparison, A wide range of f_{44} and a continuum of OOA properties from ambient PMF-derived SVOOA, and LV-OOA are shown from Ng et al. (2010). The average f_{44} for SV-OOA components are 0.07±0.04, while those for the LV-OOA components are 0.17±0.04. And Docherty et al. (2011) reported that a comparable f_{44} ratio (0.15) sampled from ambient aerosol in Riverside, California during the 2005 Study of Organic Aerosols at Riverside (SOAR). We find that the f_{44} ratio (0.17) is slightly higher than corresponding values for comparable components reported from studies at Riverside and Pasadena sites but is similar to comparable component here by combining LV-OOA and SV-OOA identified here.

Reactor SOA formed through gas -phase oxidation evolve as f_{44} increases and f_{43} decreases with photochemical age stepping from 8 hours to 4 days, consistent with previous ambient field observations from multiple field campaigns (Ng et al., 2010, Ortega et al.,

2016). The average f_{44} for 40 % RH low OH_{exp} are 0.14±0.04, while those for the high OH_{exp} components are 0.19±0.05. As excepted, the reactor f_{44} at high OH_{exp} level have the higher $f_{44,}$ consistent with previous ambient field observation from multiple field campaigns (Ng et al., 2010; Ortega et al., 2013). Additionally, reactor data with the presence of aerosol liquid water and cloud droplets have the higher f_{44} compared to that with gas phase only oxidation. The average f_{44} and f_{43} for 85 % low OH_{exp} is 0.15±0.05 and 0.04±0.02, respectively. Compare with 85 % low OH_{exp}, the average f_{44} increased to 0.22±0.02 5 and average f_{43} decreased to 0.02±0.01under 85 % high OH_{exp}. With the presence of cloud droplets, the f_{44} was further increasing to 0.17±0.05 and 0.24±0.02 for low OH_{exp} and high OH_{exp}, respectively. Lim et al. (2010) stated that the increase in m/z 44 arises from the major condensed-phase oxidation products, glyoxylic and oxalic acids, under fog- and cloud-relevant glyoxal concentrations. Kroll et al. (2011) found that aqueous oxidation of SOA materials in the presence of glyoxal leads to the production of highly oxidized, LV-OOA-like SOA. Feng et al. (2022) found that OA is more oxidized in pollution events with a higher ratio of f_{44}/ f_{43} (1.90 ± 0.54) and plumes with highly oxidized OA were strongly correlated with the high concentration of aerosol water content. We also separated the data with morning afternoon and night, which is shown in Figure 5.8b. The morning and night trends are similar, with the f_{44} increase with the amount of liquid water added in. We observed a different trend in the afternoon, with the f_{44} under gas phase oxidation is higher than that under aqueous phase oxidation.

Figure 5.9 shows the chemical composition of the reactor SOA measured by m-AMS. Box chart shows organic-related fragments (grouped as C_x, $C_xH_y^+$, $C_xH_yO^+$,

$C_xH_yO_z^+$, where x, y, z≥ 1). With morning 6-hour interval from gas-phase oxidation to aqueous phase reactions, C_xH_y+ fraction decreased from 22% to 17% and $C_xH_yO_1^+$ decreased from 26% to 19%, while $C_xH_yO_{>1}^+$ fraction went up from 28% to 32%. The fractions of $C_xH_y^+$ and $C_xH_yO_1^+$ further decreased to 15% and 17% respectively, and $C_xH_yO_{>1}^+$ fraction increased to 34% with the presence of cloud droplets. We infer that ambient precursor was further oxidized to other highly-oxidized and oxygenated compounds when aerosol liquid water or fog/cloud present.

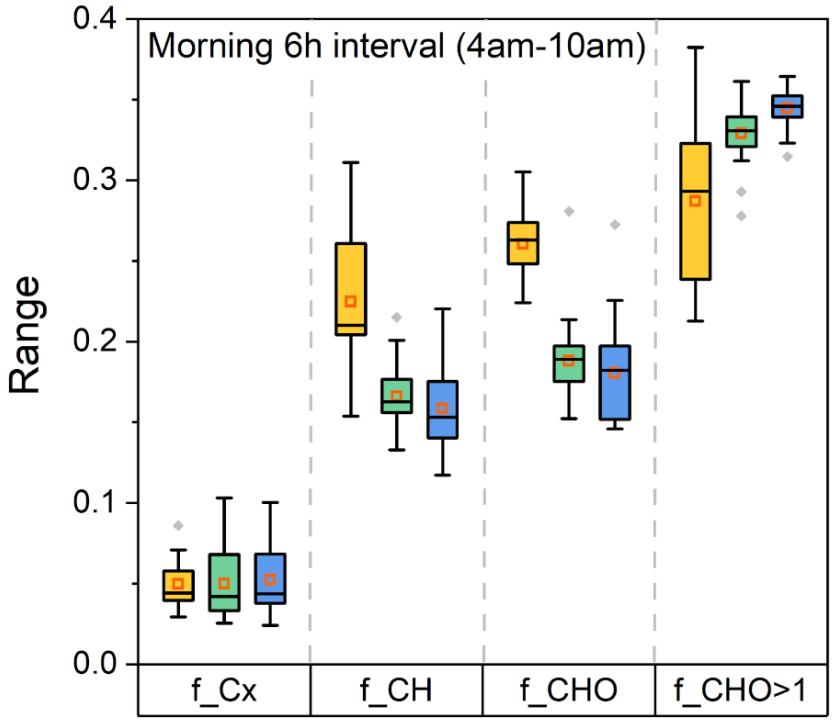

Figure 5.9: Chemical composition of the reactor OA measured by m-AMS. Box chart shows organic-related fragments (grouped as C_x, $C_xH_y^+$, $C_xH_yO^+$, $C_xH_yO_z^+$, where x, y, z≥ 1).

5.5. **Summary**

Real-time measurement of ambient SA formation and OA aging from ambient precursors was carried out with a multiphase oxidation flow reactor coupled to an AMS and SMPS during the Riverside field campaign and targeted urban emissions. This work represents the first application of an oxidation flow reactor to investigate SOA formation under aqueous-phase oxidation from ambient urban air. Compared to ambient aerosol measurements, no clear trend has been observed for all modes in this study, because only ambient precursors are sampled through the reactor and involved into oxidation reactions. Secondary aerosol formed through both gas- and aqueous-phase oxidation was found to be strongly depending on the photochemical age and the presence of aerosol liquid water or cloud droplets. As the photochemical age increases, the secondary aerosol mass increases since the chemistry is still dominated by functionalization instead of heterogeneous oxidation that leading to fragmentation. As the amount of liquids water added in, significant organic aerosol mass has been observed, which implies that the aerosol liquid water could facilitate the vapor-to-particle partitioning to form SOA or the reactions are facilitated under more aqueous environments. High OA enhancement was observed at morning and night than that at afternoon with the presence of dry seeds, aerosol liquid water and cloud droplets, which is probably related to the composition of the ambient precursor. In the afternoon, the OA mass decreases as the OH_{exp} increase at both with the presence of aerosol liquid water and cloud droplets, which indicates a faster fragmentation that is associated with photochemical processing.

The chemical evolution of SOA in the reactor was examined in this study with the AMS fractional organic contribution at m/z44 and m/z43 (f_{44} and f_{43}). Reactor gas-phase oxidation data evolve as f_{44} increases and f_{43} decreases with photochemical age stepping from 8 hours to 4 days, consistent with previous ambient field observations from multiple field campaigns. As the amount of the liquid water or cloud droplets increases, the f_{44} increases at morning and night, which indicates that highly oxygenated and high molecular weight species formed. While an opposite trend has been observed in the afternoon, with the f_{44} in gas phase is higher than that under aqueous phase oxidation, this is probably because that water soluble precursor and its oxidation product are fully reacted in the atmosphere.

This study shows that capability of APPA reactors on continuedly ambient field studies, as they allow real-time measurement of secondary aerosol formation through gas and aqueous-phase oxidation across a wide range of photochemical ages. Continuous ambient air sampling through the APPA reactor provides complementary information to the analysis of ambient data and also provide insights of secondary aerosol formation under aqueous phase oxidation. Additionally, these results help to constrain SOA models that restricted from the aqueous-phase secondary aerosol formation and to narrow the gaps between the measured and modeled SOA concentration. Future studies could guide by this study and investigate the secondary aerosol formation through aqueous-phase oxidation from different sources and regions.

5.6. **Reference**

Aljawhary, D., Zhao, R., Lee, A. K., Wang, C., and Abbatt, J. P.: Kinetics, mechanism, and secondary organic aerosol yield of aqueous phase photo-oxidation of α-pinene oxidation products, The Journal of Physical Chemistry A, 120, 1395-1407, 2016.

Allan, J. D., Jimenez, J. L., Williams, P. I., Alfarra, M. R., Bower, K. N., Jayne, J. T., Coe, H., and Worsnop, D. R.: Quantitative sampling using an Aerodyne aerosol mass spectrometer 1. Techniques of data interpretation and error analysis, Journal of Geophysical Research: Atmospheres, 108, 2003.

Allan, J. D., Delia, A. E., Coe, H., Bower, K. N., Alfarra, M. R., Jimenez, J. L., Middlebrook, A. M., Drewnick, F., Onasch, T. B., and Canagaratna, M. R.: A generalised method for the extraction of chemically resolved mass spectra from Aerodyne aerosol mass spectrometer data, Journal of Aerosol Science, 35, 909-922, 2004.

Baek, J., Hu, Y., Odman, M. T., and Russell, A. G.: Modeling secondary organic aerosol in CMAQ using multigenerational oxidation of semi-volatile organic compounds, Journal of Geophysical Research: Atmospheres, 116, 2011.

Bahreini, R., Jimenez, J. L., Wang, J., Flagan, R. C., Seinfeld, J. H., Jayne, J. T., and Worsnop, D. R.: Aircraft-based aerosol size and composition measurements during ACE-Asia using an Aerodyne aerosol mass spectrometer, Journal of Geophysical Research: Atmospheres, 108, 2003.

Bahreini, R., Ervens, B., Middlebrook, A., Warneke, C., De Gouw, J., DeCarlo, P., Jimenez, J., Brock, C., Neuman, J., and Ryerson, T.: Organic aerosol formation in urban and industrial plumes near Houston and Dallas, Texas, Journal of Geophysical Research: Atmospheres, 114, 2009.

Canagaratna, M., Jayne, J., Jimenez, J., Allan, J., Alfarra, M., Zhang, Q., Onasch, T., Drewnick, F., Coe, H., and Middlebrook, A.: Chemical and microphysical characterization of ambient aerosols with the aerodyne aerosol mass spectrometer, Mass spectrometry reviews, 26, 185-222, 2007.

Cappa, C. D. and Wilson, K. R.: Multi-generation gas-phase oxidation, equilibrium partitioning, and the formation and evolution of secondary organic aerosol, Atmospheric Chemistry and Physics, 12, 9505-9528, 2012.

Chen, T., Liu, Y., Ma, Q., Chu, B., Zhang, P., Liu, C., Liu, J., and He, H.: Significant source of secondary aerosol: formation from gasoline evaporative emissions in the presence of SO 2 and NH 3, Atmospheric Chemistry and Physics, 19, 8063-8081, 2019.

Docherty, K. S., Aiken, A. C., Huffman, J. A., Ulbrich, I. M., DeCarlo, P. F., Sueper, D., Worsnop, D. R., Snyder, D. C., Peltier, R., and Weber, R.: The 2005 Study of Organic Aerosols at Riverside (SOAR-1): instrumental intercomparisons and fine particle composition, Atmospheric Chemistry and Physics, 11, 12387-12420, 2011.

Docherty, K. S., Stone, E. A., Ulbrich, I. M., DeCarlo, P. F., Snyder, D. C., Schauer, J. J., Peltier, R. E., Weber, R. J., Murphy, S. M., and Seinfeld, J. H.: Apportionment of primary and secondary organic aerosols in Southern California during the 2005 Study of Organic Aerosols in Riverside (SOAR-1), Environmental science & technology, 42, 7655-7662, 2008.

Drewnick, F., Hings, S. S., DeCarlo, P., Jayne, J. T., Gonin, M., Fuhrer, K., Weimer, S., Jimenez, J. L., Demerjian, K. L., and Borrmann, S.: A new time-of-flight aerosol mass spectrometer (TOF-AMS)—Instrument description and first field deployment, Aerosol Science and Technology, 39, 637-658, 2005.

Dzepina, K., Volkamer, R. M., Madronich, S., Tulet, P., Ulbrich, I. M., Zhang, Q., Cappa, C. D., Ziemann, P. J., and Jimenez, J. L.: Evaluation of recently-proposed secondary organic aerosol models for a case study in Mexico City, Atmospheric Chemistry and Physics, 9, 5681-5709, 2009.

El-Sayed, M. M. H., Wang, Y., and Hennigan, C. J.: Direct atmospheric evidence for the irreversible formation of aqueous secondary organic aerosol, Geophysical Research Letters, 42, 5577-5586, 10.1002/2015gl064556, 2015.

Ervens, B. and Volkamer, R.: Glyoxal processing by aerosol multiphase chemistry: towards a kinetic modeling framework of secondary organic aerosol formation in aqueous particles, Atmospheric Chemistry and Physics, 10, 8219-8244, 2010.

Ervens, B., Turpin, B., and Weber, R.: Secondary organic aerosol formation in cloud droplets and aqueous particles (aqSOA): a review of laboratory, field and model studies, Atmospheric Chemistry and Physics, 11, 11069-11102, 2011.

Ervens, B., Sorooshian, A., Lim, Y. B., and Turpin, B. J.: Key parameters controlling OH-initiated formation of secondary organic aerosol in the aqueous phase (aqSOA), Journal of Geophysical Research-Atmospheres, 119, 3997-4016, 10.1002/2013jd021021, 2014.

Fast, J., Allan, J., Bahreini, R., Craven, J., Emmons, L., Ferrare, R., Hayes, P., Hodzic, A., Holloway, J., and Hostetler, C.: Modeling regional aerosol and aerosol precursor variability over California and its sensitivity to emissions and long-range transport during the 2010 CalNex and CARES campaigns, Atmospheric Chemistry and Physics, 14, 10013-10060, 2014.

Faust, J. A., Wong, J. P., Lee, A. K., and Abbatt, J. P.: Role of aerosol liquid water in secondary organic aerosol formation from volatile organic compounds, Environmental science & technology, 51, 1405-1413, 2017.

Gentner, D. R., Isaacman, G., Worton, D. R., Chan, A. W., Dallmann, T. R., Davis, L., Liu, S., Day, D. A., Russell, L. M., and Wilson, K. R.: Elucidating secondary organic aerosol from diesel and gasoline vehicles through detailed characterization of organic carbon emissions, Proceedings of the National Academy of Sciences, 109, 18318-18323, 2012.

George, I., Vlasenko, A., Slowik, J., Broekhuizen, K., and Abbatt, J.: Heterogeneous oxidation of saturated organic aerosols by hydroxyl radicals: uptake kinetics, condensed-phase products, and particle size change, Atmospheric Chemistry and Physics, 7, 4187-4201, 2007.

Hallquist, M., Wenger, J. C., Baltensperger, U., Rudich, Y., Simpson, D., Claeys, M., Dommen, J., Donahue, N., George, C., and Goldstein, A.: The formation, properties and impact of secondary organic aerosol: current and emerging issues, Atmospheric chemistry and physics, 9, 5155-5236, 2009.

Hansen, R., Griffith, S., Dusanter, S., Gilman, J., Graus, M., Kuster, W., Veres, P., de Gouw, J., Warneke, C., and Washenfelder, R.: Measurements of Total OH Reactivity During CalNex-LA, Journal of Geophysical Research: Atmospheres, 126, e2020JD032988, 2021.

Hayes, P. L., Carlton, A. G., Baker, K. R., Ahmadov, R., Washenfelder, R. A., Alvarez, S., Rappenglück, B., Gilman, J. B., Kuster, W., and De Gouw, J. A.: Modeling the formation and aging of secondary organic aerosols in Los Angeles during CalNex 2010, Atmospheric chemistry and physics, 15, 5773-5801, 2015.

Hersey, S., Craven, J., Schilling, K., Metcalf, A., Sorooshian, A., Chan, M., Flagan, R., and Seinfeld, J.: The Pasadena Aerosol Characterization Observatory (PACO): chemical and physical analysis of the Western Los Angeles basin aerosol, Atmospheric Chemistry and Physics, 11, 7417-7443, 2011.

Hodzic, A., Jimenez, J. L., Madronich, S., Canagaratna, M., DeCarlo, P. F., Kleinman, L., and Fast, J.: Modeling organic aerosols in a megacity: potential contribution of semi-volatile and intermediate volatility primary organic compounds to secondary organic aerosol formation, Atmospheric Chemistry and Physics, 10, 5491-5514, 2010.

Jathar, S., Cappa, C., Wexler, A., Seinfeld, J., and Kleeman, M.: Multi-generational oxidation model to simulate secondary organic aerosol in a 3-D air quality model, Geoscientific Model Development, 8, 2553-2567, 2015.

Jimenez, J. L., Canagaratna, M., Donahue, N., Prevot, A., Zhang, Q., Kroll, J. H., DeCarlo, P. F., Allan, J. D., Coe, H., and Ng, N.: Evolution of organic aerosols in the atmosphere, science, 326, 1525-1529, 2009.

Kang, E., Root, M., Toohey, D., and Brune, W.: Introducing the concept of potential aerosol mass (PAM), Atmospheric Chemistry and Physics, 7, 5727-5744, 2007.

Kroll, J. H. and Seinfeld, J. H.: Chemistry of secondary organic aerosol: Formation and evolution of low-volatility organics in the atmosphere, Atmospheric Environment, 42, 3593-3624, 2008.

Lambe, A., Ahern, A., Williams, L., Slowik, J., Wong, J., Abbatt, J., Brune, W., Ng, N., Wright, J., and Croasdale, D.: Characterization of aerosol photooxidation flow reactors: heterogeneous oxidation, secondary organic aerosol formation and cloud condensation nuclei activity measurements, Atmospheric Measurement Techniques, 4, 445-461, 2011.

Lambe, A., Chhabra, P., Onasch, T., Brune, W., Hunter, J., Kroll, J., Cummings, M., Brogan, J., Parmar, Y., and Worsnop, D.: Effect of oxidant concentration, exposure time, and seed particles on secondary organic aerosol chemical composition and yield, Atmospheric Chemistry and Physics, 15, 3063-3075, 2015.

Li, J., Han, Z., Sun, Y., Li, J., and Liang, L.: Chemical formation pathways of secondary organic aerosols in the Beijing-Tianjin-Hebei region in wintertime, Atmospheric Environment, 244, 117996, 2021.

Lim, Y., Tan, Y., Perri, M., Seitzinger, S., and Turpin, B.: Aqueous chemistry and its role in secondary organic aerosol (SOA) formation, Atmospheric Chemistry and Physics, 10, 10521-10539, 2010.

Lindinger, W., Hansel, A., and Jordan, A.: On-line monitoring of volatile organic compounds at pptv levels by means of proton-transfer-reaction mass spectrometry (PTR-MS) medical applications, food control and environmental research, International Journal of Mass Spectrometry and Ion Processes, 173, 191-241, 1998.

Liu, Y., Herdlinger-Blatt, I., McKinney, K., and Martin, S.: Production of methyl vinyl ketone and methacrolein via the hydroperoxyl pathway of isoprene oxidation, Atmospheric Chemistry and Physics, 13, 5715-5730, 2013.

Matsunaga, A. and Ziemann, P. J.: Gas-wall partitioning of organic compounds in a Teflon film chamber and potential effects on reaction product and aerosol yield measurements, Aerosol Science and Technology, 44, 881-892, 2010.

McNeill, V. F., Woo, J. L., Kim, D. D., Schwier, A. N., Wannell, N. J., Sumner, A. J., and Barakat, J. M.: Aqueous-phase secondary organic aerosol and organosulfate formation in

atmospheric aerosols: a modeling study, Environmental science & technology, 46, 8075-8081, 2012.

Ng, N., Canagaratna, M., Zhang, Q., Jimenez, J., Tian, J., Ulbrich, I., Kroll, J., Docherty, K., Chhabra, P., and Bahreini, R.: Organic aerosol components observed in Northern Hemispheric datasets from Aerosol Mass Spectrometry, Atmospheric Chemistry and Physics, 10, 4625-4641, 2010.

Ortega, A., Day, D., Cubison, M., Brune, W. H., Bon, D., De Gouw, J., and Jimenez, J.: Secondary organic aerosol formation and primary organic aerosol oxidation from biomass-burning smoke in a flow reactor during FLAME-3, Atmospheric Chemistry and Physics, 13, 11551-11571, 2013.

Palm, B. B., Campuzano-Jost, P., Day, D. A., Ortega, A. M., Fry, J. L., Brown, S. S., Zarzana, K. J., Dube, W., Wagner, N. L., and Draper, D. C.: Secondary organic aerosol formation from in situ OH, O 3, and NO 3 oxidation of ambient forest air in an oxidation flow reactor, Atmospheric Chemistry and Physics, 17, 5331-5354, 2017.

Palm, B. B., Campuzano-Jost, P., Ortega, A. M., Day, D. A., Kaser, L., Jud, W., Karl, T., Hansel, A., Hunter, J. F., and Cross, E. S.: In situ secondary organic aerosol formation from ambient pine forest air using an oxidation flow reactor, Atmospheric Chemistry and Physics, 16, 2943-2970, 2016.

Pandis, S. N., Wexler, A. S., and Seinfeld, J. H.: Dynamics of tropospheric aerosols, The Journal of Physical Chemistry, 99, 9646-9659, 1995.

Pankow, J. F.: An absorption model of the gas/aerosol partitioning involved in the formation of secondary organic aerosol, Atmospheric Environment, 28, 189-193, 1994.

Peng, J., Hu, M., Shang, D., Wu, Z., Du, Z., Tan, T., Wang, Y., Zhang, F., and Zhang, R.: Explosive secondary aerosol formation during severe haze in the North China Plain, Environmental Science & Technology, 55, 2189-2207, 2021.

Peng, Z. and Jimenez, J. L.: KinSim: A Research-Grade, User-Friendly, Visual Kinetics Simulator for Chemical-Kinetics and Environmental-Chemistry Teaching, 2019.

Peng, Z., Day, D., Stark, H., Li, R., Lee-Taylor, J., Palm, B., Brune, W., and Jimenez, J.: HO x radical chemistry in oxidation flow reactors with low-pressure mercury lamps systematically examined by modeling, Atmospheric Measurement Techniques, 8, 4863-4890, 2015.

Pun, B. and Seigneur, C.: Investigative modeling of new pathways for secondary organic aerosol formation, Atmospheric Chemistry and Physics, 7, 2199-2216, 2007.

Richards-Henderson, N. K., Hansel, A. K., Valsaraj, K. T., and Anastasio, C.: Aqueous oxidation of green leaf volatiles by hydroxyl radical as a source of SOA: Kinetics and SOA yields, Atmospheric Environment, 95, 105-112, 10.1016/j.atmosenv.2014.06.026, 2014.

Saha, P. K., Reece, S. M., and Grieshop, A. P.: Seasonally varying secondary organic aerosol formation from in-situ oxidation of near-highway air, Environmental science & technology, 52, 7192-7202, 2018.

Sareen, N., Waxman, E. M., Turpin, B. J., Volkamer, R., and Carlton, A. G.: Potential of Aerosol Liquid Water to Facilitate Organic Aerosol Formation: Assessing Knowledge Gaps about Precursors and Partitioning, Environmental Science & Technology, 51, 3327-3335, 10.1021/acs.est.6b04540, 2017.

Sareen, N., Carlton, A. G., Surratt, J. D., Gold, A., Lee, B., Lopez-Hilfiker, F. D., Mohr, C., Thornton, J. A., Zhang, Z., Lim, Y. B., and Turpin, B. J.: Identifying precursors and aqueous organic aerosol formation pathways during the SOAS campaign, Atmospheric Chemistry and Physics, 16, 14409-14420, 10.5194/acp-16-14409-2016, 2016.

Seinfeld, J. H. and Pandis, S. N.: Atmospheric chemistry and physics: from air pollution to climate change, John Wiley & Sons2016.

Shrivastava, M., Cappa, C. D., Fan, J., Goldstein, A. H., Guenther, A. B., Jimenez, J. L., Kuang, C., Laskin, A., Martin, S. T., and Ng, N. L.: Recent advances in understanding secondary organic aerosol: Implications for global climate forcing, Reviews of Geophysics, 55, 509-559, 2017.

Volkamer, R., Jimenez, J. L., San Martini, F., Dzepina, K., Zhang, Q., Salcedo, D., Molina, L. T., Worsnop, D. R., and Molina, M. J.: Secondary organic aerosol formation from anthropogenic air pollution: Rapid and higher than expected, Geophysical Research Letters, 33, 2006.

Xu, N. and Collins, D. R.: Design and characterization of a new oxidation flow reactor for laboratory and long-term ambient studies, Atmospheric Measurement Techniques, 14, 2891-2906, 2021.

Xu, N., Le, C., Cocker, D. R., and Collins, D. R.: An oxidation flow reactor for simulating and accelerating secondary aerosol formation in aerosol liquid water and cloud droplets, Atmospheric Measurement Techniques Discussions, 1-41, 2022.

Youn, J.-S., Wang, Z., Wonaschuetz, A., Arellano, A., Betterton, E. A., and Sorooshian, A.: Evidence of aqueous secondary organic aerosol formation from biogenic emissions in the North American Sonoran Desert, Geophysical Research Letters, 40, 3468-3472, 10.1002/grl.50644, 2013.

5.7. **Supplementary Materials**

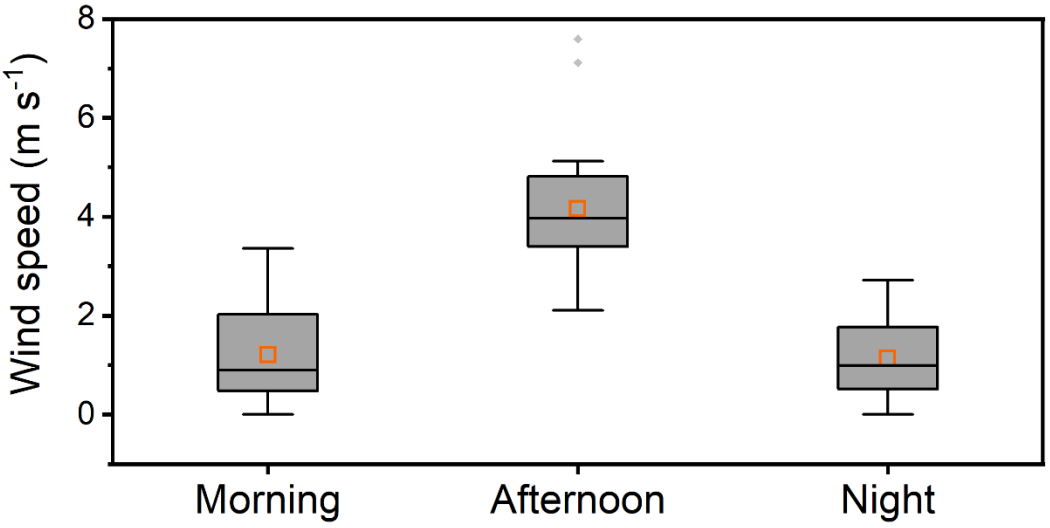

Figure 5.10: Wind speed during the whole sampling period.

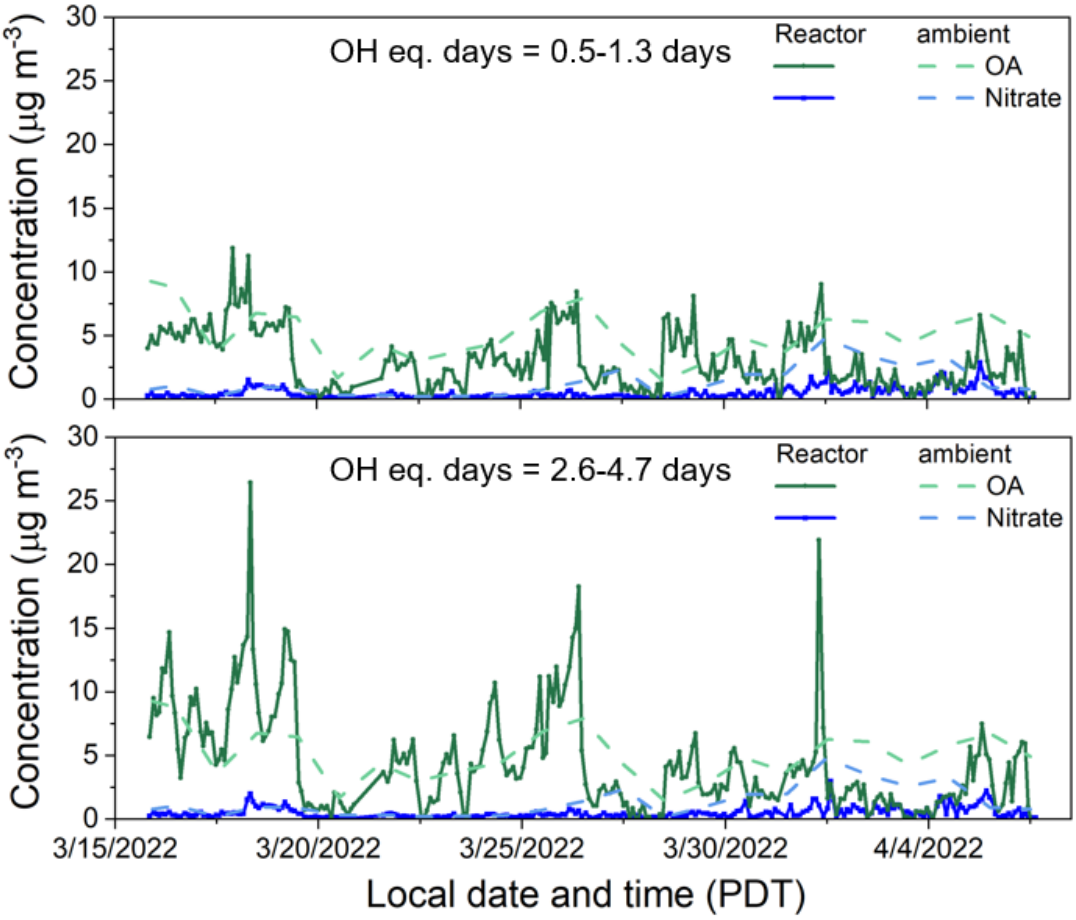

Figure 5.11: Time series of reactor species mass concentrations at low OH_{exp} (top) and high OH_{exp} (bottom) under 40 % RH (dry seed mode) during the sampling period.

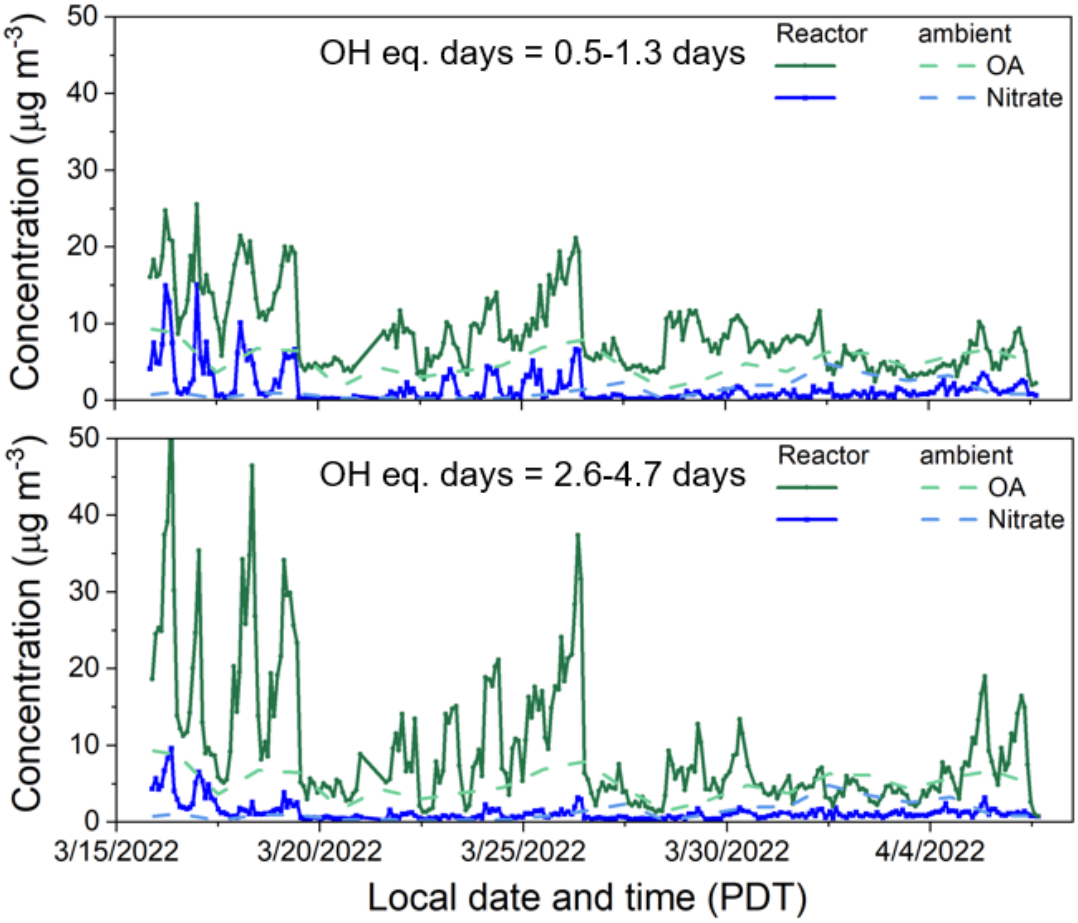

Figure 5.12: Time series of reactor species mass concentrations at low OH_{exp} (top) and high OH_{exp} (bottom) under 85 % RH (ALW mode) during the sampling period.

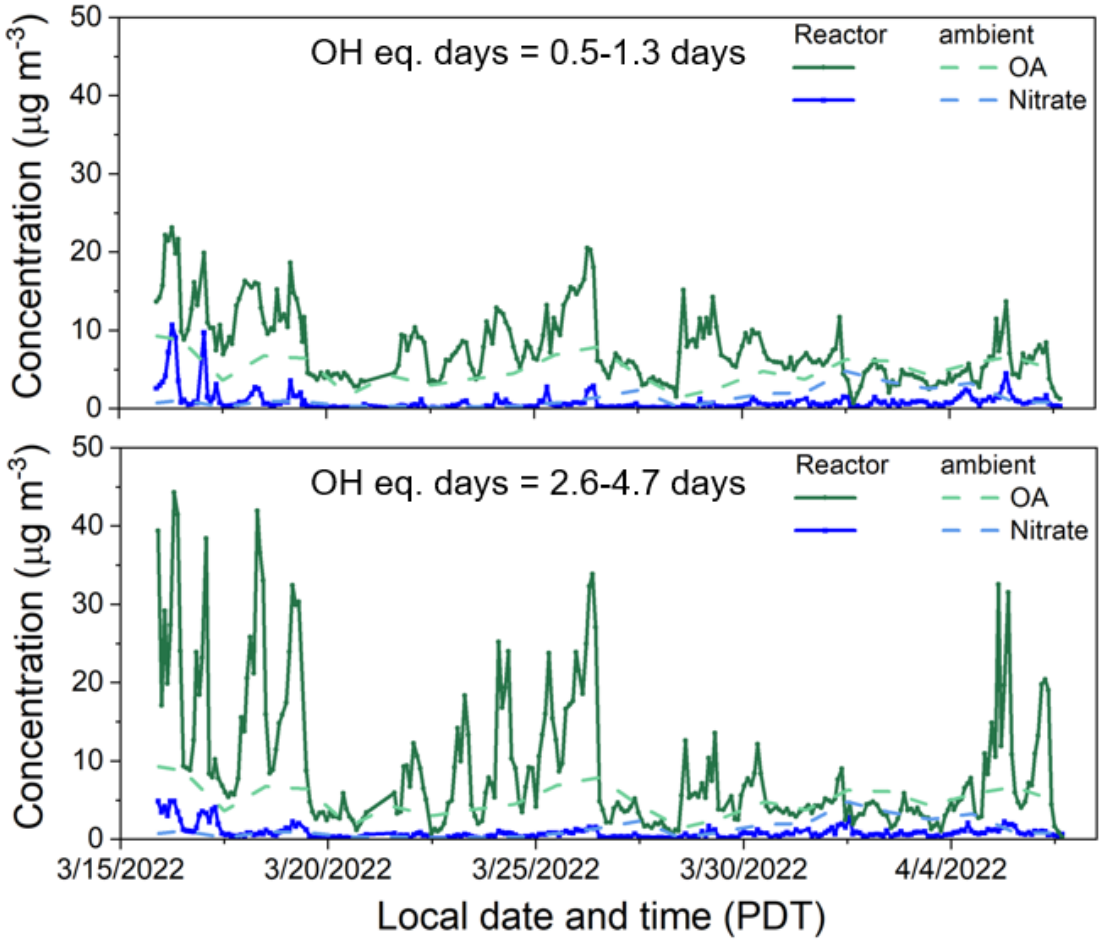

Figure 5.13: Time series of reactor species mass concentrations at low OHexp (top) and high OH_{exp} (bottom) under 100 % RH (cloud mode) during the sampling period.

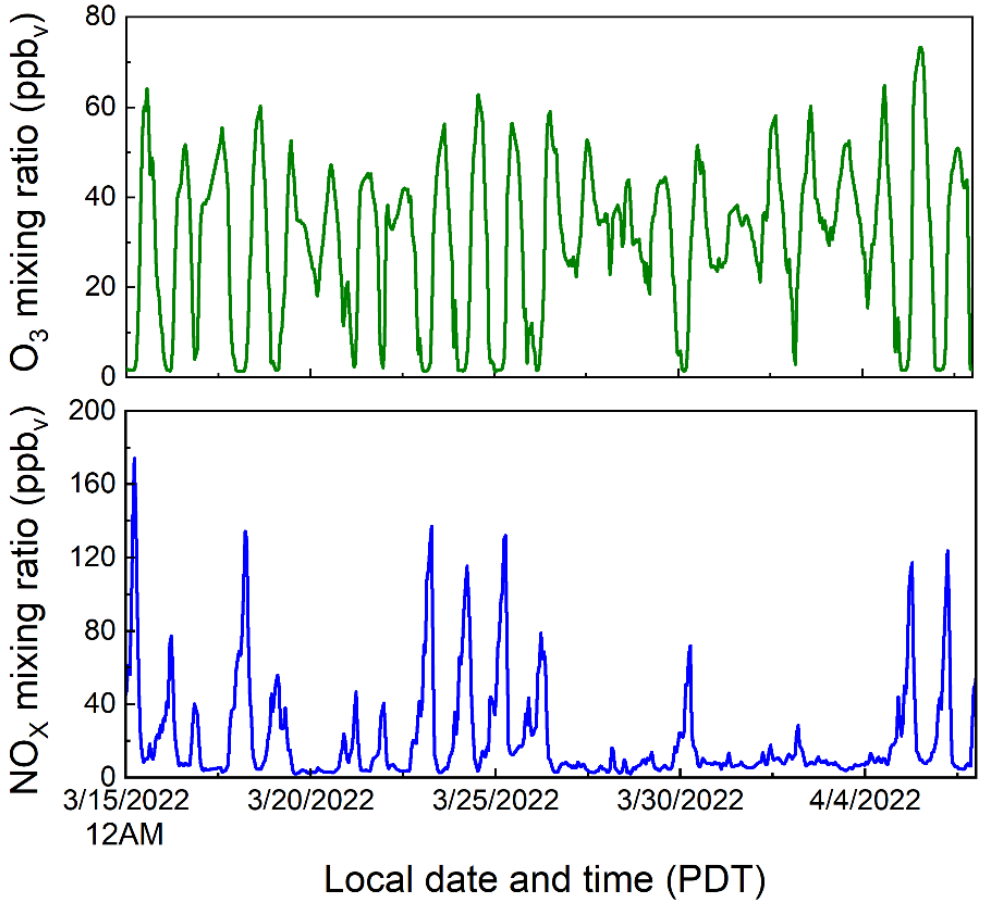

Figure 5.14: O_3 and NOx mixing ratio.

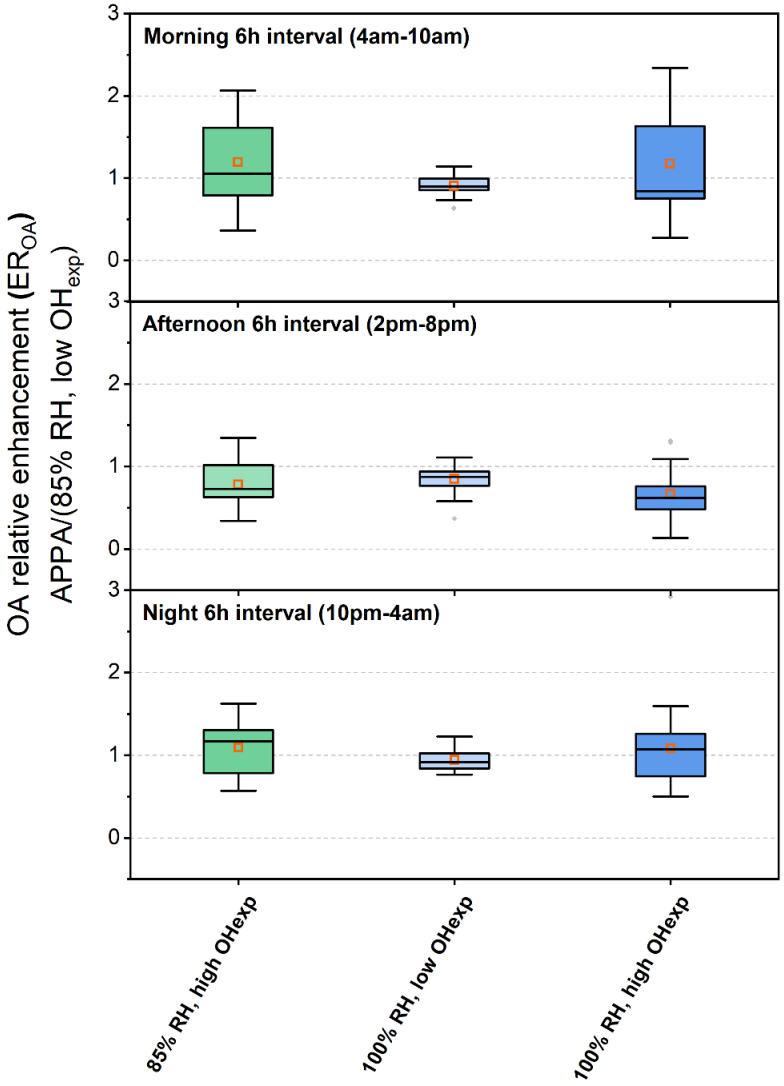

Figure 5.15: Relative OA enhancement (ER_{OA} =reactor SOA/85% low OH_{exp} OA) vs. estimated reactor photochemical age and sample modes for selected 6-hour interval period of (a) morning (4 am- 10 am), (b) afternoon (2 pm- 8 am) and (c) night (10 pm- 4 am).

6. Understanding the Atmospheric Chemistry and Physicochemical Properties of Secondary Aerosol Formation From Gas- and Aqueous-Phase Oxidation of Dimethyl Sulfide (DMS)

6.1. Abstract

Secondary marine aerosol influences clouds and climate. Dimethyl sulfide (DMS), a dominant natural volatile organic compound released from the ocean, could form new particles after being oxidized to sulfuric acid and secondary organic aerosol (SOA), which play a vital role in secondary marine aerosol formation. Although the detailed processes of DMS leading to SOA formation have been reported in modeling studies, more information is needed for predicting and quantifying the different DMS oxidation products under atmospheric conditions. Systematic studies of gas- and aqueous-phase oxidation of DMS were carried out in a multiphase oxidation flow reactor (OFR), the Accelerated Production and Processing of Aerosols (APPA) reactor. Experiments were performed in the presence of dry, aqueous, or activated seed particles inside the APPA, where the relative humidity (RH) was maintained between 40 and 100%. We characterized the formation yields and chemical composition of resulting aerosols produced from the oxidation of DMS with OH radicals and O_3 under variable precursor concentration, seed type, and oxidation time scale. Further, we characterized secondary aerosol formation yield as a function of the OH/O_3 oxidant ratio for aqueous-phase oxidation in the presence of cloud droplets. Our analyses

indicated a significantly higher secondary aerosol yield from the OH-initiated oxidation of DMS with ammonium sulfate seed. Additionally, the formation of sulfuric acid and methanesulfonic acid highly depends on OH exposure levels and the aerosol liquid water/cloud droplets concentration. Our analyses also revealed the formation of highly-oxygenated long-lived organic products from DMS oxidation. The results are used to develop an improved understanding of the atmospheric fate of DMS and the potential impact of its oxidation products on secondary aerosol formation pathways.

6.2. **Introduction**

Atmospheric aerosol particles are the dominant source of uncertainty in the current understanding of climate change (Fuzzi et al., 2006; Seinfeld et al., 2016; Bellouin et al., 2020). The uncertainty associated with atmospheric aerosol is directly linked to natural aerosols (Chen and Penner, 2005; Carslaw et al., 2013; Yoshioka et al., 2019). The most abundant natural aerosols found in marine environments consist of primary particles (sea salt with various organic compounds) and secondary particles, predominantly comprising of non-sea-salt sulfate (Andreae and Rosenfeld, 2008; Mayer et al., 2020). Dimethyl sulfide (DMS; CH_3SCH_3) is the largest contributor (27 Tg of S $year^{-1}$) to natural gas-phase sulfur emissions and plays the dominant source of uncertainty in the current understanding of climate change (Lucas and Prinn, 2005; Barnes et al., 2006; Carslaw et al., 2010) because of its role in secondary aerosol formation. Sulfuric acid (H_2SO_4) and methanesulfonic acid (MSA; $CH_3S(O)(O)OH$) are the two main aerosol-phase oxidation products of DMS that are formed through a cascade of oxidation steps in both the gas and particle phases. They affect the marine atmosphere by promoting formations of new particles and cloud condensation nuclei (CCN), thus impacting formation and properties of marine clouds and therefore the climate (Putaud et al., 1999; Castebrunet et al., 2009; Perraud et al., 2012; Hodshire et al., 2019).

The DMS chemistry under both gas and aqueous phase oxidation is highly complex and uncertain. In the gas phase, the OH-initiated oxidation of DMS proceeds through either a H-abstraction that leads to the formation of low-volatility acids, MSA and H_2SO_4 (Barnes

et al., 1996; Librando et al., 2004) or undergoes the addition pathway in which dimethyl sulfoxide (DMSO; CH_3SOCH_3) are mainly formed and further oxidized to MSA (Hoffmann et al., 2016; Barone et al., 1996; Fung et al., 2022; Sørensen et al., 1996). Recent studies have discovered another major DMS gas-phase autoxidation product, hydroperoxymethyl thioformate (HPMTF; $HOOCH_2SCHO$), which may likely contribute to particle formation and growth and is essential in models for matching to the global in situ observations of more than 30% of oceanic DMS emitted to the atmosphere forms HPMTF (Veres et al., 2020; Wu et al., 2015; Berndt et al., 2019). The aqueous-phase DMS oxidation reactions are expected to occur within aerosol water or cloud droplets, where DMS is firstly oxidized by ozone to form DMSO. DMSO is highly water soluble ($H\sim 10^7$ M atm^{-1}) and can be oxidized to MSA or SO_2 in both gas- and aqueous-phases (Lee and Zhou, 1994). The sulfate and MSA formed through aqueous phase oxidation may have implications for aerosol size distribution and cloud microphysical properties (Zhu et al., 2006; Gershenzon et al., 2001; Barnes et al., 2006). Accurate parameterizations are needed in current chemical transport and global climate models for investigations of the contribution of DMS oxidation products to the global sulfate aerosol burden and cloud microphysical properties (Bopp et al., 2004; Thomas et al., 2010; Saltelli and Hjorth, 1995; Kloster et al., 2006). Though the mechanism of DMS oxidation has been accordingly represented in several modeling studies in the past decades, most of the studies still included limited oxidation mechanisms by underestimating or neglecting the chemical processes under the aqueous phase, which negatively impacts quantifying the products yields of DMS oxidation and the accuracy of estimating the climatic influence of marine

aerosols (Ye et al., 2021; Novak et al., 2022; Cope et al., 2022; Mardyukov and Schreiner, 2018). In addition, a few chamber studies have investigated the evolution of aerosol particles produced through the multiphase DMS chemistry combined with model productions (Rosati et al., 2021; Wollesen De Jonge et al., 2021; Shen et al., 2022; Ye et al., 2022). However, none had the ability to perform comprehensive measurements the formation of the aerosol particles and its chemical composition of the aerosol- and gas-phase species formed with a wide range of OH_{exp} and in the presence of varying amounts of liquid water.

In this study, we investigated the DMS-derived secondary aerosol formation in both gas- and aqueous-phase in a multiphase oxidation flow reactor. Reported here is the secondary aerosol formation yield as a function of OH exposure in the presence of dry seed, aqueous seed particles or cloud droplets, for simulating the gasSA formation through gas-phase oxidation and in-cloud aqSA formation from oxidation of soluble gases produced from gas-phase photochemistry. We also characterize secondary aerosol formation as a function of oxidant (OH/O_3) ratio for gas+aqueous-phase oxidation in the presence of cloud droplets. The DMS-derived secondary aerosol formation is affected strongly by the presence and amount of liquid water and photochemical age. Further, ammonium sulfate (AS), potassium sulfate, and sodium chloride were used as acidic and neutral seeds to investigate the dependence of DMS-derived SOA yield on the different types of seed particles at different oxidation times. Significant increases in SOA yield in the presence of dry acidic seed were observed, whereas limited the secondary product formations under cloud mode, likely causing the aerosols to be more acidic. Last, we

investigated the evolution of aerosol chemical composition at a wide range of the OH_{exp} levels with the presence of dry seed, or when aerosol liquid water and cloud droplets exist. The chemical composition of aerosol particles and the formation of MSA and SA under dry conditions, in deliquesced particles, and in cloud droplets were explored. SA was found to be the main oxidation product from DMS at all studied conditions, and MSA formation was highly dependent on RH and OH_{exp}. Additionally, detailed analysis of organic compounds formed during experiments indicates formation of highly-oxygenated organic compounds and loss of organic sulfur at long OH_{exp}. The results are used to develop an improved understanding of the atmospheric fate of DMS in the presence of seed particles and the potential impact of the oxidation products.

6.3. **Materials and Methods**

6.3.1. **APPA Reactor and Experiments**

The chemicals and reagents used in this study and their purities and suppliers are listed below: DMS (≥ 99.0%, Acros Organics), potassium sulfate (≥ 99.0%, Sigma Aldrich), ammonium sulfate (≥ 99.0%, Sigma Aldrich), sodium chloride (≥ 99.0%, Sigma Aldrich), methanesulfonic acid (≥ 99.0%, Sigma Aldrich). All chemicals were used without further purification.

All experiments were performed in the Accelerated Production and Processing of Aerosols (APPA) reactor, which is shown in Figure 6.1. The APPA reactor differs from that described by Xu & Collins, (2021) and all other OFRs described in the literature (George et al., 2007; Kang et al., 2007; Huang et al., 2017), in that it is also used to simulate aqueous phase chemistry in clouds and fogs. O_3 is produced externally by an ozone generator (Jelight Co., Inc., Model 610); for standard operation of the gas and aqueous-phase DMS oxidation experiments, approximately 15% of ozone was loss by the 254 nm-emitting germicidal UV bulbs to produce OH radicals. The output of the UV lamps is controlled by a dimmable lamp ballast such that more OH radical is produced by increasing the UV intensity throughout the reactor. The OH exposure (OH_{exp}) was estimated based on the method described in previous studies (Peng et al., 2016; Peng and Jimenez, 2019; Xu et al., 2022). Temperature is controlled by water circulating through the water jacket around the reactor, for precisely controlling the reactor cell temperature and to minimize any radial or axial temperature gradients that would promote convective mixing or cause

droplet growth or evaporation. Droplets formed on monodisperse seed particles are rapidly mixed with a gas mixture passing through the inlet-gas line containing O_3, DMS, and humidified zero air. Both temperatures of the inlet-gas and inlet-aerosol line are controlled, such that the resulting relative humidity (RH) in the reactor is between 40% to 100% RH. Hereafter the 40 %, 85 % and 100 % RH maintained inside the reactor are referred to as the dry, ALW, and cloud modes, respectively.

The particles from the reactor pass through 15 cm-long Nafion bundle, to reduce the sample RH to below 20 % before aerosol measurements are carried out. A fabricated scanning mobility particle sizer (SMPS) was used to measure the size distribution and number concentrations of the aerosols from 20 to 500 nm with 90-size bins.

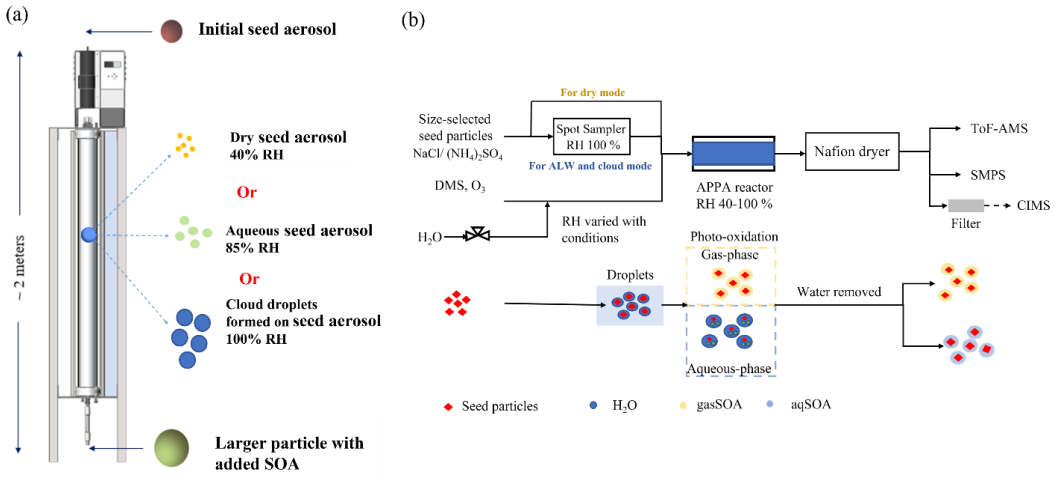

Figure 6.1: The (a) schematic setup of APPA reactor (b) experimental setup for DMS measurements.

6.3.2. **Measurements and Identification of the Chemical Composition of DMS Oxidation Products**

The real-time chemical composition of DMS particle-phase oxidation products was monitored by a mini-aerosol mass spectrometer (mAMS) coupled with a compact time-of-fight (C-ToF) mass spectrometer (Aerodyne Research) during AS seeded experiments. Due to the high vaporization temperature and ionization energy in mAMS, samples aerosol components were fragmented into small ions. Based on previous studies and mass spectrum obtained by sampling pure MSA with mAMS, several ions ($CH_3SO_2^+$ and $CH_4SO_3^+$) were selected as tracers to calculate the fractional contribution of MSA to total aerosol mass. Additionally, the fractional contribution of AS and Sulfate to total aerosol mass was also calculated based on the volume concentration of AS injected into the reactor and sulfate mass concentration measured by mAMS. Details of the calculations are provided in SI. The mAMS data were analyzed by ToF-AMS analysis toolkits Squirrel 1.61B and high-resolution (HR) analysis PIKA 1.21B.

6.4. Results and Discussions

6.4.1. DMS-Derived Secondary Aerosol Formation Under Gas- and Aqueous-Phase Oxidation

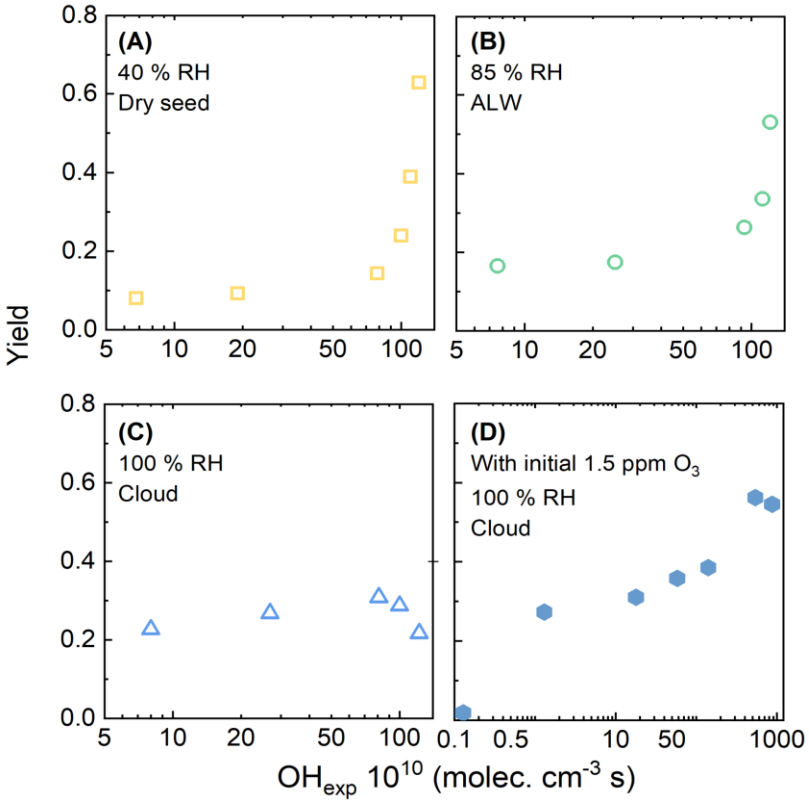

Figure 6.2: DMS-derived secondary aerosol generated in the APPA reactor as a function of OH exposure (OH_{exp}) under the modes of (A) dry seed; 40% RH (B) ALW; 85 % RH (C) cloud; 100 % RH and (D) cloud; fixed initial ozone concentration.

The effects of OH exposure on the DMS-derived secondary aerosol formation under gas- and aqueous-phase oxidation were investigated by injecting roughly 95 ppb of DMS and then measuring the growth of the added seed particles as a function of OH_{exp} and relative humidity. Figure 6.2(A) presents the secondary aerosol mass yields from gas-phase

OH oxidation of DMS in the experiments in the presence of dry ammonium sulfate seeds, with the OH_{exp}~10^{10} to 10^{12} molec. cm^{-3}. Under gas-phase oxidation in the presence of ammonium sulfate seeds, the yield is approximately 0.09 at OH_{exp} ranging from 0.5× 10^{11}-5.0× 10^{11} molec. s cm^{-3}. Secondary aerosol formation from DMS oxidation was found to be strongly dependent upon photochemical age over 3.5 days. Note that the aerosol yield under dry mode (40 % RH) increased by six times (to about 0.62) with OH_{exp} up to 1.2 ×10^{12} molec. s cm^{-3}, which corresponds to a photochemical age of two weeks with an assumed average atmospheric [OH] of 1.5 ×10^{6} molec. cm^{-3}. The increase in aerosol mass is likely due to continuous formation of sulfuric acid and oxidation of methanesulphinic acid (CH_3SOOH; MSIA) by OH to form MSA. We observed significant SOA mass formed at higher OH_{exp} (photochemical age over 2 weeks), this may indicate that the rate of possible fragmentation of SOA was much lower than the secondary aerosol formation rate under the dry seed mode. For comparison, Chen et al. (2018) reported the secondary aerosol formation from DMS gas-phase photooxidation in the chamber study is 53.6 %. Novak et al. (2021) reported that DMS-derived aerosol yield under gas-phase oxidation is 12 %. In addition, the DMS-derived secondary aerosol formation is affected strongly by the presence and amount of liquid water. Figure 6.2(B) and (C) present the DMS-derived secondary aerosol formation under the aqueous-phase oxidation, with about the same OH_{exp} range compared to the dry mode. With the amount of liquid water added in, the yield is approximately 0.18 at OH_{exp} of 0.5× 10^{11}-5× 10^{11} molec. s cm^{-3}. Compared to the dry seed mode, twice as much secondary aerosols were formed under the equivalent photochemical age of up to one week. With the OH_{exp} up to 1.2 ×10^{12} molec. s cm^{-3}, the

maximum yield of 0.55 was measured when aqueous seed particles were present in the reactor, which is lower than that through gas-phase oxidation (maximum yield of 0.62). Wollesen de Jonge et al. (2021) where a significant decrease in secondary aerosol mass productionwas observed during experiments performed under humid conditions (50 % RH–80 % RH) compared to dry conditions (0 % RH–12 % RH). This indicates that the presence of aerosol liquid water within aerosols might have facilitated the fragmentation of particle-phase products or inhibited further oxidation of semi- or non-volatile compounds formed under gas-phase chemistry, or it could have changed the split between different reaction pathways.

Note that we observed a significantly different pattern of secondary aerosol formation when the cloud droplets were present in the reactor, as shown in Figure 6.2(C). Under cloud mode, more secondary aerosol was generated under low OH_{exp} (i.e., photochemical age shorter than 1 week), then the yield curve started falling off around the equivalent photochemical age of 8 days. Additionally, this may indicate that either fragmentation pathways become dominant at long photochemical ages or the oxidation pathways and thus volatility of the DMS aging products change under cloud conditions. Also, this probably indicates the significant role of HPMTF formation by autoxidation of $CH_3SCH_3OO\cdot$ radical through gas-phase DMS oxidation. Since HPMTF is a large fraction of the gas-phase products, it contributes indirectly to particle growth through aqueous phase oxidation to form SO_2 and thus sulfate.Overall, further measurements are needed for understanding the importance of HPMTF on DMS-derived secondary aerosol formation, especially under cloud conditions.

The effect of oxidant competition on DMS secondary aerosol formation was also investigated in this study. Unlike the method described in the previous section, to investigate the competition between aqueous ozone and gas phase OH radical oxidation pathways for the DMS-derived secondary aerosols, we introduced a fixed concentration of ozone (roughly 1.5 ppm) in the beginning and then gradually increased the amount of OH radical accumulated inside the reactor by adjusting the UV light intensity. The light intensity can be adjusted over a wide range through a combination of adjustment of the voltage output of the UV lamp or partial blocking of the UV bulbs using a sliding baffle. The yield as a function of the overall OH_{exp} with the fixed ozone concentration is shown in Figure 6.2(D). As reported in previous studies (Chen et al., 2018; Wollesen De Jonge et al., 2021), the injected DMS was firstly oxidized by aqueous ozone to DMSO, which resulted in almost no secondary aerosol in the presence of abundant ozone and few OH radicals. When the OH radical increased through the reactor, the amount of secondary aerosol formed inside the reactor increased. The secondary aerosol yield with the presence of cloud droplets increased with OH_{exp} up to the maximum of 8×10^{12} molec. s cm^{-3}, which indicates that DMSO was rapidly oxidized by aqueous OH radicals to MSIA and then MSIA and was oxidized by aqueous O_3 to MSA.

6.4.2. **Effect of Seed on OH-Initiated DMS Oxidation**

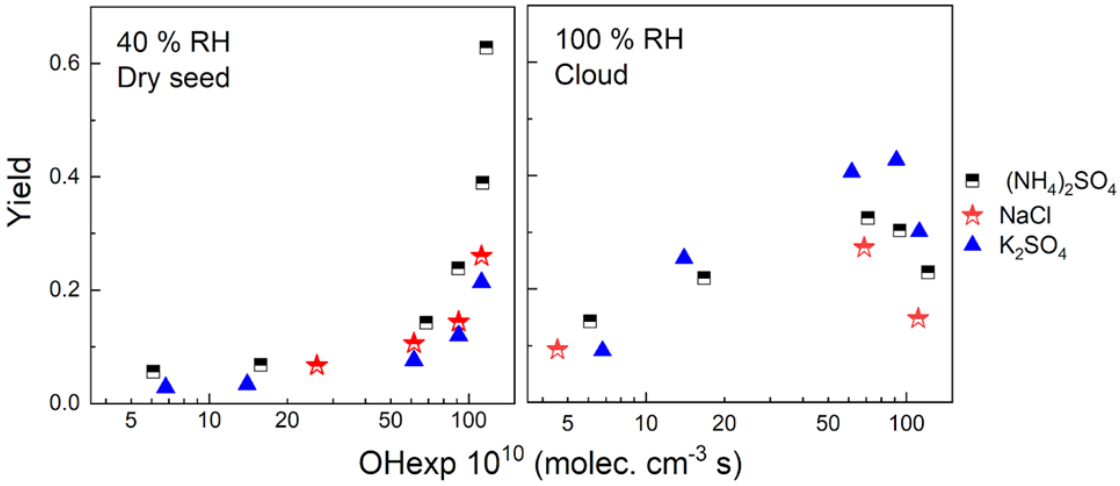

Figure 6.3: Calculated DMS-derived secondary aerosol mass yields as a function of OH exposure, with different seed particles present.

It is necessary to investigate the formation of secondary aerosols in the presence of different seed compositions due to the large amount and varying types of inorganic species present in the atmosphere. Here we consider aerosol formation in the presence of $(NH_4)_2SO_4$, NaCl, and K_2SO_4. NaCl and $(NH_4)_2SO_4$ are the major inorganic aerosol species that are involved in the marine cloud cycles. The introduced $(NH_4)_2SO_4$ seed particles are considered as dry and aqueous acidic seeds while NaCl and K_2SO_4 seed particles are considered as dry and aqueous neutral seeds. Figure 6.3(A) shows the increase in yield as a function of OH_{exp} in the presence of dry acidic and neutral seeds. For easy comparison, the dry seed number concentrations were fixed for all experiments, to eliminate the effect of dry seed sink on the result. In the presence of dry seed only, no significant enhancement in yield was observed at OH_{exp} up to 5×10^{11} molec s cm^{-3}. The generated aerosol mass

and SOA yield were nearly the same throughout experiments with dry $(NH_4)_2SO_4$, NaCl, and K_2SO_4. At higher OH_{exp} (photochemical age over 1 week), a significant increase in SOA yields in the presence of dry acidic seed was observed. The aerosol mass yield was increased by a factor of 2.3 in the presence of ammonium sulfate seeds compared with K_2SO_4 and NaCl seeds. It is possible that acid-catalyzed heterogeneous reactions on $(NH_4)_2SO_4$ seed enhanced secondary aerosol generation by transforming the organic aerosol products. Dry acidic $(NH_4)_2SO_4$ seed aerosols have been proposed to initiate and facilitate the formation of high-molecular-weight and low-volatility products (e.g. oligomers) through acid-catalyzed particle-phase heterogeneous reactions (Lu et al., 2009; Sareen et al., 2010). Although the concentrations of DMS in our experiments are several orders of magnitude higher than that in the ambient atmosphere, the effect of high concentrations of dry $(NH_4)_2SO_4$ aerosols is still expected to be prevalent in the atmosphere since total organic aerosol mass loadings is low; therefore, the influence of dry ($(NH_4)_2SO_4$ could still be high in the ambient. It is worth noting that with cloud droplets present (shown in Figure 6.3(B)), the DMS secondary formation is higher in the presence of potassium sulfate seeds than with the other two seed types. The first logarithmic acid dissociation constants (pKa) of SO_2 and MSA are 1.81 and 1.92, respectively (Chen et al., 2012; Hodshire et al., 2018), resulting in a significant decrease in the pH of the droplets by the amount of SO_2 and MSA dissolved into the droplets. We expect the pH of $(NH_4)_2SO_4$ droplets to be approximately 3.7 at the maximum OH_{exp} (roughly 1×10^{12} molec. s cm^{-3}), by using extend AIM aerosol thermodynamic model that for calculating gas/liquid partitioning in aerosol systems containing organic and inorganic components and water.

We hypothesize that the acidity of K_2SO_4 seeds in the presence of water influenced the heterogeneous chemistry of the products, similar to what was observed for dry $(NH_4)_2SO_4$ seeds.

6.4.3. **Chemical Composition of DMS-Derived Aerosol**

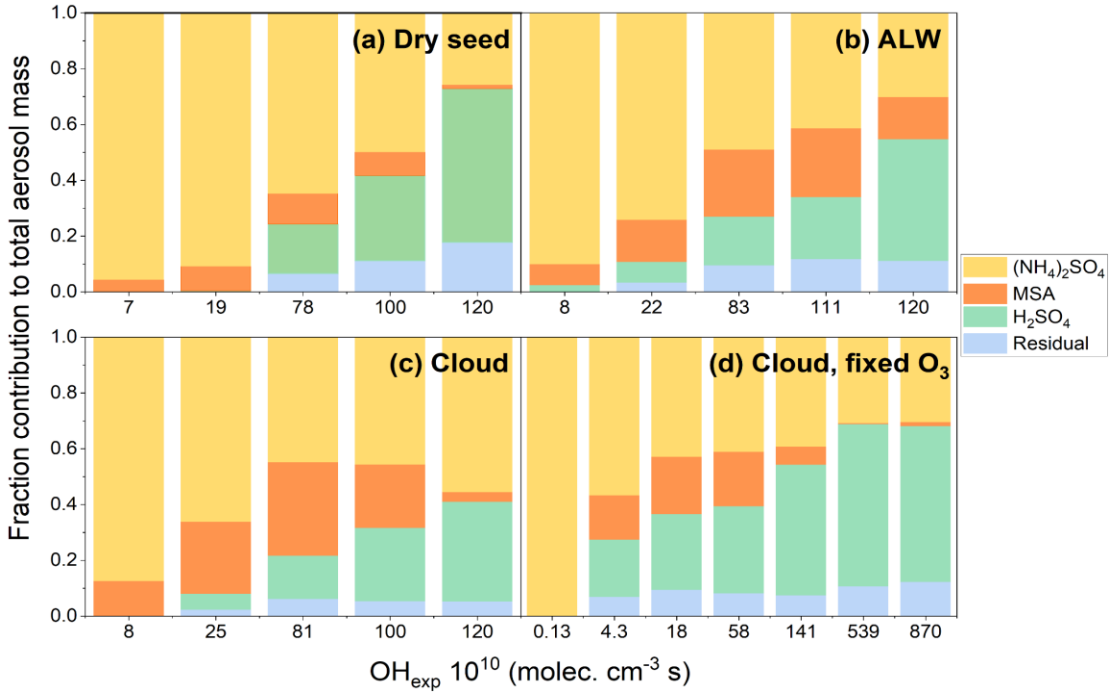

Figure 6.4: Contribution of ammonium sulfate seed (AS, $(NH_4)_2SO_4$), methanesulfonic acid (MSA, $CH_3S(O)_2OH$), sulfuric acid (SA, H_2SO_4) and residuals to total aerosol mass under the modes of (A) dry seed; 40% RH (B) ALW; 85% RH (C) cloud; 100% RH and (D) cloud 100% RH with fixed initial ozone concentration.

Chemical compositions of DMS-derived aerosols under different experimental conditions in the presence of ammonium sulfate seed particles were explored. Organic compounds (including MSA and residual organics) and sulfuric acid were shown to be the main aerosol phase products of DMS oxidation (Figure 6.4). As mentioned above, under

low RH, gas-phase OH oxidation conditions, previous studies suggested that DMS mainly goes through two reaction pathways, namely OH-addition and H-abstraction pathways (Hoffman et al. 2016). Both pathways generate SO_2, SO_3 (which further react to produce SA), and MSA as important and stable products as well as various intermediates (Wollesen de Jonge et al. 2021). Among these intermediates, HPMTF (CH_2(OOH)SCHO), a highly oxygenated long-lived DMS oxidation product and a sulfur reservoir, has been less studied compared to MSA or SA as its formation and atmospheric importance were recently discovered (Wu et al. 2014, Veres 2020). In this system, under low-RH (Figure 6.4A), as the yield of secondary aerosols increased with increase in photochemical age, the fraction of SA to the total aerosol mass increased from zero to 55%, showing a strong OH_{exp} dependence. The fraction of MSA was lower, ranging between 4-11% with OH_{exp} below 100×10^{10} molec. s cm^{-3}, and dropped to <2 % at the highest OH_{exp} (120×10^{10} molec. s cm^{-3}). Overall, these results suggest that as the contribution of secondary aerosol from DMS oxidation became important compared to that of the seed particles (with OH_{exp} higher than 20×10^{10} molec. s cm^{-3}), the main secondary aerosol component was SA, indicating that SA was the most stable DMS aerosol oxidation product after long OH aging under dry condition. This observation is consistent with the model results from Hoffman et al. (2021) who suggested gas-phase formation of MSA was not important. Moreover, the decreased fraction of MSA at the highest OH_{exp} could be explained by heterogeneous oxidation of MSA by additional OH (Mungall et al. 2017). Ye et al,. (2020) also observed a rapid decay of MSA at higher OH_{exp} in a chamber experiment under dry conditions, and suggested that

in addition to OH oxidation, there might be other important chemical or physical MSA loss processes to explain the decay of aerosol phase MSA.

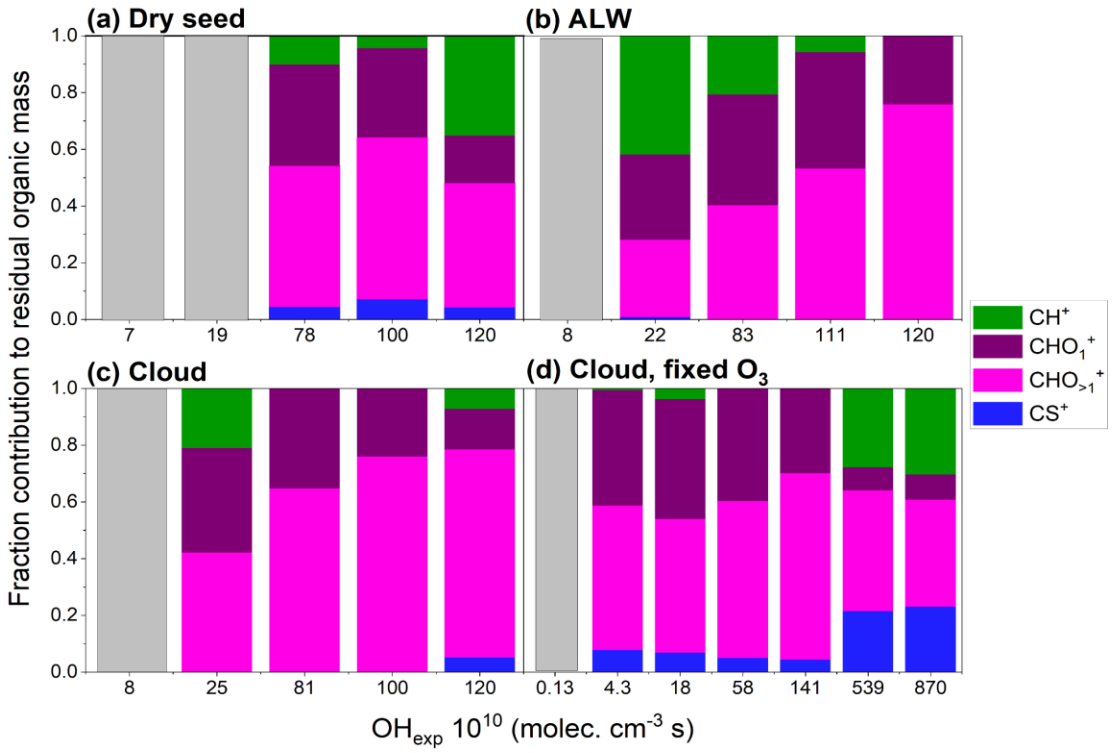

Figure 6.5: Contribution of different organic families to residual organic mass under the modes of (A) dry seed; 40% RH (B) ALW; 85% RH (C) cloud; 100% RH and (D) cloud 100% RH with fixed initial ozone concentration. Based on the structure of DMS, we assumed only four kinds of ions contributed to the formation of DMS organic oxidation products. These were categorized into CH^+ family (no oxygen- or sulfur- containing ions), CHO_1^+ family (one oxygen- containing ions), $CHO_{>1}^+$ family (more than one oxygen containing ions), and CS+ family (sulfur containing ions).

In addition to SA, the organic components (including MSA and residual organics plotted in Figure 6.4) also played a role in controlling secondary aerosol yield and the resulting particle chemical properties. Figure 4 shows the mass fractions of different mAMS-defined organic families to residual organics. Under dry conditions, unlike MSA

formation, the contribution from residual organics to aerosol mass shows a continuous increase with increasing OH_{exp} (from zero to 18%). With OH_{exp} 78×10^{10}-100×10^{10} molec. s cm^{-3}, the main composition of residual organics were highly-oxygenated compounds (fractions of $CHO_{>1}^{+}$ were over 50%) . At the highest OH_{exp} under dry conditions (120×10^{10} molec. s cm^{-3}), as the MSA contribution to total aerosol mass dropped to nearly zero, the composition of residual organics showed a dramatic change, with fraction of CH^{+} increasing from less than 10% to 35% while the fraction of oxygen-containing ions decreasing from nearly 90% to 60%, suggesting prevalence of heterogeneous reactions of MSA and/or contribution of other long-lived intermediates of DMS oxidation such as HPMTF to the aerosols. Additionally, even though we saw a rapid decrease of MSA and increase of SA and residual organics under the highest OH_{exp}, the CS^{+} fraction did not increase, indicating conversion of S from organosulfur into inorganic sulfur, and possibly to SA. Overall, these observations indicate that the organic formation pathway under dry conditions was influenced by OH_{exp} in the system and after long photochemical aging time (of about 14 days), MSA may not be a stable oxidation product.

Hoffman et al. (2021) estimated 78% of DMS was oxidized by O_3 in the aqueous phase to DMSO during daytime in-cloud periods, which is highly soluble. Additionally, next generation oxidation products of DMSO in the aqueous phase are also soluble; thus, the authors suggested that in deliquesced particles and/or cloud droplets, aqueous-phase reactions are the dominant pathway for forming DMS oxidation products. For example, DMSO would further be oxidized by OH in the aqueous phase and form MSIA; then MSIA is oxidized by O_3 or OH to form the stable products including MSA, SO_3, and SO_2. The

main source of SA from aqueous-phase reactions would be oxidation of SO_3 from $CH_3SO_3^{\bullet}$ radical or SO_2 from $CH_3SO_2^{\bullet}$ radical (Berresheim et al. 2014, Wollesen de Jonge et al. 2021). Additionally, Wollesen de Jonge et al. (2021) suggested that HPMTF may be oxidized by aqueous-phase OH and produce SO_2. In the presence of aerosol liquid water (Figure 6.4B), similar to the results from dry conditions, the formation of SA was enhanced at higher OH_{exp}. Particle-phase MSA fractions (7-25%) were higher under 85% RH compared to dry conditions at similar OH_{exp}, with the peak fraction (24-25%) observed at OH_{exp} 80×10^{10}-100×10^{10} molec. s cm^{-3}. Since modeling studies suggested that gas-phase reactions account for only 2% of MSA production based on the DMS gas-phase oxidation mechanism of the Master Chemical Mechanism version 3.2 (MCMv3.2; Hoffman et al. 2016), we infer that the enhancement in MSA formation under 85% RH conditions was because of the presence of aerosol liquid water and through aqueous-phase reactions. Additionally, similar to the results under dry conditions, MSA fraction significantly decreased (from 32 to 15%) at the highest OH_{exp}, while no decrease in secondary aerosol yield or SA fraction was observed, indicating that at extremely high OH_{exp}, either the aqueous-phase reaction to form MSA was inhibited or additional OH led to other MSA chemical losses.

In the aqueous aerosol particles, the fraction of residual organics (Figure 3B) was 3% at OH_{exp} 22×10^{10} molec. s cm^{-3} and stayed relatively stable (10-12%) with OH_{exp} 80×10^{10}-120×10^{10} molec. s cm^{-3}. Regardless of the decrease or increase of other organic families' fraction, the fraction of CH^+ decreases monotonically (from 42% to zero) with an increase in OH_{exp}, indicating the reactive loss of hydrocarbon precursors and the formation

of RCO and RCO2 functional groups due to functionalization reactions. Unlike the results from dry mode (i.e., only gas phase oxidation condition), the fraction of $CHO_{>1}^{+}$ showed a continuous increase at higher OH_{exp}, and the fraction of CHO_1^{+} first showed an increase (30%-41%) with OH_{exp} 20×10^{10}-110×10^{10} molec. s cm^{-3}, but then decreased to 24% at the highest OH_{exp}. Additionally, CS^{+} fraction remained almost zero. All of these observations indicate that compared to the aerosols formed under dry conditions, in the aqueous aerosol particles, the residual organics were mainly made of oxygenated compounds, the oxygenation extent showed an OH_{exp} dependence, and the organosulfur compounds formed in this system were exclusively in the form of MSA.

When cloud droplets were present in the system (Figure 3C), SA formed with OH_{exp} 25×10^{10}-120×10^{10} molec. s cm^{-3}, and its fraction increased (6%-36%) with an increase in OH_{exp} despite the decrease in secondary aerosol yield at the two highest OH_{exp} (Figure 1C). However, at OH_{exp} 120×10^{10} molec. s cm^{-3}, SA fraction under cloud mode was lower than its fraction under 85% RH (36% vs. 44%). With OH_{exp} 8×10^{10}-81×10^{10} molec. s cm^{-3}, MSA fraction increased (13%-34%) with increase in OH_{exp}, and MSA formation was enhanced by the presence of cloud droplets compared to the aqueous aerosol particles at 85% RH. When the OH_{exp} increased under cloud mode, MSA fraction decreased to 23% at OH_{exp} 100×10^{10} molec. s cm^{-3} and further down to 3% at OH_{exp} 120×10^{10} molec. s cm^{-3}. The reduction in MSA was more significant under cloud mode than it was at 85% RH, indicating that the effects of the proposed inhibition of aqueous-phase reactions at longer photochemical age and/or other MSA chemical losses were stronger with enhanced liquid water content in cloud droplets. The reduced importance of MSA and possibly MSIA under

high OH_{exp} led to the decrease in $CH_3SO_3^{\bullet}$, an important precursor for SA formation (Wollesen de Jonge et al. 2021). Additionally, under 100% RH, we expect a lower contribution from the gas-phase H-abstraction reaction of DMS, which can also lead to reduced SA formation, compared to 40% and 85% RH conditions. Thus, overall, the presence of cloud droplets facilitated the aqueous-phase reactions, resulting in higher fractions of MSA and SA under low and medium levels of OH_{exp} compared to lower RH conditions. On the other hand, at extremely high OH_{exp}, the reduced MSA formation influenced the resulting SA fraction.

In cloud droplets, the fraction of residual organics at different OH_{exp} was 30-55% lower than the corresponding values under 85% RH (Figure 6.4C). The residual fraction was 2% at OH_{exp} 25×10^{10} molec. s cm^{-3} and increased to 6% at OH_{exp} 81×10^{10} molec. s cm^{-3} then dropped slightly to 5% at OH_{exp} 100×10^{10}-120×10^{10} molec. s cm^{-3}. Both the mass fraction of residual organics and its relationship with MSA fraction and OH_{exp} are different under 85% RH and 100% conditions, indicating that enhanced aerosol liquid water content influenced the aerosols' organics formation. With increase in OH_{exp} from 25×10^{10} to 100×10^{10} molec. s cm^{-3}, CH^+ fraction decreased from 21% to zero and CHO_1^+ decreased from 37% to 24%, while $CHO_{>1}^+$ fraction increased from 42% to 76%, indicating that athigher OH_{exp}, residual organic components became more oxidized. When the OH_{exp} increased to 120×10^{10} molec. s cm^{-3}, small fractions of CH^+ and CS^+ appeared (7% and 5%, respectively) and both CHO_1^+ and $CHO_{>1}^+$ fraction decreased (to 14% and 73%, respectively). We infer that similar to the results from 40% RH experiments at the highest OH_{exp}, this observation is related to the reduced formation of MSA, indicating that either

MSA was further oxidized to other highly-oxidized and organosulfur-containing compounds or non-MSA organic compounds were formed in the presence of additional OH.

As shown in Figure 3D, under cloud mode, varying OH concentrations with a fixed initial O_3 concentration in the system influenced the resulting MSA vs. SA fractions. With very low concentration of OH in the reactor, it is likely that only a small fraction of DMSO was oxidized to MSIA with limited OH; DMSO's contribution to droplet/particle growth was minor, thus, leading to a very low secondary aerosol yield (<2%) (Figure 1D). Later, when OH_{exp} increased, higher secondary aerosol yields (30-56%) were observed. However, with secondary aerosol yields increasing, MSA fractions remained at around 16-20% with OH_{exp} 4.3×10^{10}-58×10^{10} molec. s cm^{-3}, then decreased to 6% at 141×10^{10} molec. s cm^{-3}, and further decreased to around 1% when OH_{exp} was higher than 500×10^{10} molec. s cm^{-3}. Unlike the MSA, SA fraction kept increasing with increasing OH_{exp} (21% to 58% at OHexp 15×10^{10}-539×10^{10} molec. s cm^{-3}) and so did secondary aerosol yield. However, at the highest OH_{exp} (870×10^{10} molec. s cm^{-3}), both secondary aerosol yield and SA fraction (56%) showed slight decreases compared to previous OH_{exp} level (539×10^{10} molec. s cm^{-3}). Overall, SA fractions were comparable or higher than MSA fractions and/or residual organic fractions. Furthermore, sulfate fractions showed a similar trend with OH_{exp} in this system as secondary aerosol yield, indicating that sulfate was the main contributor to droplet/particle growth. We infer that as OH_{exp} increased in the reactor, MSIA was more likely to go through the OH oxidation pathway (as opposed to oxidation by ozone) and form sulfate instead of MSA as the final stable product. We also believe that at the highest

OH_{exp}, the aqueous O_3 concentration, was significantly decreased then there might not have been enough aqueous phase O_3 to react with MSIA compared to previous conditions, hence, multi-generation oxidation products and the overall secondary aerosol yield.

Figure 6.5D shows the results from evaluating the influence of OH vs. O_3 oxidants on organic composition with the presence of cloud droplets. At OH_{exp} 4.3×10^{10}-141×10^{10} molec. s cm^{-3}, residual organic compounds formation and composition did not change significantly; the main composition of residual organics were oxygen-containing compounds. When OH_{exp} increased to 539×10^{10}-870×10^{10} molec. s cm^{-3}, MSA fraction decreased while the residual organics fraction increased (from 8% to 12%). Furthermore, the composition of the residual organics changed dramatically with the presence of large fraction of CH^+ and CS^+, and a significant decrease in the fractions of both CHO_1^+ and $CHO_{>1}^+$, indicating that similar to the results from 100% RH experiments mentioned above, at very high OH_{exp} levels in the system, the organic formation tend to follow a non-MSA pathway and the resulting organics are organosulfur- and oxygen-containing compounds.

6.5. **Conclusion**

This study investigated secondary aerosol formation through gas-phase DMS oxidation, and also measured the secondary aerosol formed from the complex mixture of DMS-derived gas-phase oxidation products that were further oxidized through aqueous-phase reactions. Our analysis revealed that the DMS-derived secondary aerosol formation through the gas- and aqueous-phase oxidation is strongly affected by the photochemical age and the concentration of aerosol liquid water/cloud droplets. The formation of DMS-derived secondary aerosol increased with the OH_{exp} levels and significant secondary aerosol mass was observed under the equivalent photochemical age of over one week for an assumed average atmospheric [OH] of 1.5×10^6 molec. cm^{-3}. We showed that the mass of secondary products formed through aqueous-phase oxidation is significant and it may potentially provide opportunities for understanding the evolution of the DMS-derived gas-phase oxidation products through aqueous-phase pathways. With the amount of liquid water added in, twice as much secondary aerosol mass was formed under the equivalent photochemical age of up to one week while fragmentation of particle-phase products occurred under the photochemical age of two weeks in the presence of liquid water within aerosols. The effects of oxidant competition and aerosol acidity on DMS-derived secondary aerosol formation were also investigated. Based on our results, a rapid decrease of MSA was observed with the higher OH/ozone ratio, which indicates that MSA may not be a persistent product through aqueous-phase oxidation, and it is likely that the observed sulfate was formed through another pathway, such as DMS→ HPMTF→ SO_2.

Approximately a factor of two increase in secondary aerosol mass was observed in the presence of dry acidic seeds, which may indicate that dry acidic seed aerosols could initiate and facilitate the formation of high-molecular-weight and low-volatility products (e.g., oligomers) through acid-catalyzed particle-phase heterogeneous reactions. However, acidity level may alter the aqueous-phase pathways and the main secondary products, resulting in less conversion of DMS to further oxidized products.

Our results also highlighted the influence of aerosol liquid water content and OH exposure levels on the chemical composition of DMS oxidation products. The formation and fraction of SA in the resulting aerosols showed strong dependence on OH_{exp} under all studied conditions while MSA formation was more complicated, and its formation depended both on OH_{exp} and RH. Our results at high $OH_{exp\ indicate}$ that MSA may also undergo heterogeneous oxidation with additionalOH and possibly other chemical or physical loss processes. Alternatively, the MSA precursors (including DMSO, MSIA etc.) may undergo other reaction pathways and form oxygenated-organic compounds instead of MSA at high OH_{exp}, which could also explain the lower contribution ofMSA and the change in the residual organic composition under extremely high OH_{exp}. We conclude that over open ocean, the presence of aerosol liquid water and clouds may alter MSA formation pathway and concentration compared to dry conditions, while SA remains the main DMS oxidation product at high OH_{exp}. It is also important to note that presence of cloud droplets decreased secondary aerosol yield and resulted in the loss of MSA at high OH_{exp}. Although traditionally MSA has been considered to be the most important DMS aqueous-phase oxidation product in the presence of OH and O_3, our study indicates that some highly-

oxygenated organic compounds formed possibly through MSIA OH oxidation will be very stable in the atmosphere after long photochemical aging, and their contribution to the DMS-derived secondary aerosols is non-negligible.

6.6. **References**

Andreae, M. and Rosenfeld, D.: Aerosol–cloud–precipitation interactions. Part 1. The nature and sources of cloud-active aerosols, Earth-Science Reviews, 89, 13-41, 2008.

Barnes, I., Becker, K., and Patroescu, I.: FTIR product study of the OH initiated oxidation of dimethyl sulphide: Observation of carbonyl sulphide and dimethyl sulphoxide, Atmospheric Environment, 30, 1805-1814, 1996.

Barnes, I., Hjorth, J., and Mihalopoulos, N.: Dimethyl sulfide and dimethyl sulfoxide and their oxidation in the atmosphere, Chemical reviews, 106, 940-975, 2006.

Barone, S. B., Turnipseed, A. A., and Ravishankara, A.: Reaction of OH with Dimethyl Sulfide (DMS). 1. Equilibrium Constant for OH+ DMS Reaction and the Kinetics of the OH⊙ DMS+ O2 Reaction, The Journal of Physical Chemistry, 100, 14694-14702, 1996.

Bellouin, N., Quaas, J., Gryspeerdt, E., Kinne, S., Stier, P., Watson-Parris, D., Boucher, O., Carslaw, K. S., Christensen, M., and Daniau, A. L.: Bounding global aerosol radiative forcing of climate change, Reviews of Geophysics, 58, e2019RG000660, 2020.

Berndt, T., Scholz, W., Mentler, B., Fischer, L., Hoffmann, E. H., Tilgner, A., Hyttinen, N., Prisle, N. L., Hansel, A., and Herrmann, H.: Fast peroxy radical isomerization and OH recycling in the reaction of OH radicals with dimethyl sulfide, The Journal of Physical Chemistry Letters, 10, 6478-6483, 2019.

Bopp, L., Boucher, O., Aumont, O., Belviso, S., Dufresne, J.-L., Pham, M., and Monfray, P.: Will marine dimethylsulfide emissions amplify or alleviate global warming? A model study, Canadian Journal of Fisheries and Aquatic Sciences, 61, 826-835, 2004.

Carslaw, K., Boucher, O., Spracklen, D., Mann, G., Rae, J., Woodward, S., and Kulmala, M.: A review of natural aerosol interactions and feedbacks within the Earth system, Atmospheric Chemistry and Physics, 10, 1701-1737, 2010.

Carslaw, K., Lee, L., Reddington, C., Pringle, K., Rap, A., Forster, P., Mann, G., Spracklen, D., Woodhouse, M., and Regayre, L.: Large contribution of natural aerosols to uncertainty in indirect forcing, Nature, 503, 67-71, 2013.

Castebrunet, H., Martinerie, P., Genthon, C., and Cosme, E.: A three-dimensional model study of methanesulphonic acid to non sea salt sulphate ratio at mid and high-southern latitudes, Atmospheric Chemistry and Physics, 9, 9449-9469, 2009.

Chen, Y. and Penner, J. E.: Uncertainty analysis for estimates of the first indirect aerosol effect, Atmospheric Chemistry and Physics, 5, 2935-2948, 2005.

Chen, Q., Sherwen, T., Evans, M., and Alexander, B.: DMS oxidation and sulfur aerosol formation in the marine troposphere: a focus on reactive halogen and multiphase chemistry, Atmospheric Chemistry and Physics, 18, 13617-13637, 2018.

Cope, J. D., Bates, K. H., Tran, L. N., Abellar, K. A., and Nguyen, T. B.: Sulfur radical formation from the tropospheric irradiation of aqueous sulfate aerosols, Proceedings of the National Academy of Sciences, 119, e2202857119, 2022.

Fung, K. M., Heald, C. L., Kroll, J. H., Wang, S., Jo, D. S., Gettelman, A., Lu, Z., Liu, X., Zaveri, R. A., and Apel, E. C.: Exploring dimethyl sulfide (DMS) oxidation and implications for global aerosol radiative forcing, Atmospheric Chemistry and Physics, 22, 1549-1573, 2022.

Fuzzi, S., Andreae, M., Huebert, B., Kulmala, M., Bond, T., Boy, M., Doherty, S., Guenther, A., Kanakidou, M., and Kawamura, K.: Critical assessment of the current state of scientific knowledge, terminology, and research needs concerning the role of organic aerosols in the atmosphere, climate, and global change, Atmospheric Chemistry and Physics, 6, 2017-2038, 2006.

Gershenzon, M., Davidovits, P., Jayne, J., Kolb, C., and Worsnop, D.: Simultaneous uptake of DMS and ozone on water, The Journal of Physical Chemistry A, 105, 7031-7036, 2001.

George, I., Vlasenko, A., Slowik, J., Broekhuizen, K., and Abbatt, J.: Heterogeneous oxidation of saturated organic aerosols by hydroxyl radicals: uptake kinetics, condensed-phase products, and particle size change, Atmospheric Chemistry and Physics, 7, 4187-4201, 2007.

Hodshire, A. L., Campuzano-Jost, P., Kodros, J. K., Croft, B., Nault, B. A., Schroder, J. C., Jimenez, J. L., and Pierce, J. R.: The potential role of methanesulfonic acid (MSA) in aerosol formation and growth and the associated radiative forcings, Atmospheric Chemistry and Physics, 19, 3137-3160, 2019.

Hoffmann, E. H., Tilgner, A., Schrödner, R., Bräuer, P., Wolke, R., and Herrmann, H.: An advanced modeling study on the impacts and atmospheric implications of multiphase dimethyl sulfide chemistry, Proceedings of the National Academy of Sciences, 113, 11776-11781, 2016.

Huang, Y., Coggon, M. M., Zhao, R., Lignell, H., Bauer, M. U., Flagan, R. C., and Seinfeld, J. H.: The Caltech Photooxidation Flow Tube reactor: design, fluid dynamics and characterization, Atmospheric Measurement Techniques, 10, 839-867, 2017.

Kang, E., Root, M., Toohey, D., and Brune, W.: Introducing the concept of potential aerosol mass (PAM), Atmospheric Chemistry and Physics, 7, 5727-5744, 2007.

Kloster, S., Feichter, J., Maier-Reimer, E., Six, K. D., Stier, P., and Wetzel, P.: DMS cycle in the marine ocean-atmosphere system–a global model study, Biogeosciences, 3, 29-51, 2006.

Lee, Y. N. and Zhou, X.: Aqueous reaction kinetics of ozone and dimethylsulfide and its atmospheric implications, Journal of Geophysical Research: Atmospheres, 99, 3597-3605, 1994.

Librando, V., Tringali, G., Hjorth, J., and Coluccia, S.: OH-initiated oxidation of DMS/DMSO: reaction products at high NOx levels, Environmental Pollution, 127, 403-410, 2004.

Lu, Z., Hao, J., Takekawa, H., Hu, L., and Li, J.: Effect of high concentrations of inorganic seed aerosols on secondary organic aerosol formation in the m-xylene/NOx photooxidation system, Atmospheric Environment, 43, 897-904, 2009.

Lucas, D. and Prinn, R.: Parametric sensitivity and uncertainty analysis of dimethylsulfide oxidation in the clear-sky remote marine boundary layer, Atmospheric Chemistry and Physics, 5, 1505-1525, 2005.

Mardyukov, A. and Schreiner, P. R.: Atmospherically relevant radicals derived from the oxidation of dimethyl sulfide, Accounts of chemical research, 51, 475-483, 2018.

Mayer, K. J., Wang, X., Santander, M. V., Mitts, B. A., Sauer, J. S., Sultana, C. M., Cappa, C. D., and Prather, K. A.: Secondary marine aerosol plays a dominant role over primary sea spray aerosol in cloud formation, ACS central science, 6, 2259-2266, 2020.

Novak, G. A., Fite, C. H., Holmes, C. D., Veres, P. R., Neuman, J. A., Faloona, I., Thornton, J. A., Wolfe, G. M., Vermeuel, M. P., and Jernigan, C. M.: Rapid cloud removal of dimethyl sulfide oxidation products limits SO2 and cloud condensation nuclei production in the marine atmosphere, Proceedings of the National Academy of Sciences, 118, e2110472118, 2021.

Novak, G. A., Kilgour, D. B., Jernigan, C. M., Vermeuel, M. P., and Bertram, T. H.: Oceanic emissions of dimethyl sulfide and methanethiol and their contribution to sulfur dioxide production in the marine atmosphere, Atmospheric Chemistry and Physics, 22, 6309-6325, 2022.

Peng, Z. and Jimenez, J. L.: KinSim: A Research-Grade, User-Friendly, Visual Kinetics Simulator for Chemical-Kinetics and Environmental-Chemistry Teaching, 2019.

Peng, Z., Day, D. A., Ortega, A. M., Palm, B. B., Hu, W., Stark, H., Li, R., Tsigaridis, K., Brune, W. H., and Jimenez, J. L.: Non-OH chemistry in oxidation flow reactors for the study of atmospheric chemistry systematically examined by modeling, Atmospheric Chemistry and Physics, 16, 4283-4305, 2016.

Perraud, V., Bruns, E. A., Ezell, M. J., Johnson, S. N., Yu, Y., Alexander, M. L., Zelenyuk, A., Imre, D., Chang, W. L., and Dabdub, D.: Nonequilibrium atmospheric secondary organic aerosol formation and growth, Proceedings of the National Academy of Sciences, 109, 2836-2841, 2012.

Putaud, J., Davison, B., Watts, S., Mihalopoulos, N., Nguyen, B., and Hewitt, C.: Dimethylsulfide and its oxidation products at two sites in Brittany (France), Atmospheric Environment, 33, 647-659, 1999.

Rosati, B., Christiansen, S., Wollesen de Jonge, R., Roldin, P., Jensen, M. M., Wang, K., Moosakutty, S. P., Thomsen, D., Salomonsen, C., and Hyttinen, N.: New Particle Formation and Growth from Dimethyl Sulfide Oxidation by Hydroxyl Radicals, ACS Earth and Space Chemistry, 5, 801-811, 2021.

Saltelli, A. and Hjorth, J.: Uncertainty and sensitivity analyses of OH-initiated dimethyl sulphide (DMS) oxidation kinetics, Journal of atmospheric chemistry, 21, 187-221, 1995.

Sareen, N., Schwier, A., Shapiro, E., Mitroo, D., and McNeill, V.: Secondary organic material formed by methylglyoxal in aqueous aerosol mimics, Atmospheric Chemistry and Physics, 10, 997-1016, 2010.

Seinfeld, J. H., Bretherton, C., Carslaw, K. S., Coe, H., DeMott, P. J., Dunlea, E. J., Feingold, G., Ghan, S., Guenther, A. B., and Kahn, R.: Improving our fundamental understanding of the role of aerosol− cloud interactions in the climate system, Proceedings of the National Academy of Sciences, 113, 5781-5790, 2016.

Shen, J., Scholz, W., He, X.-C., Zhou, P., Marie, G., Wang, M., Marten, R., Surdu, M., Rörup, B., and Baalbaki, R.: High Gas-Phase Methanesulfonic Acid Production in the OH-Initiated Oxidation of Dimethyl Sulfide at Low Temperatures, Environmental science & technology, 2022.

Sørensen, S., Falbe-Hansen, H., Mangoni, M., Hjorth, J., and Jensen, N.: Observation of DMSO and CH3S (O) OH from the gas phase reaction between DMS and OH, Journal of Atmospheric Chemistry, 24, 299-315, 1996.

Thomas, M. A., Suntharalingam, P., Pozzoli, L., Rast, S., Devasthale, A., Kloster, S., Feichter, J., and Lenton, T.: Quantification of DMS aerosol-cloud-climate interactions using the ECHAM5-HAMMOZ model in a current climate scenario, Atmospheric Chemistry and Physics, 10, 7425-7438, 2010.

Veres, P. R., Neuman, J. A., Bertram, T. H., Assaf, E., Wolfe, G. M., Williamson, C. J., Weinzierl, B., Tilmes, S., Thompson, C. R., and Thames, A. B.: Global airborne sampling reveals a previously unobserved dimethyl sulfide oxidation mechanism in the marine atmosphere, Proceedings of the National Academy of Sciences, 117, 4505-4510, 2020.

Wollesen de Jonge, R., Elm, J., Rosati, B., Christiansen, S., Hyttinen, N., Lüdemann, D., Bilde, M., and Roldin, P.: Secondary aerosol formation from dimethyl sulfide–improved mechanistic understanding based on smog chamber experiments and modelling, Atmospheric Chemistry and Physics, 21, 9955-9976, 2021.

Wu, R., Wang, S., and Wang, L.: New mechanism for the atmospheric oxidation of dimethyl sulfide. The importance of intramolecular hydrogen shift in a CH3SCH2OO radical, The Journal of Physical Chemistry A, 119, 112-117, 2015.

Ye, Q., Goss, M. B., Isaacman-VanWertz, G., Zaytsev, A., Massoli, P., Lim, C., Croteau, P., Canagaratna, M., Knopf, D. A., and Keutsch, F. N.: Organic Sulfur Products and Peroxy Radical Isomerization in the OH Oxidation of Dimethyl Sulfide, ACS Earth and Space Chemistry, 5, 2013-2020, 2021.

Ye, Q., Goss, M. B., Krechmer, J. E., Majluf, F., Zaytsev, A., Li, Y., Roscioli, J. R., Canagaratna, M., Keutsch, F. N., and Heald, C. L.: Product distribution, kinetics, and aerosol formation from the OH oxidation of dimethyl sulfide under different RO 2 regimes, Atmospheric Chemistry and Physics Discussions, 1-18, 2022.

Yoshioka, M., Regayre, L., Pringle, K., Johnson, J., Mann, G., Partridge, D., Sexton, D., Lister, G., Schutgens, N., and Stier, P.: Ensembles of global climate model variants designed for the quantification and constraint of uncertainty in aerosols and their radiative forcing, Journal of Advances in Modeling Earth Systems, 11, 3728-3754, 2019.

Zhu, L., Nenes, A., Wine, P. H., and Nicovich, J. M.: Effects of aqueous organosulfur chemistry on particulate methanesulfonate to non–sea salt sulfate ratios in the marine atmosphere, Journal of Geophysical Research: Atmospheres, 111, 2006.

7. Conclusions

Overall, this thesis has sought to obtain a better understanding of secondary aerosol formation and properties that formed through both gas- and aqueous-phase oxidation from several laboratory and field studies. To achieve this, two types of reactors - the Particle Formation Accelerator (PFA) and the Accelerated Production and Processing of Aerosols (APPA) reactor have been developed. For optimizing the flow tube design and to improve the accuracy of the atmospherically relevant SA measurements, this work firstly characterized the experimental uncertainties associated with measurements and evaluate the design of reactors and their roles in SA-forming systems. In addition, this work quantified the secondary aerosol formation through gas- and aqueous-phase oxidation from various precursors in a laboratory environment and report the aqueous-phase measured yields, as a function of parameters such photochemical age, relative humidity and seed types. Finally, this work obtained data during one or more field campaigns to help bridge the gap between the laboratory experimental results and ambient observations of SA formation and to integrate these results in models and/or model parameterizations.

In Chapter 2, we designed and constructed a new all-Teflon reactor, the Particle Formation Accelerator (PFA) OFR, and characterized it using both experimental measurements and CFD modeling. Its performance was examined and evaluated through laboratory measurements and with ambient air. The reactor response and characteristics were compared with those from a smog chamber (Caltech) and other oxidation flow reactors (the Toronto Photo-Oxidation Tube (TPOT), Caltech Photooxidation Flow Tube

(CPOT), the TUT Secondary Aerosol Reactor (TSAR), quartz and aluminum versions of Potential Aerosol Mass reactors (PAMs), and the Environment and Climate Change Canada OFR (ECCC-OFR)). Our results show that OH_{exp} can be varied over a range comparable to that of other OFRs, with the dependence on UV lamp power, RH, and O_3 concentration characterized and reported. The particle transmission efficiency is improved to 75 % in the size range from 50 to 200 nm by minimizing static charge on the PFA, PTFE, and ePTFE surfaces. Particle and gas residence time distributions (RTDs) were investigated by computational simulation and experimental verification. The flow through the reactor is nearly laminar with narrower RTDs than reported for OFRs with greater diameter-to-length ratios. The mass yields of SOA from the oxidation of α-pinene and *m*-xylene in the presence and absence of seed particles were further investigated. At comparable OH exposure, the *m*-xylene and α-pinene SOA yields are slightly higher than those in the quartz-PAM and TPOT, but lower than in the aluminum-PAM., while agree with in 12 % for comparable OH exposures ($\sim 10^{11}$ molec. cm^{-3} s) compared to those in the Caltech chamber. The presence and concentration of seed particles was shown to have a significant effect on SOA yield. The SA production from ambient air was studied in Riverside, CA. The mass concentration of SA formed in the reactor was about twice the mass concentration of the ambient aerosol at the same time. Overall, the computational and experimental results indicate that the PFA OFR is suitable for laboratory studies and for field use that includes measurement of rapidly changing ambient concentrations. Future efforts will include adding direct measurement of OH_{exp} during measurements, development of an OH_{exp} estimation description for the PFA OFR comparable to that

reported for other OFRs, and further exploring the influence of OH reactivity on OH_{exp} and of seed particles on SOA yield. We will also expand upon measurements of the composition of the particulate products and gaseous precursors during one or more field studies to evaluate how well the PFA OFR simulates atmospheric chemistry that typically requires hours or days.

In Chapter 3, the secondary aerosol formation from gas- and aqueous-phase chemistry was investigated by a new all-Teflon flow cell reactor. The Accelerated Production and Processing of Aerosols (APPA) reactor was designed and has primarily been used as an oxidation flow reactor, with photolysis of externally generated O_3 providing an OH exposure of between 8×10^{10} molec. cm^{-3} s and 1.2×10^{12} molec. cm^{-3} s over the ~150 s mean gas residence time. The geometry, inlet and outlet designs, and tight temperature control result in minimal mixing and a narrow residence time distribution. The most unique aspect of the reactor is the ability to vary the liquid water content present in aqueous aerosol or ~3.3 mm diameter cloud droplets that are formed on monodisperse seed particles and flow through the reactor together with the O_3, OH, and reactive precursor gases. A set of measurements for a prescribed gas mixture or ambient air can thus investigate the amount, properties, and composition of secondary aerosol formed across a matrix of conditions spanning both OH_{exp} and RH/LWC. The experimental system is fully automated and designed for continuous operation over extended periods of time. A series of experiments and numerical simulations summarized here explored the characteristics and capabilities of the reactor system. Example results reported here provide a preview into ongoing work investigating the roles of aerosol liquid water and cloud water in aerosol

formation for i) a range of organic precursor gases and ii) ambient air over multi-week sampling periods.

In chapter 4, severteen water insoluble volatile organic compounds (VOC) from source categories of vehicle exhaust, biogenic, biomass burning, and volatile chemical products (VCPs) were selected and their derived secondary aerosol formation through gas- and aqueous-phase oxidation under equivalent photochemical age roughly one days to two weeks were investigated. The SOA formed through both gas- and aqueous-phase oxidation were found to be strongly dependent upon the photochemical age and in the presence of aerosol liquid water or cloud droplets. The results show that most of the biogenic VOCs significantly contributes to the gasSOA burden than the other three emission categories. In addition, the aqueous-phase oxidation of volatile organic compounds can be significantly contributed to the SOA mass. With increasing aerosol liquid water concentration, the SOA formed from anthropogenic and biomass burning VOCs contributes substantially to the total SOA burden. Significant SOA formed was detected and no plateau of SOA yield were observed under cloud conditions, which suggests a dependence on LWC. Compounds formed when aerosol liquid water or cloud droplets are present are more highly oxidized and have higher molecular weight than those when only dry seed particles present. Considering the relatively high annual global emissions of those selected compound, the secondary aerosol formation from the oxidation of these precursors may be ubiquitous. Future research is warranted to quantify secondary products from precursors that can react with ozone, study their fates and reactivities, and model their formation processes. In addition, the mechaniums for the formation of aqSOA are currently understudied. Future

research is warranted to quantify the mechanisum and pathways from this group of precursors in ambient sample, study their fates and reactivities, and model their formation processes.

In chapter 5, real-time measurement of ambient SA formation and OA aging from ambient precursors was carried out with the APPA reactor coupled to an AMS and SMPS during the Riverside field campaign and targeted urban emissions. This chapter represents the first application of an oxidation flow reactor to investigate SOA formation under aqueous-phase oxidation from ambient urban air. Compared to ambient aerosol measurements, no clear trend has been observed for all modes in this study, because only ambient precursors are sampled through the reactor and involved into oxidation reactions. Secondary aerosol formed through both gas- and aqueous-phase oxidation of ambient precursors was found to be strongly depending on the photochemical age and the presence of aerosol liquid water or cloud droplets. Secondary aersol formed with the presence of cloud droplets is slighly lower than that when the aerosol liquid water exists, which is opposite trend observed from the aqueous-phase phtooxidation of water insuable VOCs, and indicates that the ambient precursors are distinct from the VOCs described in previous labortary studies. High OA enhancement was observed at morning and night than that at afternoon with the presence of dry seeds, aerosol liquid water and cloud droplets, which is probably related to the composition of the ambient precursors. The chemical evolution of OA in the reactor was examined in this study with the AMS fractional organic contribution at m/z44 and m/z43 (f_{44} and f_{43}). Reactor gas-phase oxidation data evolve as f_{44} increases and f_{43} decreases with photochemical age stepping from serveral hours to 2 days, consistent

with previous ambient field observations from multiple field campaigns. As the amount of the liquid water or cloud droplets increases, the f_{44} increases at morning and night, which indicates that highly oxygenated and high molecular weight species formed. This study shows that capability of APPA reactors on continuedly ambient field studies, as they allow real-time measurement of secondary aerosol formation through gas and aqueous-phase oxidation across a wide range of photochemical ages. Continuous ambient air sampling through the APPA reactor provides complementary information to the analysis of ambient data and also provide insights of secondary aerosol formation under aqueous phase oxidation. Additionally, these results help to constrain SOA models that restricted from the aqueous-phase secondary aerosol formation and to narrow the gaps between the measured and modeled SOA concentration. Future studies could guide by this study and investigate the secondary aerosol formation through aqueous-phase oxidation from different sources and regions.

In chapter 6, this study investigated secondary aerosol formation through gas-phase DMS oxidation, and measured the secondary aerosol formed from the complex mixture of DMS-derived gas-phase oxidation products that further oxidized through aqueous-phase reactions. Our analysis revealed that the DMS-derived secondary aerosol formation through the gas- and aqueous-phase oxidation is strongly affected by the photochemical age and the aerosol liquid water/ cloud droplets concentration. The formation of DMS-derived secondary aerosol increased with the OH_{exp} levels and significant secondary aerosol mass was observed under the equivalent photochemical age of over one week for an assumed average atmospheric [OH] of 1.5×10^6 molec. cm^{-3}. We showed that the mass

of secondary products formed through aqueous-phase oxidation is significant and it may potentially provide opportunities for understanding the evolution of the DMS-derived gas-phase oxidation products through aqueous-phase pathways. With the increasing amount of cloud droplets , twice as much secondary aerosol mass was formed under the equivalent photochemical age of up to one week and fragmentation of particle-phase products happened under the photochemical age of two weeks with the presence of liquid water within aerosols. The effects of oxidant competition and aerosol acidity on DMS-derived secondary aerosol formation were also investigated in this study. Based on our results, a rapid decrease of MSA has been observed with the higher OH/ozone ratio, which indicates that MSA may not be a persistent product through aqueous-phase oxidation and it's likely the observed sulfate was formed through another pathway, such as DMS→ HMPTF→ SO_2. Approximately two times increase in secondary aerosol mass has been observed with the presence of dry acidic seeds, which may indicate that dry acidic seed aerosols could initiate and facilitate the formation of high-molecular-weight and low-volatility products (e.g. oligomers) through acid-catalyzed particle-phase heterogeneous reactions. However, the acidity level may alter the aqueous-phase pathways and main secondary products, resulting in less conversion of DMS to further oxidized products. Our results also highlighted the influence of aerosol liquid water content and OH exposure levels on the chemical composition of DMS oxidation products. The formation and fraction of SA in resulting aerosols showed strong dependence on OH_{exp} under all studied conditions; while the MSA formation was more complicated, and its formation depended both on OH_{exp} and RH. It is also noticeable that MSA may have gone through heterogeneous oxidation with extra OH

and possibly other chemical or physical loss processes. Alternatively, the MSA precursor (including DMSO, MSIA etc.) may have gone through other reaction pathways and form oxygenated-organic compounds instead of MSA eventually, which could also explain the loss of MSA and the change of residual organics composition under extremely high OH_{exp}. We conclude that over open ocean, the presence of aerosol liquid water and clouds may alter MSA formation pathway and concentration compared to dry conditions, while SA remains the main DMS oxidation product at long OH_{exp}. It is also important to note that presence of cloud droplets decreased secondary aerosol yield and resulted in the loss of MSA at high OH_{exp}. Although traditionally MSA was considered to be the most important DMS aqueous-phase oxidation product in the presence of OH and O_3, our study indicates that some highly-oxygenated organic compounds formed possibly through MSIA OH oxidation will be very stable in the atmosphere after long photochemical aging, and their contribution to the DMS-derived secondary aerosol is non-negligible.

.